LIÈGE université Sciences

Academic year 2022-2023

STATIC AND DYNAMIC PROPERTIES OF SELECTED MICROMAGNETIC DEVICES

Emile FOURNEAU

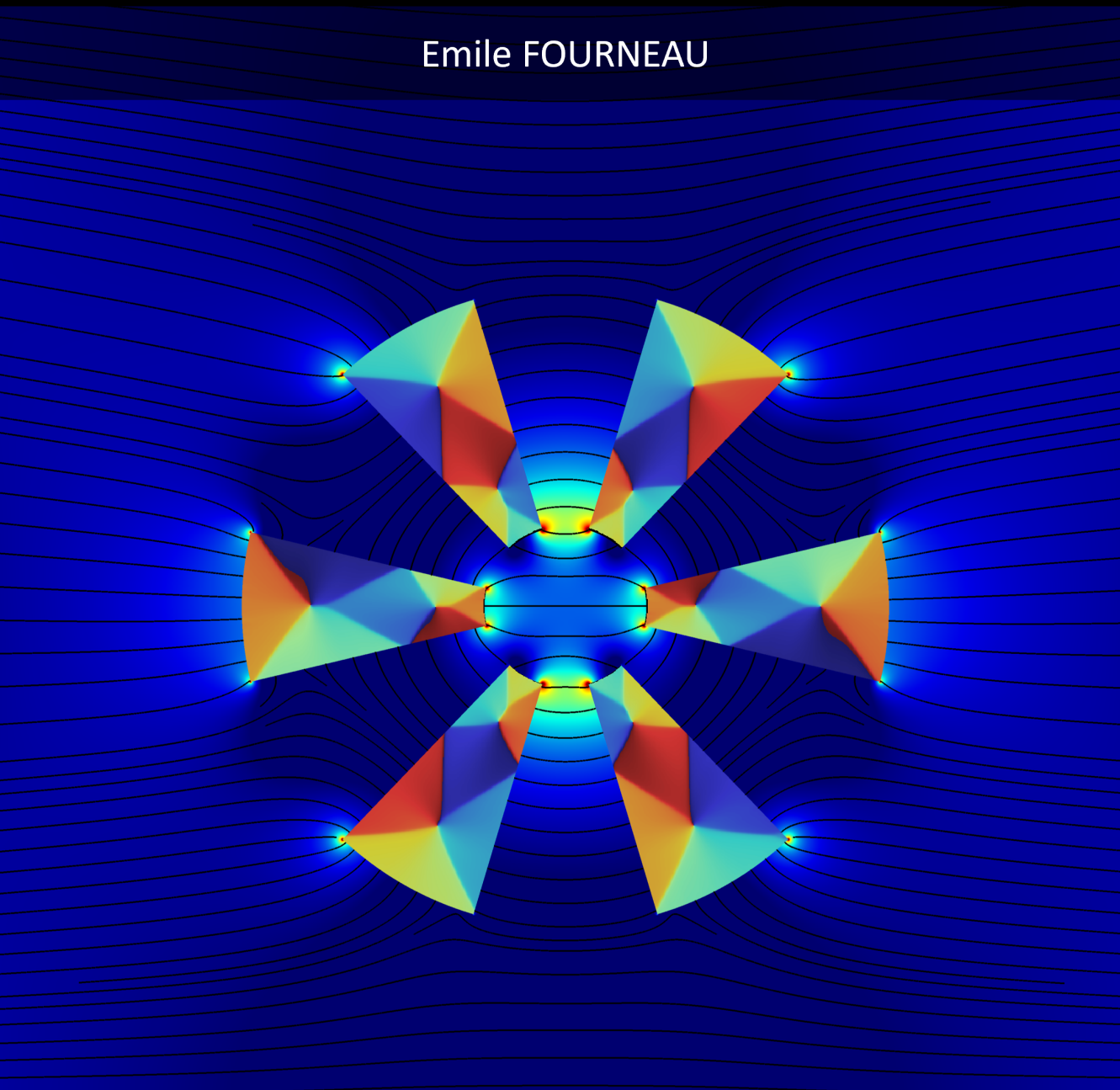

Faculty of Sciences, Univertsity of Liège,
Q-MAT Center, CESAM Research Unit
-
Solid-state Physics: Interfaces and Nanostructures,
Experimental Physics of Nanostructured Materials

Static and dynamic properties of selected micromagnetic devices

Emile Fourneau

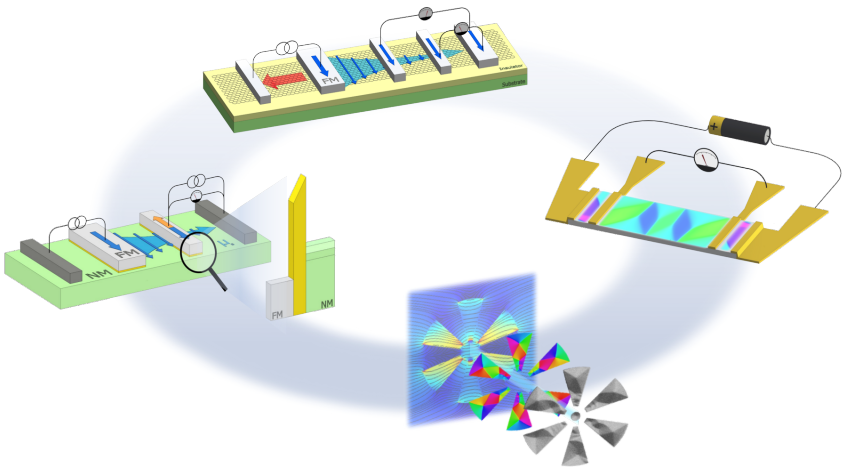

October 2022

Ph.D. thesis committee :

Chairman :
Prof. Dr. M. VERSTRAETE, University of Liège (Liège, Belgium)

Secretary :
Prof. Dr. B. VANDERHEYDEN, University of Liège

Advisors :
Prof. Dr. N. D. NGUYEN, University of Liège
Prof. Dr. A. V. SILHANEK, University of Liège

Jury members :
Dr. E. BOUSQUET, University of Liège
Prof. Dr. I. A. FISCHER, Brandenburg Techn. U. (Cottbus, Germany)
Prof. Dr. B. VAN WAEYENBERGE, U. Gent (Gent, Belgium)

Dissertation presented in partial fulfilment of the requirements for the degree of Doctor in Science. The manuscript was defended during a public oral examination on the 15th of November 2022.

Abstract

Magnetic properties of matter are essential for a wide range of current and future technologies, especially in the domain of microelectronics for which spintronics is largely involved in the next generations of devices. This dissertation, composed of two distinct parts, presents an original research work on microscopic magnetic devices allowing the control and detection of static magnetic fields (part I), and the transmission and sensing of pure spin currents (part II).

Firstly, the development of metasurfaces composed of a concentric arrangement of micrometer-wide ferromagnetic petals and allowing the magnetic flux concentration is investigated. Micromagnetic simulations demonstrate the importance of the magnetic domains configuration on the linear response of the device. In the operating regime of the device, a concentrated magnetic field around two times the external field is predicted irrespective of the in-plane applied field direction. The experimental proof-of-concept is demonstrated with 60 nm-thick permalloy structures. The concentration gain is obtained by optically tracking the magnetic vortex at the center of a permalloy disk sensor, using Kerr microscopy.

The second study presented in this thesis focuses on the sharp magnetoresistance changes, triggered by out-of-plane magnetic fields, probed in thin permalloy strips grown on monocrystalline lanthanum aluminate substrates. Micromagnetic simulations are used to evaluate the resistance changes of the strips at different applied field values and directions and correlate them with the magnetic domain distribution. The experimentally observed sharp magnetic switching, tailored by the shape anisotropy of the strips, is properly

accounted for by the numerical simulations when considering an important substrate-induced uniaxial magnetic anisotropy with a main direction sligthly tilted from the out-of-plane direction.

The second part of this thesis is devoted to non-local spin-valves made of ferromagnetic tunnel junctions and implemented for electron spin injection, transport and detection of pure spin currents.

We first demonstrate that the non-linear electrical transport occurring in tunnel junctions may lead to a spin-to-charge conversion efficiency larger than 10 times the spin polarization of the tunnel barrier when the latter is under a bias voltage of a few millivolts. The underlying mechanisms are attributed to the tunnel-barrier deformation and the conduction-band shift resulting from a change of the applied voltage. An approximated analytical expression predicting the detector spin sensitivity is suggested. Calculations performed for different barrier shapes show that this enhancement is present in oxide barriers as well as in Schottky-tunnel barriers, and that it depends on the intensity of the spin accumulation generated in the channel. Moreover, although reduced at high temperatures, the spin signal remains superior to the value predicted by the linear model.

Finally, we demonstrate that the Hanle precession method as conventionally applied is no longer accurate when the distance between the inner and outer electrodes becomes smaller than 6 times the spin diffusion length, leading to errors as large as 50% for the calculation of the spin figures of merit. We suggest simple but efficient approaches to circumvent this limitation by addressing a revised version of the Hanle fit function and by proposing a refined fabrication process for four-terminal non-local spin valves.

Résumé

Les propriétés magnétiques de la matière sont au centre de nombreuses technologies actuelles et futures, particulièrement dans le domaine de la micro-électronique où les nouvelles générations de dispositifs à venir font la part belle au magnétisme, notamment sous l'impulsion de la spintronique. Dans la présente thèse, structurée en deux parties, nous rapportons les travaux de recherche réalisés sur quatre dispositifs magnétiques à l'échelle micro et nanoscopique permettant le contrôle et la détection, dans la partie I, de champs magnétiques statiques et, dans la partie II, de courants de spin.

En premier lieu, le développement de métasurfaces composées d'un agencement concentrique de pétales microscopiques ferromagnétiques et permettant la concentration de flux magnétique est examiné. Des simulations micromagnétiques permettent de démontrer l'importance de la configuration adoptée par les domaines magnétiques sur le régime de réponse linéaire du dispositif. Dans ce régime de fonctionnement du dispositif, un pouvoir de concentration permettant de doubler l'intensité du champ au centre du dispositif est prédit, l'effet demeurant indépedant de la direction du champ appliqué. Le fonctionnement du dispositif est prouvé expérimentalement via la fabrication de structures en permalloy de 60 nm d'épaisseur pour lequel le gain est obtenu en traquant, par microscopie Kerr, le déplacement d'un vortex magnétique dans un capteur placé au centre du dispositif.

La deuxième étude présentée dans cette thèse s'intéresse à la réponse magnétoresistive abrupte induite par un champ magnétique hors du plan, qui est observée dans des films minces de permalloy structurés sous forme de barreaux microscopiques sur substrat d'aluminate de lanthane. Des simulations micromagnétiques permettent d'attribuer le changement de résistance à une

variation de la distribution des domaines dans le plan du film. Nos mesures expérimentales montrent que l'intensité du champ hors du plan nécessaire à la rotation de l'aimantation dans le plan dépend de la géométrie du barreau. Les simulations micromagnétiques démontrent que ce phénomène ne peut être expliqué qu'en considérant la présence d'une forte anisotropie uniaxiale induite par le substrat et légèrement inclinée par rapport à la direction normale du film.

La seconde partie de cette thèse est consacrée aux vannes de spin non locales, des dispositifs composés de jonctions tunnel ferromagnétiques et servant à l'étude de l'injection, du transport et de la détection de courants pures de spin.

Tout d'abord, nous démontrons que le transport électrique non-linéaire propre aux jonctions tunnel peut mener à une efficacité d'interconversion spin-charge jusqu'à 10 fois plus grande que la polarisation de spin de la barrière lorsqu'une tension de quelques mV est appliquée à cette dernière. L'effet est attribué à la déformation de la barrière tunnel et au déplacement relatif de la bande de conduction du canal de spin, tous deux induits par l'application d'une tension électrique. Une solution analytique prédisant l'intensité du mécanisme est proposée. Des simulations réalisées pour différentes formes de barrière mettent en évidence que l'augmentation de l'efficacité est également présente dans des barrières tunnel de type Schottky et qu'elle dépend de l'intensité du courant de spin injecté dans le canal. Les résultats montrent également que, malgré une forte diminution à plus haute température, l'effet reste conséquent à température ambiante.

Enfin, dans une dernière étude, nous démontrons que la méthode dite de précession de Hanle, communément utilisée pour évaluer la longueur de diffusion des spins, donne lieu, en l'état, à des imprécisions de l'ordre de 50% lorsque la distance entre les électrodes internes et externes est inférieure à 6 fois la longueur de diffusion de spin. Une alternative simple mais efficace est proposée pour contourner cette limitation, en utilisant une version adaptée de la fonction d'ajustement de Hanle et en épurant le procédé de fabrication du dispositif de vannes de spin.

Acknowledgement

Although my name is alone on the cover page of this dissertation, this thesis results definitively from a teamwork. I would like to acknowledge everyone that help me to accomplish this work.

First, I would like to express my gratitude to the jury for taking the time to review my thesis and assisting to my defense.

I would like to thank Anna Palau and her group (ICMAB-CSIC) for the fruitful collaborations and hopefully those to come. Many thanks to Vojtěch Uhlíř and all people from CEITEC magnetism for their hospitality and warm welcome. Especially, I would like to thank Jon Ander Arregi. Those two weeks in Brno were pleasant and scientifically successful thanks to you. And sorry again for your finger.

Obviously, I need to thank my co-promoters Duy Nguyen and Alejandro Silhanek, for the opportunity they had given to me 6 years ago as well as for all the constructive discussions and feedback. Duy, thank you for your kindness and your patience. I really appreciated the trust you place in me, especially regarding the pedagogical tasks. I certainly learn from you the will to constantly look after the best ways for teaching science. Alejandro, thank you for the second breath you bring to my thesis with the multiple projects that I needed to run full bore. I liked all the discussions we had, scientific or not. Particularly, the football discussion which were sadly not welcomed with other members of the lab since their interest for football is equivalent to their skills on the pitch. No hard feelings, guys.

Speaking of them, I would like to acknowledge all my former and current colleagues, Jonathan, Jeremy, Xavier, Joseph, Sylvain, Thomas, Simon, Sunil,

Naama, François, Suraj and Stefan. Thank you for the smartest and stupidest things you taught me in the lab and outside. From the conception of VIVALDI to the political discussions about bourgeoisie or hunting, each "van Aert vs van der Poel" debate, the electronics projects and the tool debugging, I appreciated every moments in your company. Thanks also to Nicolas, my young padawan. I am sure that your thesis will be successful but, here is my final advise: in case of doubt, turning left is always better.

Je n'ai jamais été du style à prendre régulièrement des nouvelles des gens qui comptent pour moi. Mais je dois reconnaître que ces derniers mois, j'étais loin d'être l'amis, le frère, le fils, le petit-fils et le parrain qu'ils méritent. J'espère que vous me pardonnerez pour ce long tunnel d'égoïsme. Merci à ma famille pour leur patience et leur présence, et merci à tous mes amis pour les moments d'évasion, de sport et de rire.

Enfin, Alice, pour tout ce que tu m'apportes tous les jours depuis plus de 8 ans, pour tous ce que tu as enduré pour nous deux ces derniers temps mais aussi pour cette magnifique page de garde, je ne pourrais jamais te remercier assez. Je t'aime.

Pour conclure et parce qu'il faut garder une part d'enfant en soi, je ne résiste pas à l'idée de terminer ce chapitre par les mots du plus grand d'entre-nous.

La passion et les rêves sont comme le temps, rien ne peut les arrêter et il en sera ainsi tant qu'il y aura des hommes prêts à donner un sens au mot "liberté".
Gol D. Roger

Contents

List of Figures

Acronyms

2T two-terminal.

3T three-terminal.

4T four-terminal.

AFM atomic force microscopy.

AMR anisotropy magnetoresistance.

B tunnel barrier.

BCC body-centered cubic.

DOS density of states.

DP D'yakonov-Perel'.

EA easy axis.

ECP electrochemical potential.

EY Elliott-Yafet.

FCC face-centered cubic.

FEM finite element method.

FM ferromagnetic.

FoM Figure of merit.

FWHM full width at half maximum.

HA hard axis.

HCP hexagonal close packing.

IP in-plane.

IPM ideal paramagnetic material.

LAO Lanthanum aluminate.

LLG Landau-Lifshitz-Gilbert.

LSV local spin valve.

MD multi-domains.

MFC magnetic flux concentrator.

MFM magnetic force microscopy.

MOKE magneto-optical Kerr effect.

MR magnetoresistance.

NLSV non-local spin valve.

NM non-magnetic.

OOP out-of-plane.

PM paramagnetic.

PMA perpendicular magnetic anisotropy.

PPMS physical property measurement system.

Py Permalloy.

RA resistance-area.

SC semiconductor.

SD single domain.

SEM scanning electron microscopy.

SHPM scanning Hall probe microscopy.

SOC spin-orbit coupling.

SQUID superconducting quantum interference device.

SV spin valve.

WKB Wentzel–Kramers–Brillouin.

1 Introduction

Technologies relying on magnetism and magnetic materials are everywhere and could be traced back to centuries ago when permanent magnets were the essential component of navigational compasses [1]. Nowadays, magnetic components occupies a central place in everyday life, playing a major role in commonly and intensively used high-tech and are expected to remain a key building block in future technologies [2, 3]. Among the more common examples of commercial applications, one can cite the field of medicine with magnetic resonance imaging, computers, data storage devices, credit cards within the domain of information and communication, as well as engineered machines such as electric motors, household appliances, and many more.

The continuous strive for miniaturization of electronic components has been the driving force to achieve amazing developments on micro and nanofabrication in the recent decades.

Magnetic materials have not been exempted from this trend. Within this context, the fundamental need for mastering the magnetic response at micrometer scales requires a deep understanding of the magnetic moment distribution in the systems of interest. This imperative has been enabled thanks to the development of micromagnetic simulations with a remarkable power of high accuracy predictions. In addition, the realm of microscale systems has permitted the unprecedented possibility to transfer information through spin currents. Unlike electronic communications that can operate a large scales by virtue of charge conservation, spin is a non-conserved quantity and small scale is a requisite for transport and manipulation of spin currents. Although these two subdomains, *Micromagnetics* and *Spintronics*, are to a large extent intertwined, the former mainly deals with localized moments whereas the latter frequently implies delocalized spin carriers, leading them

to be typically addressed as separate topic in the literature.

In this thesis, magnetic-based devices relying on both of these fields of low-dimensional magnetism are investigated. The first part is devoted to the influence of magnetic domain distribution in microscopic technologically-relevant designs while the second part focuses on particularities of devices used for the generation and detection of spin currents. For the sake of clarity, a specific introduction is proposed for each domain in the two following subsections, and the detailed motivation and structure of this work are presented in the last section.

Magnetism in mesoscopic structures

The existence of magnetic materials can find satisfactory explanation only through the prism of quantum mechanics as it involves the concept of spin. The understanding and prediction of magnetic materials can in principle be achieved through ab initio calculations based on Schrödinger's equations. However this approach is not suited for micrometer-scale devices due to the exceedingly large number of atoms. Among the models proposed to enable calculations of relatively large volumes, the micromagnetic theory turns out to be perfectly suited for microscopic description of magnetic domains and their interfaces (domain walls). This theory was first postulated by Landau and Lifshitz [4] in 1935 on the basis of the pionneer domains theory of Weiss [5] and the experimental works of Bitter [6] and Sixtus and Tonks [7]. The model will finally be completed and summarized in the 1960s by Brown in his work entitled "Micromagnetics" [8]. Micromagnetism describes the magnetization at an intermediate scale where the quantum description of individual spins is hidden inside the concept of a mean local magnetic moment and the interactions with its neighboors are described by the Landau-Lifshitz-Gilbert (LLG) equation in presence of an effective field [9]. Although the model has existed for 50 years, the general complexity of the LLG equation limits the cases for which an analytical solution can be found to rather simple cases. Therefore, it is only with the progress in high-throughput computation, together with the development of numerical solvers (such as MuMax^3 [10], OOMMF [11]) that Micromagnetics took off.

Nowadays, micromagnetics proves its efficiency to predict static domains arrangement and dynamic response to external stimuli in many kinds of applications. Simulations lead to considerable improvements in the down-scaling of currently used magnetic devices such as hard-drives [12], random access memories [13, 14] or flux concentrators [15], but also help in the understanding and the development of future technologies based on skyrmions

[16, 17] or magnons [18, 19].

One specific category of materials that takes advantages of micromagnetic simulations are magnetic metamaterials and metasurfaces. They are artificial materials media patterned in such a way that unique properties, unreachable with bulk or thin film samples, are obtained. Metasurfaces were initially suggested for optics and the fabrication of negative refractive index superlenses [20]. Recently, remarkable performances of magnetic cloacking and flux concentration at low-frequency have been predicted based on metamaterials combining permanent magnets and superconductors [21, 22]. The efficiency of this technology has already been experimentally demonstrated at the macroscopic scale [23, 24] and its equivalent at the microscale would greatly improve the performance of magnetic sensors in integrated circuits and bear promising perspectives in energy harvesting and magnetic shielding.

Spintronics

Spintronics, the combination of spin and electronics, is the field of condensed matter physics that deals with the transfer and manipulation of spins. Spintronics is a serious contender to classical electronics, offering better performances in terms of energy dissipation and processing speed, coupled with the non-volatility of permanent magnets [25, 26].

The first theoretical works by Mott including the spin degree of freedom for the study of electron transport in ferromagnetic metals opened the path to the concept of magnetoresistance, i.e. the influence of magnetic fields on the electrical resistance [27]. Later on, the discovery of giant magnetoresistance by Fert [28] and Grünberg [29], is considered as the turning point for the development of spintronics, for which they were awarded by the Nobel prize in 2007. Giant magnetoresistance and tunnel magnetoresistance rely on the transfer of spins through a heterostructure made of two ferromagnetic layers separated by a few nanometer-thick non-magnetic film, thinner than the spin diffusion length. These so-called spin-valves will be at the origin of many spin-based devices such as the spin transistor proposed by Datta [30] or spin-RAMs [31].

The second generation of spintronic devices is based on the transport and manipulation of pure spin currents, free of any thermal loss induced by Joule heating [32]. There exist several techniques to generate a pure spin current in non-magnetic materials such as spin pumping triggered by ferromagnetic resonance, ligth-induced spin generation [33] or thermally-driven spin injection [34], although electrical spin injection currently remains the more suited method regarding the technological interest of integrating

spin-based technologies on mainstream electronic chips manufactured in semiconductor industry.

The major issues of Spintronics are the improvement of injection efficiency, diffusion distance and manipulation. In that context, the non-local spin-valves method is a popular approach to evaluate the performance of materials for the propagation of pure spin current. Recently, major improvements have been achieved for spin injection in 2D materials [35], leading to an efficient detection of spin current after propagation over more than ten micrometers[36]. Despite the fact that the non-local spin-valves technique is considered as well-established, the continuous enhancement of device fabrication methods, the development of new types of materials used as spin transport media or the diversity of measurement configurations require constant updates regarding the method to evaluate the spin figures of merit such as the spin lifetime or the spin diffusion length.

Outline of the thesis

In this dissertation, we have investigated the static and dynamic properties of selected micromagnetic devices involving microscale magnetic sensors and flux concentrators (part I) as well as spintronic devices (part II). The manuscript is divided in two blocks, each containing three chapters.

The first part, entitled *Micromagnetism*, gathers the works on devices relying on the static response of patterned ferromagnets.

Chapter 2 presents a theoretical background describing the important notions about ferromagnetism and magnetic domains. This chapter introduces the theory of Micromagnetism as well as the experimental techniques for magnetic domains observation that are used in the two following chapters.

In **Chapter 3**, a prototype of magnetic flux concentrator made of thin film metamaterials is investigated on the basis of results obtained previously with a macroscopic equivalent device. The system is studied theoretically, considering first the linear magnetic response and then including the non-linearity of ferromagnets by means of micromagnetic simulations. In the last part of the chapter, the efficiency of the flux concentrator is experimentally-verified using Kerr microscopy.

Chapter 4 is devoted to the interpretation of the remarkable response of a planar magnetic sensor to the presence of an out-of-plane magnetic field. The experimental observations are first presented and then, in a second part, micromagnetic simulations are used to give an interpretation to the origin of the unexpected out-of-plane sensitivity.

The second part of this dissertation deals with the concept of *Electrical Spin Injection*.

First, in **Chapter 5**, the theoretical background introducing the concept of electrical spin injection essential for the understanding of the subsequent chapters is presented. This chapter addresses the notions of spin current, spin filtering resistance as well as the working principle of spin-valves and the Hanle precession.

In **Chapter 6**, a work focusing on the impact of the biased modulation of the detection efficiency in non-local spin-valves is summarized. The light is shed on the origin of this mechanism which leads to a giant spin detection efficiency and on the impact of the type of tunnel barrier. Finally, we deliver a discussion on how the nonlinear spin transport fundamentally induces an error for the extraction of spin lifetime.

Chapter 7 is also devoted to non-local spin-valves devices. In this chapter, we demonstrate the importance of the external electrodes for the extraction of spin figures of merits when working with media that exhibit large spin propagation length. A solution to simplify the fabrication and the measurement process is proposed along with an adapted equation to identify the spin lifetime.

Finally, in **Chapter 8**, we conclude by summarizing the main findings of this thesis and by offering some additional remarks and perspectives for future research direction.

Part I

Micromagnetism

2

Magnetic texture in ferromagnetic micro-structures

2.1 Introduction

In its simplest definition, a ferromagnetic (FM) material is a material characterized by a spontaneous magnetization which generates a strong magnetic field in its vicinity. The overall phenomenon is made possible by the alignment of the atomic magnetic moments towards a common direction in a limited region called magnetic domain. The behavior of ferromagnetic materials immersed into a magnetic field is directly related to the nucleation, distribution and mobility of domains. The domain size and the defect types at the interface between two domains (domain walls) are also important factors, particularly when dealing with sub-millimeter magnetic devices due to the limited domain dimensions. In this chapter, we will review the notions that are necessary for the definition of FM materials and introduce the micromagnetic equations, a powerful theory that allows us to compute ferromagnetic properties of micrometer-scale devices. We first introduce the concept of magnetic moment as the fundamental bricks to understand FM properties and provide a description of the interaction of a set of magnetic moments. Secondly, we describe the ferromagnetic figures of merit in a macro-scale environment, along with the concept of magnetic domains which are central in the first part of this thesis. Then, we present in details the micromagnetic theory and derive the mathematical expression of the different energy contributions in the context of the continuum approximation. Finally, in the last section, we focus on the magnetic reversal process in the specific case of magnetic thin films with micrometer scale ferromagnetic patterns.

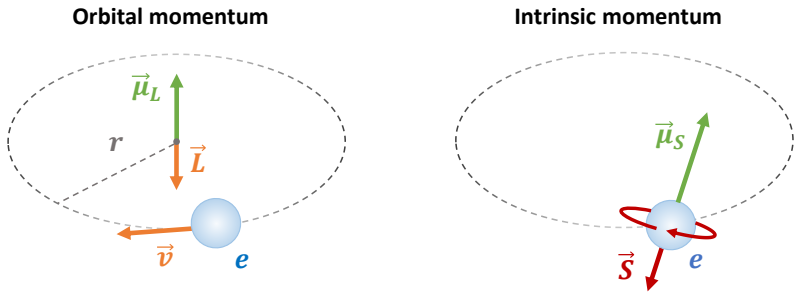

Figure 2.1: *Schematic illustration of electrons orbital (left) and spin (right) magnetic moments. Note that, since the electron has a negative charge, the respective magnetic moments are aligned in the opposite direction to the angular momentum and spin vector.*

2.2 Magnetic moments and interactions

While it can be approached by means of semi-classical physics, the origin of the magnetic moment of an atom can only be rigorously described by a quantum mechanic theory as stated by the Bohr-Van Leeuwen theorem [37]. The magnetic moment is intrinsically linked to the angular momentum of electrons. Firstly, the magnetic moment is related to the orbital angular momentum which can be classically pictured as the magnetic field produced by the current of a single electron orbiting around a nucleus. In atoms, angular and magnetic momentum have the same direction and are proportional:

$$\boldsymbol{\mu}_{\mathrm{L}} = \gamma \mathbf{L}, \tag{2.1}$$

where $\gamma = \dfrac{-e}{2m_e}$ is the gyromagnetic ratio of an electron. Note that since $\gamma < 0$, the angular momentum $\mathbf{L}$ and $\boldsymbol{\mu}_{\mathrm{L}}$ have opposite orientations.

Secondly, the magnetic moment has another contribution emerging from the relativistic quantum-mechanical description of the electron and known as the intrinsic spin angular momentum S (see Figure 2.1). From Dirac's equation, it results that the magnetic moment of an electron along the spin direction is given by

$$\mu_{\mathrm{s}} = g\mu_B m_{\mathrm{s}}, \tag{2.2}$$

where g is the Landé g-factor and is approximately -2 for electrons, μ_B is Bohr's magnetron and m_{s} is the spin quantum number. Even though the spin has quantum mechanic origin, in the framework of this thesis, we will assume a classical description of the electron spin contribution to the

magnetic moments, which is expressed as follows:

$$\boldsymbol{\mu_s} = \frac{g\mu_B}{\hbar}\mathbf{S} \tag{2.3}$$

with $\mathbf{S}$ a vector with modulus $\hbar/2$. The total magnetic moment of an atom will depend on the spin and the angular momentum of all its localized electrons. In the case of an isolated atom, the L and S configuration minimizing the energy of the system can be estimated by following the empirical Hund's rules [38]. It is therefore straightforward that elements having electronic configuration with unpaired electrons such as d-type ferromagnetic materials (Fe, Ni, etc.) will exhibit a higher magnetic moment. Finally, it is worth noting that atom nuclei also possess an intrinsic magnetic momentum but the magnitude of the latter is negligible compared to the contribution of electrons since the gyromagnetic ratio (γ) is inversely proportional to the particle mass.

The magnetic field generated by a ferromagnet results from the contribution of every atom and is expressed as the magnetization vector $\mathbf{M}$, a magnetic moment per unit volume. In other words, the larger the atomic magnetic moment, the higher the magnetization. The maximal value of the magnetization, the saturation magnetization M_s, is reached when all magnetic moments are aligned in the same direction, which can be achieved by applying an external magnetic field. In contrast to that, in the case of a set of randomly orientated magnetic moments, the magnetization tends to zero whatever the intensity of the magnetic moment. This simple fact shows that a strong atomic magnetic moment is not enough to explain the magnetism of matter. Indeed, in every magnetic material, a progressive decrease of magnetization is observed for any magnetic materials when approaching the Curie temperature T_C since thermal excitation tends to randomize the local direction of $\boldsymbol{\mu}$, as illustrated in Figure 2.2(a). The Curie temperature reflects the stability of the magnetic moments ordering despite the thermal perturbations and therefore, it acts as an indicator of how strongly moments do interact. It is worth noting that the Curie temperature of the material and the intensity of the magnetic moment of its atoms are not correlated, as shown in Figure 2.2(b) for typical ferromagnetic materials[1] [39, 40]. The behavior of a given magnetic material does not only depend of the mean intensity of the magnetic moments but also on their interactions. In fact, most of ferromagnetic properties such as the intensity of the spontaneous magnetization, its response to an external magnetic field or the way it is

[1]Note that the magnetic moment is not an integer multiple of μ_B because of spin-orbit coupling interactions or non-localized electrons in metallic materials. The link between ferromagnetism and conduction electrons is discussed in the second part of the manuscript.

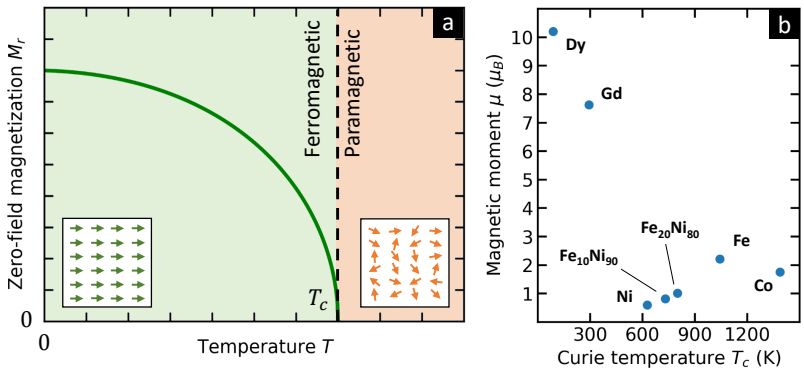

Figure 2.2: *(a) Example of the temperature dependence of the magnetization in the absence of an external field for a ferromagnetic materials. Above the Curie temperature T_C, thermal agitation randomizes the direction of magnetic moments. (b) Comparison of common ferromagnetic materials in term of Curie temperature and magnetic moment.*

affected by confinement, result from the interplay between different magnetic interactions. In the following, we will briefly introduce these interactions as it will help us to understand the main features of ferromagnetic materials. Figure 2.3 summarizes the main interactions: (a) exchange interaction, (b) Zeeman, (c) dipolar interaction and (d) spin-orbit coupling interaction.

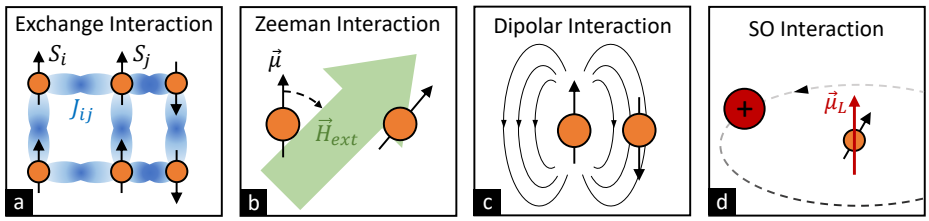

Figure 2.3: *Summary of the main interactions acting between magnetic moments.*

- **Exchange interaction:** The alignment of neighboring magnetic moments in ferromagnets is attributed to the exchange interaction. This is a short-range interaction based on quantum mechanical considerations of two indistinguishable particles (such as electrons) imposing a specific symmetry of the joint wavefunction depending on their spin configuration (due to Pauli's exclusion principle). Consequently, exchange interaction induces a different energy cost for parallel and anti-parallel

spin configuration. In essence, Pauli's exclusion principle forces the spatial separation of electrons with identical spin which, in turn, minimizes the Coulomb repulsion between them. Exchange can be *direct* when it only implies electrons of neighbouring atoms (requiring overlapping of wave functions) or *indirect* through an intermediary such as conduction electrons in transition metals or non-magnetic ions in ionic solids [41]. The energy related to the exchange interaction between different spin S_i is given by

$$E = -\sum_{i,j} J_{\mathrm{ij}} \mathbf{S}_i \cdot \mathbf{S}_j, \tag{2.4}$$

where J_{ij} is the exchange integral between spin i and j. In ferromagnetic materials, J_{ij} is positive, ensuring a natural parallel configuration of the magnetic moments.

- **Zeeman interaction:** The magnetic moments tend to align with an external field $\mathbf{H_a}$ [38]. This interaction is described by an energy which depends on the relative orientation of the magnetic moment compared to the external field

$$E = -\boldsymbol{\mu} \cdot \mu_0 \mathbf{H_a}, \tag{2.5}$$

where μ_0 is the vacuum permeability. The Zeeman interaction is the interaction triggering the change of magnetization by means of an external field. The stronger the magnetic field, the more stable the parallel configuration between $\boldsymbol{\mu}$ and $\mathbf{H_a}$.

- **Dipole-Dipole interaction:** The magnetic dipolar interaction refers to the interaction between a magnetic moment and the field generated by another magnetic moment. This interaction depends on the intensity and the degree of alignment of both magnetic moments. Considering two magnetic dipoles μ_i and μ_j separated by a distance $\mathbf{r}$, the energy related to their interaction is given by

$$E = \frac{\mu_0}{4\pi r^3} \left[\boldsymbol{\mu}_j \cdot \boldsymbol{\mu}_i - \frac{3}{r^2} (\boldsymbol{\mu}_i \cdot \mathbf{r})(\boldsymbol{\mu}_j \cdot \mathbf{r}) \right], \tag{2.6}$$

where μ_0 is the vacuum permeability. In contrast to the exchange interaction, the dipole-dipole interaction is long-range, tends to pull together opposite poles, and is much weaker than the exchange interaction.

- **spin-orbit coupling (SOC):** In a semi-classical approximation, one can describe the SOC interaction as a Zeeman interaction between the magnetic momentum of the spin and a field generated by the movement

of nucleus orbiting around the electron [42]. This field can be expressed as a function of the angular momentum **L** through

$$\mathbf{B} = (\mathbf{E} \times \mathbf{v})/c^2 = \frac{-1}{rc^2}\nabla V(\mathbf{r} \times \mathbf{v}) = -\frac{\mathbf{L}}{m_e r c^2}\nabla V, \tag{2.7}$$

where m_e is the electron mass and c the speed of light in vacuum. **v** is the electron velocity, **E** and **V** are respectively the electric field and potential it experiences, and r its distance from the nucleus. Therefore, using the definition of Eq. (2.5)[2], the energy related to spin-orbit coupling is

$$E_{SO} = -\frac{1}{2}\boldsymbol{\mu_s} \cdot \mathbf{B} = \frac{g\mu_B}{2c^2\hbar m_e r}\frac{dV(r)}{dr}\mathbf{S} \cdot \mathbf{L}. \tag{2.8}$$

This effect refers to the interaction between orbital and spin magnetic moments. As the crystal lattice defines the orbital direction through the crystal field, the coupling between spin and orbital momenta can give rise to a preferential crystalline direction for the alignment of the spin magnetic moments called the magneto-crystalline anisotropy (see section 2.4.2) [43]. Spin-orbit coupling is also at the origin of others interesting phenomena of magnetism such as magnetostriction or the antisymmetric exchange (also known as the Dzyaloshinskii–Moriya interaction) which are not introduced in this work.

Depending on the dominant magnetic interactions in a given material, magnetic moments will be ordered differently, leading to various types of magnetism. In the absence of any external field, magnetic materials in which exchange interaction is weak have no net magnetization. A non-zero magnetic field leads to the alignment of the moments parallel (*paramagnetic* materials) or anti-parallel (*diamagnetic* materials) to the applied field. For materials with strong exchange interactions, magnetic moments will spontaneously order either in a parallel configuration (*ferromagnetic* materials) or anti-parallel configuration (*antiferromagnetic* materials if the magnitude of opposed magnetic moments are equals leading to a zero net magnetization, and ferrimagnetic materials if the sublattices magnetization are inequivalent). In this work, we will focus on ferromagnetic materials.

2.3 Characterization of the ferromagnetic state

At the macroscopic scale, the magnetic order can be described by the material permeability μ, the ratio between the magnetic flux **B** in the material and

[2]The factor 1/2 comes from the proper treatment of relativistic effects in the calculations.

the external field $\mathbf{H_a}$, leading, for a homogeneous and isotropic magnetic material, to the constitutive relation

$$\mathbf{B} = \mu \mathbf{H_a} = \mu_0 (1 + \chi_m) \mathbf{H_a}, \tag{2.9}$$

where χ_m is the magnetic susceptibility:

$$\chi_m = \frac{\partial M}{\partial H_a}. \tag{2.10}$$

For weakly ordered magnetic materials under low $\mathbf{H_a}$ (i.e. far below the saturation field), χ_m is either a positive (paramagnetism) or a negative (diamagnetism) constant while it is highly field-history-dependent for ferromagnets. The previous equation is only suited for materials showing a linear response to an external field. A more accurate description requires to deal with the magnetization $\mathbf{M}$ itself.

$$\mathbf{B} = \mu_0 \left[\mathbf{H_a} + \mathbf{M}(\mathbf{H_a}) \right]. \tag{2.11}$$

The hallmark of ferromagnetic materials is the irreversible nonlinear change of the magnetization $\mathbf{M}$ with the applied field $\mathbf{H_a}$. As presented in Figure 2.4, the magnetic response depends on the former magnetic history and depicts an hysteretic loop. After being fully magnetized, a ferromagnet conserves part of its magnetization, called remanent magnetization $\mathbf{M}(0) = \mathbf{M_r}$, in absence of external field. Consequently, a coercive field $\pm H_c$ has to be applied in order to achieve $\mathbf{M} = \mathbf{0}$[3].

2.3.1 Rigidity and remanent magnetization

The remanent or spontaneous magnetization was explained in the first modern theory of ferromagnetism by Pierre-Ernest Weiss who postulated that ferromagnetism is due to a large internal molecular field proportional to the magnetization and reproduced qualitatively well the variation of the spontaneous magnetization with temperature as illustrated in Figure 2.2. Thirty years later, Heisenberg proved that this fictive molecular field is due to the exchange interaction between magnetic moments of the material[4] [44]. When

[3] It is worth noting that the coercive field is sometimes defined as the field needed to bring the total magnetic flux $\mathbf{B}$ to zero. Based on Eq. (2.11), the coercive field in a homogeneous ferromagnet is given by $\mathbf{H}_c = -\mathbf{M}(\mathbf{H_c})$, which does not correspond to a zero magnetization. Nevertheless, as the magnetization varies strongly with the applied field in the vicinity of the coercive field, both definitions lead to values of $\mathbf{H_c}$ close to each other.

[4] Note that exchange interaction does not imply a strong magnetic field such as that imagined by Weiss, it is rather a matter of electrostatic interactions.

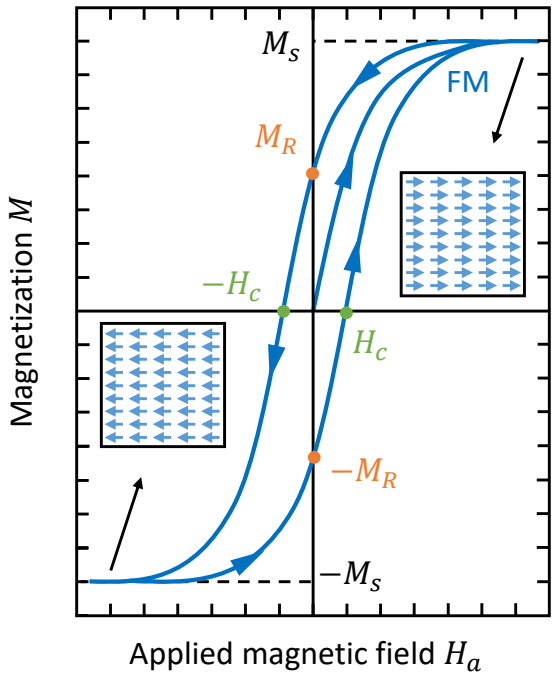

Figure 2.4: *Schematic representation of the hysteresis loop of a ferromagnetic material.*

cooling down a ferromagnetic sample, the rotation symmetry C_∞ is broken because the strong exchange correlation overcomes the thermal agitation and the system has to choose a preferential magnetic orientation. If the lower-symmetry state is not homogeneous (i.e. the mean magnetization points to variable directions at different regions of the sample), forces will appear reflecting the additional energy cost due to the exchange interaction. This results in a rigidity of the system [45]. Another scenario ermerges in paramagnetic (PM) materials (ferromagnet above their Curie temperature), the C_∞ symmetry is preserved all over the magnetic sample and slightly perturbed in presence of Zeeman interaction. The high symmetry state corresponding to randomly oriented magnetic moments is recovered as soon as the field is turned off since the effect of exchange interaction is weak compared to that of thermal agitation. Although the origin of remanent magnetization and its temperature dependence is hosted in the definition of exchange interaction, the following experimental observation yet remains unclear. Some ferromagnetic materials can have zero remanent magnetization, which is normally the characteristic of paramagnetic materials, thus suggesting that no exchange

interaction is acting in those systems. Experimentally, it can be achieved in a simple manner by cooling down from above the Curie temperature in absence of any magnetic field. However, in the same kind of materials, the saturation magnetization is obtained for an applied field as low as 1 μT while much higher field ($\simeq$ 1 T) are required to magnetize classical paramagnets (typical virgin magnetization curves are presented in Figure 2.5(a)). In order to reconcile the absence of remanent magnetization with the large permeability of soft ferromagnet, one need to introduce the notion of domains.

2.3.2 Magnetic domains

In a ferromagnetic sample, the magnetization breaks into regions called *magnetic domains* in which all magnetic moments are oriented in a common direction even when an external field is applied. The net magnetization is given by the relative orientation of the different domains composing the ferromagnetic sample. In particular configurations, domains compensate each other such that the measured magnetization is zero in the absence of magnetic field, macroscopically masking the strong exchange interactions at the origin of the rigidity of the domains. The huge permeability of soft ferromagnetic materials is also a manifestation of domains. Indeed, ferromagnets are more easily magnetized because their magnetic moments are already aligned to some extent. The magnetization change is not associated to a general alignment of moments but to the growth of already aligned domains. The latter corresponds to a progressive movement of symmetry defects called domain walls as sketched in Figure 2.5(b). Assuming that no other defects are present in the sample, domain walls propagation is an energetically favorable process.

Following the first experimental evidences of magnetic domains, Landau and Lifshitz presented a solution for the existence of domains: domains exist to minimize the free energy of the system associated to the magnetic stray field [46]. The exchange is not the only source for magnetic energy. The total energy of the system also invloves the dipolar interaction between magnetic moments and the magnetic field they generate inside and outside the material. At short distances, the dipolar interaction is negligible compared to the exchange energy. However, the more aligned the magnetic moments are, the stronger the cumulative field they produced is, and, as a result, the energy related to their interactions becomes less and less negligible as the domain size increases. Eventually, in a finite size magnet, the field generated within and around the ferromagnet contains a large part of the system's energy density $B^2/2\mu_0$. Inside the sample, this field is named *demagnetization*

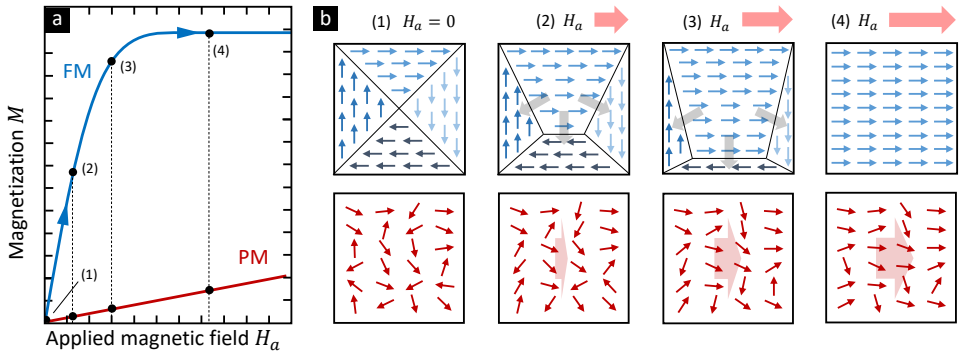

Figure 2.5: *Comparison between a typical ferromagnet with domain structure and a paramagnet in terms of (a) their respective virgin magnetization curves, and (b) the arrangement of their magnetic moments.*

field as it is opposed to the magnetization direction and it is called *stray field* outside[5]. In order to reduce the stray field, magnetic moments have to be parallel to the edge of the sample, implying the presence of multiple domains. Energy related to the stray field can be avoided if domains are organized in such a way that north and south poles are as close as possible, leading ideally to a flux-closure arrangement (i.e. a head-to-tail organization of magnetic domains also called Landau patterns). This effect is presented in Figure 2.6 where the intensity of the stray field has been calculated for different domain distributions. The larger the number of domains in a flux-closure arrangement, the lower the energy related to the stray field. From this statement, one concludes that a ferromagnetic material would break in an infinity of domains. However, as shown in panel (d) of Figure 2.6, a finite number of magnetic domain is obtained. That brings us to the following question: what is the ingredient limiting the subdivision of domains ? The answer involves the energy cost associated to the interface between two domains. The boundary between adjacent magnetic domains is called a domain wall. The different kinds of domain walls are defined by the angle between domains (90° as in panel (d) of Fig. 2.6 or 180° in panel (b) and (c)) and the direction of rotation of the magnetic moment inside the wall. In the transition between two domains, the magnetization can rotate in the plane of the wall or perpendicularly to the latter, corresponding to Bloch and Néel walls, respectively (Figure 2.7(a)).

In the domain wall, the progressive inclination of neighboring magnetic moments (and thus spins) causes an increase of the exchange energy. Based

[5]It is also referred as dipolar field or magnetostatic field in many references.

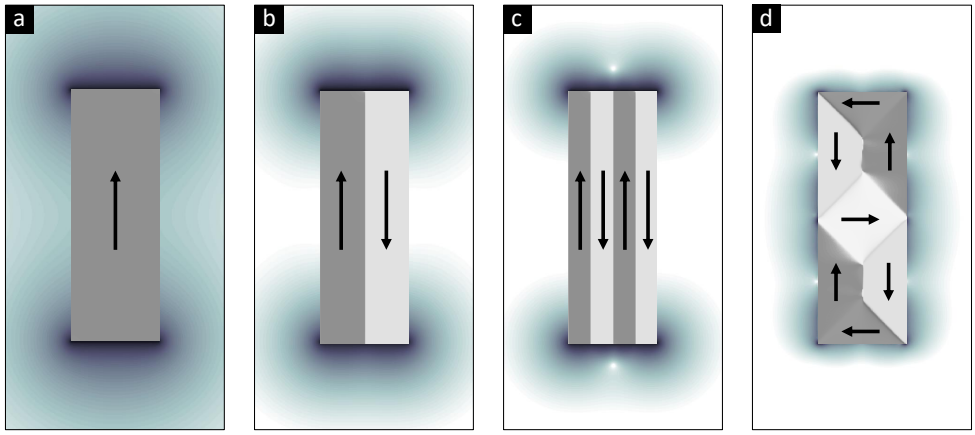

Figure 2.6: *Reduction of the stray field when the mangetization breaks into domains. Results obtained by micromagnetic simulation are shown for a micrometer-scale bar of Permalloy (a) in a saturated state, (b-c) with magnetic domains pinned in artificial configurations and (d) in a relaxed structure cooled down from above its Curie temperature.*

on Eq. (2.4), the energy cost for a small inclination θ is approximately $JS^2\theta^2$. Assuming a 180° wall where the total rotation is the contribution of N successive inclinations $\theta = \pi/N$, the density of energy is expressed as

$$\sigma_w = \frac{J\pi^2 S^2}{Na^2}, \tag{2.12}$$

where a is the inter-atomic distance and $1/a^3$ the atomic density. The result suggests that domain walls should expand to maximize their length $\delta_w = aN$ and reduce their energy. Giant domain walls would be experimentally observed if ferromagnetic energy was perfectly isotropic, which is not the case. At this point, some clues have already been given for the existence of favored magnetization directions resulting, for example, from the spin-orbit coupling interaction which gives rise to a dependence between the spin orientation and the crystalline lattice, or from the necessity to reduce the stray field by aligning the magnetic moments with the sample edges. One generally refers to the easy axis (EA) and the hard axis (HA) of a ferromagnet to depict the direction of the lowest and highest energies. In order to minimize the total energy of the system, domains are constrained to remains along the EA and therefore, by definition, domain walls do not. Consequently, there is an additional energy cost proportional to the difference of energy density between the easy and hard axis $K = (K_{HA} - K_{EA})$, called anisotropy constant, which restricts the domain wall size. The typical width δ_w is approximated

by

$$\delta_w = Na = \pi\sqrt{\frac{2JS^2}{aK}}, \tag{2.13}$$

reflecting the iternal competition between the degree of anisotropy of a ferromagnet and its rigidity. This is illustrated in panel (b) of Figure 2.7 where the domain configuration of thin magnetic disks with EA in $\hat{\mathbf{x}}$ and $\hat{\mathbf{y}}$ is shown as a function of the magnetic anisotropy constant K. With increasing anisotropy, the domains align with EA and the width of the domain walls is reduced.

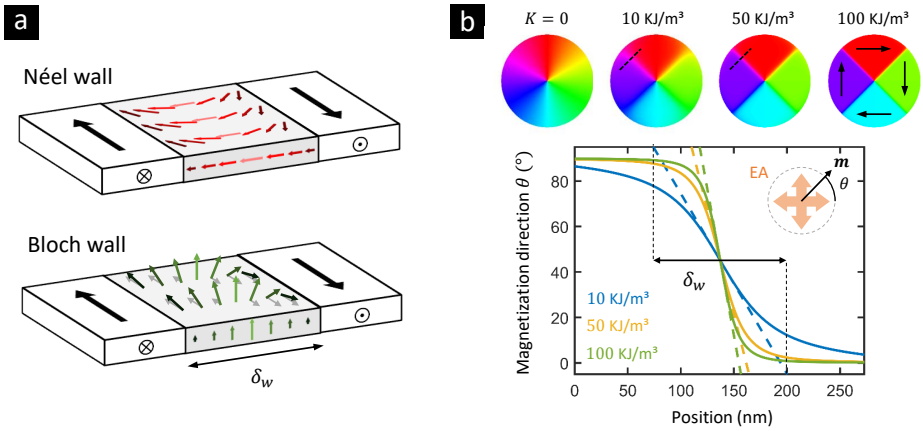

Figure 2.7: *(a) Comparison between Bloch and Néel 180° walls. (b) Effect of the magnetic anisotropy on the domain walls width in very thin magnetic disks. The plot shows the rotation of magnetization along the black dashed lines indicated on the disks.*

Under the action of an external magnetic field, magnetic domains and domain walls grow in size, move and rotate in order to minimize the energy of the system. Magnetic moments try to align with the external field. The overall result is the complex nonlinear response summarized by the hysteresis loop shown in Figure 2.4. When dealing with microscopic ferromagnetic devices, the domain configuration may be critical and one can not rely on macroscopic approaches based on Maxwell's equations where the domain distribution is hidden in a global magnetization M. In order to predict the magnetization process of a ferromagnet, one have to deal with the interplay of different interactions between magnetic moments at the appropriate scale. In the following section, we present how the theory of micromagnetism offers a way to deal with the puzzling phenomenon of domains distribution.

2.4 The micromagnetic theory

As described in the previous section, the magnetic domain structure is intrinsically linked to a range of different interactions between the magnetic moments of atoms. This statement suggests that calculations at the atomic level are needed to capture the fine details of a ferromagnetic material. However, at micrometer and even nanometer scales, one have to deal with an extremely high number of magnetic moments and the description of the magnetization within this atomistic approach would be an extremely demanding computational effort. Moreover, in most cases, when the response of a micro or nano-patterned ferromagnetic layer is studied upon the application of an external field, there is no need for a complete description of the magnetic moment of each atom. The investigation of the magnetic domain distribution and their motions is sufficient.

2.4.1 Continuum approximation

The most efficient way to describe a ferromagnet with micro or nano-scale dimensions is the theory of micromagnetism which relies on the continuum approximation, i.e. replacing the discrete array of atoms that composes the ferromagnet by a smooth analytical function of the space coordinates representing the local magnetization:

$$\mathbf{M}(\mathbf{r}) = M_s \mathbf{m}(\mathbf{r}), \tag{2.14}$$

where $\mathbf{m}$ is a unit vector. This approximation assumes that the local magnetization has a uniform magnitude and the only degree of freedom is its orientation. Through this approach, one divides the studied material into volumes ΔV in which the magnetization is defined as the mean value of the magnetic moment of each atom contained in the volume as represented in Figure 2.8(a). For computational purposes, each cell may contain a large number of magnetic moments. However, the discretization volume must be small enough to agree with the hypothesis of a smooth variation of $\mathbf{m}$ between two succesive volumes. At this point, it may be important to justify the use of a discrete system in a continuum approximation. The idea is that the exchange interaction largely dominates the short range interactions between localized magnetic moments (here cells of volume ΔV) and therefore, tends to align all the moments in the same direction. In comparison, the dipolar interaction is substantially weaker on a short range and induces negligible deviation of $\mathbf{m}$ from one cell to the next. $\mathbf{M}(\mathbf{r})$ can therefore be considered as a continuous

function with smooth variations as long as the size of the discretization cell is much shorter than the length on which the magnetization vector can reverse (see Figure 2.8(b)).

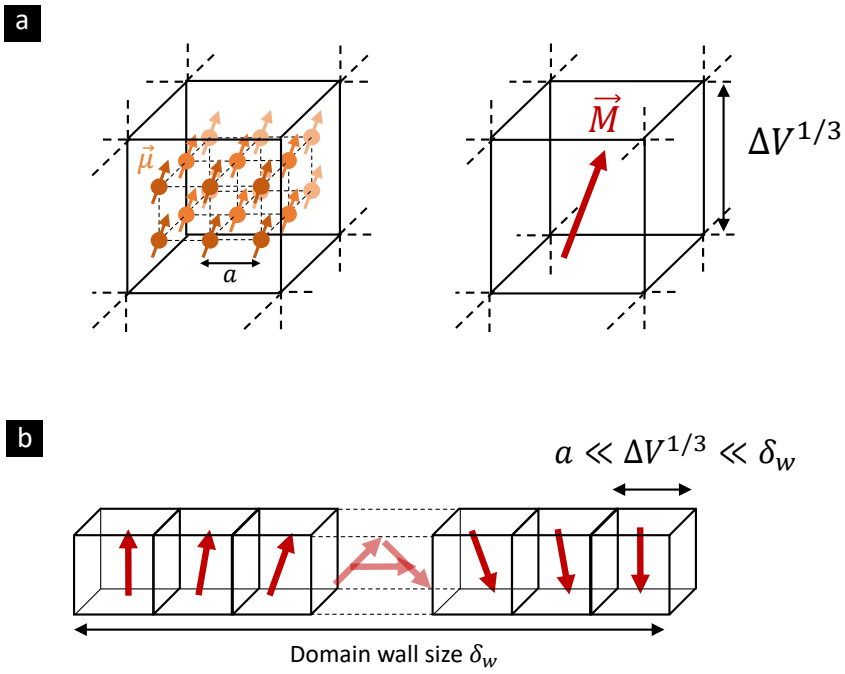

Figure 2.8: *Micromagnetic cell size limitations. (a) A micromagnetic cell contains a large number of atoms. The local magnetization* $\mathbf{M}(\mathbf{r})$ *corresponds to the mean value of all magnetic moments* $\boldsymbol{\mu}$ *per unit volume. (b) The cell size has to be large compared to the mean distance between two spins a and small compared to the domain wall length* δ_w *in order to fulfill the continuum approximation hypothesis.*

2.4.2 Magnetic energies

The micromagnetic theory was first introduced by W. F. Brown as a continuum theory of magnetically-ordered materials [8]. It postulates that the domain distribution in a ferromagnet results from the minimization of the free energy which is a function of the local magnetization $\mathbf{M}(\mathbf{r})$. Therefore, using variational principle and assuming an infinitesimal change $\delta\mathbf{m}(\mathbf{r})$, the

minimization leads to

$$\delta E\left[\mathbf{m}(\mathbf{r})\right] = E\left[\mathbf{m}(\mathbf{r}) + \delta\mathbf{m}(\mathbf{r})\right] - E\left[\mathbf{m}(\mathbf{r})\right] = 0. \tag{2.15}$$

In order to minimize the energy of the system and obtain the magnetization landscape, we need a mathematical expression for the different contributions to the free energy in the ferromagnet as a function of the local magnetization $\mathbf{M}(\mathbf{r})$. As those energy terms rely on magnetic interactions, the free energy is given by the sum of the exchange, dipolar (or magnetostatic), anisotropic and Zeeman energies,

$$E = E_{\text{ex}} + E_{mag} + E_{anis} + E_{\text{Z}}. \tag{2.16}$$

This expression has to be evaluated in each point of the material. The magnetic energy for a discrete volume of the magnetic material ΔV can be expressed as

$$\Delta E = \frac{1}{2}\mu_0 M_{\text{s}}\mathbf{m}(\mathbf{r}) \cdot \mathbf{H}_{\text{eff}}(\mathbf{r})\Delta V, \tag{2.17}$$

where $\mathbf{H}_{\text{eff}}$ is an effective magnetic field defined as the sum of different magnetic fields of origin corresponding to the energies in Eq. (2.16),

$$\mathbf{H_{eff}} = \mathbf{H_{ex}} + \mathbf{H_{demag}} + \mathbf{H_{anis}} + \mathbf{H_{Z}}. \tag{2.18}$$

The form of Eq. (2.17) is similar to Eq. 2.5 describing the Zeeman energy except for the factor $1/2$ which translates the fact that $\mathbf{H}_{\text{m}}$ is induced by the magnetization $\mathbf{M}$ itself[6].

In the following, each of the four energies as well as their equivalent contribution to the total effective magnetic field are explained and detailed.

Exchange energy

Assuming a constant amplitude for the ith and the jth spins and considering a small misalignment ϕ_{ij} between them, the Heisenberg exchange energy (Eq. 2.4) can be expressed as

$$E_{\text{ex}} = -2\sum_{i,j} J_{\text{ij}} S^2 \cos\left(\phi_{\text{ij}}\right) \simeq -2\sum_{i,j} J_{\text{ij}} S^2 \left[1 - \frac{\phi_{\text{ij}}^2}{2} + \mathcal{O}\left(\phi_{\text{ij}}^4\right)\right]. \tag{2.19}$$

[6]Indeed, this definition represents the sum of the interactions between each magnetic moment contained in the volume ΔV. Every individual magnetic moment are contained in $M_{\text{s}}\mathbf{m}$ and the magnetic field $\mathbf{H}_{\text{m}}$ comes also from the contribution of every magnetic moment in the volume ΔV. When considering the total energy, the interaction of the magnetic moment i with the magnetic moment j is therefore counted twice: once with the couple $(m_{\text{j}}, H_{\text{eff,i}})$ and once with the couple $(m_{\text{i}}, H_{\text{eff,j}})$. As both terms describe the same energy, a factor $1/2$ has to be added.

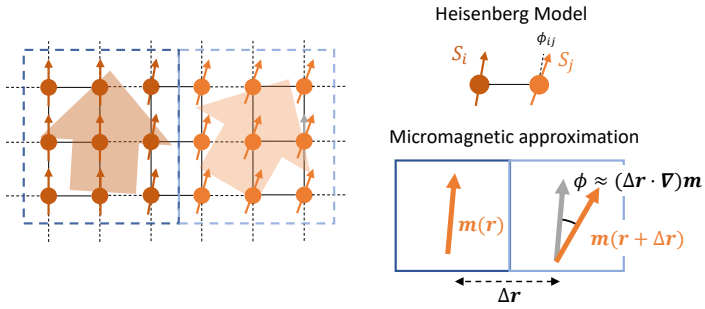

Figure 2.9: *Illustration of the micromagnetic approximation in the Heisenberg model. Vectorial representation of spins are replaced by the local magnetization and the tilt is expressed by the gradient of magnetization.*

However, in the micromagnetics formalism, the key element is not the electron spin **S** but the local average magnetic moment **m**. A model based on Heisenberg Hamiltonian is proposed to include exchange interaction between closest cells as sketched in Figure 2.9. To do so, Eq. (2.19) is modified by assuming that the angle between neighboring magnetic moments is related to the gradient of **m** multiplied by Δr, the mean distance between adjacent cells:

$$(\Delta \mathbf{r} \cdot \nabla)\, \mathbf{m} \simeq |\mathbf{m}(\mathbf{r}) - \mathbf{m}(\mathbf{r} + \Delta \mathbf{r})| = \sin(\phi) \simeq \phi, \tag{2.20}$$

leading to the following expression for the exchange energy,

$$E_{\text{ex}} \simeq C + \sum_{i,j} J_{\text{ij}} S^2 \left[(\Delta \mathbf{r} \cdot \nabla)\, \mathbf{m}\right]^2 \tag{2.21}$$

with C a constant. As the exchange interaction is related to the overlapping of wavefunctions, only the nearest neighbours of each moment are included in the summation. In the case of a simple cubic lattice, assuming a constant $J_{\text{ij}} = J$ and dropping the constant term C since an energy is defined up to a constant, the exchange energy for each cell with volume ΔV can be expressed as

$$\Delta E_{\text{ex}} \simeq \frac{E_{\text{ex}}}{a^3} \Delta V \simeq A |\nabla \mathbf{m}|^2 \Delta V \tag{2.22}$$

with $A = 2 Z_c S^2 J / a$ being a constant value related to the materials properties and called the exchange stiffness constant. Here, a is the periodic lattice parameter and Z_c is the number of atoms per cell ($Z_c = 1$ for simple cubic, $Z_c = 2$ for body-centered cubic (BCC), $Z_c = 4$ for face-centered cubic (FCC) and $Z_c = 2\sqrt{2}$ for hexagonal close packing (HCP)). The range of value for

A is about tens of pJ/m for ferromagnets (10 pJ/m for Permalloy (Py) and 31 pJ/m for Co). It is worth noting that $|\nabla \mathbf{m}|^2$ is not a regular gradient and stands for $(\nabla m_x)^2 + (\nabla m_y)^2 + (\nabla m_z)^2$.

From Eq. (2.17), one can derive an effective magnetic field from the magnetic energy by taking the *functional derivative* of the energy density with respect to the magnetic moment $\mathbf{m}$,

$$\mathbf{H} = \frac{1}{M_s \mu_0 \Delta V} \frac{\delta E[\mathbf{m}]}{\delta \mathbf{m}} = \frac{1}{M_s \mu_0 \Delta V} \left[\frac{dE[\mathbf{m}]}{d\mathbf{m}} - \nabla \cdot \frac{dE[\mathbf{m}]}{d\nabla \mathbf{m}} \right]. \tag{2.23}$$

Applying Eq. (2.23) to the exchange energy gives the exchange field expressed by

$$\mathbf{H_{ex}} = -\frac{2A}{M_s \mu_0} \nabla^2 \mathbf{m}. \tag{2.24}$$

Magnetostatic energy

As briefly introduced in section 2.3.2, the dipolar interactions between magnetic moments aligned by the exchange interaction and the demagnetization field they produce leads to a significant magnetostatic energy. As it is a long-range phenomenon, one can not consider only the closest neighbours but sum the dipolar interaction between the mean magnetic moment of each of the N cells, which implies N^2 operations. Instead, micromagnetism formulation relies on another method based on Maxwell's equations to determine the magnetostatic (also called demagnetization) energy, E_{demag}. Applying the Maxwell's second and fourth laws in a magnetic material and in absence of any current or charge electric field, leads to the following results:

$$\begin{aligned} \nabla \cdot \mathbf{B} = \nabla \cdot (\mathbf{H_m} + \mathbf{M}) = 0, \\ \nabla \times \mathbf{H_m} = 0, \end{aligned} \tag{2.25}$$

where $\mathbf{H_m}$ is the internal magnetic field generated by the magnetization $\mathbf{M}$. The second equation implies that $\mathbf{H_m}$ can be expressed as the gradient of a scalar potential ϕ_m, leading to equations with the same structure as the electrostatic version of Maxwell's equations:

$$\mathbf{H_m} = -\nabla \phi_m, \tag{2.26}$$

$$\nabla \cdot \mathbf{H_m} = -\nabla \cdot \mathbf{M} = \rho_m. \tag{2.27}$$

In this formalism, ρ_m is equivalent to a magnetic charge induced by the magnetization. Combining both equations (2.26) and (2.27) leads to a Poisson's

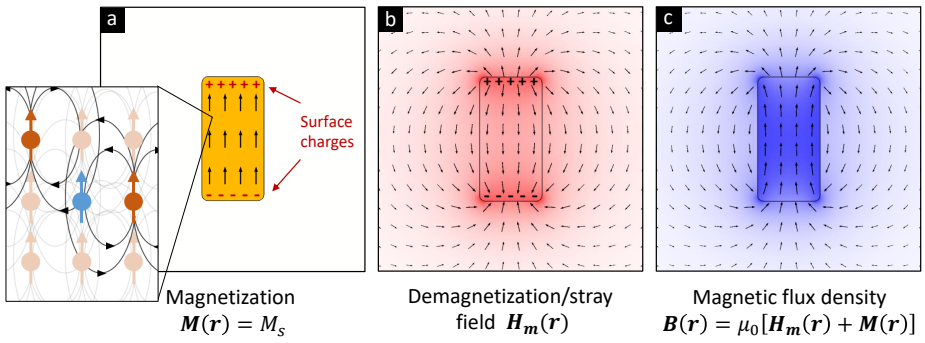

Figure 2.10: *Representation of the demagnetization effect in a uniformly magnetized rectangular ferromagnet. (a) The dipolar interaction between each magnetic moments (illustrated in the inset sketch) is expressed by virtual magnetic charges. (b) The magnetic charges generate a demagnetization field opposed to the magnetization inside the sample and a stray field outside. (c) The magnetic flux density generated by each magnetic moment is obtained by summing the demagnetization field and the sample magnetization.*

equation form with a well known solution:

$$\phi_m(\mathbf{r}) = \frac{1}{4\pi}\int_{R^3}\frac{\rho_m(\mathbf{r}')}{|\mathbf{r}-\mathbf{r}'|}d^3\mathbf{r}'. \tag{2.28}$$

In a finite material, the magnetization abruptly vanishes at the boundaries of the material. Therefore, the integration all over the space is limited to an integration over the volume of the ferromagnet V plus a surface term

$$\phi_m(\mathbf{r}) = \frac{1}{4\pi}\int_V\frac{\rho_m(\mathbf{r}')}{|\mathbf{r}-\mathbf{r}'|}dV + \frac{1}{4\pi}\int_S\frac{\sigma_m(\mathbf{r}')}{|\mathbf{r}-\mathbf{r}'|}dS, \tag{2.29}$$

with $\sigma_m(\mathbf{r}') = \mathbf{M}(\mathbf{r}')\cdot\mathbf{n}$, the surface magnetic charge. For a uniformly magnetized sample, $\rho_m = 0$ inside the sample. The potential ϕ_m and therefore the demagnetization field $\mathbf{H_m}$ are induced by the surface magnetic charges at the extremity of the magnet as illustrated in Figure 2.10. The field $\mathbf{H_m}$ is opposed to the magnetization inside the sample. In other words, the demagnetization field tries to demagnetize the sample to suppress the magnetic charges and to reduce the magnetostatic energy. To do so, magnetic moments tend to align parallel to the edges and therefore, in samples with an anisotropic geometry (nanowire, rectangular stripes, ect.), it results in a shape-induced energetically favorable direction of magnetization, also called *shape anisotropy*. As discussed previously, the same effect is responsible for the formation of

domains and flux-closure magnetic patterns where no magnetic charges lie at the sample surface. From Gauss's theorem, the second term of Eq.(2.29) can be rewritten as a volume integral, leading to a new formulation of the magnetic scalar potential

$$\phi_m(\mathbf{r}) = \frac{1}{4\pi}\int_V \mathbf{M}(\mathbf{r}')\cdot\nabla'\frac{1}{|\mathbf{r}-\mathbf{r}'|}dV. \tag{2.30}$$

From Eq. (2.26), it results that $\mathbf{H_m}$ can be expressed as the convolution product between the magnetization $\mathbf{M}$ and $\mathcal{N}$ called the demagnetization tensor:

$$\begin{aligned}\mathbf{H_m}(\mathbf{r}) &= -\frac{1}{4\pi}\int_V \mathbf{M}(\mathbf{r}')\nabla\nabla'\frac{1}{|\mathbf{r}-\mathbf{r}'|}dV \\ &= -\left[\mathbf{M} * \mathcal{N}\right](\mathbf{r}).\end{aligned} \tag{2.31}$$

The last formulation of Eq.(2.31) is suited for numerical simulation because $\mathcal{N}$ only depends on the geometry and therefore has to be computed only once at the beginning of the calculation, greatly accelerating the computational process. In very specific cases, an analytic solution exists for the demagnetization tensor $\mathcal{N}$, strongly simplifying the interpretation of demagnetization. This is discussed with more details in Box 2.1.

The demagnetization energy in a volume ΔV is calculated as the dipole interaction between $\mathbf{H_m}$ and $\mathbf{M}$.

$$\Delta E_{\text{demag}} = -\frac{\mu_0 M_s}{2}\mathbf{m}\cdot\mathbf{H_m}\Delta V \tag{2.32}$$

where the $1/2$ factor comes from the self-induction of the magnetic field by the magnetization (double count with r and r' for the calculation of $\mathbf{H_m}$). The total magnetostatic energy is given by the integral over the space of Eq. (2.32). As $\mathbf{m}$ is null outside the magnetic sample, the integration volume can be reduced to the magnet's volume V only. The same equation can be written as a function of the demagnetization field all over the space. Knowing that $\mathbf{B} = \mu_0(\mathbf{H}+\mathbf{M})$ and $\int \mathbf{B}\cdot\mathbf{H} = 0$ [47], the total magnetostatic energy is given by

$$E_{\text{demag}} = -\frac{\mu_0 M_s}{2}\int_V \mathbf{m}\cdot\mathbf{H_m}\, d^3r = \frac{\mu_0}{2}\int H_m^2\, d^3r, \tag{2.33}$$

which is always positive and is minimized by limiting the demagnetization field inside and the stray field outside the sample.

When considering the specific case of thin films, the demagnetization field is non-zero only in the OOP direction (see Box 2.1) and the magnetostatic

Box 2.1: **The demagnetization factors**

The complex picture of the demagnetization field is drastically simplified when the specific case of an ellipsoidal sample in a uniform magnetization state is considered. It turns out that $\mathbf{H_m}$ is also uniform and collinear with $\mathbf{M}$. When the magnetization along the principal directions of the ellipsoid is considered, the demagnetization tensor can be written as a diagonal matrix

$$\mathbf{N} = \begin{pmatrix} N_x & 0 & 0 \\ 0 & N_y & 0 \\ 0 & 0 & N_z \end{pmatrix}, \tag{2.34}$$

where the diagonal terms are named demagnetization factors and the trace $N_x + N_y + N_z = 1$, translating the intuitive fact that the demagnetization in one specific direction depends on the geometry in the two other directions. The value of the demagnetization factors for a general ellipsoid with diagonals a, b, c, along the c direction is given by

$$N_c = \frac{1}{2}\int_0^\infty \frac{ds}{\sqrt{(1+s)^3(1+s\tau_a^2)(1+s\tau_b^2)}}, \tag{2.35}$$

where $\tau_a = a/c$ and $\tau_b = b/c$, and the components N_a and N_b are easily obtained by rotation.

More interestingly, the demagnetization factors can be deduced based on symmetry considerations for basic shapes as summarized in Fig. 2.11. Intuitively, in a spherical sample, there is no preferential direction and therefore demagnetization factors are isotropic, $N_x = N_y = N_z = 1/3$. The same result is obtained from Eq. (2.35) for $\tau_a = \tau_b = 1$. In the same vein, an infinite thin film with uniform magnetization can be seen as an ellipsoid with a finite diameter only in the direction perpendicular to the plane. The surface magnetic charges are maximized in the case of an out-of-plane (OOP) configuration and negligible in the plane of the film. Therefore, defining the normal direction as that of $\mathbf{e}_z$ direction, $N_z = 1$ is the only non-zero term.

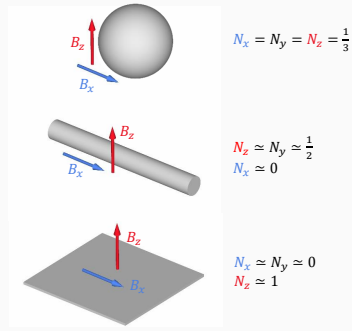

Figure 2.11: *Example of standard geometries for which the demagnetization factors have an analytical solution.*

energy is given by

$$\Delta E_{\text{demag}} = -\frac{\mu_0 M_s}{2}\mathbf{m}\cdot(-M_s\mathbf{m}_z)\,\Delta V = \frac{\mu_0 M_s^2}{2}\cos^2(\theta)\Delta V, \tag{2.36}$$

where θ is the angle between $\mathbf{M}(\mathbf{r})$ and $\mathbf{e}_z$. Consequently, in very thin film, domains naturally lie in the sample plane to reduce the stray field. In the same vein, the nature of domain walls in thin films also relies on the minimization of the magnetostatic energy and the dependency with the sample thickness can be unveiled with basic considerations. Indeed, as illustrated in Figure 2.12(a), a domain wall can be approximated as an infinite ellipsoidal cylinder delimited by the domain wall width δ_w and the film thickness t. The wall

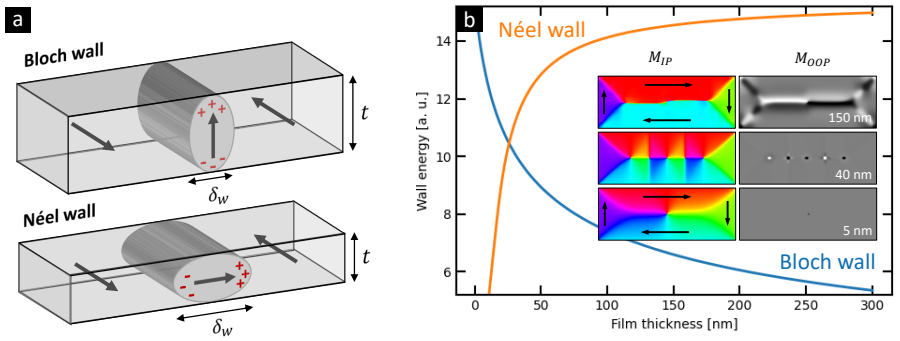

Figure 2.12: *(a) Domain walls approximated by an infinite ellipsoidal cylinder. (b) Thickness dependence of the domain wall energy density for a Py thin film, using the approximation presented in panel (a). The inset panel shows the magnetization for 5-, 40- and 150-nm-thick rectangular stripes. M_{IP} and M_{OOP} indicate the in-plane and out-of-plane magnetization, respectively.*

is supposed to be uniformly magnetized with an effective magnetization $\mathbf{M_e} \simeq \mathbf{M_s}/\sqrt{2}$ [48]. Depending on the type of wall, the magnetization is OOP, inducing surface magnetic charge (Bloch wall) or is in-plane (IP) and induces bulk magnetic charges (Néel wall). The demagnetization factor for an infinite ellipsoidal cylinder with diameters a and b, along diameter a is $N = b/(a+b)$ [49] and therefore, the demagnetization energy per unit volume is

$$E_{Bloch} = \frac{\mu_0 M_e^2}{2}\frac{\delta_w}{\delta_w + t} \qquad \text{and} \qquad E_{Neel} = \frac{\mu_0 M_e^2}{2}\frac{t}{\delta_w + t}. \tag{2.37}$$

The total magnetic energy of the wall (including the exchange energy as in eq. 2.12) is plotted in Figure 2.12(b) for the specific case of a permalloy thin film. A transition between Néel and Bloch wall is observed at a critical thickness around 30 nm. In the inset panel, the magnetization distribution in rectangular stripes with various thicknesses is presented, showing Néel walls in very thin samples and Bloch walls in thicker one. For intermediate thickness values, domain walls are generally formed by a mixture of Bloch and Néel walls forming cross-tie domain walls (as for the 40-nm-thick example in the panel (b)) or asymmetric Bloch or Néel walls [50]. More information about the variety of domain walls can be found in [44].

Anisotropic energy

Geometrical confinement is not the only factor giving rise to magnetic anisotropy. Depending on their crystal structure, ferromagnetic materials

may have easy axes along specific directions of the lattice. This effect is due to the spin-orbit interaction that tends to align the spin magnetic moment with the orbital angular momentum. As the direction of the latter is fixed by the crystal lattice via electrostatic crystal field and exchange interactions, it gives rise to a crystalline orientation that minimizes the free energy of the system [51]. This is generally named *magnetocrystalline anisotropy*. Another important origin for anisotropy is *induced anisotropy* related to external stress or annealing process. In the specific case of thin films, in addition to an important strain anisotropy naturally induced by the epitaxial mismatch with the substrate or by a growth-induced texture (columnar grains, etc.), there exists a *surface anisotropy* which results from the change of the lattice symmetry at the surface.

The free energy related to anisotropy is only determined by the relative orientation of the local momentum with a directional vector $\mathbf{u_k}$. As for shape anisotropy, it is worth noting that the direction matters but not the orientation, meaning that the same energy is obtained for a local magnetization $\mathbf{m}(\mathbf{r})$ and $-\mathbf{m}(\mathbf{r})$. In a general way, the anisotropic energy in micromagnetism is given by

$$\Delta E_{\text{anis}} = f\left(\mathbf{m}, \mathbf{u_k}\right). \tag{2.38}$$

In the most common situation, the system has only one privilegided direction that differs from any other, and it is called uniaxial anisotropy. The energy then only depends on the angle θ that the magnetization $\mathbf{m}$ forms with that particular direction. ΔE_{anis} is an even function expressed as a Taylor expansion, usually limited to 2 or 3 terms,

$$\begin{aligned}\Delta E_{\text{anis}} =& \sum_{n=0}^{\infty} K_{\text{un}} \sin^{2n}(\theta)\, \Delta V \\ =& K_{\text{u0}} \Delta V + \sum_{n=1}^{\infty} K_{\text{un}} \left[1 - \left(\mathbf{m}\cdot\mathbf{u_k}\right)^{2n}\right] \Delta V \\ =& \left[K_{\text{u0}} + K_{\text{u1}} + K_{\text{u2}} - K_{\text{u1}}\left(\mathbf{m}\cdot\mathbf{u_k}\right)^2 - K_{\text{u2}}\left(\mathbf{m}\cdot\mathbf{u_k}\right)^4 + \mathcal{O}(\theta^6)\right] \Delta V\end{aligned} \tag{2.39}$$

The K_{un} coefficents are the uniaxial anisotropy constants having units of energy density. The constant term may be set to 0 and therefore, the magneto-crystalline energy is categorized following by the sign of K_{u1} and K_{u2}, defining u_{k} as an easy- or a hard-axis (or easy-plane). The blue curve in Figure 2.13(a) shows the variation of the energy with the magnetization orientation for a sample with uniaxial anisotropy as indicated in the inset sketch. The equivalent anisotropic field $\mathbf{H}_{anis}$ is easily obtained applying the Eq. 2.23 to

the anisotropic energy

$$\begin{aligned}\mathbf{H}_{anis} =& \frac{1}{M_s \mu_0 \Delta V} \frac{\delta \Delta E_{anis}}{\delta \mathbf{m}} \\ =& \frac{1}{M_s \mu_0} \left[2K_{u1} \left(\mathbf{m} \cdot \mathbf{u_k} \right) + 4K_{u2} \left(\mathbf{m} \cdot \mathbf{u_k} \right)^3 \right] \mathbf{u_k}.\end{aligned} \tag{2.40}$$

In the literature, the uniaxial anisotropy energy is more often presented as a function of θ, the angular deviation between m and the easy axis, and limited to the lowest order

$$\Delta E_{anis} \simeq K_{u1} \sin^2(\theta). \tag{2.41}$$

This formulation is also well suited to include strain induced or surface anisotropy in thin films replacing the coefficient K_{u1} in Eq. (2.41) by an effective constant [52–54]

$$K_{eff} = K_{u1} + \frac{K_s}{t} + \frac{3}{2} \lambda_s \sigma, \tag{2.42}$$

where K_s is the surface coefficient, t the film thickness, σ the uniaxial stress intensity and λ_s the saturation magnetostriction. Surface and stress effects generally induce an OOP anisotropy which gives rise to a competition with the shape IP anisotropy and the development of stripes domains (IP domains with a slight OOP component alterning between up and down orientation, and separated by Bloch walls) at a given critical thickness. Figure 2.13(b) summarizes the different configurations for the OOP domains in thin films depending on the thickness of the sample, and the ratio between K_u and the shape anisotropy of a thin film (see Eq. (2.36)) labelled as the quality factor Q. When $Q > 1$, the magnetization is mainly oriented OOP while for $Q < 1$, the shape anisotropy dominates over the perpendicular anisotropy and the magnetization lies IP. Stripes domains are formed as a compromise between reducing energy from OOP anisotropy and limiting the stray field by an alternation of positive and negative surface magnetic charges.

Some mainstream ferromagnetic materials such as Ni and Fe exhibit a lattice with a cubic symmetry and therefore three easy-axes along three orthogonal directions (see [45] for more details). The difference of energy between uniaxial and multiaxial (cubic) anisotropy is shown in Figure 2.13(a) as a function of the magnetization vector direction.

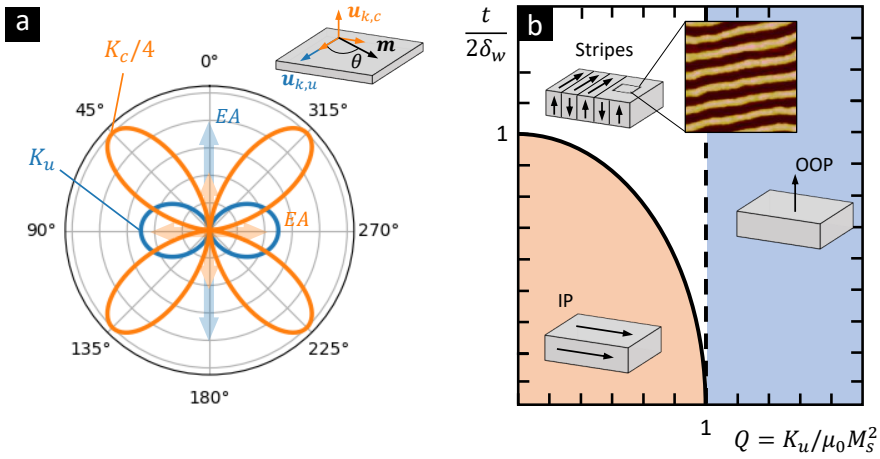

Figure 2.13: *(a) In-plane (IP) energy variation with magnetization direction for a uniaxial (blue) and cubic (orange) anisotropy. K_u and K_c are the uniaxial and cubic anisotropy coefficient, respectively. (b) Effect of out-of-plane (OOP) uniaxial anisotropy and thickness on the domain arrangement in thin films. Inset shows a magnetic force microscopy image of stripe domains in a 200 nm thick permalloy thin film.*

Zeeman energy

Finally, the Zeeman energy is the magnetic energy related to the alingment of the magnetic moments with an external magnetic field $\mathbf{H_a}$,

$$\Delta E_Z = -\mu_0 M_s \mathbf{m}(\mathbf{r}) \cdot \mathbf{H_a}(\mathbf{r}) \Delta V. \tag{2.43}$$

2.4.3 The magnetic ground state

Summing up all contributions described previously, the total magnetic energy all over the volume of a FM sample can be expressed by

$$E_{tot}[\mathbf{m}] = \int_V \left[A|\nabla \mathbf{m}|^2 - \frac{\mu_0 M_s}{2} \mathbf{m} \cdot \mathbf{H_m}[\mathbf{m}] + f(\mathbf{u_k}, \mathbf{m}) - \mu_0 M_s \mathbf{m} \cdot \mathbf{H_a} \right] d\mathbf{r}^3. \tag{2.44}$$

The stable magnetization texture for a FM system corresponds to the local minimum of the free energy landscape and is therefore the one that satisfies Eq. (2.15) for an energy $E_{tot}[\mathbf{m}]$ such that

$$\begin{aligned} \delta E_{tot}[\mathbf{m}] = \int_V \Big[& 2A \nabla \mathbf{m} \cdot \nabla \delta \mathbf{m} - \mu_0 M_s \mathbf{H_m} \cdot \delta \mathbf{m} + \frac{\partial f}{\partial \mathbf{m}} \delta \mathbf{m} \\ & - \mu_0 M_s \mathbf{H_a} \cdot \delta \mathbf{m} \Big] d\mathbf{r}^3 = 0. \end{aligned} \tag{2.45}$$

where $\nabla \mathbf{m}$ and $\nabla \delta \mathbf{m}$ are used as notations for $\nabla m_x + \nabla m_y + \nabla m_z$ and $\nabla \delta m_x + \nabla \delta m_y + \nabla \delta m_z$ respectively. Using the divergence distribution properties and the divergence theorem leads to a new form of the minimization equation involving the effective magnetic field

$$-\mu_0 M_s \int_V \mathbf{H}_{eff} \cdot \delta \mathbf{m} \, dV + 2A \int_S (\mathbf{n} \cdot \nabla) \mathbf{m} \cdot \delta \mathbf{m} \, dS = 0. \tag{2.46}$$

One of the main assumptions of the continuum model is the fixed norm for the local magnetic moment. As a consequence, the small change of magnetic moment perpendicular to the local magnetization can be expressed as a change of orientation $\delta \mathbf{m} = \mathbf{m} \times \delta \boldsymbol{\theta}$. Therefore, solving Eq. (2.46) for a generic change $\delta \boldsymbol{\theta}$ is equivalent to solve

$$\begin{aligned} \mathbf{m} \times \mathbf{H}_{eff} &= \mathbf{0} \quad \forall \mathbf{r} \in V \\ \mathbf{m} \times (\mathbf{n} \cdot \nabla) \mathbf{m} &= \mathbf{0} \quad \forall \mathbf{r} \in S \end{aligned} \tag{2.47}$$

This latter formulation is referred as Brown's equations. The first equation assumes that a stable configuration for domain distribution is found as soon as the effective magnetic field aligns with the magnetic moments at all points of the FM volume. In other words, no local magnetic moment has to undergo a non-zero magnetic torque. The second equation can be further simplified since $|\mathbf{m}| = 1$, implying that the magnetic moment and the normal component to the surface of its gradient are necessarily perpendicular. The condition on the FM surfaces simply imposes that $(\mathbf{n} \cdot \nabla) \mathbf{m} = 0$. In the absence of surface anisotropy, the condition can be understood intuitively as follows: as surface magnetic moments only have one neighbour in the normal direction of the boundary, these surface moments have to be parallel to this neighbour (inside the body), otherwise they experience an exchange torque that cannot be compensated.

2.4.4 Characteristic lengths

In micromagnetics, the competition between the exchange energy and the magnetostatic energy is characterized by an exchange length defined by

$$l_{ex} = \sqrt{\frac{2A}{\mu_0 M_s^2}}. \tag{2.48}$$

It represents the shortest distance within which the magnetization can twist. Exchange interaction would like to maintain the magnetization aligned and therefore induces a rotation over a wide distance. However, in the transition

region, i.e. the domain wall, the magnetization goes through a hard axis in its transition between two domains aligned with the easy-axis. Therefore a thick domain wall costs more energy and a balance, described by the exchange length, has to be found. For micromagnetic simulations, the size of the discretization cells is based on the exchange length and smaller values are mandatory to accurately calculate the energy cost of domain walls. When the system is subjected to an important magnetocrystalline or induced anisotropy, a better definition of the exchange length is based on the first order anisotropic coefficient

$$l_{ex} = \sqrt{\frac{A}{K_{eff}}}. \tag{2.49}$$

Finally, Q, which is the ratio between both definitions of the exchange length (also named quality factor) gives an information on the type of ferromagnet:

$$Q = \frac{2K_{eff}}{\mu_0 M_s^2}. \tag{2.50}$$

If $Q > 1$ the sample is classified as a hard magnet while for soft ferromagnetic materials $Q \ll 1$. Devices studied in this thesis are all made of soft ferromagnets where shape anisotropy dominates.

2.5 Magnetization reversal in small structures

As presented in Figure 2.4, one important property of ordered magnetic materials is the phenomenon of magnetization reversal taking place for applied fields close to the coercive field H_c. This is particularly the case for the applications studied in this thesis. Indeed, anisotropic magnetoresistance sensors, magnetic flux concentrators and non-local lateral spin valves require an accurate prediction of the coercive field and more generally the shape of the hysteresis loop for external fields close to H_c. There are two major mechanisms involved in the magnetization reversal process: (i) coherent rotation of magnetization of a domain and (ii) domain growth via displacement of domain walls. Their relative importance depends on many factors such as the sample shape, the domain walls stability, the defect density or the magneto-crystalline anisotropy.

In a very small magnetic structure, domain walls are not energetically favorable and only a single domain (SD) is formed. The reversal mechanism is therefore based on the coordinated rotation of the magnetization. More precisely, there are three different modes of reversal for SD particles (see

Figure 2.14(a)). The first is the coherent rotation where all magnetic moments remain aligned and rotate simultaneously. Secondly, there is the curling mode where domains twist into a vortex-like state in order to reduce the stray field induced when the magnetization deviates from the easy axis. The third mode, named buckling, is a combination of both other modes. The competition between those three modes depends on the size and shape of the particle [55]. For example, considering a cylindrical particle, the reversal mode switches from a coherent to a curling mode when the radius increases. In contrast, the buckling mode is more represented in a thin film with small rectangular shapes.

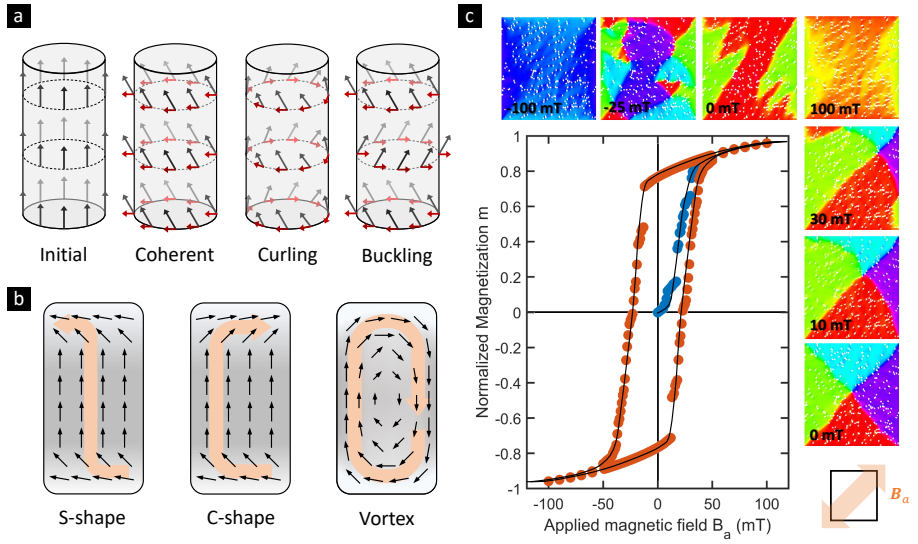

Figure 2.14: *(a) Illustration of single-domain particle reversal mechanism. (b) Examples of deviation from the uniform magnetization induced by demagnetization effects. (c) Complex hysteresis loop obtained by micromagnetic simulations of a square thin film sample including effects of magnetocrystalline anisotropy, demagnetization and structural defects. The orientation of the applied flux density is sketched in the bottom-right corner.*

The simplest and generally used analytical model to approximate the magnetization reversal process and evalute the coercive field in a SD pattern is the Stoner-Wohlfarth model which deals with a SD subject to a coherent rotation. More details about this pioneer model is given in Box 2.2. A first deviation from the Stoner-Wolhfarth model occurs when thin films patterns with larger dimensions are studied. In such samples, the magnetic arrangement deviates naturally from a uniform magnetization towards more stable configurations (flux-closure domains) that influence the system coercivity (see

Box 2.2: **The Stoner-Wohlfarth model**

The Stoner-Wohlfarth model assumes the coherent rotation of a uniformly magnetized ellipsoidal particle such that demagnetization field is constant all over the particle. The magnetic hysteresis results from the competition between a uniaxial anisotropy (in the direction labelled EA in Fig. 2.15(a)) which includes both shape and crystalline origins as expressed in Eqs. (2.36) and (2.41), and the Zeeman energy for an external field $\mathbf{H_a}$ applied with an inclination α from the easy-axis (see Figure 2.15(a)). The total energy of the system is given by

$$E_{tot} = K_{\text{eff}} sin^2(\theta) + \mu_0 H_a M_s \cos(\alpha - \theta). \tag{2.51}$$

where θ is the angle between the easy-axis EA and the magnetization direction. The hysteresis loop calculated following the Stoner-Wohlfarth model depends on the direction of the magnetic field as illustrated in Figure 2.15(b). The coercive field for an external field applied parallel to the easy-axis is

$$H_c = \frac{2K_{\text{eff}}}{\mu_0 M_s} = H_k, \tag{2.52}$$

while no hysteresis loop is obtained ($H_c = 0$) when $\mathbf{H_a}$ is along the hard axis of the particle. The coercivity reflects the ferromagnet anisotropy which is responsible for the metastable configuration of the system producing a remanent magnetization.

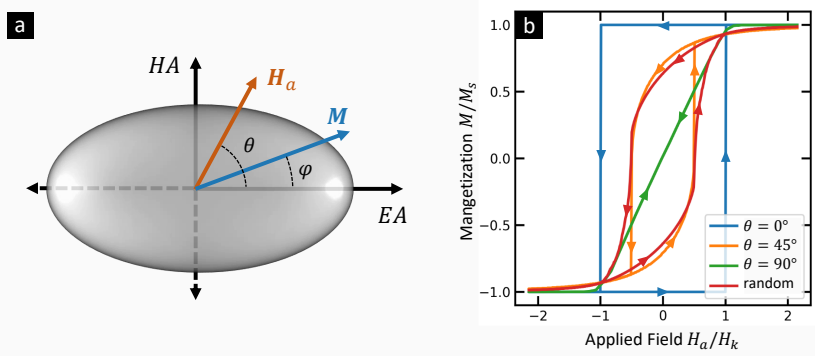

Figure 2.15: *(a) Schematic illustration of the Stoner-Wohlfarth model. (b) Hysteresis loop calculated for different directions α of the applied field H_a. The red curves correspond to the hysteresis loop of randomly oriented ellipsoidal particles.*

Figure 2.14(b)). For example, in the absence of preferential anisotropy (e.g. a disk made of soft ferromagnetic material), the more stable configuration is a single vortex for which the core position moves depending on the external field, leading to a zero coercivity. In rectangular patterns, C or S-shaped metastable states can be obtained, where both have similar stability but the first one leads to a higher coercivity than the second [56].

Naturally, as the ferromagnetic sample dimensions increase, multi-domains (MD) configurations are obtained and therefore the more energetically conve-

nient process of domain walls motion facilitates the magnetization reversal process. In fact, the hysteresis loop will exhibit features of domain nucleation, propagation and rotation reversal. The nucleation of magnetic domains are refered to as a local switching of magnetization. The solution of Stoner-Wolfarth model equals the nucleation field obtained by Brown's equations and is therefore the lower limit for the coercive field of larger ferromagnetic materials [57]. However, H_c is generally much lower than the experimental observations. This is known as Brown's paradox which is explained by the inhomogeneity of real materials [58]. Defects such as surface asperities serve as sources of nucleation because the reverse external field is enhanced by the large local demagnetization field linked to edges roughness. The propagation of freshly generated domains is limited by defects (interstitial, non-magnetic or less-magnetic inclusion, dislocation, etc.) where a difference of anisotropy and exchange transforms the site into a barrier or a trap [14]. Domain walls pinning force depends on the type, the size and the density of the defects, as well as the type of domain wall. For example, planar defects block more efficiently the domain walls than line or point defects because the wall is pinned all along the defect and not just locally. The successive translation of domain walls from one pinning site to another leads to a discretization of the hysteresis curve called Barkhausen jumps [59]. In Figure 2.14(c), an example is shown with a thin film 1x1 μm^2 soft ferromagnet with cubic anisoptropy and randomly distributed defects. The system varies with applied magnetic field due to domain walls propagation then magnetization reversal, forming complex domain structures, impossible to predict with analytical methods. In this work, magnetic domains distribution has been calculated using the GPU-accelerated micromagnetic simulation program *MuMax3*. Details are given in box 2.3.

2.6 Experimental technique for magnetic domains observation

There exist plenty of methods to evidence and observe magnetic domains and study their change under the effect of an external magnetic field. In this section, we introduce the three different techniques that have been used in this thesis: magnetic force microscopy (MFM), magneto-optical Kerr effect (MOKE) microscopy and anisotropy magnetoresistance (AMR).

Box 2.3: **MuMax3 simulation program**

Micromagnetic simulations presented in the two next chapters of this thesis have been obtained using the open-source software MuMax3 developed at the DyNaMat group at Ghent University. MuMax3 is a GPU-accelerate program based on NVIDIA GPU. The dynamics of magnetic domains is obtained by solving Landau-Lifshitz-Gilbert (LLG) equation

$$\frac{d\mathbf{m}}{dt} = -\frac{\gamma\mu_0}{1+\alpha^2}\mathbf{m}\times\mathbf{H_{eff}} - \frac{\alpha\gamma\mu_0}{M_s(1+\alpha^2)}\mathbf{m}\times(\mathbf{m}\times\mathbf{H_{eff}}), \tag{2.53}$$

using a finite-difference discretization [9, 10]. In order to find the magnetic ground state (i.e. static problems), MuMax3 provides a function to minimize the system energy while disabling the precession term of LLG equation. This results in solving Eq. (2.47).

In this thesis, a NVIDIA GeForce GTX 1650 has been used. Video memory is limited to 4 Go which corresponds to approximately 32 million finite-differential cells. In practice, this number is inferior and we limit our structures to $1000 \times 1000 \times 12$ cells. For additional resources and download links, one can consult the website https://mumax.github.io/

2.6.1 Magnetic Force Microscopy

The magnetic force microscopy is a technique adapted from atomic force microscopy (AFM) to make it sensitive to the stray field generated at the surface of a magnetic sample. AFM consists in probing the interaction force (or force gradient) between the sample surface and a tip [60]. The tip is located at the extremity of a cantilever, in turn connected to a piezoelectric scanner which controls the movement of the cantilever. The position, deflection or oscillation amplitude and frequency of the cantilever are probed using a laser and a photo-diode system as illustrated in Fig. 2.16.

Depending on the type of sample and the targeted physical properties, an AFM can run into different modes: the *contact mode* where the tip is continuously touching the sample surface, the *tapping mode* where the tip oscillates close to the surface and tap periodically the surface, and the *non-contact mode* where the tip oscillates above the sample without touching it. The different modes correspond to different regime of forces (repulsive and/or attractive) and tip-surface distance which are summarized in Fig. 2.17. In this work, only the two oscillating modes will be considered[7]. In

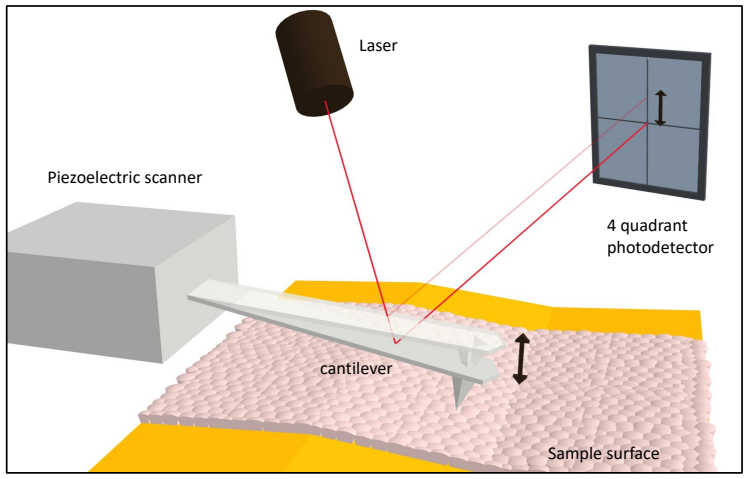

Figure 2.16: *Schematic illustration of the main components of an AFM working in tapping-mode. A piezoelectric scanner is shaking a cantilever at its resonance frequency, forcing a tip placed at its extremity to tap periodically the surface of a sample. The change of oscillation phase due to the interaction tip-sample is probed via a laser and a 4-quadrant photo-detector.*

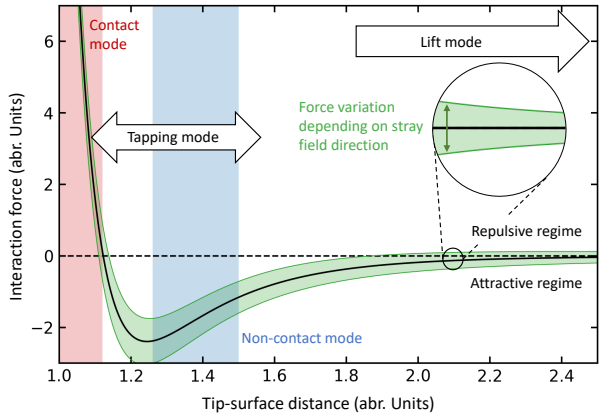

Figure 2.17: *Variation of the force between the AFM tip and the surface of the sample as a function of the distance. The distance range corresponding to different mode are indicated by colored (blue and red) area and large arrows. The green region represents the change of interaction force due to magnetic interactions.*

[7]See the following references for more details about the interest and working principle of

these modes, the cantilever is shaken at its resonance frequency. Both the amplitude and the phase of oscillations are sensitive to the intensity of the interaction forces between the tip and the surface. When the tip scans the surface of a sample, the sample-tip distance changes (and then the intensity of the interaction forces) depending on the topography of the surface. The AFM relies on a feedback loop to instantly correct the mean sample-tip distance in order to maintain a constant amplitude oscillation (or phase) while scanning the surface. Recording the variation of height with the lateral position allows the reproduction of the topography of the sample.

The same technique can be magneto-sensitive if probes coated by a magnetic layer are used [63]. In this case, the interaction forces are the combination of atomic forces and magnetic interactions. As the magnetic dipole-dipole interaction implies weak and long range forces (see section 2.2), non-contact mode at relatively large altitude ($\sim 5-50$ nm) is required. However, this mode remains affected by the sample roughness and/or eventual lithography patterns. As shown in Fig. 2.17, an increase of the lift height z will reduce the sensitivity to the topography (slope of the black curve) but also the magnetic signal intensity (amplitude of green area). In order to circumvent these issues, a two-pass scan is applied for each scan line as illustrated in 2.18. A first pass is achieved in tapping-mode to extract the surface topography. The second pass is achieved in non-contact mode (or lift mode), with a mean distance tip-sample from 10 to 100 nm modulated by the topography obtained through the first pass. During the second pass, the force endured by the tip is assumed to be only induced by the stray field at the surface of the sample and given by

$$\mathbf{F}_{t\to s}(z) = \frac{d}{dz}\left[\mu_0 \int_V (\mathbf{m}_{\text{tip}} \cdot \mathbf{H_s}(z))dV\right], \tag{2.54}$$

where $\mathbf{H_s}$ is the stray field generated by the sample and $\mathbf{m}_{\text{tip}}$ is the magnetic moment of the tip, generally approximated as a magnetic monopole oriented in the OOP direction $\pm e_z$. Considering the cantilever as a damped harmonic oscillator, it is shown that the phase shift Δf probed by the microscope can be approximated as proportional to the derivative of the magnetic force and given by

$$\frac{d}{dz}\mathbf{F}_{t\to s}(z) = \frac{2k}{f_0}\Delta f, \tag{2.55}$$

where f_0 is the resonance frequency of the cantilever and k is its stiffness constant [64]. The signal obtained by MFM is therefore proportional to the derivative of the OOP component of the stray field intensity and decreases

each mode [61, 62]

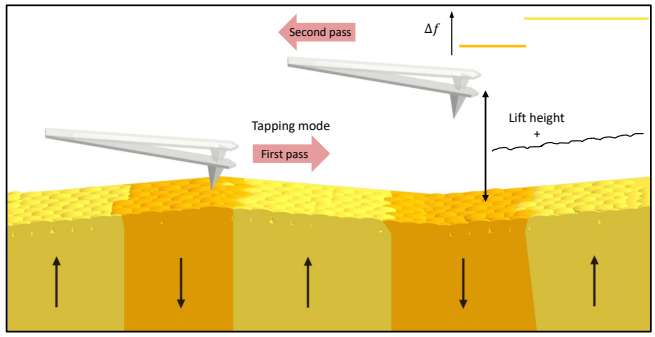

Figure 2.18: *Illustration of the two-pass method used in MFM. During the first pass in tapping-mode, the topography of the surface is registered since short range interactions are dominated by atomic forces rather than magnetic forces. During the second pass, the cantilever is lifted up several tens of nanometers and reproduces the topography of the surface, such that the Van der Waals' interactions become negligible and the tip-sample distance remains constant. The detected signal through the phase shift is therefore only due to magnetic interactions.*

sharply with the distance from the surface. In thin films, magnetic domains are generally confined IP and the stray field is more intense at the domain wall extremities, where the divergence of the magnetization is large. Therefore, it is generally assumed that the MFM image can be seen as a picture of magnetic charges. Consequently and thanks to the accurate lateral resolution (tenths of nm [65, 66]) of AFM, MFM measurements are well suited to image domain walls, leading to a clear difference between Bloch and Néel walls as shown in Fig 2.19. Domains orientation is then deduced from the observation of domain walls. Despite its high accuracy, MFM is generally used for qualitative observation since the technique has the drawback of a difficult quantitative analysis of the intensity of the stray field. Performing quantitative MFM has many constraints such as the exact knowledge of the tip magnetization, to work with tip that does not perturb sample domains (important with soft ferromagnetic samples), modelization to determine the magnetic field from the magnetic force gradient, etc. While different methods have been proposed to make it more suitable for quantitative measurements of the stray field [67, 68], MFM remains considered as a qualitative techniques, used to image micromagnetic distributions or for a geometrical quantification of domains and domain walls [69]. An example of MFM measurements is presented in Figure 2.20 for a 230-nm-thick patterned permalloy structure. The panel (a) shows the topographic image from the first pass and the panel (b) shows

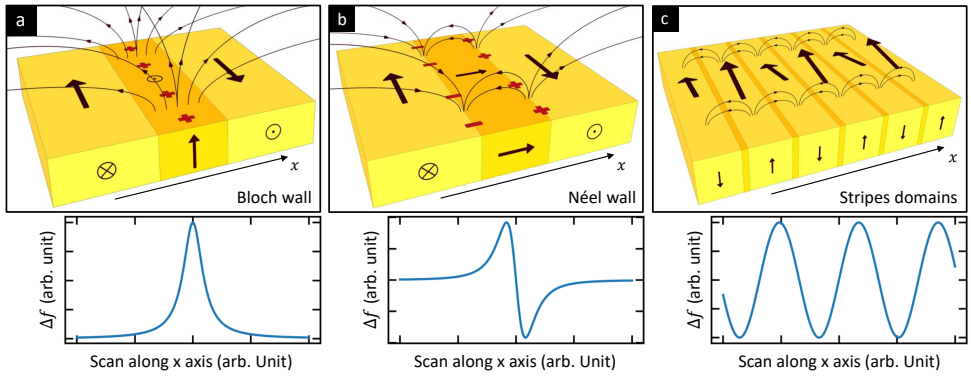

Figure 2.19: *Schematic illustration of the stray field distribution at the surface of a magnetic sample with (a) a Bloch wall, (b) a Néel wall and (c) a thin film with stripe domains, and the corresponding shape of the MFM signal (phase shift).*

the phase variation image obtained from the second pass in lift-mode, which reveals the presence of stripe domains.

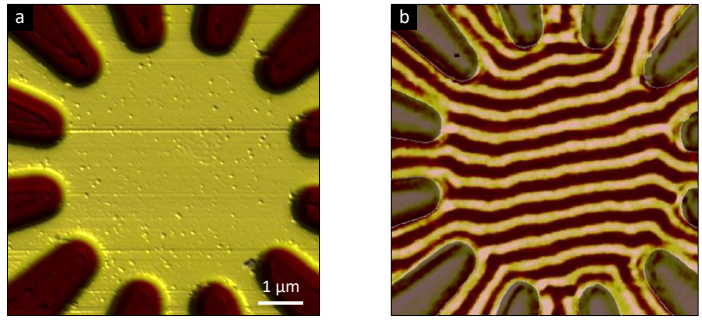

Figure 2.20: *MFM measurement of a Py patterned structure. (a) Topography of the structure and (b) Phase shift contrast from lift-mode. Results have been obtained using low momentum magnetic tip (MFM-LM-RC) and a lift height of 50 nm.*

2.6.2 Magneto-optical Kerr Effect

The Magneto-optical Kerr effect is a spin-orbit coupling related mechanism inducing the rotation of the polarization of light reflected at the surface of a magnetic sample [70]. The rotation of light by Kerr effect is phenomenologically described by the dielectric law [71]

$$\mathbf{D} = \epsilon \left(\mathbf{E} + iQ\mathbf{m} \times \mathbf{E} \right), \tag{2.56}$$

where ϵ is the regular dielectric constant and Q, known as the Voigt vector, is a material parameter approximately proportional to M_s which characterizes the intensity of the gyroelectric Kerr effect. The deviation of light polarization can be deduced, in a simplified fashion, assuming that the electric field of light excites electrons which moves along the polarization axis, represented by **E** in Fig. 2.21(a), leading to a reflected light with the same direction of polarisation **N**. Depending on the magnetization direction of the sample **m**, electrons endure a Lorentz motion $\mathbf{v_{Lor}}$ $(\mathbf{m} \times \mathbf{E})$, which gives rise to a deviation of the polarization represented by **K**. Consequently, the Kerr contrast, i.e. the amplitude of rotation of the light polarization, is proportional to the magnetization component parallel to the propagation direction of the reflected light beam [72].

The MOKE microscope is composed of an optical polarization reflection microscope based on Köhler illumination method allowing a homogeneous illumination. A complete scheme of the microscope structure is shown in Fig. 2.21(b). One key aspect of the MOKE microscope is the control of the incidence angle of light exposition. This is generally achieved using a movable slit aperture, allowing the selection of a preferential ray path (different ray paths giving different inclination of illumination are presented in Fig. 2.21(b)). Another mehtod, more suitable and used in this thesis, relies on a light source composed of a collection of 8 LED's that are switched on or off to mimic the displacement of aperture and induce a change of light inclination. In the end, the Kerr signal is translated into a contrast image via crossed polarizers, named polarizer and analyzer.

The MOKE can be used in three different configurations defined by the mutual orientations of the magnetization direction of the analyzed sample and the light polarization plane, the incidence angle and the propagation direction. Two of these configurations, the polar Kerr effect and the longitudinal Kerr effect are shown in Fig. 2.22, while the third and less commonly used transverse Kerr effect is not introduced in this work (see the following reference for a fully detailed report [71]). In the polar configuration (panel (a)), the four inner LED's are turned on in order to obtain an illumination with a perpendicular incidence. The Kerr effect is therefore sensitive to the OOP magnetization direction. In order to obtain a contrast for IP magnetic domains, it is necessary to have an oblique light incidence. The resulting image is therefore a superposition of Kerr contrast from both IP and OOP magnetization directions. While it is generally not needed for thin film where the OOP component is negligible, a pure longitudinal MOKE can be obtained by extracting differential images captured with opposite light propagation

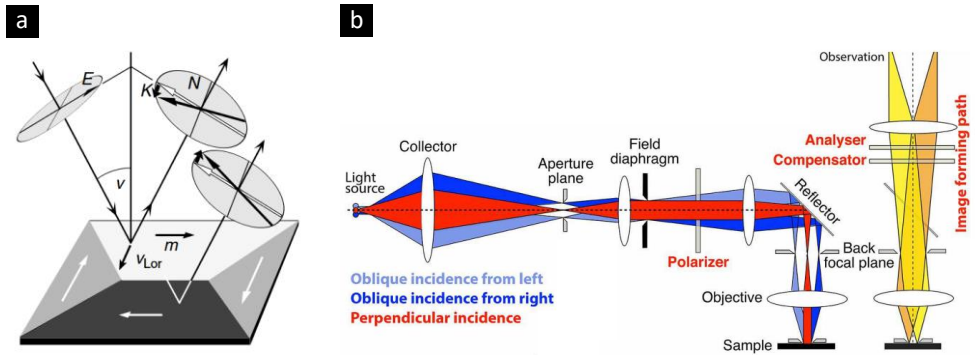

Figure 2.21: *(a) Illustration of the concept of the longitudinal Kerr effect. The deviation of the polarization (vector* **K***) is related to a Lorentz Force in the direction indicated by* $\mathbf{v_{Lor}}$*. Image taken from [71]. (b) Schematic illustration of the structure of a wide-field Kerr microscope. Red and blue colored regions represent different light pathways depending on the incident inclination of the beam. Image taken from [72].*

direction as shown in panels (c) and (d) of Fig. 2.21.

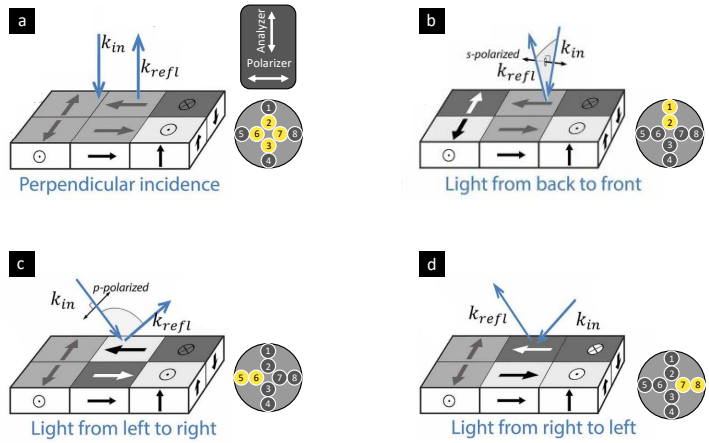

Figure 2.22: *Representation of the expect MOKE contrast under different configurations, respectively labeled (a) polar, (b) longitudinal with s-polarized incident light and (c) longitudinal in transverse direction with p-polarized light. (d) is equivalent to (c) with inverted contrast. The inset in each panel shows the respective configuration of LED's in the light source. These images are reproduced from [72].*

The figures 2.23(a-b) show MOKE results for different Py structures observed in longitudinal configuration. In panel (a), MOKE images of a 300×50

μm^2 and 30-nm-thick bar of Py are shown for two different directions of illuminations (indicated by the equivalent LED's configuration) and for intensities of external magnetic field (applied along the long side of the bar) just below and above the coercive field H_c, revealing a buckling magnetization reversal mechanism. Panel (b) shows the demagnetized state of a Py flower-like magnetic flux concentrator. The improved contrast compared to panel (b) is obtained by subtraction of images with opposed directions of light inclination. Surface defects and topographic relief are removed by subtracting a background image, which is either captured at saturated magnetic field, or from an average contrast over several hysteresis loops.

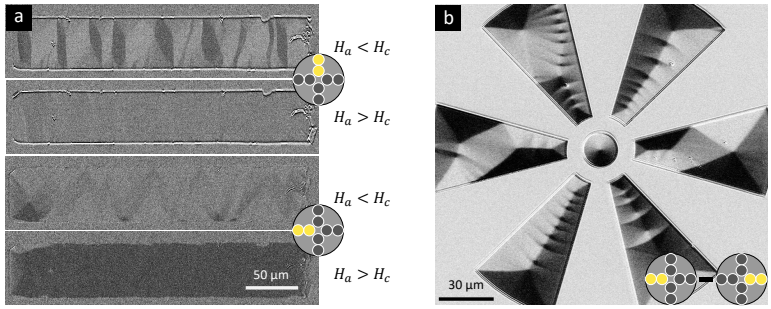

Figure 2.23: *(a) MOKE images of a single 50 µm × 300 µm × 30 nm permalloy bar at different applied fields along the horizontal direction, with light propagation directed perpendicular (top ones) and parallel (bottom ones) to the applied field. (b) Highly contrasted MOKE images of the Py magnetic flux concentrator obtained by differential images. The insets show the LED's configuration used for each images.*

2.6.3 Anisotropic magnetoresistance

Magnetoresistance stands for the change of resistance in a sample depending on the external magnetic field. In ferromagnetic material, the resistance not only depends on the field intensity but also on the relative direction of the magnetization and the applied current. This effect is named *anisotropic magnetoresistance* (AMR). The physical origin of AMR is primarily ascribed to the spin-orbit coupling affecting s-d scattering which is more effective when the plane of the orbit (depending on the magnetization direction via SOC) aligns with the current direction [73, 74].

Generally, the resistance is a few percents lower when charges are flowing along the direction of **M** than in the transverse direction. AMR is expressed in terms of minimal ($\mathbf{J} \parallel \mathbf{M}$) and maximal ($\mathbf{J} \perp \mathbf{M}$) resistances $R_{\parallel}$ and $R_{\perp}$

of the studied device. Considering a monodomain magnetic structure, the electrical resistance depends on the orientation of the magnetization with respect to the current direction [75]:

$$R(\varphi) = R_\perp + (R_\parallel - R_\perp)\sin^2\varphi, \tag{2.57}$$

with $90° - \varphi$ being the angle between the magnetization and the current as illustrated in Fig. 2.24(a) with a 4-point measurement on a patterned magnetic thin film. The angle φ is an unknown variable only meaningful in

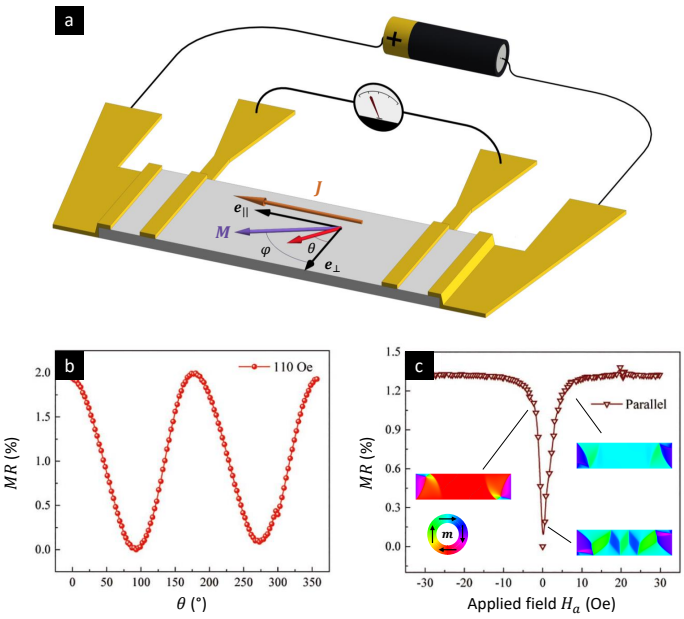

Figure 2.24: *(a) Illustration of a 4-point measurement set-up for AMR experiment in a rectangular thin film structure. (b) AMR signal as a function of the orientation of the applied field θ in a 10-nm-thick Py stripe. (c) AMR signal of a magnetization reversal process in a Py strip. The deep of resistance is explained by the magnetization reversal process. Insets are micromagnetic simulations of a strip with similar aspect ratio used to illustrate the link between domains motion and resistance change. Panel (b) and (c) are reproduced from [76]*

the context of the single domain approximation. From the Stoner-Wohlfarth model presented in Box 2.2, φ can be deduced from experimentally relevant variables H_a and θ. More generally, the variation of the resistance can be determined from the hysteresis loop according to the following equation [77]:

$$R(H) \propto [1 - (M(H_a)/M_s)^2], \tag{2.58}$$

where $M(H_a)/M_s$ is the normalized mean magnetization.

The sensitivity of the AMR is given by

$$MR(\%) = \frac{R(H_a, \theta) - R_\perp}{R_\perp} \times 100, \tag{2.59}$$

where $R(\mathbf{H_a}, \theta)$ is the resistance probed at a magnetic field intensity $\mathbf{H_a}$ and direction θ. In Fig. 2.24(b), an example of AMR change with external field applied in-plane with a varying direction θ and a fixed intensity of 11 mT in a 10 nm-thick Py stripe [76]. The symmetry of the signal indicates that $\varphi \simeq \theta$, suggesting that the Zeeman energy dominates over shape anisotropy effect, due to the high value of $\mathbf{H_a}$. The panel (c) shows the AMR signal as a function of the applied field along the long side of the same Py stripe. As the magnetic field decreases, the domains begin to misalign from the current flow direction, leading to a resistance decrease. When H_a equals the coercive field, the domains flip and the resistance increase abruptly.

3

Planar on-chip isotropic magnetic field concentrator

3.1 Introduction

In the current information and communication age, smart electronic systems, sensors, actuators, wireless, or remote monitoring technologies are experiencing rapid growth. In particular, magnetic sensors have been used to achieve many operating functions for a large variety of applications. There are many approaches to sense magnetic fields [78, 79], based on several physical principles including Hall-effect, fluxgate, anisotropic or giant magneto-resistance, magnetic tunnel junctions, superconducting quantum interference device (SQUID), or nitrogen-vacancy centres. Although enormous progress has been made to improve their performance, a considerable research effort is still needed to find new ideas enabling enhanced sensitivity, combined with low power, remote monitoring, or autonomous performance. An important problem for magnetic sensors arises from the combination of two technological trends: the need for very high sensitivities (detection and monitoring of increasingly smaller magnetic fields) and the small volume available for the magnetic sensors in increasingly more densely integrated devices. These two trends lead to a conflicting strategy: reducing the volume of the sensor could decrease its sensitivity, since the latter depends sometimes on the area threaded by the magnetic flux. A widely implemented solution for increasing magnetic concentration consists in placing the sensing area in the gap between two ferromagnetic strips [80–85]. However, the potential of magnetic flux concentration for sensing devices is currently far from being fully exploited, basically because the field in the gap between concentrators is highly inhomogeneous, strongly limiting the sensor design. As with the

sensors, further improvement of magnetic flux concentrator (MFC) could be beneficial for energy harvesters, the performance of which depends on the magnetic flux in the dedicated pick-up area [86, 87].

Recently, a new approach has been proposed to efficiently and homogeneously concentrate magnetic flux and collect energy from weak low-frequency magnetic fields and at small scales, with the potential to radically improve the efficiency of the next generation of sensors and magnetic harvesters. Indeed, a metamaterial shell composed of concentric and equidistant funnels made of ferromagnetic foils surrounding a magnetic sensor, could homogeneously enhance the magnetic field (for static and up to 100 kHz ac fields) in the sensing area, by a factor that depends on the shell radii ratio and number of funnels. This effect, however, has been only demonstrated in large-scale proof-of-principle experiments, e.g., bulky 3D concentrators or cylindrical systems [88, 89]. In on-chip devices at the microscale, where the use of sensors and small harvesters is increasingly needed, downscaling the concept of metamaterial shells to provide planar meso/micro-metasurfaces represents the next logical step. In addition, the proposed magnetic metamaterials have only been analyzed assuming that their components have a linear response, without magnetic saturation and ignoring the irreversible response of real ferromagnetic materials. Scrutinizing the influence of these effects on the response of the magnetic flux concentration and quantifying their dependence on the geometry and size of the structure will further help to the optimization of rational designs as well as identifying the operational limits.

In this work, we carry out a numerical and experimental analysis of planar magnetic field concentrators representing a miniaturized 2D version of the designs proposed in Refs.[88, 89]. The numerical simulations include the comparison between the ideal linear response and the modeling of magnetic domain structure effects in the planar metasurfaces, accounting for the non-linear dependence of the magnetic permeability of ferromagnets. We investigate in detail the effects of metasurface dimensions and geometry. We also investigate the different possibilities to experimentally measure the gain of microscale MFCs by integrating a sensor device at the center of the devices and performing magnetoresistance measurements, vortex displacement tracking or stray field quantification.

3.2 Flower-like magnetic flux concentrator design and modelling

The considered MFC consists of a flower-like structure as schematically presented in Fig.3.1, where each petal has the same angle θ and is made of a ferromagnetic material with thickness t. The inner and outer radii of the structure are R_i and R_o, respectively. This device is intended to concentrate the applied in-plane field B_a in the central gap of the flower where a magnetic sensor will be located. The intensity of the concentrated field, labeled B_0, is the average of the field in a sphere of radius $R_i/10$ centered at the geometrical center of the MFC. Note that flower-like geometry and domain structures associated to the irreversible response of the ferromagnetic components could produce a magnetic field $\mathbf{B_0}$ non-collinear with $\mathbf{B_a}$. Therefore, the figure of merit quantifying the concentration power of the device (so-called gain) is the ratio of the collinear compound of the field at the center of the flower B_0 to the applied one[1],

$$G = \frac{\mathbf{B}_0 \cdot \mathbf{B}_a}{|B_a|^2}. \tag{3.1}$$

A regime in which $G > 1$ will be referred to as concentrator, whereas if $G < 1$ the device acts as a magnetic screen or shield.

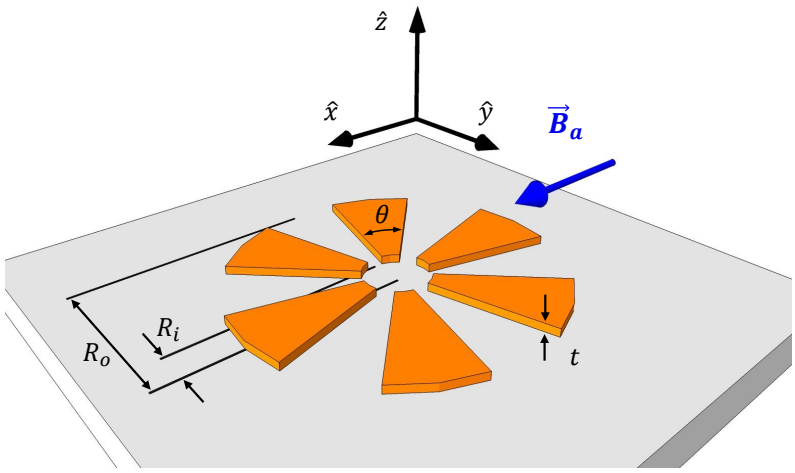

Figure 3.1: *Sketch of the magnetic flux concentrator indicating the main geometrical parameters and the applied magnetic field orientation.*

[1]This figure of merit can be adapted depending on the properties of the devices placed at the center of the flux concentrator

In the first part of this work, we will assume a homogeneous ideal paramagnetic material (IPM) adopting the same method as in [88] but including a finite film thickness. Stationary Maxwell's equations in absence of current are solved using Finite element method with the magnetostatic module of Comsol Multiphysics software. For each field configuration, a stationary solution is obtained with a relative accuracy of 10^{-5}. The simulation box has a lateral size of $10R_o$ with boundary condition $B = B_a$ and using a tetrahedral mesh grid. Otherwise explicitly indicated, all Comsol simulations have been performed for a device with $R_o = 4R_i = 20$ μm and $t = 500$ nm.

We will later on add complexity to the model by taking into account non-linear magnetic response of real ferromagnetic material. Micromagnetic modelling of the metamaterials were performed with the open-source MuMax3 program [10]. The modelled material is permalloy (Py) with magnetic saturation $M_s = 860$ kA/m, exchange stiffness $A_{ex} = 13$ pJ/m, and negligible crystal anisotropy as expected for Py. For small size structures, the discretization cell has been chosen to be smaller than the exchange length ~ 5 nm. For larger structures, we have relaxed this constraint using cell sizes ranging from 5 to 10 nm. In this case, particular care must be exerted in the analysis of the data due to the unavoidable loss of resolution for magnetic domain walls.

3.3 3D and 2D Concentrators in the ideal paramagnetic limit

Let us start by considering the ideal case of an ideal linear paramagnetic material with magnetic permeability $\mu \gg \mu_0$, being μ a temperature and magnetic field independent constant. Under this assumption, the magnetic material will not exhibit any saturation field. The first hypothesis is not too stringent, since for a typical ferromagnetic material such as permalloy, a typical value of the relative permeability is $\mu/\mu_0 \approx 10^6$. However, the linearity condition and the reversible response will only hold in a limited narrow range of applied magnetic fields. Within the hypothesis of IPM response, we will compare the performance of an infinitely long cylindrical concentrator ($t \to \infty$) with that of a planar device of finite thickness. The former, less demanding of computational resources, will be labeled as 2D manifesting the independence of the magnetic response to the $\hat{z}$-coordinate. In contrast, the thin film structures require a three-dimensional simulation cell and will be labeled as 3D.

It has been demonstrated that by properly adapting the geometry of the

MFC, a substantial amplification effect can be obtained with an optimal performance achieved in tanga-shaped concentrators [80, 90]. Later on, based on numerical simulations, Sun et al.[84] demonstrated that triangle-shaped concentrator (as the flower here proposed with only two opposing petals) offers the widest linear working range and provides a competitive magnetic gain compared to other geometries. In this section we will analyze the influence of different geometric parameters on the gain of the flower-shaped MFC.

3.3.1 Influence of petal opening angle

In what follows we will assume $\mu/\mu_0 \approx 10^6$ for the ferromagnetic material, and we will analyze the gain of the device for a constant applied field $B_a = 5$ mT along the $\hat{x}$-axis (bisector of a petal). We will start by investigating the influence of the petal angle θ for a MFC composed of N_p petals. Figure 3.2 shows the gain G versus the angle of the petal for (a) a 2D and (b) a 3D device, and for $N_p = 2, 4, 6$. Since the maximal petal angle θ_{max} for which the petals start to overlap depends on the number of petals as $\theta_{max} = 2\pi/N_p$, the abscissa axis of Fig. 3.2 has been normalized by θ_{max}. Note that $N_p = 2$ outperforms devices with higher N_p nearly in the whole angular range θ/θ_{max}. Hence, it is not surprising that commercially available MFCs as well as most of previous investigations have focused on $N_p = 2$. Interestingly, thin films devices may offer a higher gain than macroscopic 2D devices if the angle of the petals is properly chosen. This is so because the thin films are able to concentrate field lines above and below the surfaces laying in the $\hat{x}$-$\hat{y}$ planes. Indeed, Fig. 3.2(b) shows that for thin film structures, there is an optimum angle θ_{opt} for which the gain achieves a maximum value. For $\theta < \theta_{opt}$ the petal collects less magnetic flux simply because the cross section of the petal decreases. For $\theta > \theta_{opt}$ magnetic field lines reconnect, bridging the gap between the petals without reaching the center of the device. Eventually, at an angle θ_{shield}, the gain $B_0/B_a < 1$ and the device screens the center from the applied field behaving as a shield or magnetic field attenuator. The angles θ_{opt} and θ_{shield} as a function of N_p presented in Fig. 3.2(c) depict a monotonous decreasing functionality proportional to N_p^{-1} naturally arising from the upper bound limit $\theta_{max} = 2\pi/N_p$.

3.3.2 Influence of thickness

As we mentioned above, thin film devices have a higher gain (i.e. perform better) than macroscopic devices since they are able to collect magnetic field

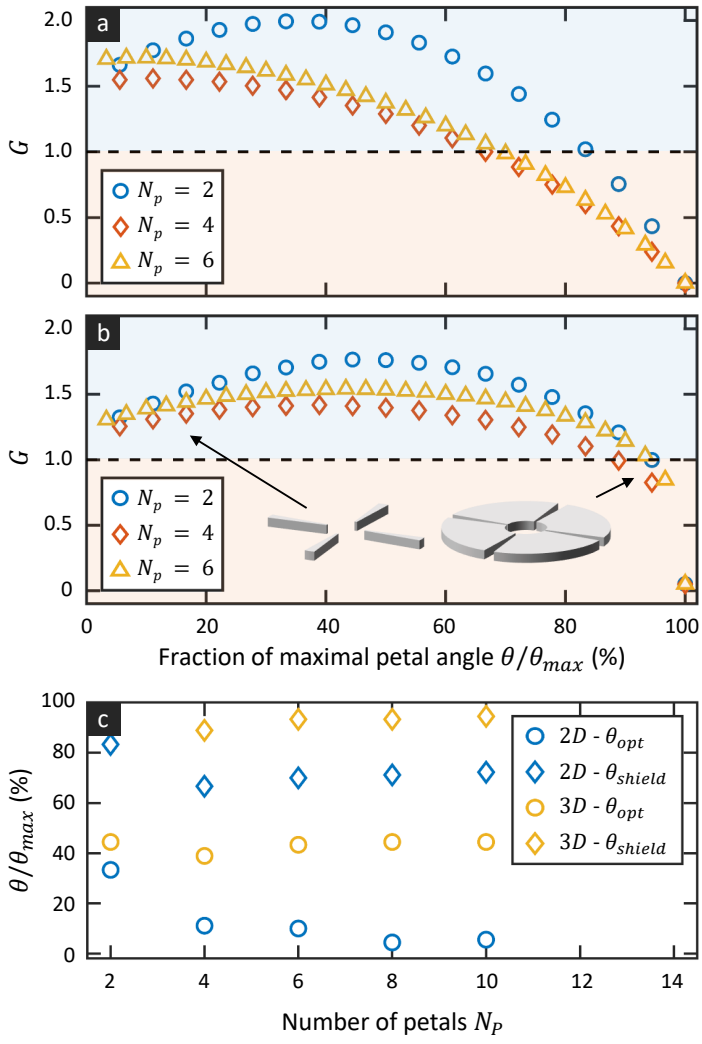

Figure 3.2: *Variation of the petal opening angle θ. Gain $G = (\mathbf{B}_0 \cdot \mathbf{B}_a) / |B_a|^2$ as a function of $\frac{\theta}{\theta_{max}} = N_p \frac{\theta}{2\pi}$ for flowers with 2, 4 and 6 petals for an infinitely thick device (a) and a thin film ($t = 100$ nm) device (b). At $\theta = \theta_{max}$ (100%), the petals touch each other and represent a solid ring, therefore the metamaterial becomes a shield and the magnetic field at the center is lower than the applied field. In panel (c), θ_{opt}, the opening angle for which the FC is optimized, and θ_{shield}, the angle for which it transits from concentrator to magnetic shield, are plotted as a function of the number of petals.*

lines from above and below the plane of the device. However, due to their limited thickness, a non-negligible part of the field lines leak out and do not contribute to increase the gain, i.e. the surface on which the field spreads is much larger than the thickness. This observation might suggest that there should exist an optimum thickness of the MFC. This effect is demonstrated in Fig. 3.3 where the gain as a function of the device thickness t for $N_\mathrm{p} = 2, 4, 6$, is shown. In this case the angle of the petal $\theta = \theta_{\max}$ with $\theta_{\max}$ the angle at which G is maximized for a thickness $t = 0.5$ µm. The dashed lines represent the gain for infinitely long cylindrical devices (2D limit where $t \to \infty$). Note that devices thicker than a few µm outperform very thick devices, whereas an optimal gain is obtained when $t \sim 2R_\mathrm{i}$.

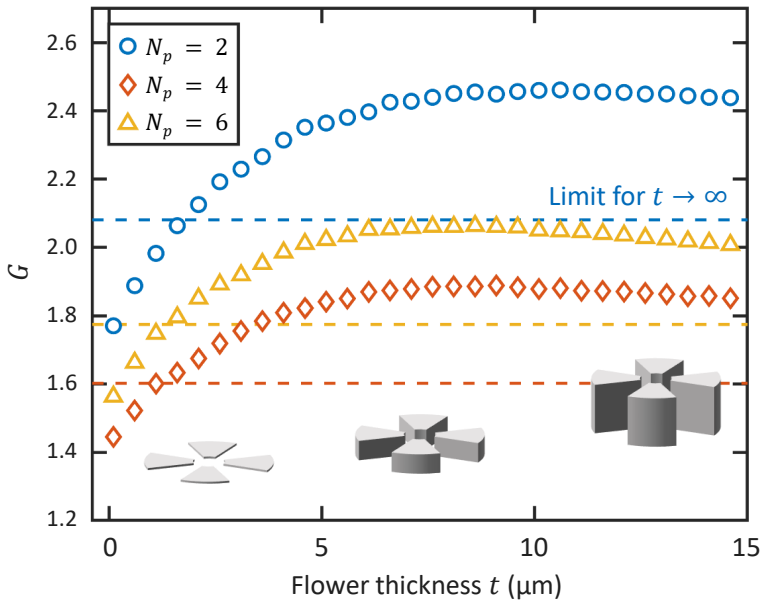

Figure 3.3: *Gain as a function the device thickness t for $N_p = 2, 4, 6$. The dashed lines represent the gain for infinitely long cylindrical devices (2D limit).*

3.3.3 Influence of in-plane field orientation

We have already pointed out that a device with two petals offers the best figure of merit. However, this is so as long as the applied field is oriented along the bisector of the petals, as schematically shown in the upper inset of Fig. 3.4. For in-plane orientation angle β away from this optimal direction

(corresponding to $\beta = 0$), the gain is rapidly reduced. This highly anisotropic response requires careful orientation of the device and the prior knowledge of the direction of the magnetic field intended to be harvested. It may be more practical for applications to increase the number of petals for the sake of rendering the device more isotropic (i.e. angular insensitive), at the expense of slightly compromising the gain. Fig. 3.4 shows that this is possible by increasing the number of petals to $N_p = 4$, irrespective of the thickness of the device. The striking fact that the gain becomes angular-independent for $N_p \geq 4$ has been confirmed for different angles of the petals and also when intercalating a perfect diamagnet ($\mu_r = 0$) into the gaps between consecutive ferromagnetic petals.

3.3.4 Influence of number of petals

Let us now investigate the evolution of the mean gain $\overline{G} = \frac{1}{2\pi}\int_0^{2\pi} G(\beta)d\beta$ as a function of the number of petals, as shown in Fig. 3.5. Blue and yellow datapoints correspond to bulk (2D limit) and film geometry, respectively. One can observe that the gain initially tends to increase as N_p increases and flattens out for $N_p > 20$. In this figure, two different angles θ are compared, namely $\theta = \theta_{opt}$ which, by definition, provides the maximum gain, and $\theta = \pi/N_p$ in such a way that the size of the gaps between consecutive petals is the same as that of the petals. Interestingly, for bulky samples, optimizing the angle leads to a substantial improvement of the device's performance. However, in thin structures the response is rather insensitive to optimization of the angle. This is not surprising since, as shown in Fig. 3.2(b) the optimal angle is rather close to π/N_p in the case of thin films samples.

3.3.5 Influence of petal length

Thin film MFC are intended to be adapted to (i) the size of the sensor, which limits the R_i and (ii) the sourrounding circuitry, which imposes a constraint on R_o. Clearly, the larger the ratio R_o/R_i the larger the gain. Within this context, it is important to know how the performance of the device evolves as the inner and outer radii change. Fig. 3.6(a) shows the gain G as a function of the petal length $L = R_o - R_i$, keeping R_o/R_i constant and for $N_p = 2, 4, 6$. Therefore in panel (a), longer petals imply larger values of R_i, being the effective gain dominated by this latter effect. In other words, the increased L does not compensate the negative effect of increasing R_i. Fig. 3.6(b) shows the gain as L increases while keeping a constant $R_o = 60$ μm. In this case, increasing L implies reducing R_i which leads to a very quick increase of the

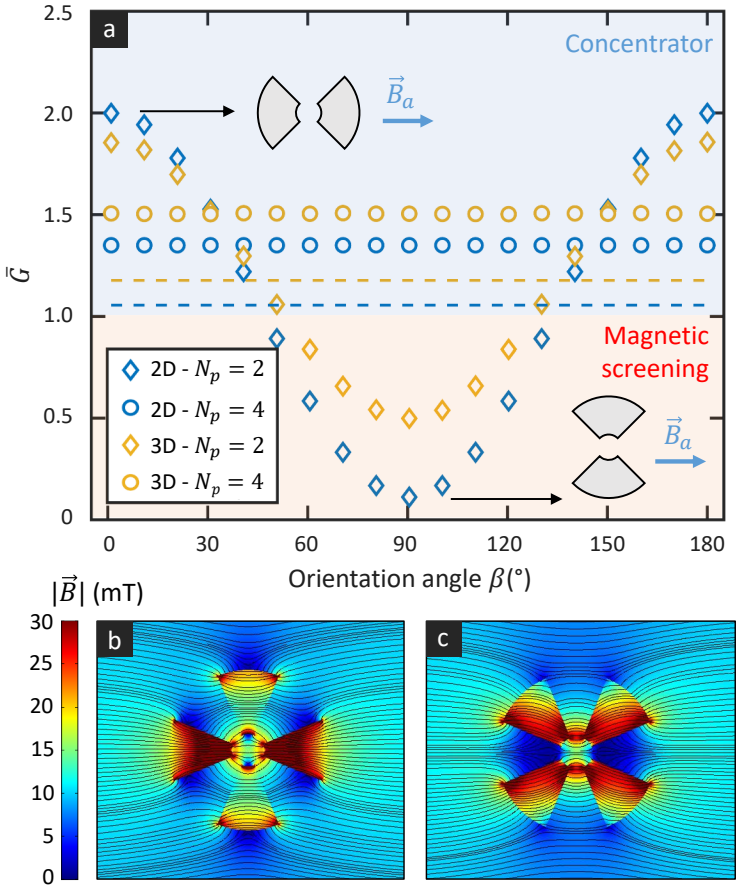

Figure 3.4: *(a) Gain as a function of the in-plane magnetic field orientation β for $N_p = 2$ and 4. The dashed lines represent the angular-average gains. Panels (b) and (c) are cut views of the device with 4 petals and different orientations immersed in an external field of 10 mT applied.*

gain following a dependence stronger than an exponential growth. Fig. 3.6(c) presents the gain as L increases while keeping a constant $R_i = 5$ μm. In this case, there is a nearly linear increasing benefit of enlarging L. In the 2D limit, it has been shown that the maximum gain possible $G_{max} = R_o/R_i$ is achieved by flower-like concentrators with alternating superconducting and ferromagnetic petals and an infinite number of petals [89]. In panels (a), the value of G_{max} is constant and equals 12. In panels (b) and (c), G_{max} is plotted (black dashed lines) for the sake of comparison.

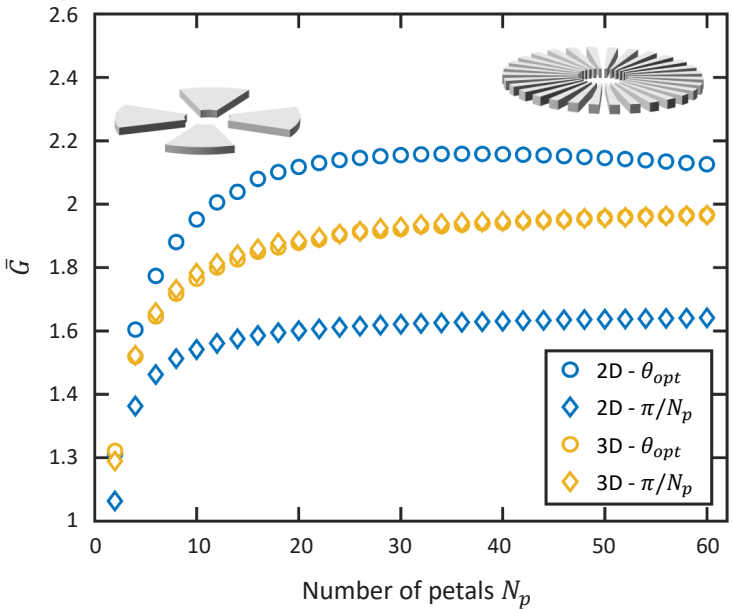

Figure 3.5: *Mean gain $\overline{G}$ as a function of N_p for $\theta = \theta_{opt}$ and $\theta = \pi/N_p$. Blue and yellow datapoints correspond to bulk (2D limit) and film geometry, respectively.*

At this point, we can summarize our results as follows: thick film ($t \sim 10$ μm) devices containing a large number of petals $N_p > 10$ with petal angle $\theta \sim \pi/N_p$ offer the best global performance in terms of gain and insensitivity to in-plane magnetic field orientation. In addition, a sur-exponential benefit in the gain can be obtained by reducing R_i whereas a linear increase of $\bar{G}$ can be obtained by increasing R_o.

3.4 Influence of non-linear magnetic response

The results presented so far include neither the effects associated to a saturation magnetization nor the consequences of magnetic domains. For a macroscopic device in a limited range of magnetic field, the hypothesis of an ideal paramagnetic material may remain reasonable. However, when scaling down towards micrometer dimensions, the magnetic domain distribution needs to be taken into account in order to accurately and realistically predict the flux concentration efficiency in a large magnetic field range.

In this section we allow the possibility to have a position-dependent

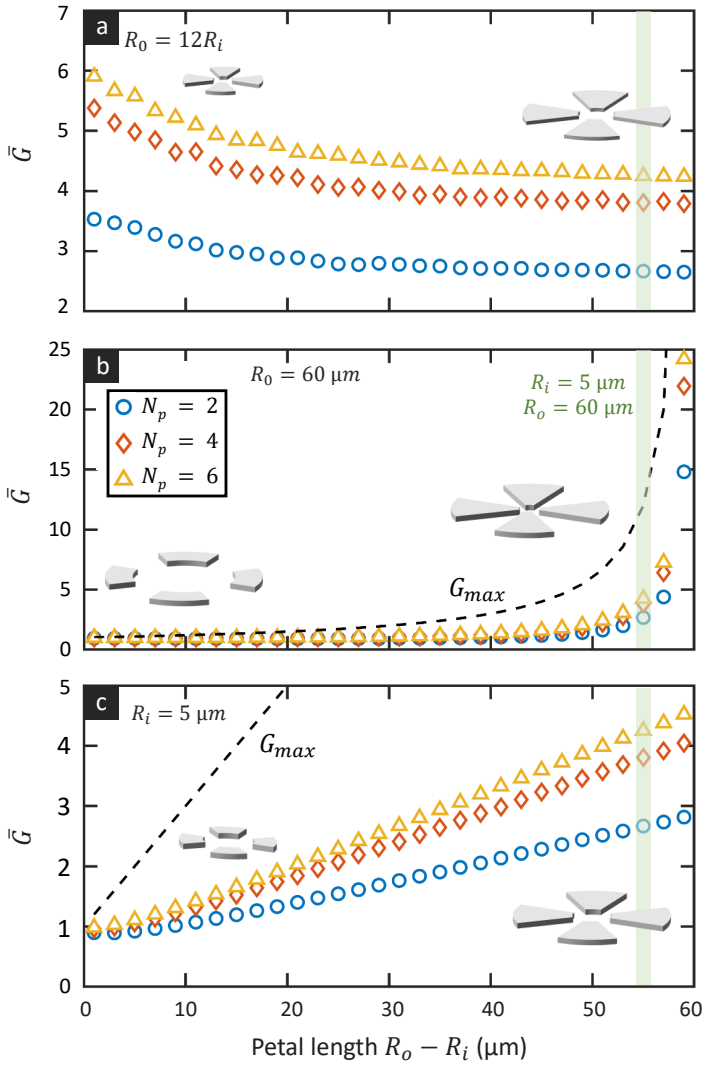

Figure 3.6: *Concentration efficiency as a function of the petal length by varying (a) both R_i and R_o while keeping their ratio constant, (b) R_i while keeping R_o constant and (c) R_o while keeping R_i constant. The green shadow highlights the configuration R_o=12R_i=60 µm.*

magnetization $\mathbf{m}(\mathbf{r})$ and calculate the resulting stray field $\mathbf{B}_s(\mathbf{r})$ which in turn will define the concentration power of the device. The Gain of the MFC is defined by Eq.(3.1) with the component of the field at the center of the structure in the applied field direction $B_0 = B_s + B_a = (\mathbf{B_s} + \mathbf{B_a}) \cdot \mathbf{B_a}/|\mathbf{B_a}|$.

In Fig. 3.7, the hysteresis cycle of B_s is plotted as a function of B_a in a MFC of 6 petals with $R_o = 5R_i = 5$ µm and a thickness $t = 80$ nm. First, we observe

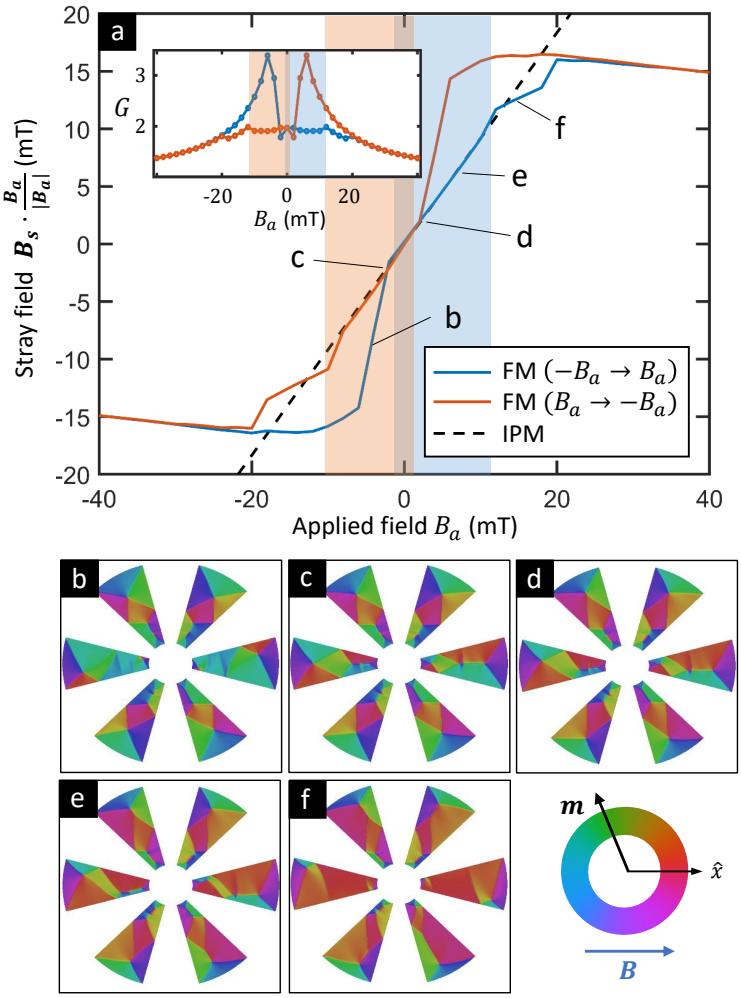

Figure 3.7: *Effect of domain distribution on a 6-petal MFC. (a) Hysteresis cycle of the stray field B_s emanating from the petals at the center of the device as a function of the applied field intensity B_a. Blue and orange lines are respectively for ascendant and descendant sweeps. The dashed black line is for the corresponding ideal paramagnetic material. Blue and orange highlighted regions show the range of applied magnetic field for which there is a linear relation between B_0 and B_a associated to the displacement of the magnetic vortex core and the domain wall. Inset image shows the corresponding gain G for each magnetic field. (b-f) Mapping of the magnetization at different fields. Panels (c) to (e) corresponds to the linear regime.*

that the linear response of the concentrator (constant gain G) is observed only within a narrow magnetic field range highlighted by a blue (orange) shaded area for ascending (descending) magnetic field sweeping. In this field

range, the domains arrange themselves to form a Landau pattern (domain closure forms a vortex core and/or cross-tie wall separating two anti-parallel domains) and the displacement of the core of the magnetic vortex as shown in panels (c-e) of Fig. 3.7, provides the linear response. For higher applied magnetic fields, the device is saturated and the stray field remains almost constant ($G = 1$). The observed slight decrease of B_s as the device reaches saturation is due to the fact that the petals with their long side perpendicular to B_a will generate a stray field in the opposite direction than those petals with their long side parallel to B_a. Therefore, the total stray field reduces while approaching the saturation. An important result that can be drawn from the analysis associated to Fig. 3.7 is that (i) the presence of magnetic domains severely reduces the field range for which the MFC concentrator can work in the linear regime and (ii) the saturation field leads to a reduction of gain with the intensity of applied field.

In the hysteresis loop of Fig. 3.7, one can observe that the transition between saturated and linear regions takes place through clear steps indicated by positions (b) and (f). This effect results from the multi-petals architecture of the device. In order to clarify this point, in Fig. 3.8, the magnetization hysteresis loop of individual petals is shown for two petals with different orientations with respect to the applied field in a 6-petal device. As expected, the transition from a mono-domain into a Landau pattern is triggered at different magnetic fields depending on the orientation of each petal. From Fig. 3.8, one can conclude that the petal limiting the performance of the device (i.e. the linear regime) is the one parallel to the applied field. The reason is that the linear regime is observed as long as the magnetic closure configuration is present, and for this particular petal the magnetic field favors more the single domain configuration and reduces the field range where the vortex state exists. In other words, shape anisotropy forces the domains to align along the long symmetry axis of the petals, stabilizing the single domain configuration of those petals with long axis matching the external field orientation.

Even if the domain distribution depends on the relative orientation of each petal, it is shown in Fig. 3.9 that a flower-like device is rather insensitive to the orientation of $\mathbf{B_a}$ when there are 4 petals or more. Panels (a) and (b) show B_s as a function of the applied field which is swept from -16 to 16 mT, respectively in 2-petal and 4-petal MFCs. Results are plotted for both symmetric configurations ($\beta = 0$ and $\beta = \pi/N_p$). Results are similar to the one previously obtained using IPM approximation (see Fig. 3.4). Note that a 2-petal device gives better concentration efficiency than a multi-petal one

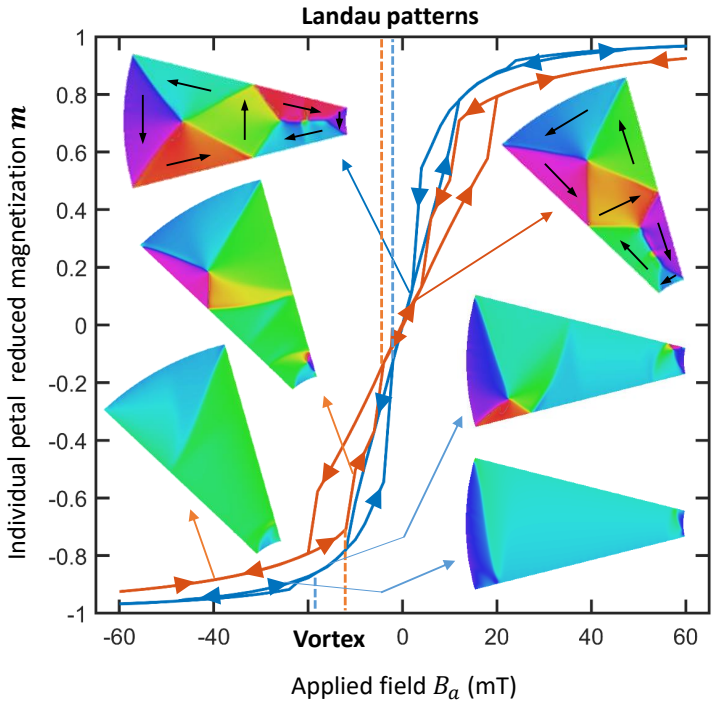

Figure 3.8: *Magnetization hysteresis of two individual petals with different orientations with respect to the horizontal applied field in a 6-petal device. Mapping of the domain are shown for three particular situations: saturation, core of magnetic vortex and anti-vortex penetration and Landau pattern (stable arrangement between the vortex and anti-vortex). For the latter, the preferential magnetization direction of each domain is indicated by black arrows. The magnetic field triggering vortex apparition and Landau pattern arrangement is indicated by dashed lines.*

when the applied field is perfectly aligned with the system. However, it becomes a magnetic shield if alignment is incorrect ($\beta = \pi/N_p$). For a 4-petal device the linear response is rather independent of the orientation angle β. The configuration where all 4 petals form an angle β with $\mathbf{B_a}$ presents a larger linear range which confirms the previous interpretation concerning the effect of shape anisotropy. The lack of sensitivity to the applied field direction implies that there is no need to carefully align the device with respect to the external field. However, this observation only holds when a full hysteresis loop is completed, meaning that domains distribution is erased at saturation. If the external field direction is changed while the system is in the linear regime, the response will slightly deviate from the ideal effect because the inner domains (those at the tip of the petals) retain the state imposed by the

initial magnetic field orientation.

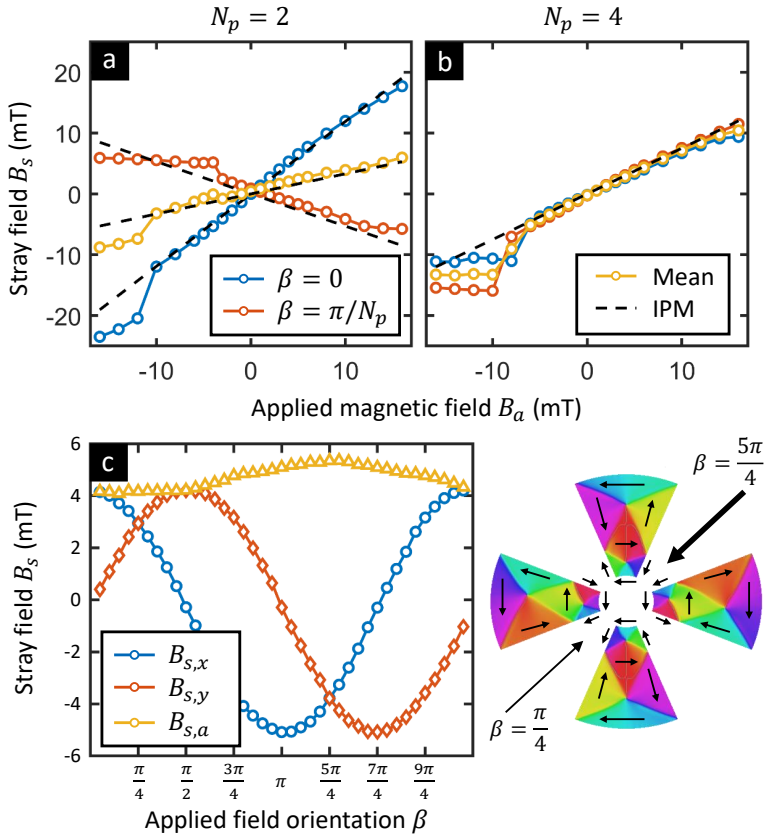

Figure 3.9: *Effect of the incident angle β on the MFC efficiency. (a-b) central demagnetization field for applied field growing from -16 to 16 mT, respectively for MFC with (a) $N_p = 2$ and (b) $N_p = 4$. Results are plotted for 2 different angles β (orange and blue) and the mean of both (yellow). Dashed lines correspond to the IPM solution. (c) Effect of the orientation of a 5 mT applied field on the central demagnetization field in a 4-petal flower. Angle is given with respect to $\hat{x}$ direction. Blue and orange curves stand for the $\hat{x}$ and $\hat{y}$ components of $\mathbf{B_s}$, and yellow is the projection of the demagnetization field in the applied field direction. The MFC is relaxed from -50 to 5 mT with $\beta = 0$ prior to compute the effect of angle variation.*

This effect is shown in Fig. 3.9(c), where the same 4-petal device is first placed in a -50 mT external field in the $\hat{x}$ direction to induce a uniform magnetization and then the field is increased to 5 mT, forming a Landau pattern as shown in the sketch. From this configuration, the device is rotated around its center while B_s is recorded as well as its $\hat{x}$ and $\hat{y}$ components. As expected, B_x and B_y follow sinusoidal curves meaning that the direction of

the concentrated field follows the orientation of the external field. However, the gain increases from 1.85 to 2.05 when rotating the sample from $\pi/4$ to $5\pi/4$. This variation can be explained by the domains distribution which is determined by the direction of the field for the last saturation, i.e. single-domain with $\beta = \pi$ orientation. Indeed, changing the orientation of the field under 5 mT does not flip the Landau pattern but it slightly modifies the size of each domains. As a consequence, the magnetic domain orientation does not vary from the initial state ($B_a = 5$ mT, $\beta = 0$) shown by domain mapping in Fig. 3.9(c). The domains distribution presents a mirror symmetry around the axis defined by $\beta = \pi/4$. As the stray field is inversely proportional to the distance, the domains closer to the center will more strongly affect B_s. As a consequence, closer domains will approach a configuration parallel to B_a for $\beta = 5\pi/4$ and anti-parallel for $\pi/4$, giving a better efficiency in the former case. In other words, the device efficiency is slightly dependent on its magnetization cycle history.

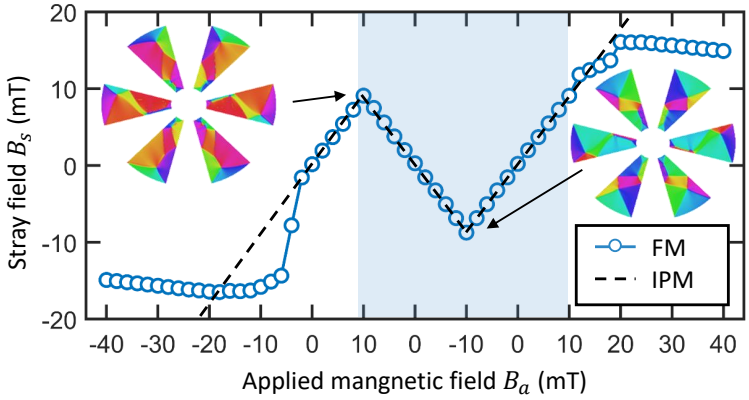

Figure 3.10: *Unfold hysteresis loop showing that the linear regime is maintained when sweeping applied field from -10 to 10 mT, as long as the Landau pattern is preserved in every petal. The highlighted region shows where the sweep is descending and the dashed black line is the result assuming an IPM behaviour.*

Fig. 3.7 shows that the ascending and descending branches of the hysteresis loop merge when approaching zero field. If within the linear regime a minor loop is made, the system remains in the linear regime. This effect is shown in Fig. 3.10 where B_s is plotted as a function of the magnetic history. Starting from a fully saturated configuration (large negative magnetic field), the magnetic field is swept from -40 mT up to 10 mT and then reduced down to -10 mT and increased again to +40 mT. The blue-shaded region

corresponds to the minor loop which exhibits a linear response, i.e. the device can sustain a variable magnetic field between -10 and 10 mT without loosing its linear behaviour.

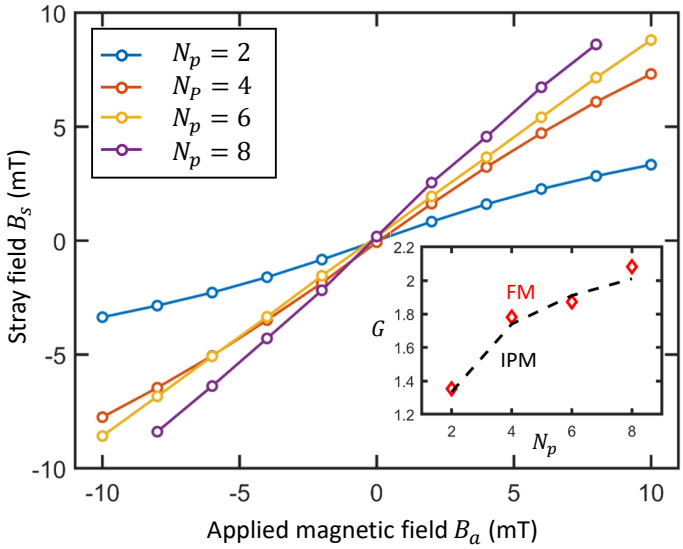

Figure 3.11: *Variation of B_s with applied field for devices with 2 to 8 petals. Inset: gain G as a function of the number of petals, compared to the IPM approximation in an identical structure.*

Fig. 3.11 shows the intensity of stray field generated at the center of the MFC with different number of petals for the linear magnetic field range. The gain $G = B_s/B_a + 1$ increases with N_p with an asymptotic saturation as displayed in the inset. Several relevant conclusions can be extracted from this figure. Firstly, the gain in the linear regime calculated using micromagnetic simulations are well approximated by the IPM hypothesis. Secondly, while it remains without hysteresis, the response in the linear regime presents an incipient saturation for high magnetic field, leading to a sigmoid shape. Thirdly, the magnetic field range for which linearity is preserved is reduced when the number of petals increases. This latter observation is related to the size (and therefore the opening angle) of the petal. Indeed, the narrower the petal, the higher the shape anisotropy and so the more favorable a single-domain configuration becomes.

Box 3.1: **Fabrication and characterization**

Multiple 60-nm-thick Py flower-shaped MFCs with various design have been fabricated on silicon substrate using RF-sputtering deposition and e-beam lithography techniques. Every concentrator has a radius ratio $R_o/R_i = 5$, with an outer radius R_o of 80 or 40 µm, and a number of petals between 2 and 8. A SEM image of a 4-petal structure is shown in Fig. 3.12. The exact thickness of the structure $t = 61 \pm 1$ nm was obtained by AFM (panel (b)). Magnetic properties of the deposited material was obtained from magnetization hysteresis loops measurement of an unpatterned Py thin film using a Quantum Design SQUID magnetometer and presented in panel (a) of Fig. 3.13. A saturation magnetization of 712 kA/m and coercive field $B_c \simeq 0.1$ mT was measured. The magnetic domains were visualized using magneto-optical Kerr effect (MOKE) microscopy. Images presented in this work are obtained after background subtraction based on the average contrast image of several hysteresis cycle and performing differential image method (see sec. 2.6.2). In Fig. 3.13(b), the domains in the demagnetized state are shown for a 6-petal structure with an outer radius of 80 µm. Landau pattern and cross-tie domain walls are clearly visible. The domains orientation is indicated with red arrows.

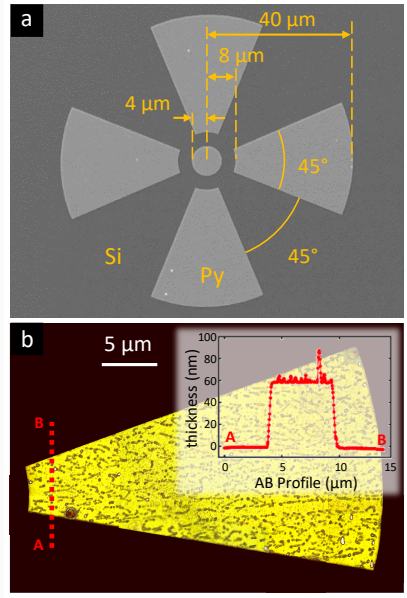

Figure 3.12: *(a) SEM image of a 4-petal flux concentrator with an outer radius $R_o = 5R_i = 40$ µm. (b) AFM image of a petal. The inset shows the sample profile along AB.*

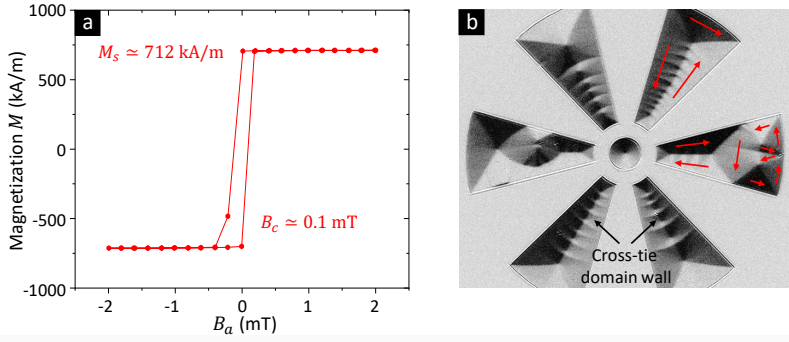

Figure 3.13: *(a) Magnetization loop of a 60-nm-thick Py thin unpatterned film. (b) MOKE image of Landau patterns with cross-tie domain walls in a 6-petal device in the demagnetized state. Red arrows show the local magnetization direction.*

3.5 Experimental quantification of MFC efficiency

In order to experimentally corroborate the tendencies revealed by the micromagnetic simulations, microscopic flower-like MFCs were fabricated (see Box 3.1 for details on the fabrication process and the device dimensions) and the domains distribution was imaged using MOKE microscopy. Experimentally, the intensity of the concentrated magnetic field is probed by adding a sensor to the device. Here, the sensor is a disk of Py with a thickness t and a radius R_d. The gain is estimated by optically tracking the position of the vortex formed in the sensor with respect to the applied magnetic field. A radius $R_d = R_i/2$ was chosen for the sensor based on simulations detailed in the last section of this chapter. The displacement of the vortex away from the disk center, δ, is supposed to evolve linearly with the magnetic field [91]:

$$\delta(B_a) = \chi_m(0)\frac{R_d B_a}{\mu_0 M_s}, \tag{3.2}$$

where $\chi_m(0)$ is the magnetic susceptibility at zero field. Therefore, the MFC's gain can be deduced from the ratio between the vortex motion of the sensor and that of an identical but isolated disk (i. e. without MFC surrounding it).

One must note that the susceptibility $\chi_m(0)$ in Eq. (3.2) can be approximated based on the dimension of the disk assuming $t \ll R_d$:

$$\chi_m^{-1}(0) \simeq \frac{t}{R_d}\left[\ln\left(\frac{8R_d}{t}\right) - \frac{1}{2}\right]. \tag{3.3}$$

However, the comparison with a reference sensor rather than using the approximation of Eq. (3.3) remains a necessity. Indeed, the equation is only valid for a perfect disk with smooth edges. In real device, the demagnetization field is partially relaxed because of the magnetic charges induced at the edge asperities, leading to a higher susceptibility. All the larger reference disks used in this work show a constant reproducible displacement rate of ~ 2.4 μm/mT while the theory suggests ~ 1.5 μm/mT, justifying the importance of a reference sensor.

In Fig. 3.14(a), the vortex displacement is plotted for a disk surrounded by a 4-petal MFC, showing clearly an increase of the slope, i.e. a higher gain G, when Landau patterns are formed in all petals (the linear regime represented by the blue region in panel (a) and (b) and MOKE images in panel(e-g)). Interestingly, the deviation from the constant gain approximation (dashed line) before entering the linear regime (precisely between -0.2 and 0 mT) was predicted by the micromagnetic simulations as depicted in Fig. 3.7(a) where

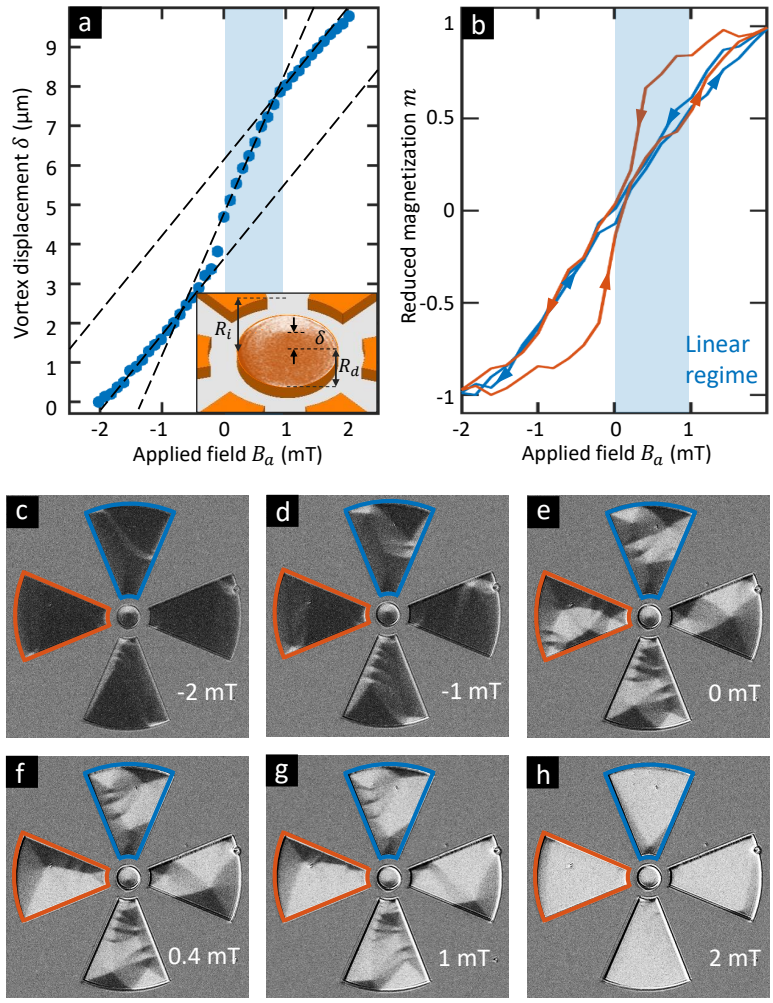

Figure 3.14: *(a) Variation of the vortex position in a disk with radius $R_d = R_i/2$ surrounded by a 4-petal MFC with radius $R_o = 5R_i = 16$ μm. The dashed lines are linear fits in and out of the linear region. (b) Hysteresis curves corresponding to a single petal obtained from contrast change in MOKE images partially presented in panels (c-h).*

an overshoot of gain is also observed. Moreover, experimental results shown in Fig. 3.14(b) corroborate the simulations showing that the linear regime is limited by the petal parallel to the applied field.

The magnetic field range for which the linear regime is observed is one order of magnitude lower in the experiments compared to the simulations. The substantial reduction of the linear region could be naturally attributed to the difference of scale and then a difference of demagnetization factor

(for practical reasons, experimental structures are one order of magnitude larger than simulated ones). Indeed, the higher the demagnetization field, the lower the inner field for a same applied field. Consequently, the annihilation field needed to erase the Landau pattern is expected to be larger for smaller devices. In our case, if we consider the petals as rectangular stripes the ratio of demagnetization factor between experimental ($L = 64$ µm and $t = 60$ nm) and simulated ($L = 4$ µm and $t = 80$ nm) structures gives approximately a factor $N_{\text{theo}} \approx 18 N_{\text{exp}}$, in agreement with our results considering the approximation of the petal shape. This suggests that the linear region could be extended by increasing the device aspect ratio t/L.

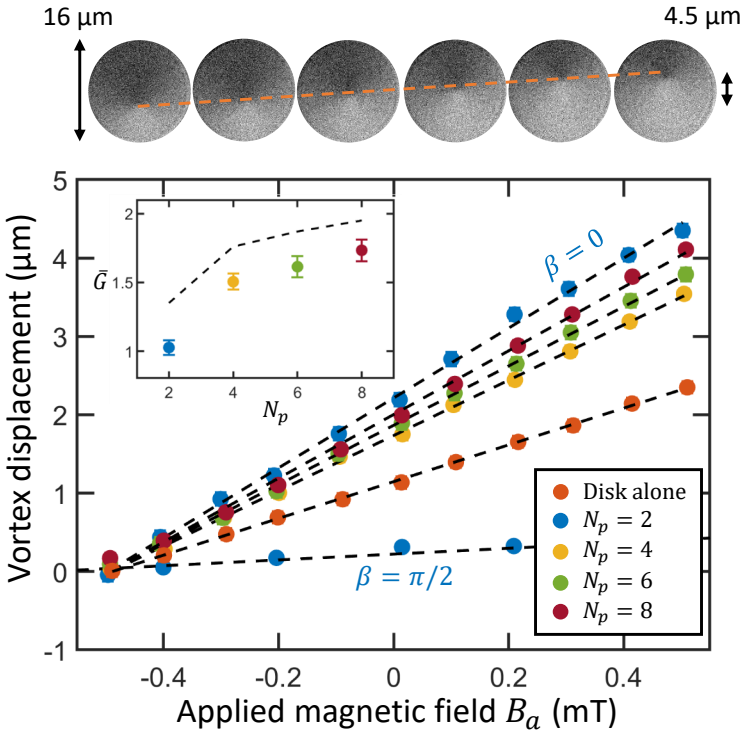

Figure 3.15: *Effect of the number of petals on the vortex displacement rate compared to a reference isolated disk (orange). The two sets of dots for the 2-petal MFC (blue) represent results obtained with the field parallel ($\beta = 0$) and perpendicular ($\beta = \pi/2$) to the petals, respectively. The inset shows the deduced mean gain $\bar{G}$ as a function of N_p, and the dashed line shows results for an IPM approximation. MOKE images at the top of the figure illustrate the vortex displacement for the case $N_p = 2$ and $\beta = 0$.*

By performing the same experiment on a disk surrounded by a MFC with a different number of petals, and limiting the analysis to the linear regime, the

tendency already predicted with simulations is nicely reproduced. Indeed, results presented in Fig. 3.15 show a clear increase of the displacement rate due to the presence of the MFC, with a mean gain $\bar{G}$ varying from 1 to 1.7 depending on N_p. As shown in the inset, the trend follows quite well the prediction based on an IPM material concerning the impact of the number of petals even if the measured gain is always inferior to the simulated one. However, such a quantitative comparison between simulation and experiment has to be treated cautiously. Firstly, the sensor probes the field on a large area while B_0 in the simulation is evaluated at the center. Secondly, despite the careful choice of the disk radius, the stray field distribution can be influenced by the presence of the sensor. Thirdly, defects inherent to the fabrication process, the Py grain structure or the formation of a magnetic deadlayer are suspected to spoil the efficiency. Especially, the presence of pinning sites could influence the domains distribution and perturb the stray field.

Finally, a particular attention is given to the 2-petal device for which the mean gain over a complete rotation of the device as calculated following the same method used for Fig. 3.4 and Fig. 3.11 leads to a negligible concentration power, i.e. $\bar{G} \simeq 1$. The detailed measurements at each angle are summarized in Fig. 3.16 where a cosinusoidal variation of the gain is obtained in a 2-petal MFC. In comparison and as predicted by simulations, a 4-petal MFC axhibits an isotropic behaviour.

3.6 Alternative methods for evaluation of the concentrator gain

In the previous section, we have demonstrated that the in-plane component of the magnetic field at the centre of the MFC can be indirectly measured by tracking the position of the magnetic vortex core in a cylindrical FM disk placed at center of the MFC. In this section, we theoretically investigate alternative techniques to evalute the gain of micrometer MFCs.

3.6.1 Magnetoresistive sensor

An elegant way to achieve this goal is to rely on the magnetoresistive response of the sensor placed at the core of the MFC. To this end, Py offers sufficient AMR response at microscales and can be electrically assessed with an additional overlay lithographic step, as schematically shown in the inset of Figure 3.17(a) (see Sec. 2.6.3 for more details on AMR).

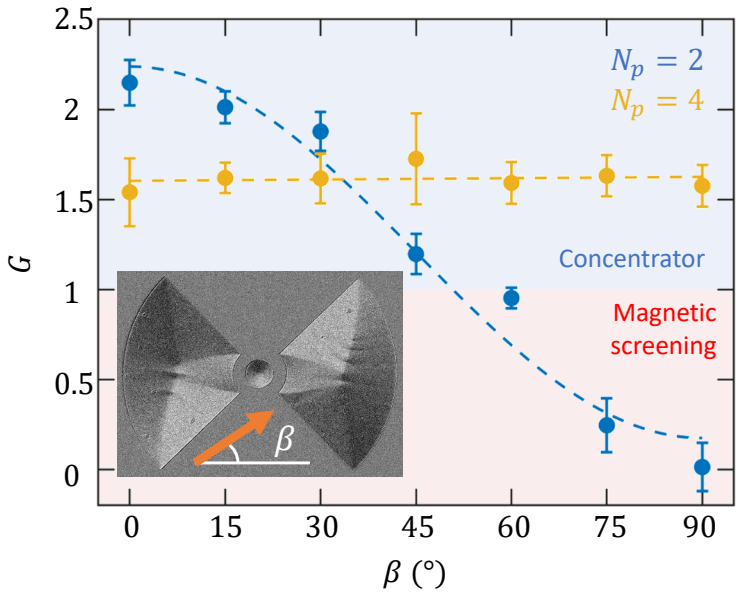

Figure 3.16: *Variation of the gain as a function of the field direction β as defined in the inset. For a 4-petal MFC (yellow dots), variations of gain are non-significant.*

The main panel of Figure 3.17(a) shows the calculated AMR response for three different devices: a disk (the AMR sensor) of radius R_d without MFC, the same sensor surrounded by a MFC ($N_p = 6$, $t = 60$ nm and $G_{max} = 4$) separated by a gap $d_{gap} = R_i - R_d = R_d$, and a sensor in direct contact with MFC. The simulations have been performed for an applied magnetic field for which the MFC exhibits a linear response and sweeping from high to low fields[2]. Due to shape anisotropy, domains in the disk-shaped sensor form a vortex which lies in the geometrical center when $B_a = 0$ and moves perpendicularly to $\mathbf{B_a}$ as the applied field changes and therefore giving a symmetric AMR signal. Comparing the isolated sensor to the concentrator with a finite gap, one can observe a clear increase of AMR response due to magnetic field concentration, as theoretically predicted in the previous sections. By taking the ratio of B_a for which equivalent AMR intensities are obtained with and without MFC, we obtain a gain $G \simeq 1.6$. A different situation emerges as soon as the sensor physically touches the MFC. Indeed, under this circumstance the AMR signal exhibits an unwanted sudden and irreversible change due to magnetization reversal process. This effect results

[2]The resistance change has been calculated in Comsol with a resistance map based on the magnetization distribution obtained by micromagnetic simulations. More information are presented in Box 4.2 in the next chapter.

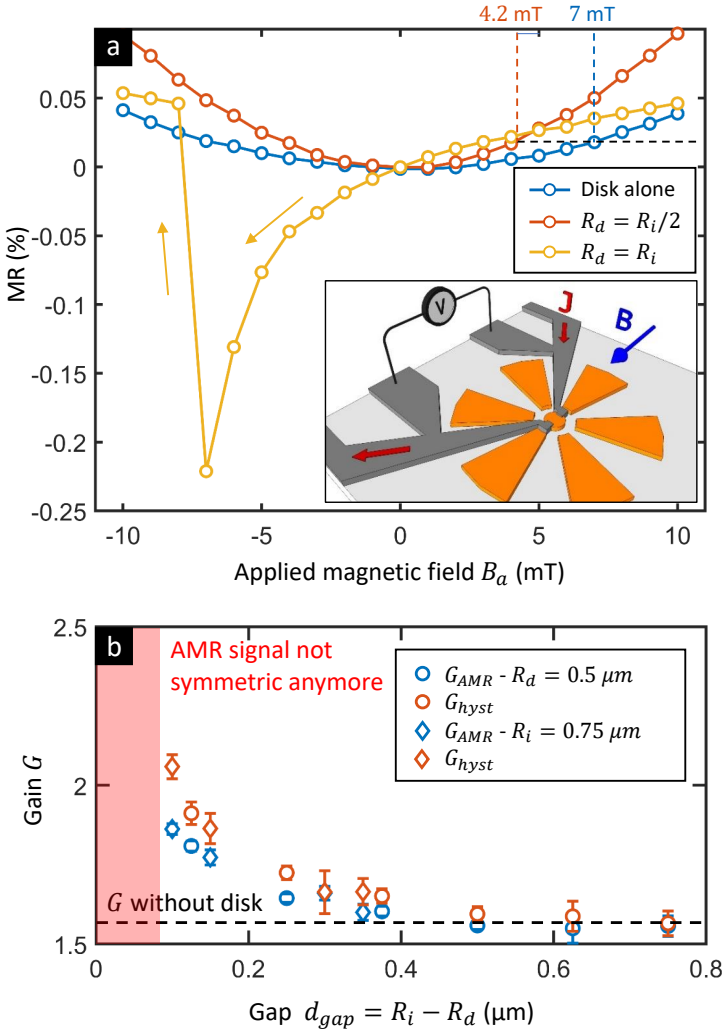

Figure 3.17: *Inset: modelled system consisting of a Py disk electrically contacted to measure the anisotropic magnetoresistance and used as a magnetic sensor. The sensor is sourrounded by a magnetic flux concentrator. In (a) the AMR response of the sensor for the case of an isolated sensor (blue points), a sensor sourrounded by a MFC but physically separated (red points), and a sensor touching the MFC (yellow points). (b) Gain calculated from both AMR signal and sensor's hysteresis loop as a function of the gap size. Micromagnetic simulations have been performed with* $R_o = 4R_i = 5$ μm *and* $t = 60$ nm.

from a complete change of domain distribution due to strong exchange interactions between sensor and MFC and as a consequence, the comparison with an isolated sensor is no longer meaningful. When a gap is allowed

between the sensor and the MFC, the remaining interaction is of dipolar origin and therefore weaker. However, d_{gap} has to be large enough in order to avoid that the sensor influences the flux concentrator and vice versa. Figure 3.17(b) shows the gain calculated from both AMR signal and disk's hysteresis loop as a function of the gap size. For gaps below 100 nm, the sensor response deviates strongly from its isolated behavior and is therefore not suited to evaluate the gain. As a rule of thumb, a good accuracy of the sensor is obtained for $d_{gap} \simeq R_{\mathrm{d}}$. For sake of completeness, calculations have been performed varying R_{i} with fixed R_{d} and the other way around, with both results confirming the same tendency. This finding suggests that our results could be valid for larger devices if the proportion between R_{o}, R_{i} and R_{d} is preserved.

3.6.2 Stray field measurement by Scanning Hall probe microscopy

An alternative method to calculate the gain of the magnetic field concentration consists in measuring the out-of-plane component of the stray-field around the disk by scanning Hall probe microscopy (SHPM) as illustrated in Figure 3.18(a). In the linear regime where the disk is in a vortex configuration, the OOP component of the stray field varies linearly with the external field. Figure 3.18(b) shows the comparison between the stray field calculated for a disk alone (dashed line) and for one surrounded by a MFC of $G_{\mathrm{max}} = 4$ (same geometry as for AMR measurements). The stray-field is calculated as the average value of the field in a circular area of diameter of 100 nm, at a distance z =100 nm above the disk (z =0 is inside the disk) and 50 nm from the disk edge. As shown in the top left inset, the gain evaluated by SHPM deviates from the theoretical gain $G \simeq 1.6$ as the probe is vertically distant from the central disk. This reduction is caused by the OOP component of the stray field emerging from the closest petal.

3.7 Conclusion

In summary, we have analyzed in detail the possibility to use FM-based metamaterials to concentrate magnetic flux at the micrometer scale. Firstly, we have demonstrated that the concentration gain of MFCs depends on the thickness of the device, with an optimal thickness proportional to the inner radius R_{i}. We have also shown that the main properties of macroscopic devices studied in [88] are reproduced in microscopic devices concerning the effect of petals number and dimension as well as the isotropic response of

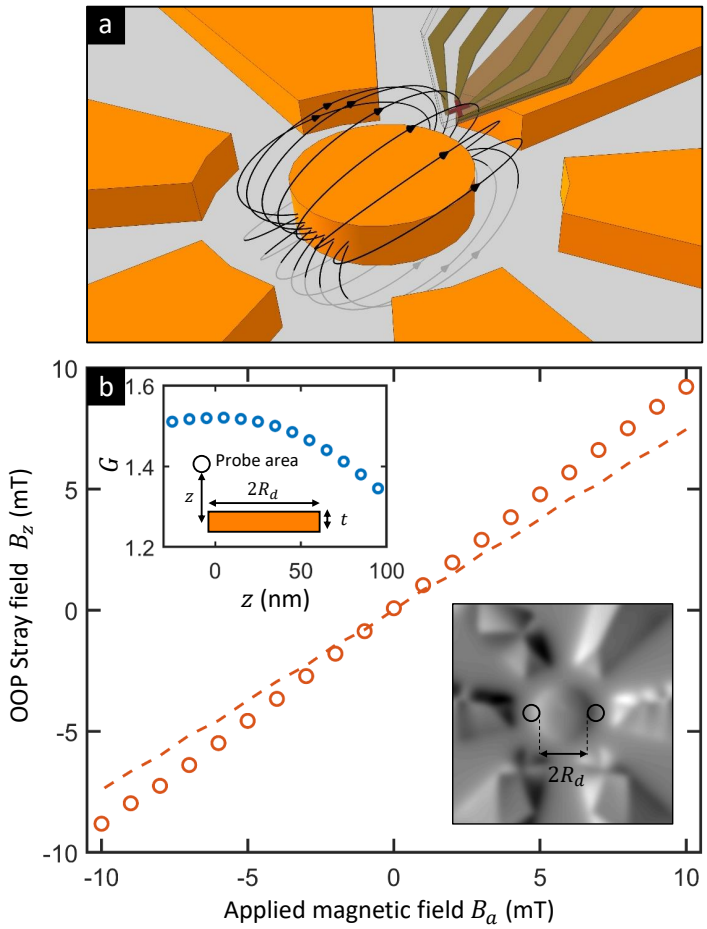

Figure 3.18: *(a) Illustration of the SHPM measurement of the stray-field produced by a central disk. (b) OOP component of the stray-field generated by a disk surrounded by a MFC (circle) and without MFC (dashed line), at a distance $z = 100$ nm up the disk center. Top left inset shows the variation of the gain as a function of the probe-disk distance. The bottom right inset shows a map of the stray-field 100 nm above the device for an applied field of -10 mT. Black circles point the areas where the field in calculated. Micromagnetic simulations have been performed with $R_o = 4R_i = 5$ µm and $t = 60$ nm.*

the concentrator.

Secondly, we have demonstated through micromagnetic simulations that the non-linear response of the ferromagnet limits the range of magnetic fields (labeled linear regime) for which the concentrator can operate efficiently, i.e. has a constant gain superior to 1. This range corresponds to the regime of stabilization of Landau pattern in each petal of the MFC. Interestingly, our

calculations show that, in the linear regime, the IPM approximation gives results in adequacy with micromagnetic simualtions.

Thridly, we experimentally confirm the theoretical predictions for devices with diameter around 100 µm. We demonstrate that the gain of on-chip MFCs can be obtained by imaging domains with MOKE microscopy and by tracking the displacement of a magnetic vortex formed in a FM disk placed at the center of the device. Our results prove that an isotropic response is obtained with a MFC composed of only 4 petals and the concentration gain measured experimentally follows the predicted trend regarding the number of petals. However, the extracted values of $\bar{G}$ are systematically inferior to the simulated one. While no clear reason has been identified, we attributed this reduced gain to the large capture surface of the sensor and the natural presence of defects in fabricated devices. In future works, a closer look should be taken concerning the sense of rotation of flux-closure pattern that could also be responsible for the discrepancy between simulations and experiments.

Comparing micromagnetic simulations with larger experimental devices, we have also observed that the extension of the linear regime is related to the demagnetization factor of the petals, suggesting that better results are expected for thicker and narrower designs.

Finally, we have suggested alternative methods for the measurement of the concentration gain. Particularly, the use of AMR measurement should offer the required accuracy for narrower MFCs.

4

Sharp in-plane magnetization reversal controlled by out-of-plane magnetic field through substrate-induced magnetic anisotropy

4.1 Introduction

Precise control of magnetic domains and magnetization reversal processes in ferromagnetic materials plays an essential role in emerging spintronic technologies. The possibility to induce sharp magnetic reversals at a given switching field has been the target of intense research, because of their considerable potential for use in sensing devices [31, 92, 93]. Among many different approaches, the anisotropic magnetoresistance (AMR) effect has been widely used to detect the variation of micromagnetic configurations and reversal processes in a large variety of magnetic structures [94–97]. In particular, magnetic sensing devices based on magnetoresistive effects have attracted large attention in the field of biosensing owing to its design simplicity, easy integration, and relatively large sensitivity as compared with other approaches [98].

Magnetoresistive sensors have generally been manufactured on structures with in-plane magnetic anisotropy. Sensing devices are usually patterned into stripes with high aspect ratio (nanorods or nanowires) to acquire tunable magnetic properties due to their shape anisotropy [92, 99, 100]. However, the sensitivity of such devices is limited by their reduced effective sensing area, and complex structures involving multi-contact stripe arrays, have to be used in order to enhance the sensor surface [93]. The development of perpendicular magnetic field sensors, based on magnetoresistance devices, is much more challenging. Materials with perpendicular magnetic anisotropy

may enable an effective solution. However, they usually require complicated multilayered stacks [101] or complex nanowire structures [92] to be able to detect magnetoresistive responses measured with the field applied perpendicular to the substrate.

In this chapter we report on anisotropic magnetoresistance effects on a series of permalloy (Py) strips of different widths and thicknesses for applied magnetic fields perpendicular to the strip plane. Sharp anomalous peaks in the magnetoresistance curves are observed, symptom of an abrupt in-plane (IP) magnetization reversal mechanism. We show that the switching field where the abrupt magnetization reversal occurs depends on the strip's width/thickness ratio. The comparison of our experimental results with micromagnetic simulations shows that a possible field misalignement can not be responsible for the IP magnetic reversal of the Py stripes whereas we demonstrate that similar sharp magnetization jumps can be obtained in presence of an uniaxial anisotropy that deviates of a few degrees from the out-of-plane (OOP) direction. We investigate the possibility that the uniaxial anisotropy is substrate-induced.

4.2 Results and discussion

Permalloy thin films of different thicknesses $t = 10 - 300$ nm were grown by sputtering on $LaAlO_3$ (LAO) single crystal substrates. Strips of different widths $w = 1 - 100$ μm and lengths $L = 100 - 200$ μm were fabricated by photolithography and lift-off techniques. Processing details can be found in Box 4.1. Figure 4.1(a) shows a schematic representation of the 4-probe transport measurement configuration along with (b) a scanning electron microscopy (SEM) image of a Py strip of $t = 30$ nm and $w = 50$ μm. Figure 4.1(c) shows a schematic representation of Py strip arrays patterned for magnetic measurements and the panels (d) and (e) are optical microscopy images of two arrays with strips of $t = 25$ nm $w = 10$ μm and 100 μm.

4.2.1 Magnetic Properties of permalloy thin films

Figure 4.3(a) shows the magnetization hysteresis loops for two Py plane films of thickness t = 10 nm and 300 nm with IP and OOP applied magnetic field. For both films, the saturation occurs at much higher magnetic field for the OOP configuration ($\mu_0 H_s \sim 1000$ mT) than for the IP configuration, a clear sign of the dominant in-plane anisotropy imposed by the sample's geometry. Insets show magnetic force microscopy (MFM) images obtained

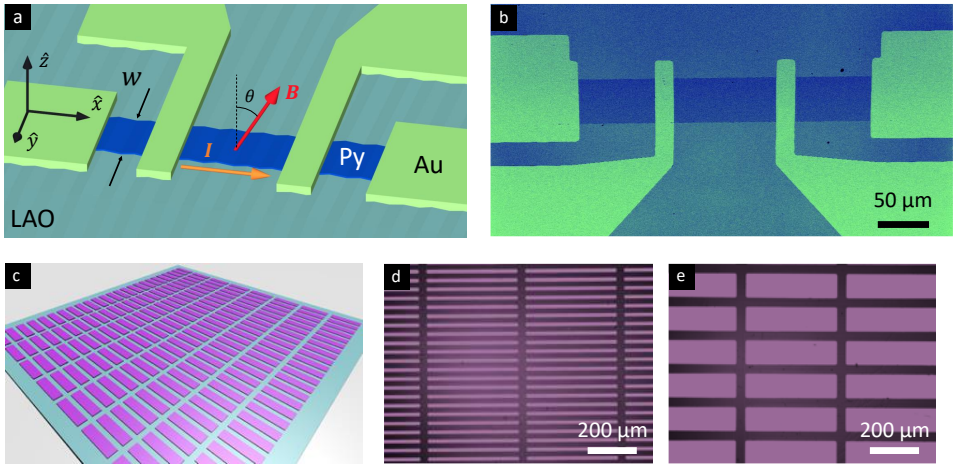

Figure 4.1: *(a) Schematic of the transport measurement configuration with the main axis, current and magnetic field direction indicated and (b) SEM false-coloured images of a Py strip (blue) with four Au contacts (green) for transport measurements. (c) Schematic representation of patterned Py strip arrays (pink) for magnetization measurements and (d-e) optical images of two arrays with strips of widths $w = 10$ µm and 100 µm.*

for Py films of t = 30 nm and 300 nm. In the thinner film large in-plane magnetic domains are separated by Néel walls. Increasing the film thickness leads to an out-of-plane component of the mainly in-plane magnetization thus forming stripe domains separated by a Bloch-type domain wall.[102]

Figures 4.3(b) and (c) show a close look of IP and OOP hysteresis loops at low fields. The IP magnetization of the 10 nm film exhibits a very sharp square loop with a saturation field of $\mu_0 H_s \sim 1$ mT and a coercive field of $\mu_0 H_c \sim 0.5$ mT. The 300 nm film shows a nearly reversible linear decrease of the magnetization from its saturated value at $\mu_0 H_s \sim 25$ mT and a square loop at low fields with $\mu_0 H_c \sim 2.5$ mT. This magnetic response, typically observed in Py films above a critical thickness, has been ascribed to the presence of a perpendicular anisotropy favoring the formation of a stripe domain structure as revealed by magnetic-force microscopy images (see right bottom panel of Fig. 4.3(a) inset). For the OOP configuration (panel (c)), coercive fields of $\mu_0 H_c \sim 10$ mT and 1.5 mT are obtained for the 300 and 10 nm films, respectively. It is interesting to note the existence of an unexpected small hysteresis loop for the 10 nm-thick sample which suggests the presence of an OOP uniaxial anisotropy. This point will be discussed more deeply in the next section in regard of the magnetoresistance measurements. The influence of the sample's width on the OOP hysteresis loop is analyzed in

Box 4.1: **Fabrication and methodology**

Permalloy, $Fe_{20}Ni_{80}$, thin films of different thicknesses were deposited at room temperature by dc magnetron sputtering at a base pressure of 10^{-6} mbar and processing Ar pressure of 3.6×10^{-3} mbar on 5 mm $\times$ 5 mm $LaAlO_3$ Lanthanum aluminate (LAO) and silicon (Si) substrates. A 2-nm capping protective layer of TiO_2 was deposited on the top of the thinner films to avoid oxidation. Atomic force microscopy images shown in Fig. 4.2 reveal that Py thin films reproduce the twinned structure of the LAO substrate with an out-of-plane tilting angle inferior to $\sim$ 0.5°. These images show large modulations of thickness ($\sim$ 20 nm) over scales of about 5 µm coexisting with a smaller scale periodic roughness ($\sim$ 1 nm) caused by the terraces in the LAO substrate. These features are absent in Si substrates. Strips of different widths were defined by photolithography and lift-off processes. Au contacts for 4-point transport measurements were deposited on top of the strips by sputtering. Magnetoresistance measurements were performed using a Quantum Design physical property measurement system (PPMS) with the sample mounted on a goniometer permitting to change the relative orientation with respect to the applied magnetic field. Magnetization hysteresis loops of permalloy films and strip arrays were measured with a Quantum Design SQUID magnetometer with IP and OOP applied magnetic fields.

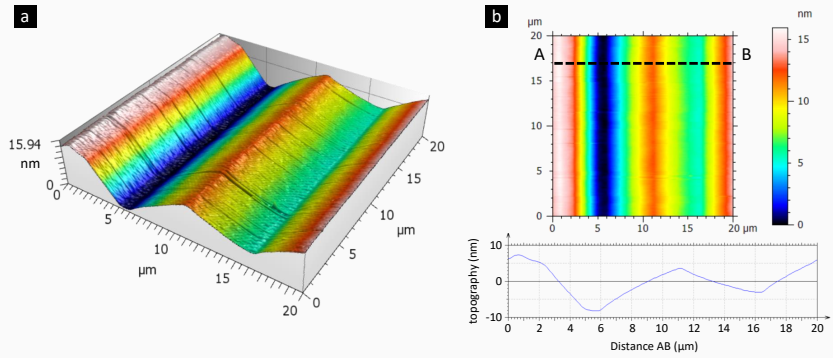

Figure 4.2: *(a) A 20 µm $\times$ 20 µm topographic AFM where one can see that the twining structure of substrate is nicely reproduced in the thin film. Considering the twinning width (4 - 10 µm) and the height ($\sim$ 20 nm) one obtains an out-of-plain tilting twin angle of $\sim$ 0.25°.*

Fig. 4.3(d) where we compare the low field hysteresis obtained for arrays of strips with $w = 10$ µm, $w = 100$ µm and an un-patterned film of the same thickness. We find that the coercive field of the strips is higher than that of the un-patterned film and increases as w decreases. This trend, also observed through magnetoresistance (MR) measurements, can be ascribed to the in-plane demagnetization factor which modifies the coercive field as $H_c \propto t/w$.

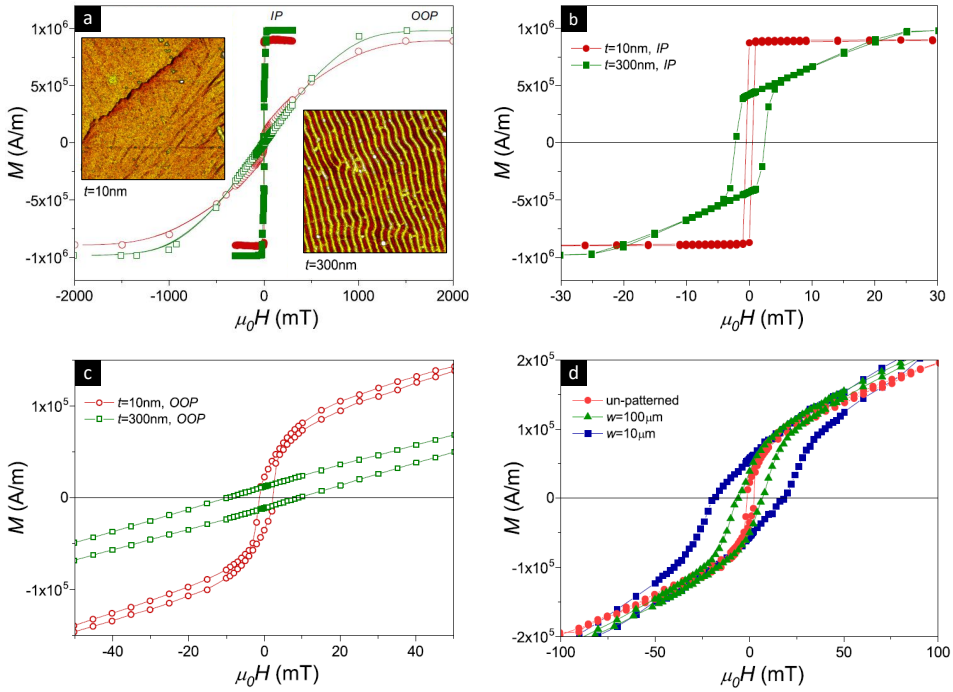

Figure 4.3: *(a) Magnetization hysteresis loops measured at 100 K with IP (closed symbols) and OOP (open symbols) applied field for unpatterned Py films of $t = 10$ nm (red circles) and $t = 300$ nm (green squares). (b) and (c) Close looks of the IP and OOP loops at low fields, respectively. (d) OOP magnetization hysteresis loops for a 25 nm-thick un-patterned film (red circles), patterned array of strips with $w = 100$ μm (green triangles) and $w = 10$ μm (blue squares). Insets in (a) show MFM images obtained at room temperature for a 30 nm film (left top panel) and a 300 nm film (right bottom panel). Black arrows indicate the direction of magnetization.*

4.2.2 Magnetoresistance measurements

Magnetoresistance measurements are used to characterize the magnetic behaviour of patterned Py strips. In this work, we define φ as the deviation from the OOP direciton such that $90^\circ - \varphi$ represents the angle between the magnetization and the current. As described in section 2.6.3, the change of resistance is given by

$$R(\varphi) = R_\perp + (R_\parallel - R_\perp)\sin^2\varphi, \tag{4.1}$$

where $R_\perp$ and $R_\parallel$ are the resistances when the magnetization is perpendicular ($\varphi = 0^o$) and parallel ($\varphi = 90^o$) to the current, respectively.

Figure 4.4(a) shows the variation of the magnetoresistance as a function of the angle θ, between the $\hat{z}$ direction and a 100 mT applied magnetic field as indicated in the sketches, obtained for a strip of thickness t =10 nm and width w = 5 μm. Results for rotation parallel and perpendicular to the applied current direction are plotted. Nearly invariant resistance values are obtained for a wide range of angles, associated to a saturated IP magnetization which is either parallel ($R_{\parallel}^{ip}$ = 543 Ω) or perpendicular ($R_{\perp}^{ip}$= 531 Ω) to the current. Sharp magnetoresistance peaks/dips appear at θ= 0° and 180°, i.e. OOP, as a consequence of rapid magnetization rotation inside the sample plane resulting from the shape anisotropy.

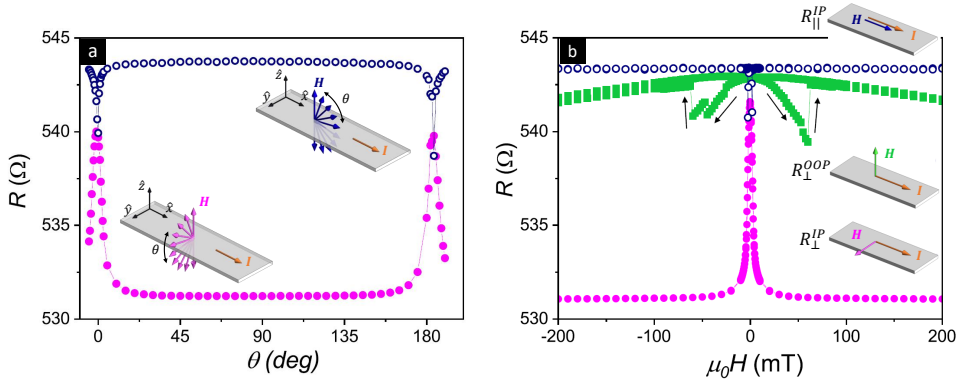

Figure 4.4: *Anisotropic magnetoresistance of a Py strip of t = 10 nm and w = 5 μm measured at 100 K (a) by rotating an applied magnetic field of 100 mT in a plane parallel (blue open symbols) and perpendicular (pink closed symbols) to the current, as schematically shown on the sketches. (b) Magnetoresistance obtained for magnetic field sweeps along the three principal axes defined by the sample geometry: IP perpendicular to the current (closed pink circles), IP parallel to the current (open blue circles) and OOP (green squares), as indicated on the sketches. Arrows show the sweeping direction of the field for the OOP curve in the irreversible region.*

Figure 4.4(b) shows the magnetoresistance curves obtained for the same strip by sweeping the applied magnetic field along the three principal directions defined by the sample geometry. i.e. magnetic field OOP, IP perpendicular to the current and IP parallel to the current (see insets and Fig. 4.1(a)). The variation of the resistance for the different configurations of applied field can be associated to the AMR effect with a coherent rotation of the magnetization, considering that the mean angle between the current and the magnetization can be determined from the hysteresis loops according to Eq. (2.58).

According to the hysteresis loops shown in Fig. 4.3(a), the IP magnetoresis-

tance (closed symbols) changes abruptly at the coercive field and corresponds to a maximum disorder of the magnetic domain distribution [103]. For the OOP configuration, a much smoother magnetoresistance variation is observed which can be associated to the wide hysteresis loop obtained for this configuration (open symbols in Fig. 4.3(a)). Strikingly, for this particular configuration, in addition to the main magnetoresistance effect associated to a coherent magnetization rotation, two symmetrical abrupt magnetoresistance jumps appear at the switching field $\mu_0 H_{sw} \sim \pm$ 60 mT. This result is surprising as, for the best of our knowledge, similar jumps in the magnetoresistance have only been reported in elongated ferromagnetic nanowires for IP magnetic field applied along its easy axis [99, 104], and attributed to a sharp switching of the magnetic moment due to a curling rotation [105–109].

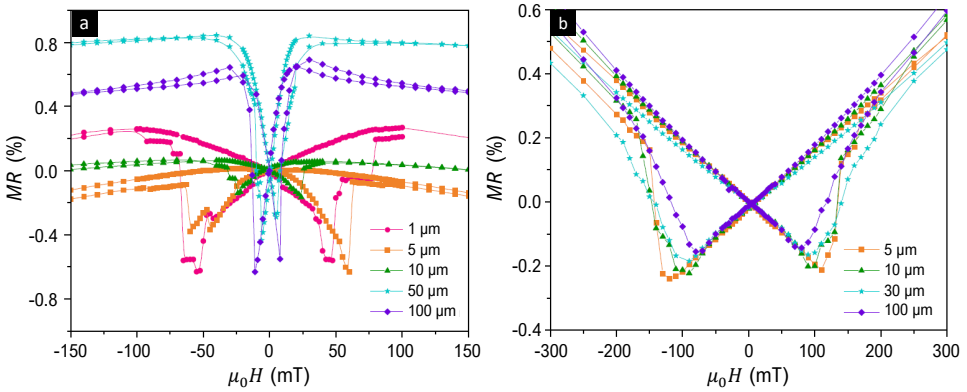

Figure 4.5: *Magnetoresistance ratio as a function of the magnetic field applied OOP at 100 K for Py strips of different widths (indicated in the legend) and thicknesses (a) $t = 10$ nm and (b) $t = 300$ nm.*

In order to elucidate the nature of the MR jumps appearing in the Py strips we have systematically investigated the OOP magnetoresistance curves obtained for strips of different geometries. Figure 4.5 shows the magnetic field dependence of the OOP magnetoresistance ratio $MR(\%) = (R(H)\text{-}R(0))\times 100/R(0)$, where $R(0)$ is the resistance at zero field and $R(H)$ the resistance in an external field H, obtained for a series of strips of different widths, w, with thicknesses $t = 10$ nm and 300 nm at 100 K. Abrupt MR changes of $\sim 0.2 - 1.6$ % are identified for all the strips. It is worth pointing out that the switching field where the magnetoresistance jumps occur lies in the range $\mu_0 H_{sw} \sim \pm$ 5 - 200 mT and strongly depends on the strip shape anisotropy.

Figure 4.6(a) shows the evolution of H_{sw}, with the strip width for samples

of different thicknesses. H_{sw} is almost independent of the width for the strips with $t = 300$ nm whereas changes about one order of magnitude with increasing the strip's width from 1 to 100 μm in the case of thinner strips with $t = 10 - 30$ nm. We have included in the figure the coercive fields obtained from the hysteresis loops shown in Fig. 4.3(d) for strips of $w = 10$ and 100 μm (star symbols) which are in good agreement with the $H_{sw}(w)$ dependence obtained from MR measurements. In Fig. 4.6(b) the switching field H_{sw} is plotted as a function of w/t and shows a collapse of the datapoints onto a single trend suggesting that demagnetization effects play an important role in determining the switching field.

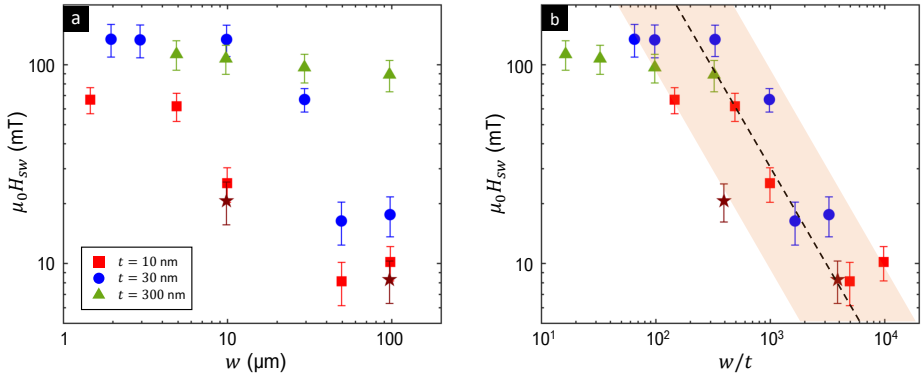

Figure 4.6: *Switching field obtained for strips of different thicknesses as a function of the strip (a) width and (b) width/thickness ratio, in a log-log representation. The black dashed line in (b) shows a t/w dependence. Star-shaped symbols represent the coercive fields of two arrays of strips obtained through magnetization hysteresis loops.*

4.2.3 Modelling of the anisotropic magnetoresistance

To gain a deeper understanding of the experimental results, we performed complementary micromagnetic and electrical transport simulations to evaluate the resistance change of the Py strips at different applied magnetic field values and directions. The modelled system consists of a ferromagnetic strip with saturation magnetization and exchange constant corresponding to conventional $Ni_{80}Fe_{20}$ alloy, absent of crystalline anisotropy and without any inhomogeneity or defect. The technical details concerning the micromagnetic simulation can be found in Box 4.2 section. Figure 4.9(a) shows the magnetization hysteresis loops along the principal axis defined by the sample geometry (see inset of Fig. 4.1(a)). Figure 4.9(b) shows the resulting

Box 4.2: **Micromagnetic and AMR simulations**

Micromagnetic simulations were performed using the open-source MuMax3 software for domain distribution calculations [10]. Due to computational limitations, simulations have been performed in structures with reduced dimensions compared to experimental devices. The length L was fixed to 10 µm while the width was optimized (w = 1-4 µm) in order to have the best compromise between maintaining the aspect ratio and avoiding large shape anisotropy for small w values.

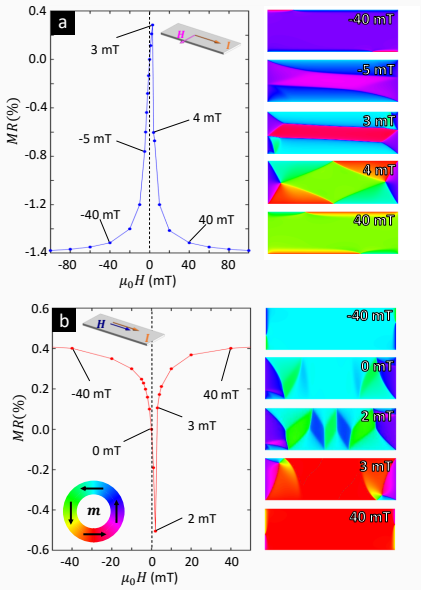

Figure 4.7: *AMR response as a function of the magnetic field applied in-plane (a) perpendicular and (b) parallel to the applied current, along with the corresponding mapping of the magnetic domains distribution for a selected set of magnetic fields.*

The IP micromagnetic cell dimensions were fixed to 10×10 nm^2 and the OOP size was set to 2.5, 5 and 10 nm for thickness of 10, 30 nm and thicker respectively. Calculations have been done using standard parameters for Py thin film M_s= 8.6 × 10^5 A/m and A_{ex}=13 pJ/m. The film is assumed to be free of magnetocrystalline anisotropy and thermal fluctuations are neglected. Examples of results obtained by micromagnetic simulation are shown in Fig. 4.7(a-b) where the change of domains distribution is shown for a variable external field applied in-plane and (a) parallel or (b) perpendicular to the main current direction. It can be observed that the switching mechanism consists of a buckling mode where the domains twist before flipping. The associated resistance change of the Py bars at different magnetic field intensities and directions is computed using the electric current module of the finite-element software COMSOL. The bulk resistivity is given by

$$\rho = \rho_\perp + \left(\rho_{||} - \rho_\perp\right) m_I^2, \qquad (4.2)$$

where m_I is the reduced magnetization in the direction parallel to the current density direction obtained from micromagnetic simulations. $\rho_\perp$ and $\rho_{||}$ are determined in order to match the total resistance obtained experimentally in our AMR measurements.

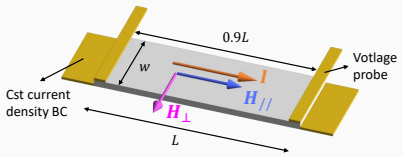

Figure 4.8: *Illustration of the AMR configuration as simulated in Comsol.*

The four-point setup is simulated with voltage pads placed at a distance of 5% of the total length from the device edges as shown in Fig. 4.8.

AMR response and Fig. 4.9(c) the sample's resistance as a function of angle

for $\mu_0 H = 100$ mT.

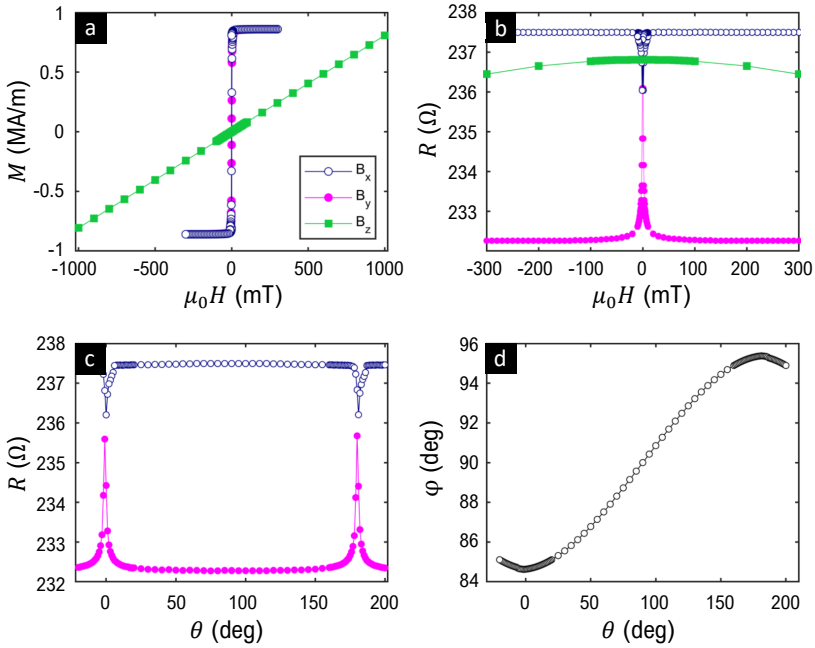

Figure 4.9: *Micromagnetic simulations of (a) magnetization hysteresis loops and (b) associated magnetoresistance, calculated considering different applied magnetic field orientations (B_x (open blue circles), B_y (closed pink circles), B_z (green squares)). (c) Angular dependence of the magnetoresistance at fixed magnetic field of 100 mT tilted along the yz plane (closed symbols) and zx (open symbols). Panel (d) shows the magnetization angle φ as a function of the magnetic field angle θ for a magnetic field of 100 mT.*

The results of the simulations are in qualitative agreement with the experimental curves shown in Fig. 4.3 and 4.4. However, for the OOP configuration (see green curves in Fig. 4.4(b) and Fig. 4.9(b)), the numerical findings fail to reproduce the abrupt magnetoresistance jumps observed experimentally. Such sharp resistance changes could be naturally accounted for by a sudden rearrangement of in-plane domains, with a disordered domain distribution at low fields switching to a x-oriented domain distribution at high fields. Indeed, in thin films, the large demagnetization field in the $\hat{z}$ direction confines the magnetization to lie in the plane of the film. This is further confirmed in Fig. 4.9(d) where the magnetization angle φ is plotted as a function of the magnetic field angle θ for 100 mT. The OOP component of the magnetization remains small (<5°) irrespective of the value of θ, and is not correlated with the angular dependence of the sample's resistance. This reinforces the idea

that the resistance changes observed during the OOP applied field sweeps are likely associated to a change of the IP magnetic domains arrangement.

In the following, we discuss two possible mechanisms leading to a fast in-plane rotation of the magnetization triggered by sweeping the OOP applied field.

Firstly, the sharp resistance change observed in the OOP magnetoresistance curves may arise from the existence of a small misalignment of the applied field, i.e. $\theta \neq 0^\circ$ [110]. In this case, the magnetization reversal should occur for a magnetic field $H_{sw}^{OOP}(\theta) = H_{sw}^{IP} \sin^{-1}(\theta)$, where H_{sw}^{IP} is the in-plane coercive field. In order to explore this possibility, we simulated the MR response for different amplitudes of misalignment by tilting the applied field towards the direction of the current (Fig. 4.10(a)) and perpendicular to it (Figure 4.10(c)). Simulations performed with a small in-plane component of the magnetic field (Fig. 4.10(a)) show a clear jump of MR associated to a fast in-plane reversal of the magnetization, and for both configurations the calculated switching fields follow the expected angular dependence as displayed in the inset of panel (a). It is worth noting that the abrupt transition corresponds to an increase of resistance (domains align parallel to the current) in the case of a B_x component misalignment while the opposite is observed for a B_y component. This is consistent with the buckling mechanism as described for the IP magnetisation reversal in Fig. 4.7.

For the sake of comparison, Fig. 4.10(b) and (d) show the experimental MR curves measured under the same conditions. Results show two important differences. First, the predicted $\sin^{-1}(\theta)$ dependence is not observed in the experimental results (see inset of panel (b)). Secondly, in the case of a B_y component (Fig. 4.10(d)), switching peaks do not exhibit the behavior predicted by the numerical model in panel (c). This discrepancy between simulations and experiments suggests that an unwanted magnetic field misalignment does not provide a satisfactory explanation for the experimental results.

A possible alternative mechanism giving rise to an IP switching triggered by an OOP external magnetic field could be magnetic anisotropy, so far ignored in our model. While both *bcc* and *fcc* Py structures exhibit negligible magneto-crystalline anisotropy, Py thin films may exhibit an important perpendicular magnetic anisotropy (PMA). This induced magnetic anisotropy is attributed to the internal stress coupled with non-zero magnetostriction coefficient and/or from columnar grains separated by nonmagnetic intergrain boundaries [111]. For films thicker than a critical thickness (around 200 nm), the stress induced anisotropy is not negligible anymore compared to the shape anisotropy and the PMA becomes visible as Py domains arrange

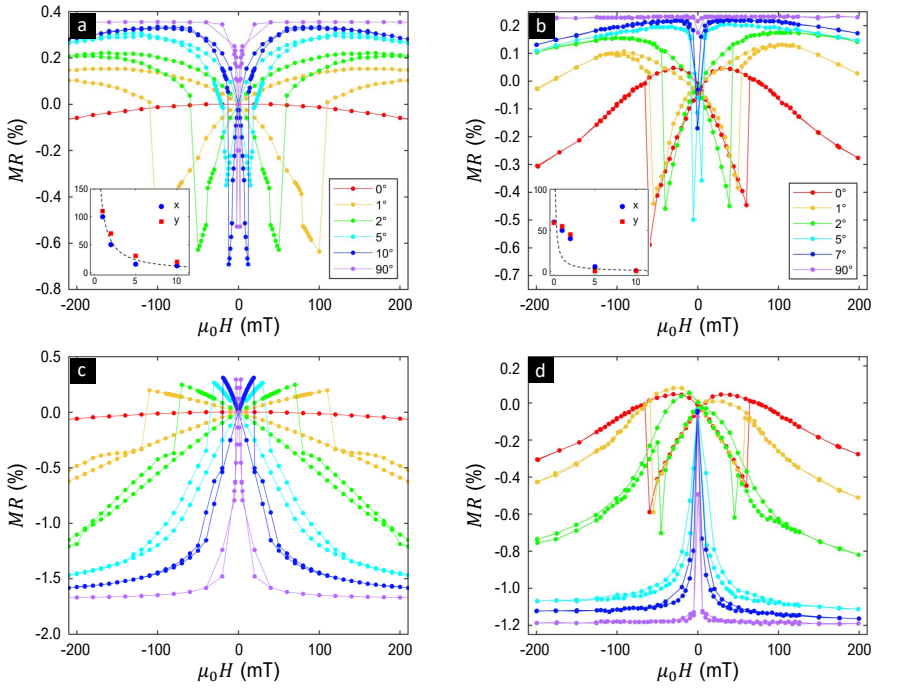

Figure 4.10: *(a) and (c) Numerical simulations of the magnetoresistance for a device with $t = 30$ nm and $w = 4$ µm for an OOP applied field with a small misalignment angle θ towards and perpendicular to the direction of the current, respectively. (b) and (d) Experimental magnetoresistance curves measured for a strip of $t = 30$ nm and $w = 30$ µm at the same applied field conditions as (a) and (c), respectively. The insets in panel (a) and (b) show the computed and experimental switching fields as a function of the misalignment angle for tilting towards the x and the y axes. The dashed black lines correspond to a $\sin^{-1}(\theta)$ variation.*

themselves in stripes (as indeed seen in the bottom inset of Fig. 4.3(a)). For films below the critical thickness, the shape anisotropy masks the effect of the induced uniaxial anisotropy but the latter is expected to be stronger as the stress induced by the substrate tends to relax in thicker films. Indeed, the PMA is expected to evolve as t^{-2} for thin films [112]. For 50 nm-thick films or thinner, the crystal anisotropy coefficient may be as high as K_{u1} =100 kJ/m^3 without leading to any nucleation of stripes domains because of the strong shape anisotropy. However, we postulate that an induced anisotropy can give rise to an IP magnetization reversal triggered by OOP magnetic field if the direction of the uniaxial anisotropic vector slightly deviates from the normal direction to the film. Such a deviation from the perfectly OOP case is

possible notably because of misalignment between the sputtering source and the sample [113–117] or due to the presence of stray field in the vicinity of the sputter head [118]. In addition, surface magnetic anisotropy and/or additional magnetostriction anisotropy may be induced at the interface between the Py film and substrate or a cap layer [119, 120].

To qualitatively illustrate how the magnetic anisotropy can account for the OOP AMR response observed experimentally, we will assume a uniaxial anisotropy with an easy-axis $\mathbf{u_k}$ in the x-z plane with an angle β from the OOP direction. The intensity of the associated anisotropy field H_k can be approximated by

$$\mathbf{H_k} \simeq \frac{2K_{u1}}{\mu_0 M_s} (\mathbf{m} \cdot \mathbf{u_k}) \mathbf{u_k} \tag{4.3}$$

with K_{u1} the anisotropy energy density. The IP component of the anisotropy field depends both on IP and OOP components of the magnetization,

$$H_{k,IP} = \frac{2K_{u1} \sin\beta}{\mu_0 M_s} [m_x \sin\beta + m_z \cos\beta]. \tag{4.4}$$

Therefore, for a positive applied field (and so $m_z > 0$), the IP effective field will favor domains aligned in the direction of $\mathbf{u_k}$ while the opposite is true for a negative OOP external field, leading to the possibility to induce a magnetization switch. In order to favour a magnetic reversal, the x-directed domains have to sustain an anisotropy field oriented in the opposite direction with a large enough intensity ($B \sim 1$ mT for the Py bars in this work). Based on Eq. (4.4) and assuming a zero in-plane coercive field, the anisotropy field is opposed to the IP magnetization if $m_z < 0$ and $|m_z|/m_x > \tan(\beta)$, which is approximated to $90^\circ - \varphi > \beta$ with φ the magnetization angle with respect to the OOP direction. An example is illustrated in Fig. 4.11(a) corresponding to the simulated AMR signal of a 10 μm × 1 μm strip with a thickness of 30 nm and uniaxial magnetic anisotropy $K_{u1} = 120$ kJ/m^3 with an easy-axis forming an angle $\beta = 5.7^\circ$ from the normal direction to the film. In this figure one can observe two sharp MR increases symmetrically distributed around zero field, which are triggered by a perfectly aligned OOP magnetic field. The switching field can be tuned through different properties of the device. In addition to the width of the stripe, the switching field can be controlled through the intensity and inclination of the induced uniaxial anisotropy. The panel (b) of Fig. 4.11 shows the variation of the switching field for the same device as panel (a) but with different intensities of induced anisotropy. As expected from Eq. (4.4), H_{sw} decreases linearly with the anisotropy energy constant. Using $K_{u1} \simeq 125$ kJ/m^3, the computed switching field is close to the

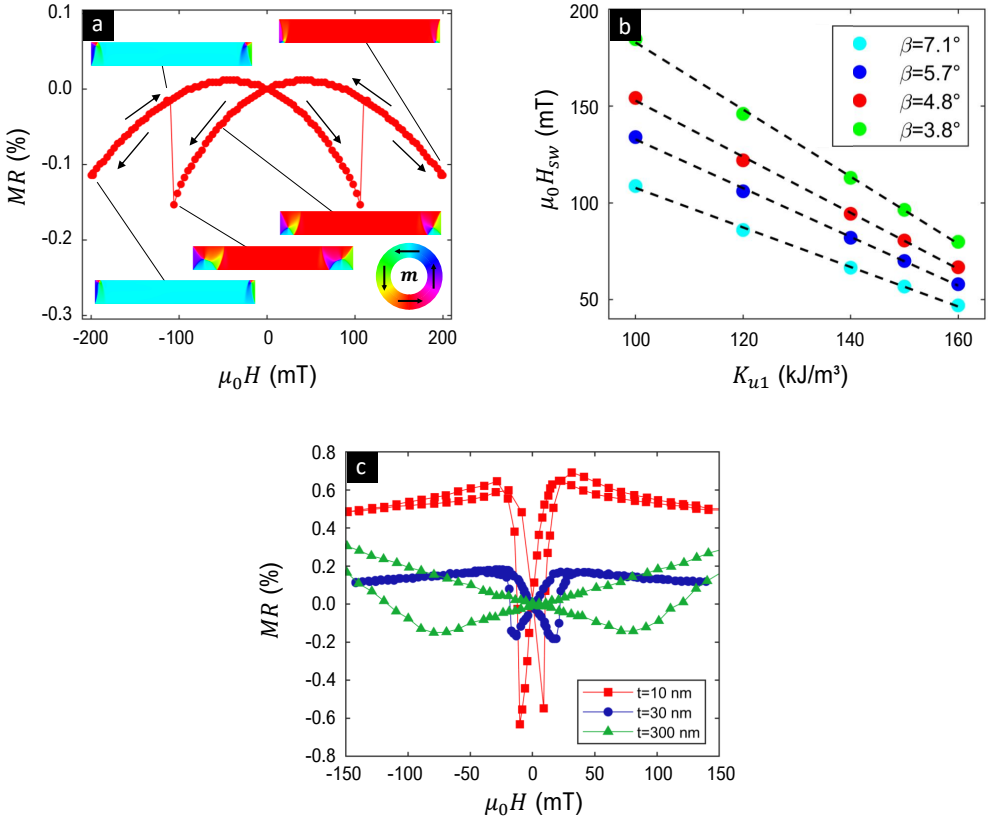

Figure 4.11: *(a) Simulation of the magnetoresistance response of a 1-µm-wide and 30-nm-thick Py bars with tilted uniaxial anisotropy under perfectly OOP magnetic field. The arrows show the magnetic field sweep direction. The color maps represent the in-plane component of domains for a selection of magnetic field during the descending sweep. (b) Variation of the switching field with the anisotropy vector direction and intensity. (c) Magnetoresistance curves measured for Py strips of $w = 100$ µm and different thicknesses.*

experimental value of 100 mT shown in Fig. 4.6 for a magnetic bar of 1 µm wide. It is worth noting that this K_{u1} remains far from the maximal induced uniaxial anisotropy for a 30-nm-thick sample without stripes domain which is given by $K_{int} = 4\pi^2 A/t_{fm}^2 \simeq 500$ kJ/m^3 [112]. Interestingly, a reduction of the switching field and an increase of the MR are experimentally observed for thinner samples as shown in panel (c). This supports the hypothesis that the OOP anisotropy is related to the stress induced by the LAO substrate, which is more relaxed in thicker sample.

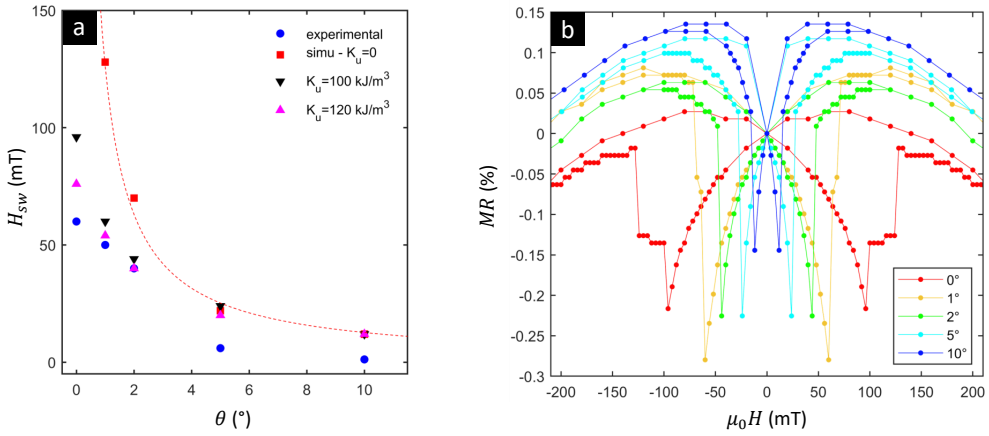

Figure 4.12: *(a) Comparison of the switching field intensity H_{sw} as a function of the external field direction between experimental results (blue dots) and simulations with different intensity of anisotropy. The presence of a nearly perpendicular uniaxial anisotropy ($K_{u1} > 0$) leads to switching fields with a tendency in agreement with experimental observations. (b) AMR responses for different tilted external field, corresponding to the black triangles of panel (a). The simulation is done for a 3-µm-wide and 30-nm-thick stripe with slightly inclined PMA ($\beta = 5.7°$ and $K_{u1} = 100$ kJ/m^3).*

As demonstrated through micromagnetic simulations, the existence of a uniaxial anisotropy with a direction tilted of few degrees from the OOP direction explains the rotation in-plane of magnetic domains without applying any IP external field. Moreover, by comparing the switching fields predicted by micromagnetic simulations with the experimental results, it is observed that the deviation from the $1/\sin\theta$ can be reproduced as presented in Fig. 4.12(a) where blue dots correspond to the switching field measured by magnetoresistance and reported in Fig. 4.10. In the absence of induced anisotropy (red squares), the switching field increases as $1/\theta$ for the smallest angles. When $K_{u1} > 0$ are considered (pink and black triangles), the predicted switching field increases more smoothly (depending on the intensity of K_{u1}) as the applied field aligns with the OOP direction. For stronger misalignment of the external field, the switching field becomes nearly independent of K_{u1} since the IP component of the applied magnetic field due to the misalignment dominates the reversal mechanism[1]. Finally, it is important to note that

[1]It must be noted that a difference of switching field is expected between the simulations with $K_{u1} = 0$ and $K_{u1} = 100 - 120$ because of the IP component of the uniaxial anisotropy varies from 0 to $K_{u1}\sin(5.7°) \simeq K_{u1}/10$. However, it remains negligible compared to the shape anisotropy.

the discrepancy between simulated and measured switching field for large inclination angles is expected and can be explained by both the device size difference and/or the Brown's paradox (see Sec. 2.5). The panel (b) of Fig. 4.12 shows details of the AMR curves for $K_{u1} = 100$ kJ/m^3 for which sharp resistance change are observed, reproducing our experimental observations.

4.3 Conclusions

In summary, we have demonstrated the possibility to induce sharp magnetization reversals triggered by out-of-plane magnetic fields in permalloy strips on LAO substrates, producing large and abrupt magnetoresitance changes (1 - 2 %) at moderate switching fields (5 - 100 mT). Micromagnetic simulations have been implemented to elucidate the nature of the magnetoresistance jumps observed experimentally and assume the existence of an important magnetic uniaxial anisotropy with the particularity to be slightly deviated from the OOP direction. The intensity of this effect could be related to the transfer of the structural modulations on the LAO substrate towards the Py film deposited on top. We are able to tailor the magnetic switching field by the shape anisotropy through the strip width thickness ratio. These results may be relevant in a future generation of magnetoresistive sensors and functional devices working with a perpendicular applied field.

Part II

Electrical spin injection

5

Spin current injection and transport in non-magnetic media

5.1 Introduction

The injection, transport and detection of carriers with spin orientation along a common direction in a non-magnetic (NM) material are cornerstones of spintronics. This can be performed using the intuitive and efficient method of electrical spin injection where an out-of-equilibrium spin density is induced in the NM layer by the application of a bias voltage at a ferromagnetic/non-magnetic (FM/NM) interface. As a current flowing in a non-magnetic material is naturally unpolarized regarding the spin orientation, the preferential out-of-equilibirum spin texture is expected to relax and fade out while moving away from the injection point. Naturally, the efficiency of the electrical spin injection strongly depends on the material and the interface properties of the bilayer.

This chapter aims at giving a brief introduction on the concept of all-electrical spin injection, transport and detection. The first section is devoted to the description of the generation of a spin texture in a non-magnetic material. The notions of spin accumulation and spin current are introduced through the standard model of Valet and Fert [121]. Based on this model, the importance of the contact resistance to solve the problem of interface conductance mismatch is highlighted. The second section focuses on the electrical detection of a spin current, by means of spin valve (SV) and the Hanle precession method. The different types of devices used to experimentally measure the spin transfer efficiency are also presented.

Parts of this chapter are derived from the works reported in [32, 122–126],

where the reader can find complementary details of interest.

5.2 Electrical spin injection

5.2.1 Two-current model and spin current

For a diffusive medium in which most of scattering events[1] preserve the charge carrier spin, transport can be expressed in terms of two nearly independent channels [27, 127]. In the framework of a linear regime (i.e. weak deviation from equilibrium regime), the spin drift-diffusion equation is generally formulated in term of the spin-dependent electrochemical potential (ECP) μ defined as

$$\mu = \mu_{\text{ch}} - eV, \tag{5.1}$$

where μ_{ch} is the chemical potential which accounts for the kinetic energy of the carriers and which corresponds to the energy required to add an electron to the system. In the linear regime, the change in carrier density is linearly related to the change in the chemical potential as $\delta n \simeq \delta\mu_{\text{ch}} N(E_{\text{F}})$, with $N(E_{\text{F}})$ the density of states (DOS) at the Fermi level. In Eq. (5.1), V is the electrical potential which accounts for the potential energy of electrons. From Eq. (5.1), it is straightforward to note that a gradient of ECP includes the effect of a carrier concentration gradient ∇n (diffusion described by the coefficient D) as well as that of an electric field $E = -\nabla V$ (drift), both effects being equivalent owing to Einstein's relation $\sigma = e^2 N(E_{\text{F}}) D$ [124]. Therefore, a spin-dependent charge current in the context of a diffusive linear regime can be expressed as

$$J_{\pm} = \frac{\sigma_{\pm}}{e} \nabla \mu_{\pm}, \tag{5.2}$$

where $+$ and $-$ represent the up and down orientations for the spin. In the following and without loss of generality, we arbitrarily define the up-state "+" as the majority one. The spin-dependent conductivity is noted $\sigma_{\pm}$ and the degree of polarization of the conductivity, also called spin selectivity,, is defined as

$$\alpha = \frac{\sigma_+ - \sigma_-}{\sigma_+ + \sigma_-} = \frac{\sigma_+ - \sigma_-}{\sigma}, \tag{5.3}$$

where σ is the conductivity when the spin degree of freedom is not considered. In a NM material, the conductivity is assumed to be spin independent and

[1] Considering a non-magnetic medium or a ferromagnetic medium at $T \ll T_{\text{Curie}}$, magnon-electron scattering is frozen out and spin-flip events are only governed by spin-orbit interactions on defects on impurities [121].

therefore $\alpha_{NM} = 0$[2]. However, in FM materials such as transition metals, the DOS and the Fermi velocities differ for each spin sub-band as required by the exchange splitting at the origin of ferromagnetism. The spin-dependent conductivity is therefore expressed as

$$\sigma_{\pm} = \frac{1 \pm \alpha}{2}\sigma. \tag{5.4}$$

The origin of the sub-band splitting and the consequences on the conductivity of each spin-channel in a ferromagnetic metal are briefly detailed in Box 5.1.

To complete the two-current model, it is necessary to introduce the spin-dependent conservation equations. Due to spin-flip scattering events, an out-of-equilibrium density of spin generated in a medium is forced to relax. Considering $\tau_{sf,\pm}$ as the average lifetime for a spin $\pm$ to flip to the opposite state $\mp$ and $\delta n_{\pm} = \mu_{\pm} N_{\pm}(E_F)$ the excess concentration of carriers with spin $\pm$ in a given medium, the spin-flip processes combined with the conservation of the total charge $n = n_+ + n_-$ imply for a steady-state situation, that

$$\nabla \cdot J_{\pm} = \mp e \left(\frac{N_+ \mu_+}{\tau_{sf,+}} - \frac{N_- \mu_-}{\tau_{sf,-}} \right) = \mp e \frac{N_{\pm}}{\tau_{sf,\pm}} \mu_s, \tag{5.6}$$

where $\mu_s = \mu_+ - \mu_-$ is the spin accumulation. The second identity is justified by the absence of net spin scattering at equilibrium, which imposes that $N_+ \tau_{sf,-} = N_- \tau_{sf,+}$. From equations 5.2 and 5.6, and by virtue of Einstein's relation, it is observed that the spin accumulation follows a diffusive equation that reads

$$\nabla^2 \mu_s = \frac{\mu_s}{\lambda_{sf}^2}, \tag{5.7}$$

where $\lambda_{sf}^2 = D\tau_{sf}$, $D = \dfrac{(N_+ + N_-)D_+ D_-}{(D_+ N_+ + D_- N_-)}$ and $\dfrac{1}{\tau_{sf}} = \dfrac{1}{\tau_{sf,+}} + \dfrac{1}{\tau_{sf,-}}$. It is worth noting that in a NM material, where there is no distinction between the up and the down version of the mentioned quantities, the following holds: $D_{NM} = D_+ = D_-$ and $\tau_{sf,NM} = \tau_{sf,+}/2 = \tau_{sf,-}/2$. The factor $1/2$ reflects the fact that both flips, from up to down and the opposite, account for the same reduction of spin density.

Before going further into the application of the two-current model for electrical spin injection, the notion of spin current needs to be clarified. The charge current density $\mathbf{J} = \mathbf{J}_+ + \mathbf{J}_-$ flowing in a ferromagnetic metal gives

[2]When a spin density is injected into a NM material, the concentration of spin up carriers in the conduction band is larger than the spin down concentration, leading to $\sigma_+ > \sigma_-$. However the spin accumulation is considered as negligible compared to the total carrier concentration, i.e. $\sigma_+ - \sigma_- \ll \sigma$

Box 5.1: **Stoner Ferromagnetism - Exchange splitting**

In ferromagnetic metals, electrons responsible for the magnetic properties are delocalized and hybridize in bands [124]. The origin of ferromagnetism resides in the spontaneous spin-dependent band splitting which can be interpreted by the Stoner criterion [128]. Basically, Stoner's model assumes that the bands are shifted to favor the spin direction that minimizes the total energy. It occurs in materials for which the reduction of exchange energy E_{ex} due to the spin alignment overruns the increase of kinetic energy E_{ki} produced by moving low energy spin-down electrons to populate high-energy spin-up family, as illustrated in Fig. 5.1(a).

In 3d transition metals, the magnetic moment is linked to the shifted d sub-band while the conduction is mainly due to s sub-band electrons which have a higher mobility. The spin-dependent conduction is explained by Mott's model where s-like electrons are assumed to endure scattering processes between s and d bands with negligible spin-flip [27]. Therefore, the higher the DOS at the Fermi level in the d-like sub-bands, the lower the electrons mean lifetime $\tau_{\pm}$ and the lower the spin channel conductivity, which is expressed as

$$\sigma_{\pm} = \frac{e^2 m^{\star} n}{\tau_{\pm}}, \tag{5.5}$$

where n and $m^{\star}$ are the concentration and effective mass of electrons in the s-like sub-bands. In the drawing of Fig. 5.1(b), the spin up conductivity is expected to be larger than that of the spin down.

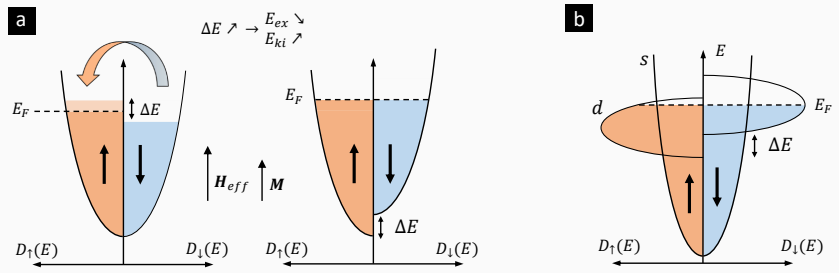

Figure 5.1: *Stoner ferromagnetism model. (a) A self-induced spin unbalance gives rise to a decrease of the exchange energy ΔE_{ex} and an increase of kinetic energy ΔE_{ki}. Stoner ferromagnetism is permanent if $\Delta E_{ex} + \Delta E_{ki} < 0$. (b) Simplified rigid band model with spin-dependent band shift in a transition metal.*

rise to a net spin current density $\mathbf{J}_{\text{s}} = \mathbf{J}_{+} - \mathbf{J}_{-}$ from which we define a spin current polarization, a scalar quantity that is expressed by

$$P_{\text{J}} = \frac{J_{+} - J_{-}}{J_{+} + J_{-}}. \tag{5.8}$$

In the context of electrical spin injection, the spin current is mathematically expressed by the difference between the spin up and down charge currents, with units of A/m^2. However, strictly speaking, charge and spin currents have

different units. In order to express correctly the transfer of spin momentum, the defining expression for the spin current has to be divided by the Josephson constant $2e/h$. Depending on the intensity and propagation direction of the current in both channels, the current can be a pure charge current (no spin preference), a spin-polarized charge current or fully spin-polarized as described in Fig. 5.2. Eventually, it is possible to obtain a pure spin current when spin up and down currents flow in opposite direction with the same intensity. Moreover, one should notice that a spin current is defined by a propagation direction (as charge current) and a spin projection direction. Therefore, it has to be represented by a tensor. Nevertheless, in this work, we will generally deal with only one spin projection direction and therefore the spin current will still be considered as a vector.

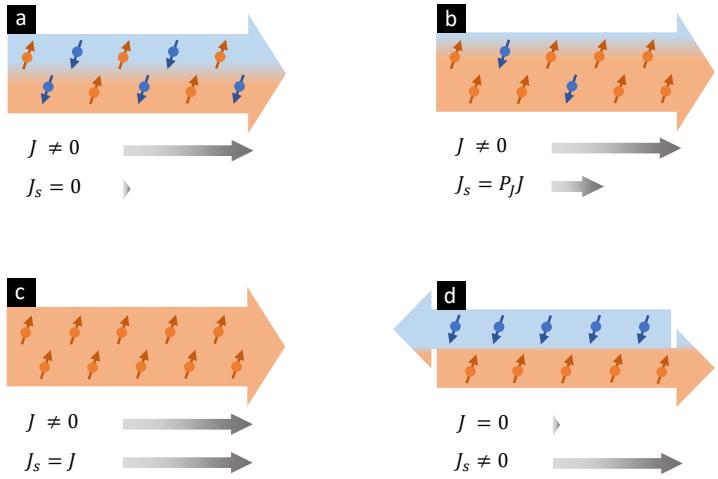

Figure 5.2: *Different types of spin current carried by electrons. (a) Unpolarized charge current, (b) spin-polarized charge current, (c) fully spin-polarized charge current and (d) pure spin current.*

5.2.2 FM/NM interface: Valet-Fert Model

The concept of electrical spin injection implies the transfer of spin carriers from a FM layer into a NM one. Here, we consider the simple 1D model (similar to the one developed by Valet and Fert [121]) where a bias V_{app} is applied to a FM/NM junction of length $2L$ with the interface defined in $x = 0$, as illustrated in Fig. 5.3(a). The abrupt change of spin-dependent conductivity at the interface induces an accumulation of spin which diffuses and relaxes outwards the junction in both directions. From Eqs. (5.2) and

(5.7), and assuming that the charge current is conserved, the exact solutions for the spin-dependent ECPs are given by

$$\begin{aligned}\mu_{\pm}^{\mathrm{F}}(x) &= -eV_{\mathrm{app}} - \frac{eJ}{\sigma^{\mathrm{F}}}(x+L) \pm (1 \mp \alpha)e\alpha J \frac{r_{\mathrm{s}}^{\mathrm{F}} r_{\mathrm{s}}^{\mathrm{N}}}{r_{\mathrm{s}}^{\mathrm{F}} + r_{\mathrm{s}}^{\mathrm{N}}} e^{x/\lambda_{\mathrm{sf}}^{\mathrm{F}}} \\ \mu_{\pm}^{\mathrm{N}}(x) &= -\frac{eJ}{\sigma^{\mathrm{N}}}(x-L) \pm e\alpha J \frac{r_{\mathrm{s}}^{\mathrm{F}} r_{\mathrm{s}}^{\mathrm{N}}}{r_{\mathrm{s}}^{\mathrm{F}} + r_{\mathrm{s}}^{\mathrm{N}}} e^{-x/\lambda_{\mathrm{sf}}^{\mathrm{N}}},\end{aligned} \tag{5.9}$$

where indices F and N refer to the FM and NM layers respectively, $r_{\mathrm{s}}^{\mathrm{i}} = \frac{1}{1-(\alpha^{\mathrm{i}})^2}\frac{\lambda_{\mathrm{sf}}^{\mathrm{i}}}{\sigma^{\mathrm{i}}}$ is the spin resistance-area (RA) product ($\Omega\mathrm{m}^2$) and J is the charge current flowing through the device [121]. As represented in Fig. 5.3(b), the injection induces a split of the spin-dependent ECP, i.e. a spin accumulation $\mu_{\mathrm{s}} = \mu_+ - \mu_-$, which diffuses from the interface following an exponential decay. Consequently to the presence of the spin accumulation, the total resistance of the junction deviates from the expected Ohm's law $V_{\mathrm{app}}^0 = JL(1/\sigma^{\mathrm{F}} + 1/\sigma^{\mathrm{N}})$. The applied voltage rises by $V_{\mathrm{spin}} = V_{\mathrm{app}} - V_{\mathrm{app}}^0$ directly proportional to $\mu_{\mathrm{s}}(0)$ such that the total resistance-area of the system contains an additional "spin-coupled" term δR reflecting the presence of a spin transfer into the NM layer and given by

$$\delta R = \frac{V_{spin}}{J} = \frac{\alpha}{2J}\frac{\mu_{\mathrm{s}}(0)}{e} = \alpha^2 \frac{r_{\mathrm{s}}^{\mathrm{F}} r_{\mathrm{s}}^{\mathrm{N}}}{r_{\mathrm{s}}^{\mathrm{F}} + r_{\mathrm{s}}^{\mathrm{N}}} > 0. \tag{5.10}$$

The presence of an additional resistance (named *spin bottleneck effect* in the pioneering work of Johnson and Silsbee [129] or *spin backflow* [130]) is explained by the fact that the diffusive spin current flowing back into the FM layer induces a charge current (as $\alpha \neq 0$) opposite to the current generated by the power supply. It is worth noting that δR is independent of the current density direction and is always positive.

As presented in Fig. 5.3(c), the conversion of the spin-polarized current (in the FM) into an unpolarized current (in the NM) does not occur abruptly but over a distance characterized by the spin diffusion lengths. As a result an out-of-equilibrium spin-polarized current is generated in the NM layer in the vicinity of the interface. The polarization at the interface is given by

$$P_{\mathrm{j}}(0) = \alpha \frac{r_{\mathrm{s}}^{\mathrm{F}}}{r_{\mathrm{s}}^{\mathrm{N}} + r_{\mathrm{s}}^{\mathrm{F}}}. \tag{5.11}$$

The Valet-Fert model of spin injection can be summarized through an equivalent electrical circuit illustrated in Fig. 5.3(d) composed of two parallel channels describing the spin-dependent current densities in the vicinity of

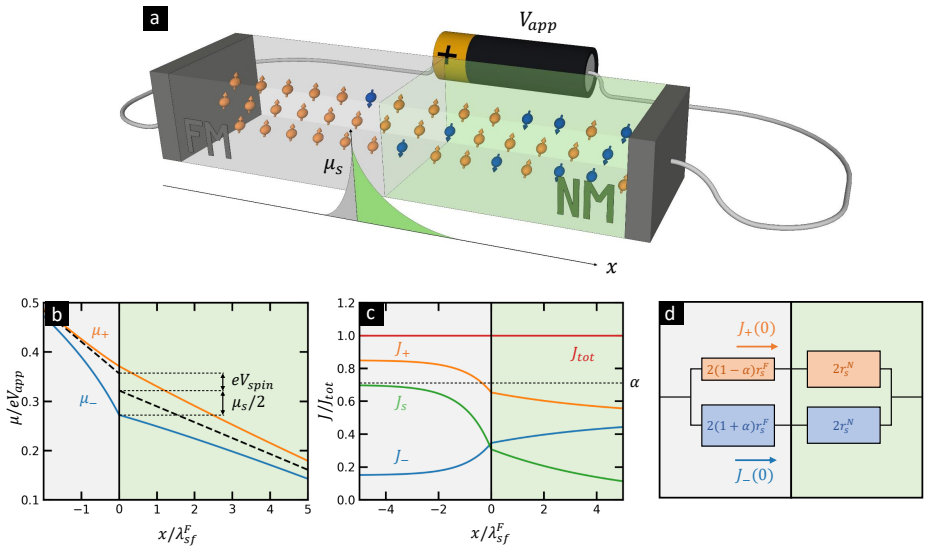

Figure 5.3: *Electrical spin injection principle. (a) Illustration of a basic structure composed of a FM/NM bilayer for electrical spin injection experiment. (b) Variation of the ECP $\mu_\pm$ (orange and blue) along the FM/NM bilayer. The black dashed line represents the potential drop in both region without taking the spin accumulation in account. Results are plotted for $\alpha = 0.7$, $r^F_s = 1.25\ r^N_s$. (c) Variation of the different current densities. The spin polarization P_J is transferred into the NM layer. (d) Two-currents equivalent electrical circuit. The current in the spin up channel is larger than the spin down current.*

the interface (where the out-of-equilibrium spin texture has not vanished). Resistances are replaced by spin-RA of up and down channels. Equivalently to Ohm's law, the spin accumulation is related to the spin current density via a spin resistance:

$$\frac{\mu_s(0)}{e} = 2r^N_s J_s(0). \tag{5.12}$$

The spin-coupled resistance and the spin current polarization are optimized when the spin resistance of the FM layer dominates the NM-related one, namely $r^N_s \ll r^F_s$. In general, the spin diffusion lengths do not contribute positively to this condition since values of $\lambda^F_{sf} \ll \lambda^N_{sf}$ for common FM metals (Co, Fe, etc.) are typically used as electrodes. This criterion is even less respected, when electrical spin injection is performed into semiconductors where one has $\sigma^N/\sigma^F \ll 1$, leading to weak spin injection efficiency $P_J(0) \simeq 1\%$. This issue is known as the *conductivity mismatch* [131].

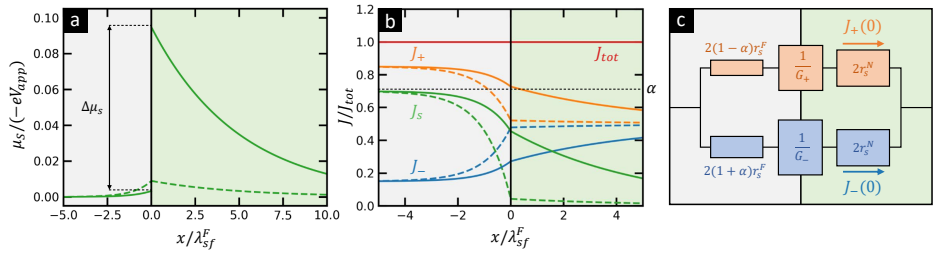

Figure 5.4: *Comparison between the spin injection efficiency for a junction with spin-dependent interface resistance (solid lines - $\alpha = 0.7$, $R_c = 10\ r_s^N = 20\ r_s^F$ and $P_G = 0.5$) and without interface resistance (dashed lines - $R_c = 0$), from the viewpoint of (a) spin accumulation and (b) spin current in the vicinity of the interface. (c) Equivalent electrical circuit including the interface resistance.*

5.2.3 Spin-filtering interface resistance

In order to circumvent the drastic reduction of the spin polarization caused by the conductivity mismatch, a possible solution is to add a spin-filtering interface resistance between the FM and the NM layers [132]. In the basic model we have discussed, such a resistance corresponds to a discontinuity of ECP, $\Delta\mu_\pm(0) = \mu_\pm^{\mathrm{F}}(0) - \mu_\pm^{\mathrm{N}}(0)$. If we note $G_\pm$ the spin-dependent conductances of the additional interface layer, the spin-polarization and the contact resistance of the barrier are

$$P_{\mathrm{G}} = \frac{G_+ - G_-}{G_+ + G_-} = \frac{G_{\mathrm{s}}}{G} \qquad \text{and} \qquad R_{\mathrm{c}} = \frac{1}{(1-P_{\mathrm{G}}^2)G}. \tag{5.13}$$

Considering the continuity of the spin current at the interface, the polarization of the injected current becomes

$$P_{\mathrm{j}}(0) = \frac{\alpha r_{\mathrm{s}}^{\mathrm{F}} + P_{\mathrm{G}} R_{\mathrm{c}}}{r_{\mathrm{s}}^{\mathrm{F}} + r_{\mathrm{s}}^{\mathrm{N}} + R_{\mathrm{c}}}, \tag{5.14}$$

and the spin-coupled resistance induced by the spin accumulation is given by

$$\delta R = \frac{r_{\mathrm{s}}^{\mathrm{N}}\left(P_{\mathrm{G}}^2 R_{\mathrm{c}} + \alpha^2 r_{\mathrm{s}}^{\mathrm{F}}\right) + r_{\mathrm{s}}^{\mathrm{F}} R_{\mathrm{c}}\left(\alpha - P_{\mathrm{G}}\right)^2}{R_{\mathrm{c}} + r_{\mathrm{s}}^{\mathrm{N}} + r_{\mathrm{s}}^{\mathrm{F}}}. \tag{5.15}$$

In the case of a transparent contact, $R_{\mathrm{c}} = 0$ (meaning that $P_{\mathrm{G}} = 0$, the two latter relations reduce to Eqs. (5.11) and (5.10) and the backflow is no longer blocked, leading to a drastic reduction of the interface spin polarization. Alternatively, when the contact resistance dominates the system, one has $R_{\mathrm{c}} \gg r_{\mathrm{s}}^{\mathrm{N}} > r_{\mathrm{s}}^{\mathrm{F}}$, the spin-polarization of the current tends towards the polarization

of the interface layer $P_j(0) \simeq P_G$ and the conductance mismatch is fully compensated. The comparison between both extreme cases is shown in Figure 5.4(a) and (b). A highly resistant contact coupled with a large value of P_G is obtained by the presence of a tunnel barrier (insulating layer or Schottky barrier) at the FM/NM interface as the tunnel current directly depends on the DOS of the FM electrode [133]. A model based on Slonczewski's work [134], that captures the main trend of spin-dependent tunneling is presented in Box 5.2. The efficiency of a spin tunnel barrier can be further enhanced with barriers showing a spin-dependent transmission probability as spin-symmetry barriers or spin-filtering barriers made of magnetic insulators [135, 136].

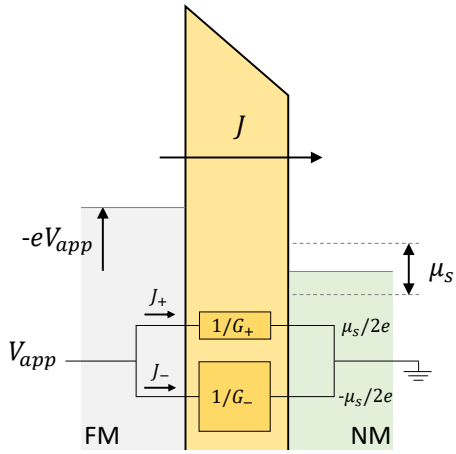

Figure 5.5: *Schematic illustration of the linear model. The difference of applied bias coupled to the spin-dependent conductance of the barrier gives rise to a spin voltage* $V_{spin} = P_G\mu_s/2$.

The concept of electrical spin injection is often summarized in the case of the ideal configuration which considers that the junction is totally dominated by a large constant spin-dependent interface resistance (does not depend on the applied voltage, neither on the spin accumulation). The equivalent circuit shown in Figure 5.4(c) is therefore simplified, keeping only $1/G_+$ and $1/G_-$ as origins of the total voltage drop occuring at the interface. As the bias voltage in each branch differs because of the spin accumulation in the NM layer, the two-current model rewrites as

$$J_\pm = G_\pm \left(V_{\text{app}} \mp \frac{\mu_s}{2e} \right), \tag{5.16}$$

leading to

$$V_{app} = \frac{J}{G} + P_G \frac{\mu_s}{2e} = J\,(R + \delta R) \Longleftrightarrow J = \frac{1}{R}\,(V_{app} - V_{spin})\,. \tag{5.17}$$

This simplified model is known as the linear model and is generally acceptable for weak values of the applied voltage V_{app}.

5.3 Electrical spin detection

5.3.1 Spin-valves

The detection and quantification of spin accumulation is done by probing the resistance change it induces. This is achieved by adding a second FM electrode as detector to form a FM/NM/FM heterostructure also called a *spin-valves* device and represented in Fig.5.7(a). If a constant current density is applied to the device and the spin-valve total resistance is probed in parallel ($\uparrow\uparrow$) and anti-parallel ($\uparrow\downarrow$) magnetic configurations for the FM electrodes, the exact solution for the resistance change can be expressed as [139]

$$\begin{aligned} R_{\uparrow\downarrow} - R_{\uparrow\uparrow} &= \frac{2\left(\alpha r_s^F + P_G R_c\right)^2}{\left(R_c + r_s^F\right)\cosh\left(\frac{L}{\lambda_{sf}^N}\right) + \frac{r_s^N}{2}\left[1 + \left(\frac{R_c}{r_s^N}\right)^2\right]\sinh\left(\frac{L}{\lambda_{sf}^N}\right)} \\ &\approx 4P_G^2 r_s^N \sinh^{-1}\left(\frac{L}{\lambda_{sf}^N}\right) \end{aligned} \tag{5.21}$$

where L is the distance between both FM electrodes that are assumed to be identical. The change of resistance with the magnetic configuration is attributed to the weaker scattering of electrons at the FM/NM interface when their spin orientation is parallel to the electrode [140]. Depending on the electrodes magnetic configuration, the spin accumulation diffusing from both FM/NM interfaces will interfere constructively or destructively. This effect is plotted in Fig.5.7(a).

Although the two-terminal (2T) or local spin valve (LSV) structure is the simplest design to evaluate the relevant parameters for the electrical spin injection, the technique suffers from some drawbacks. First, the necessity to work with a tunnel contact to optimize the spin current implies that the resistance of the device is generally important (several kΩ) leading to a weak magnetoresistance signal proportional to r_s^N/R_c (see Fig.5.7(b) for the competition between the injection and the detection efficiencies in LSV as

Box 5.2: **Spin-dependent tunnel conductance - Slonczewski's model**

The spin dependence of a tunnel barrier can be evaluated considering a Slonczewski-like model [134], i.e. a two-current approach (assuming no spin-flip scattering) based on Tsu-Esaki equations [137]. The FM left electrode is considered as a metal fulfilling Stoner condition with spin-shifted parabolic bands [138] (see Figure 5.6(a)). The current density is given by

$$J_{\pm} = \frac{e}{h}\int_{U_{\pm}^{F}}^{\infty} dE_x\ T(E_x)\times \left[n_t^N(E_x, \frac{\mu_v}{2}) - n_t^F(E_x, -\frac{\mu_v}{2})\right] \tag{5.18}$$

where $E_x = U_{\pm}^{F} + \hbar^2 k_x^2/2m^\star$ is the longitudinal component of the total energy (with $m^\star$ the effective mass of electrons), $U_{\pm}^{F}$ is the energy of the bottom of the FM conduction band, $T(E_x)$ is the transmission probability and n_t is the carrier density at finite temperature for transverse components of the energy E_{xy}, also called Tsu-Esaki supply function. Considering a trapezoidal barrier with a height $\phi_B(z)$ and thickness w, the transmission probability using a Wentzel–Kramers–Brillouin (WKB) approximation is expressed as

$$T(E) = e^{w\sqrt{8\pi m^\star(\phi_B - E)}/h}. \tag{5.19}$$

The transverse DOS n_t is given by

$$n_t(E,\mu) = \frac{4m^\star k_B T\pi}{h^2}\times \ln\left[1+\exp\left(\frac{\mu - E}{k_B T}\right)\right]. \tag{5.20}$$

The difference between the spin up and the spin down components of the current density is given by the area under the curve displayed in Fig. 5.6(b) where the effect of the band spin-shift is clearly visible. In panel (c), P_G is plotted as a function of the applied bias voltage $V_{app} = -\mu_v/e$ while the inset presents the change of contact resistance. It shows that a large contact resistance R_c is obtained with a non-zero spin-filtering effect P_G, solving the resistance mismatch issue of electrical spin injection.

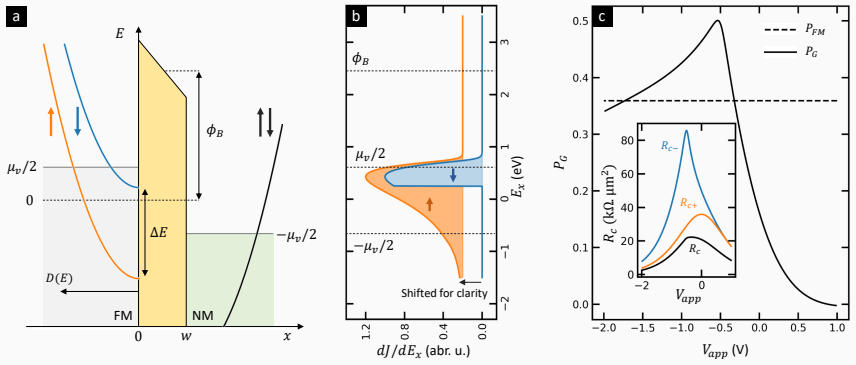

Figure 5.6: *(a) Illustration of the FM tunnel barrier. (b) Distribution of spin current densities with the longitudinal energy. (c) Bias dependence of the conductance spin-polarization and (inset) the contact resistance. Calculations are performed for $\phi_B = 2.5$ eV, $\Delta E = 1.75$ eV and $w = 1.5$ nm.*

function of R_c). It can therefore be difficult to distinguish the spin signal from the noise signal. Moreover, due to the presence of a simultaneous charge current flowing through this device, spurious field-dependent fluctuations of resistance can be induced by Hall effect, AMR, etc. [141].

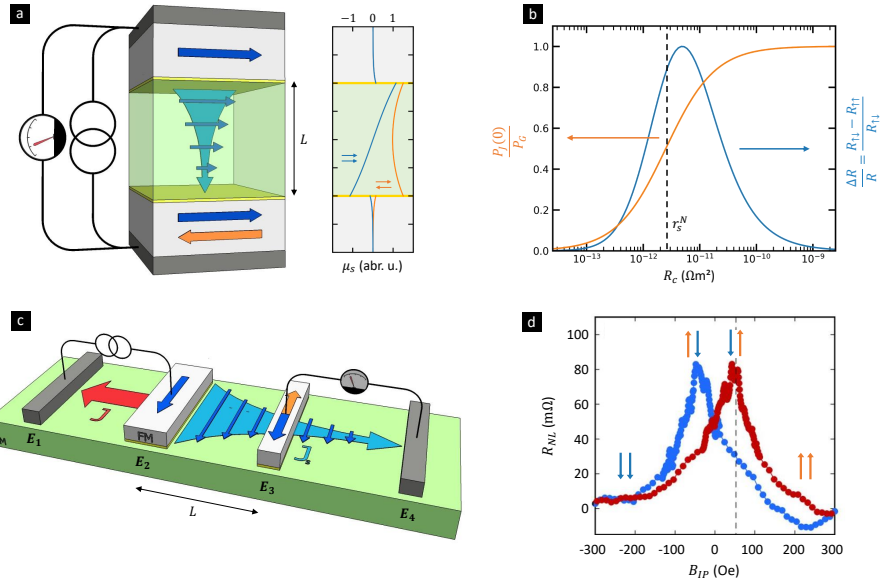

Figure 5.7: *(a) Illustration of a LSV device. The blue and orange arrows show the magnetization direction of the FM electrodes. The adjacent plot shows the spin accumulation along the device for both magnetic configurations of the valves. (b) Variation of the current spin-polarization and the magnetoresistance detection signal as functions of the tunnel contact resistance (adapted from [142]). (c) Illustration of a NLSV design. (d) First experimental results of NL electrical spin injection and detection in Si at low temperature obtained by van't Erve et al. Adapted from [143].*

For these reasons, a four-terminal (4T) design, or non-local spin valve (NLSV) as illustrated in Fig. 5.7(c) is generally preferred. In such a device, a current is applied between a FM injector (electrode E_2) and the reference electrode (E_1). While the charge current is confined in the left part of the device (between E_1 and E_2), the spin current generated at the FM/NM interface under electrode E_2 also diffuses towards the detection electrode E_3. Therefore, a non-zero spin accumulation lies under the detection electrode. The work of Johnson and Silsbee [144] proved that the inverse mechanism of electrical spin injection, referred to as spin-charge coupling effect, also takes place. This means that the presence of an out-of-equilibrium spin population at a FM/NM interface induces an electromotive force (or a current)

in a open-(close-)circuit. The voltage bias is measured between the detector and the second reference electrode (E_4) placed far enough where the spin accumulation vanished due to spin relaxation mechanisms. Since the spin accumulation generally produces a weak signal (between a few μeV and a few meV), the use of the linear model is justified and from Eq. (5.17), one determines that the open-circuit voltage probed in a NLSV experiment $\Delta V_{\mathrm{NL}} = V_{\uparrow\downarrow} - V_{\uparrow\uparrow}$ equals two times the spin voltage and is given by

$$\Delta V_{\mathrm{NL}} = 2V_{\mathrm{spin}} = P_{\mathrm{G}} \frac{\mu_{\mathrm{s}}(L)}{e}, \tag{5.22}$$

where $\mu_{\mathrm{s}}(L)$ is the spin accumulation at the distance L from the injector. From Eqs. (5.9) and (5.12), it is straightforward that the NL electrical potential will exponentially decrease with the distance L and can thus be rewritten as a non-local resistance

$$R_{\mathrm{NL}} = \frac{\Delta V_{\mathrm{NL}}}{2J} = \frac{\mu_{\mathrm{s}}(0)}{2e} \exp\left(-L/\lambda_{\mathrm{sf}}^{\mathrm{N}}\right) \approx \frac{1}{2} P_{\mathrm{G}}^2 r_{\mathrm{s}}^{\mathrm{N}} \exp\left(-L/\lambda_{\mathrm{sf}}^{\mathrm{N}}\right), \tag{5.23}$$

where the second identity is verified when $R_{\mathrm{c}} \gg r_{\mathrm{s}}^{\mathrm{N}}, r_{\mathrm{s}}^{\mathrm{F}}$. The term P_{G}^2 comes from the spin conductance of the tunnel barriers at the injector and the detector. Almost systematically, both electrodes have a similar tunnel spin conductance P_{G} as they are made of the same materials and therefore Eq. (5.23) remains exact in the context of the linear model. However, as discussed in box 5.2, the spin conductance of a tunnel barrier P_{G} depends on the bias voltage which is never zero at the injector. For a more general expression of the non-local resistance, the term P_{G}^2 is sometimes replaced by the product of distinct spin polarizations for the injector and detector, $P_{\mathrm{inj}} P_{\mathrm{det}}$. In the context of perfect tunnel contacts ($R_{\mathrm{c}} \gg r_{\mathrm{s}}^{\mathrm{N}}$), the injector spin polarization equals the polarization of the injection current $P_{\mathrm{inj}} = P_{\mathrm{J}}$. Regarding the detector spin polarization, it is defined as the spin detection efficiency and is proportional to the ratio of the detected charge voltage (Eq. (5.17)) divided by the spin accumulation, $P_{\mathrm{det}} = 2V_{\mathrm{spin}}/e\mu_{\mathrm{s}}$. The non-local resistance R_{NL} is proportional to the spin polarization of the current generated at the injector P_{inj}. Others parameters from Eq. (5.23) are generally known or may be determined independently. The injector spin polarization is therefore experimentally extracted from the non-local spin resistance by varying the injection current while keeping the detecting electrodes in an open-circuit configuration. Considering the extrapolated value of the R_{NL} at zero injection current, one can deduce the zero-bias spin conductance of the tunnel barrier, i.e. P_{G}.

It is useful to note as well that the switching between the two possible spin-valve configurations ($\uparrow\uparrow, \uparrow\downarrow$) is achieved by an external magnetic field

parallel to the electrode's easy-axis[3], requiring a different coercive field for each electrode. This is generally obtained by tuning the electrode's width. When those widths are non-negligible compared to the channel length, it becomes necessary to integrate the spin signal over the electrodes' width to compensate the deviation from the simple exponential decrease [145].

One last final remark is considered for the device geometry regarding the spin resistance. The definition of the spin resistance area in Eq. (5.12) is based on a 1D model, i.e. a FM/NM contact with infinite area and infinite NM channel, where the volume of spin accumulation is only limited by the spin relaxation along the channel $V_{acc}^{1D} \sim \lambda_{\mathrm{sf}}^{\mathrm{N}} W_{\mathrm{x}} W_{\mathrm{y}}$, with $A = W_{\mathrm{x}} W_{\mathrm{y}}$ the contact area. If the spin accumulation volume is confined by the device dimensions, the definition of the spin resistance needs to be scaled by a geometrical factor V_{acc}^{1D} / V_{acc} [130]. Different cases are illustrated in Fig. 5.8. Typically, in a NLSV where the channel is a NM thin film of thickness $t \ll \lambda_{\mathrm{sf}}^{\mathrm{N}}$ and the injector width is narrow, i.e. $W_{\mathrm{x}} \ll \lambda_{\mathrm{sf}}^{\mathrm{N}}$, the spin resistance area is

$$r_{\mathrm{s}}^{\mathrm{N}} = \frac{\lambda_{\mathrm{sf}}^{\mathrm{N}}}{\sigma^{\mathrm{N}}} \frac{V_{acc}^{1D}}{W_{\mathrm{y}} t \lambda_{\mathrm{sf}}^{\mathrm{N}}} = R_{sq} \lambda_{\mathrm{sf}}^{\mathrm{N}} W_{\mathrm{x}}, \tag{5.24}$$

where R_{sq} (Ω) is the sheet resistance of the thin film.

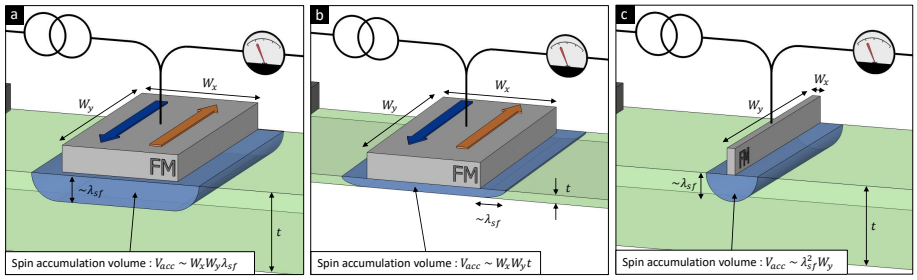

Figure 5.8: *Illustration of the confinement effect for 3D electrical spin injection for the limiting cases (a) $W_x, W_y, t \gg \lambda_{sf}$, (b) $W_x, W_y \gg \lambda_{sf} \gg t$ and (c) $W_y \gg \lambda_{sf} \gg t, W_x$.*

From a spin-valves experiment, the extraction of the spin diffusion length remains complicated because it requires to perform length-dependent experiments (same design but changing the channel length L) in order to decorrelate λ_{sf} from the spin-polarization factor.

[3]Most of the time, electrodes have a rectangular stripe-like shape with an easy-axis perpendicular to the channel direction. The huge shape anisotropy gives abrupt transition between saturated magnetization in opposite directions when the external field equals the coercive field.

5.3.2 Hanle effect

An alternative and more reliable method, the Hanle effect, consists in controlling the intensity of the spin accumulation in the NM channel by forcing the precession of the injected spins with an external perpendicular magnetic field. Indeed, in a diffusive transport, the spins reach the detector following many different paths. For a precession (Larmor) frequency $\omega_L = \gamma B$ (γ is the gyromagnetic ratio of the electron), a spread of traveling time Δt results in spins at the detector with a spread of phase $\Delta\phi = \Delta t \omega_L$, which tends to a randomly-distributed spin orientation for large B values and therefore to a zero spin voltage. Considering a spin population n_s diffusing in the channel without drift (such as in NLSV), the spin current conservation expressed by the steady-state continuity Eq. (5.6) can be adapted by including the precession term to give a Bloch-like equation [144]:

$$0 = \mathbf{n}_s \times \gamma \mathbf{B} + \frac{\mathbf{n}_s}{\tau_{sf}} + D\nabla \mathbf{n}_s, \tag{5.25}$$

where the local magnetic moment is induced by the out-of-equilibrium spin concentration in the three directions of space $\mathbf{n_s}$. It should be noted that Bloch's original equations postulate the existence of two different time constants T_1 and T_2. The first one represents the relaxation time for the increase of the component along the applied field while T_2 deals with the relaxation of precessing transverse components. Following the assumption of Johnson and Silsbee, here, it is assumed that $T_1 = T_2 = \tau_{sf}$ [144]. The origin of the spin relaxation mechanisms is multiple and a brief summary is offered to the reader in Box 5.3. Considering a constant injection rate J_s/e at the injecting electrode, the solution for the component of $\mathbf{n}_s$ parallel to the FM electrode magnetization direction (the $\hat{x}$ component in Fig. 5.9(a)) is

$$n_{s,x}(y) = \frac{1}{2}\frac{J_s}{e}\sqrt{\frac{\tau_{sf}}{D_s}}F(b,l), \tag{5.26}$$

The function $F(b, l(y))$ is defined as

$$F(b,l) = \frac{1}{\sqrt{2}}\frac{1}{f^2(b)-1}\left[f(b)\cos\left(\frac{l(y)b}{f(b)}\right) - \frac{b}{f(b)}\sin\left(\frac{l(y)b}{f(b)}\right)\right]\exp\left(-l(y)f(b)\right), \tag{5.27}$$

where we introduce the reduced spin-flip lifetime

$$b = \gamma B_z \tau_{sf}, \tag{5.28}$$

the reduced spin diffusion length

$$l(y) = \sqrt{\frac{y^2}{2\tau_{sf}D_s}}, \tag{5.29}$$

and

$$f(b) = \sqrt{1 + \sqrt{1 + b^2}}. \tag{5.30}$$

The NL resistance area detected by a weakly coupled ($R_c \gg r_s^N$) FM electrode separated from the injection point by a channel of length L is

$$\begin{aligned} R_{NL} &= \frac{V_{NL}}{J} = \frac{P_G \mu_s(L)}{2eJ} = \frac{P_G n_s(L)}{eJN(E_F)} \\ &= \frac{1}{2} P_G^2 r_s^N F\left[l(L), b\right]. \end{aligned} \tag{5.31}$$

In Fig. 5.9(b), the normalized value of the NL resistance-area is plotted as a function of the magnetic field for different values of the channel length. In absence of external magnetic field, Eq. (5.31) reduces to Eq. (5.23).

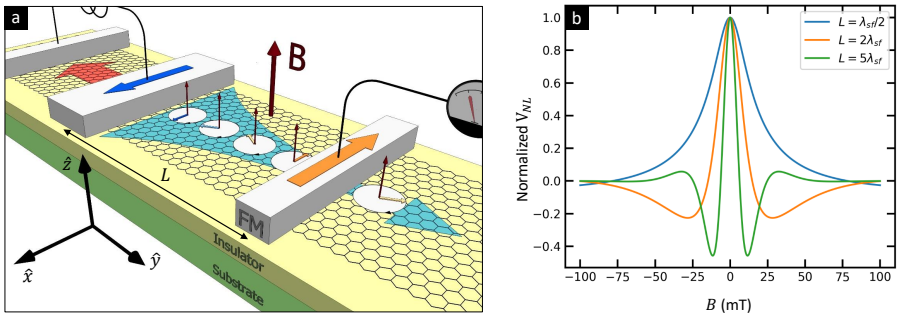

Figure 5.9: *(a) Illustration of a NLSV (with a graphene channel in this example) under perpendicular magnetic field (Hanle effect). The precession of spins while diffusing is represented by the rotating arrows. (b) Example of NL spin voltage as a function of the magnetic field for different channel lengths (with $\tau_{sf} = 3$ ns and $D = 0.03$ m^2/s).*

5.3.3 Three-terminal geometry

Using the Hanle effect, all-electrical spin injection and detection can be achieved using only a single FM electrode. In a three-terminal (3T) device, a spin accumulation is generated by injecting a charge current between a FM electrode and the left reference electrode while a spin voltage is detected through a Hanle precession experiment using the right reference electrode as represented in Fig. 5.12(a). As no SV effect is required, the coercive field of the FM electrode becomes irrelevant and therefore there is no design restriction in 3T design, i.e. the FM electrode can be very large and does not require complex lithography process.

Box 5.3: **Spin relaxation mechanisms**

Spin-flip mechanisms originate from the interaction of electrons with their environment. The two main sources of spin relaxation mechanisms rely on the spin-orbit coupling and the momentum scattering [123, 146]. The Elliott-Yafet (EY) mechanism assumes that the spin-flip phenomenon occurs during a scattering process [147]. In presence of spin orbit interaction, Bloch states are mixtures of both spin directions. Consequently, even a spin-independent scattering event (electron-phonon or electron-(non-magnetic)defect) can induce a spin flip, leading to a spin relaxation time τ_{sf} proportional to the momentum scattering time, τ_e:

$$\tau_{sf} \approx a^2 \tau_e, \tag{5.32}$$

where the probability factor is the ratio between the spin-orbit coupling amplitude and the energy separation between spin bands, namely $a = \lambda_{so}/\Delta$.

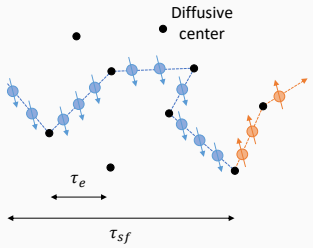

Figure 5.10: *Illustration of the EY spin relaxation mechanism.*

The second type of scattering is the D'yakonov-Perel' (DP) mechanism [148]. It was demonstrated that in a crystalline system with a lack of inversion symmetry, there is a difference between the up and down spin energy bands dependent on the carrier momentum [149]. This energy change has an effect analog to the Zeeman effect for spin in an effective Rashba-like magnetic field dependent on the electron momentum. Consequently, between two scattering events, the spin will precess around the effective field, triggering a phase change and then a relaxation effect. At each scattering center, the momentum and therefore the precession axis are randomly adjusted, acting as a reinitialization of the relaxation process. In opposite to the EY, the DP mechanism decreases with the momentum scattering rate:

$$\tau_{sf} \approx \frac{b^2}{\tau_e}, \tag{5.33}$$

where $b = \lambda_R$ is the intensity of the Rashba field.

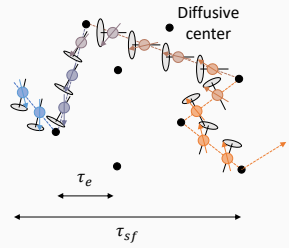

Figure 5.11: *Illustration of the DP spin relaxation mechanism.*

The dominant mechanism is generally determined by measuring the change of spin relaxation time as a function of the diffusion constant that are both obtained by performing Hanle experiments with NLSV.

In some specific cases, the spin relaxation effect can also be induced by other mechanisms, due to the interactions between the electron's spin with the nuclear spin (hyperfine interaction - often negligible) or the spin electron-hole interaction (Bir-Aronov-Pikus effect - in materials with a high hole density such as heavily doped p-type semiconductor) [123].

The change of spin accumulation with the intensity of the external magnetic field is obtained by considering Eq. (5.31) where the spin channel is

limited to the region under the FM/NM interface. It assumes that injected spin carriers can contribute to the spin voltage until they diffuse away from the electrode. With Hanle precession, the preferential spin direction is lost and the spin population decreases, vanishing at infinite magnetic field. As demonstrated by Dash et al. [150], if the electrode dimensions are large compared to the spin diffusion length, Eq. (5.31) is reduced to a simple Lorentzian function from which the spin lifetime can be extracted, namely

$$\mu_s(B) = \frac{\mu_s(0)}{1 + (\gamma B \tau_{sf})^2}. \tag{5.34}$$

In order to obtain the spin diffusion length λ_{sf}, a 3T Hanle measurement

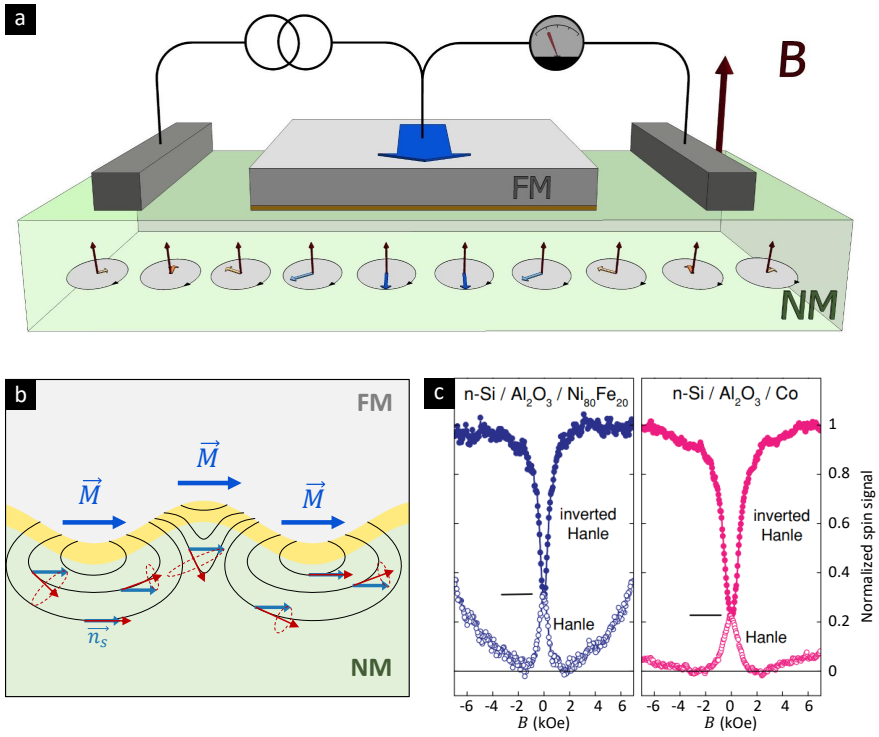

Figure 5.12: *(a) Illustration of 3T device under perpendicular magnetic field. The spins are injected and detected by the same electrode. The precession decorralates the detected mean spin direction from the injection direction, reducing the intensity of the spin voltage. (b) Illustration of the zero-field precession induced by the interface roughness. (c) Results for the Hanle and inverted Hanle precession experiments in 3T devices. Panels (b) and (c) are reproduced from [151].*

has to be coupled with electrical transport experiment to obtain the electron

diffusion constant D, which is generally a good approximation for the spin diffusion constant in a NM material.

While the absence of a diffusive channel greatly simplifies the design of 3T devices compared to 4T NLSV, it suffers from drawbacks that leads to ambiguous experimental results in contrast to the predictions of the standard theory. Mainly, 3T measurements do not guarantee that the probed spin signal comes from injected spin carriers in the conduction band rather than from localized states in the tunnel barrier (or at the interface between an oxide and a depletion layer) [152]. Moreover it does not take into account the important impact of a bias detector which will be discussed deeply in the next chapter [153]. Finally, an overestimation of the spin signal can also be induced by effects present in both 3T and 4T design such as the inhomogeneity of the spin current density or the artificial broadening of the Hanle signal due to magnetostatic fringe fields arising from the roughness of the interface between the tunnel barrier (B) and the non-magnetic layer (NM) as illustrated in Fig. 5.12(b) [151]. The latter point can be quantified by probing the intensity of the inverted Hanle effect, i.e the change of spin voltage with the intensity of the in-plane magnetic field. In Fig. 5.12(c), examples of the Hanle and inverted-Hanle spin signal for 3T devices made with different FM electrodes are presented. For low magnetic field, the expected Lorentzian curves are obtained while at higher magnetic field, the signal is perturbed as the FM electrode magnetization (and therefore the injected spins) aligns itself with the external field.

6

Origin of the giant spin detection efficiency in biased tunnel-barrier electrical spin detector

This chapter is based on the following publication:

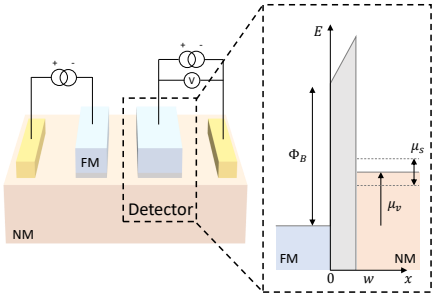

"*Origin of the Giant Spin-Detection Efficiency in Tunnel-Barrier-Based Electrical Spin Detectors*",
E. Fourneau, A. V. Silhanek and N. D. Nguyen,
Phys. Rev. Appl., **14**, 024020 (2020)

6.1 Introduction

All-electrical injection, transport and detection of a spin-polarized current in a non-magnetic (NM) medium are cornerstones of spintronics. In the past years, encouraging results were obtained on spin-polarized current injection into mainstream group-IV semiconductors (SCs) such as Si [145, 154, 155] and Ge [156–158] at room temperature, as well as into other promising materials such as graphene [159, 160]. As developed in the previous chapter, ferromagnetic (FM) tunnel junctions are widely regarded as one of the best approaches to both generate a spin polarization into a SC and convert it into a voltage signal. This is in part due to the limited spin absorption in the FM and the reduced conductance mismatch [139].

Nowadays, the literature is abundant on works quantifying the performance of a FM tunnel barrier to generate and detect a spin signal in a SC as well as in evaluation of the spin lifetime [130]. Promising results have been reported over the last decade with a surprising and unexpected spin detection efficiency (i.e. the conversion factor from spin accumulation to charge voltage), demonstrating in some cases a pick up voltage higher than the injected spin signal [156, 161–163]. This outstanding spin detection was reported for devices where the FM tunnel contact used for detection was biased, as in technologically relevant devices [30, 164–167]. This amplification effect offers an interesting perspective for on-chip integration of spin-based circuits and has attracted considerable attention from theoretical standpoint. Indeed, various tentative mechanisms were proposed over the recent years to explain the observed large spin detection efficiency, such as two-step tunneling [152, 168], thermionic emission [169] or lateral current inhomogeneity [150], to name just a few. Unfortunately, none of the above mentioned mechanisms seems to satisfactorily account for all the experimental findings.

Recently, it has been experimentally established that some discrepancies between experiments and theoretical calculations find their origin in the energy dependence of the carrier transmission probability in the tunnel junction [162, 163, 170–175]. This suggests that a description based on a non-linear transport of spin should be invoked [176]. Although preliminary ideas in this direction were already advanced some ten years ago, it is not until recently that non-linearities have been recognized as an essential ingredient for the understanding of FM tunnel junctions.

In this chapter, we analyse the implications of non-linearity in FM tunnel junctions using a theoretical approach, including crucial aspects overlooked in previous studies while directly responsible for the giant spin detection

efficiency. Through this approach, we explain how a spin signal can be converted into a charge signal with an effective efficiency of several hundreds of percent. It is worth noting that the obtained results apply to any spin detection device composed of a FM/SC contact where a direct tunnelling transport occurs, thus including not only oxide or Schottky tunnel barriers, but also various pseudo-substrates such as graphene and other 2D materials.

In the first part of this chapter, the underlying mechanisms responsible for this remarkably efficient spin detection are identified and the way each parameter influence the enhancement is discussed. An approximated analytical expression for the detector spin sensitivity with applied bias, $P_{\text{det}}(V)$, is presented. The second part focuses on the impact of the barrier shape, showing that this enhancement is present at any tunnel barriers even if the dominant mechanisms differs with the barrier type. Then, although the spin signal is reduced at high temperatures, it remains superior to the value predicted by the linear model. Our findings shed light into the interpretation and understanding of electrical spin detection experiments and open paths to optimize the performance of spin transport devices.

6.2 Non-linear model of spin detection

As presented in the previous chapter, the mechanism of electrical spin detection by spin-charge coupling effect consists in the presence of a voltage bias to compensate the charge current induced by the transfer of a pure spin current from the NM layer into the FM one, and is synthesised by Eq. (5.17). According to this linear model, in an open-circuit configuration, the compensation voltage (or spin voltage) V_{spin}, is directly proportional to the spin accumulation under the detector $V_{\text{spin}} = \dfrac{P_{\text{G}}}{2e}\mu_{\text{s}}$, where P_{G} is the spin conductance of the tunnel barrier. Since the linear model for spin transport is based on the Ohm's law, the tunnel barrier is therefore considered as a conductance G independent of any applied voltage. While this consideration is unrealistic as tunnelling process is strongly non-linear and is the essence of the spin filtering effect, the linear model can be considered as accurate when the voltage bias applied to the detector is limited to the spin-coupling signal (of the order of the spin accumulation, i.e. a few meV) and therefore is weak compared to the barrier height. However, this approximation is not relevant anymore when an electrical bias is applied to the detector.

Indeed, although the linear theory for spin injection and detection captures the essential mechanisms of these processes, deviations from the linear

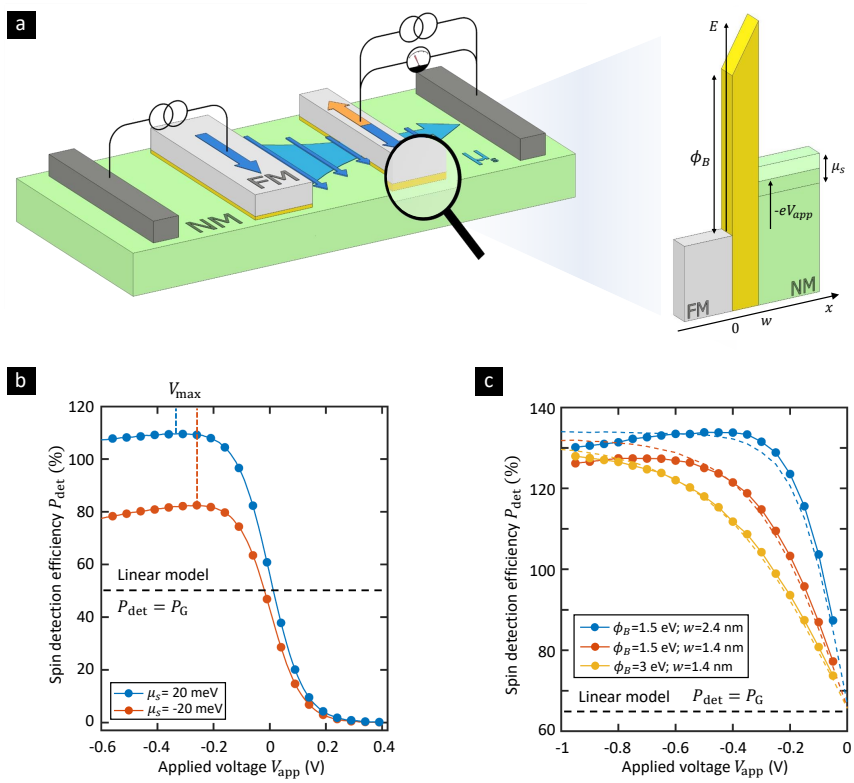

Figure 6.1: *Nonlinear spin detection efficiency under bias. (a) Schematic energy band diagram of the FM/B/NM tunnel contact under a bias, where $\mu_v = -eV_{app}$ is the applied ECP, w and ϕ_B are the width and the height of the barrier. A drawing of the spintronic device is also provided for clarity. (b) Computed spin detection efficiency with tunnel bias for two different spin accumulations μ_s ($w = 4$ nm; $\phi_B = 1$ eV; $P_G = 50\%$; $T = 1$ K). The dashed line is obtained by cancelling the barrier deformation under bias, corresponding to the linear model. (c) Spin detection efficiency as a function of applied voltage for different barriers. Dashed lines correspond to results reported in Ref. [176].*

model have been systematically reported in experiments based on 3-terminal (3T) Hanle devices and in 4T devices where both injector and detector are under bias [130, 165]. Recently, Jansen *et al*. [176] investigated the change of non-local resistance with respect to the detector bias voltage, performing non-local spin-valves experiments (see Eq. 5.23). As only the spin accumulation generated at the injector depends on the magnetic configuration of the electrodes, the spin-valve resistance is expected to be independent of spin accumulation induced by the current flowing through the detector. They observed that the spin detection efficiency P_{det} at a tunnel junction strongly depends on the applied bias, deviating from the value P_{G} predicted by the linear model, leading to a detection efficiency superior to 100% and offering therefore a way to magnify the detected spin accumulation.

In their work, the authors pointed out that the spin signal amplification is inherent to the non-linear transport occurring at the tunnel junction which arises from the dependence of the transmission probability with the energy of injected carriers. In simple words, since the transmission probability increases with energy, the preferential spin population will undergo a higher impact than the minority spin population when changing the applied voltage. Naturally, the increase of P_{det} with the applied voltage could be attributed mainly to this effect.

While this reasoning seems to qualitatively capture the trend observed in most experimental results, there still exists some features that remain unexplained [176]. Notably in their explanation of the origin of the non-linearity, the fact that the increase of applied voltage needed to compensate the loss of current after spin precession (i. e., the spin voltage) becomes sensitive to the increase of junction bias, leading to a P_{det} *independent* on the bias. Moreover, their model looks limited as it may not be able to justify why a signal differing of several order of magnitude is pointed out in many spin tunnel devices [130].

6.2.1 Model and hypotheses

In order to investigate more deeply the mechanisms governing this non-linear detection in various tunnel junctions, an incremental approach is used, which in complexity is progressively added to the model. We focus first on the simplest model of a tunnel barrier between two metals (FM/B/NM) where the effects of the barrier deformation under bias are thoughtfully investigated. Then, the NM metals is replaced by a highly degenerate SC in order to evaluate the impact of a band gap, the degeneracy level and the energy dependence of the DOS. At a later stage, we address the variation

of the tunnel barrier shape to compare the detection efficiency of oxide and Schottky tunnel barriers. Information regarding equations and computational details are summarized in Box 6.1.

Box 6.1: **Modelling details**

Calculations were performed using Matlab to solve the spin-dependent non-linear tunnel transport equations based on the two-channel model. The spin dependent description of the tunnel current density adapted from Eq. (5.18) is used for a semi-classical approach:

$$J_{\pm} = \frac{e}{h}\frac{1 \pm P_G}{2}\int_{-\infty}^{\infty} dE_z\; T(E_z)\left[n_t^N\left(E_z, \mu_v \pm \frac{\mu_s}{2}\right) - n_t^F\left(E_z, 0\right)\right], \tag{6.1}$$

where E_x is the longitudinal component of the energy of the carrier and $n_t^i(E,\mu)$ is the transverse density of states defined in Box 5.2. The problem is presumed to be stationary in order to match with the experimental measuring conditions of usual spin detection experiments. We use the WKB approximation where the transmission function is given by [177]

$$T(E) = e^{\left(\frac{2}{h}\int_{z_L}^{z_R}\sqrt{2\pi m^{\star}\left[\phi_B(z,V_{app})-E\right]}dz\right)}, \tag{6.2}$$

with $m^{\star}$ the electron effective mass, $\phi_B(z, V_{app})$ the barrier profile and x is the space coordinate perpendicular to the barrier plane (Fig. 1(a)), with z_L and z_R the left and right turning points of the barrier (where $\phi_B = E$). The WKB method presents certain limitations regarding the range of energy for the particle and the barrier profile steepness as it assumes that the wave number varies slowly with the position [178]. This hypothesis is satisfied for a large trapezoidal barrier (i.e., when $w\sqrt{\phi_{mean}} \gg 0.4$ nm $eV^{1/2}$, w being the barrier width) [179]. For barriers with a geometry such that a narrowing of the barrier width takes place at higher potential as for a Schottky tunnel barrier, it has been shown that the WKB approximation can predict tunnel current with appreciable accuracy if the barrier lowering is neglected [180, 181].

The spin voltage is obtained by comparing the total current under a given bias V_{app} in the presence of a spin accumulation μ_s in the NM layer, with the total current corresponding to a compensated bias $V_{app} + V_{comp}$ in absence of spin accumulation. The spin voltage V_{spin} equals the voltage V_{comp} for which both total currents are identical:

$$J\left(V_{app}, \mu_s\right) = J\left(V_{app} + V_{comp}, 0\right) \tag{6.3}$$

Indeed, in a typical spin detection experiment with voltage biased detector, the applied voltage is compensated with a voltage V_{spin} to maintain a constant current through the junction irrespective of the level of spin accumulation.

In our formalism, it is assumed that the spin dependence of the carrier transport has two origins. Firstly, the density of carriers with spin up and down in the NM layer will differ even if the DOS is spin-independent. This

effect is due to the presence of a spin accumulation and is expressed in the 2D electron density. Secondly, the spin conductance of the barrier P_G varies with the applied voltage as it depends on the tunnel transmission function and the FM DOS which varies strongly from one material to another. A possibility to include the energy-dependent DOS into the calculation is to consider a parabolic DOS with a shift of energy between spin up and down, giving a spin conductance P_G which decreases with the applied bias similar as shown in Eq. (5.18) of Box 5.2. However, in this work, we intentionally ignore this variation in order to highlight the effect of tunnel barrier on the detected signal. Instead, in Eq. (6.1), the difference of density of state for the FM material is considered as constant and fixed to P_G. Further discussion on the combined effects of tunnel barrier and the energy-dependent FM DOS on the spin detection efficiency can be found in the appendix B.

In this model, it is assumed that a preferential spin population has been generated in the NM via an external mechanism (e.g., spin carriers are electrically injected from another FM contact, or via optical generation), leading to a splitting of the ECP $\mu_s = \mu_+ - \mu_-$ at the B/NM interface (see Fig. 6.1(a)). It is worth noting that, as the amplitude of the spin accumulation induced by the electrical spin injection is proportional to the charge current density flowing through the FM/B/NM junction (see section 5.2.2), no experiment with a bias detector can avoid the presence of a local spin accumulation[1]. This assumption is achieved in order to highlight the increase of the detection efficiency with the applied voltage but without dealing with the unavoidable self-induced spin signal. Later in this chapter, we will discuss the importance of the local spin to ensure a better comparison with experimental results. Finally, it is also considered that the spin accumulation under the detector is homogeneous (i.e. the detector width is much smaller than the diffusion length).

6.2.2 Origin of the non-linear dependence $\mathbf{P_{det}(V_{app})}$

Let's first investigate the case of a rectangular tunnel barrier (B) in a three-layer stack FM/B/NM (Fig. 6.1(a)). Although this model has already been studied previously [176], in the present work the FM quasi Fermi level is set as the reference electrode and the oxide barrier deformation with applied

[1] In the work of Jansen *et al.* [176], it is postulated that a NLSV experiment allows one to only probe the spin accumulation from the injector. However we will show that detection efficiency depends on the spin accumulation under the detector, $\mu_s^{det} \pm \mu_s^{inj}$.

voltage is considered. As for the linear model, we consider that the spin accumulation is homogeneous and generated via an external mechanism. We also assume that the intensity of the spin accumulation is not perturbed by the change of the voltage bias. Indeed, the spin accumulation generated by the detector current as well as the impact of a drift effect in the channel can be excluded by adopting an adequate experimental protocol[2] [182]. As

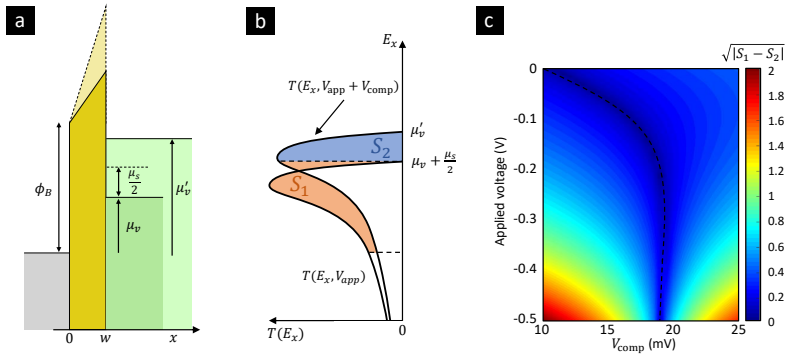

Figure 6.2: *(a) Schematic representation of the barrier deformation for two different values of the applied voltage associated to $\mu_v = -eV_{app}$ (light color) and $\mu'_v = -eV_{app} - eV_{comp}$ (dark color). (b) Sketches of the corresponding transmission function under these conditions: the hatched areas correspond to the two contributions to current variation due to the bias change. S_1 is integrated from $-\infty$ to $\mu_v + \mu_s/2$ and represents the change of current due to the reduction of the barrier permeability compensated by the increase of available carriers with longitudinal energy lower than $\mu_v + \mu_s/2$. In the linear regime of spin detection, $S_1 = 0$. S_2 is integrated from $\mu_v + \mu_s/2$ to μ'_v and corresponds to the gain of current resulting from the enhancement of V_{spin} in comparison with the linear model. (c) The variation of $\sqrt{|S_1 - S_2|}$ with the spin voltage and the applied bias. Along the dashed line, both areas are equals and $V_{comp} = V_{spin}$.*

illustrated in Fig. 6.1(b), the spin detection efficiency P_{det} strongly depends on the junction bias. At 0 V, the spin detection bears the value that is predicted by the linear model. However, when the structure is under a non-zero external bias, P_{det} strongly deviates from the linear model, increasing or decreasing in magnitude for negative bias (spin extraction regime) and positive bias (spin injection regime), respectively. While the general behaviour of P_{det} as function of V_{app} is similar to the results of Jansen *et al.* [176], our findings provide

[2]To ensure that the enhancement of the spin signal is only due to an increase of the spin detection efficiency and not due to drift effect, a two-step measurement is suggested. For each injector bias voltage V_{inj}, the spin signal is detected for a 0 V bias at the detector, $V_{\text{det}} = 0$ V and for $V_{\text{det}} = V_{\text{inj}}$ (this equality has to be corrected if both electrodes have not the same area). This approach allows to avoid spin drift effect in the channel as well as the change of spin accumulation with injection current level.

further unanticipated features. First of all, the non-linear effect does not show a perfect odd symmetry and $P_{det}(V)$ exhibits a non-monotonic dependence (not due to a change of P_G), leading to a maximal detection efficiency for a specific voltage V_{max} . Secondly, the maximal value of P_{det} is not limited to $2P_G$. Moreover, the value depends on the tunnel barrier dimensions as it will be demonstrated below. Finally, P_{det} is very sensitive to the intensity of the spin accumulation in the vicinity of the barrier. Concerning the origin of this non-linearity, it has been previously suggested that the general behaviour of P_{det} as function of V_{app} for both injection and extraction regimes may be related to the steepness of the energy dependence of the barrier transmission function $dT(E)/dE$ [176]. Indeed, the spin accumulation mainly affects the transport of electrons of higher energy. As the bias decreases ($V_{app} < 0$), high energy electrons have an increasingly dominating contribution to the device current as consequence of the exponential energy dependence of $T(E)$, thus leading to a higher impact of the spin accumulation on the carrier transport. On the other hand, for positive biases, the spin accumulation impacts the tail of the transmission function, resulting in a weaker perturbation of the transport through the barrier. Consequently, the more prominent is the slope of $T(E)$, the more important is the non-linearity of the spin detection.

6.2.3 Effect of the barrier deformation

Although the steepness of the transmission function is correlated with the non-linear behaviour of $P_{det}(V_{app})$, it is not directly responsible for the change of spin detection efficiency. In this section, we demonstrate that the enhancement of P_{det} is actually determined by the deformation of the barrier when the device is under an applied bias. As shown in Fig. 6.2(a), a variation of the bias leads to a deformation of the barrier, producing a significant change in the transmission function. For negative biases, the barrier height mean value increases when V_{app} becomes more negative. In the same way, the voltage compensation V_{comp} also triggers a reduction of transmission through the barrier, therefore resulting in a positive reinforcement of this potential compensation, and then a higher P_{det}. In Fig. 6.2(b), we show a sketch of the energy dependence of the transmission function through a barrier under two different biases, respectively $\mu_v = -eV_{app}$ in presence of a spin accumulation μ_s and $\mu'_v = -eV_{app} - eV_{comp}$ in absence of spin accumulation. For the sake of simplicity, we will consider a barrier spin polarization of $P_G = 100\%$ (the effect of the barrier spin polarization at zero bias will be discussed later). Moreover, without loss of generality, calculations are done for a positive spin accumulation. As presented in Fig. 6.1(b), the general

behaviour of $P_{det}(V)$ remains unchanged and the rationale proposed hereafter to explain the enhancement of P_{det} is valid irrespective the value of μ_s: the tunnel current in a spin detection experiment is proportional to the integrated transmission $T(E_x)$ from $E_x = -\infty$ to the value of the ECP associated to the applied bias, at low temperature. By integrating from $-\infty$, we assume that the potential energy of the metal is far below its Fermi level, which is an acceptable approximation as the contribution of low-energy carriers decreases exponentially [178]. The areas resulting from the integration, which determine the spin detection efficiency, are highlighted in the drawing of Fig. 6.2(b). The area S_1 corresponds to the effect of electrons with a longitudinal energy lower than $\mu_v + \mu_s/2$. The area represents the decrease of the tunnel current resulting from the reshaping of the barrier, partially compensated by a gain due to the increase of available carriers (with longitudinal energy between $\mu_v + \mu_s/2$ and $\mu_v + \mu_{comp}$). The area S_2 corresponds to the gain of current due to the increase of the bias (from $|\mu_s/(2e)|$ up to V_{comp}). As a voltage compensation of $|\mu_s/(2e)|$ corresponds to the prediction of the linear model, S_2 directly reflects the non-linearity. As demonstrated in the appendix A.1, S_1 and S_2 may be approximated as follows:

$$S_1 \simeq \int_0^{\mu_v+\mu_s/2} \left[-V_{comp} \frac{df(E_x, V_{app})}{dV} (\mu_v + \mu_{comp} - E_x) - \left(\mu_{comp} - \frac{\mu_s}{2} \right) \right] \times T(E_x, V_{app}) dE_x \tag{6.4}$$

$$S_2 \approx \frac{1}{2} \left(\mu_{comp} - \frac{\mu_s}{2} \right)^2 T(\mu_v, V_{app}) \tag{6.5}$$

where $f(E_x, V_{app})$ is directly related to the transmission function defined in Eq.(5) through $T(E_x, V_{app}) = \exp[f(E_x, V_{app})]$. As we mentioned above, the area S_1 is composed of two terms. The first one is positive (for negative bias) and corresponds to the barrier deformation. The second one is negative when $\mu_{comp} > \mu_s/2$ and reflects the gain of carriers with a high total energy that will participate to the current. The increase of voltage V_{comp} needed to obtain a perfect compensation of S_1 by S_2 is the spin voltage $V_{spin} = (\mu_v - \mu'_v)/(-e)$ that is measured in a spin detection experiment. As soon as $S_2 > 0$, the response becomes non-linear and the spin voltage will become larger than $P_G \mu_s/2$.

In Fig. 6.2(c) we show the difference $|S_1 - S_2|$ for a specific range of bias and voltage compensation. The dashed line denotes the combinations for which both integrals are equals. This line reproduces the behaviour of the spin detection efficiency as a function of the junction voltage, as shown in Fig. 6.1(b,c), with a sharp rise followed by a slow decay of the spin detection

efficiency as voltage increases in absolute value. As a key consequence, we realize that the relative evolutions of S_1 and S_2 ultimately determine P_{det} through a link between the bias and the energy dependencies of the tunnel barrier transmission. In Figs. 6.3(a) and (b), we plot the evolution of both areas, as function of V_{app} and V_{comp}, respectively, offering a graphical resolution of the spin detection experiment. Such a plot represents a powerful tool to track the value of quantities like S_1 and S_2 which are essential to understand the electrical spin detection mechanism in presence of a non-linear transport.

In what follows, we will focus exclusively on negative values of the applied voltage since for this voltage polarity an increase of the spin detection efficiency is expected. First, we observe in Fig. 6.3(a) that, for large polarizations, both integrals are exponential functions of V_{app} with a similar exponential decay, while S_1 deviates abruptly from this decay for weak polarizations until it becomes negative. In Fig. 6.3(b), it is shown that S_2 increases with the compensation voltage when the applied voltage is kept constant while S_1 decreases. Based on these equations and on Fig. 6.3(b), we observe that $S_2(V_{\text{comp}})$ shows a parabolic evolution with a slope determined by the transmission probability of a particle with longitudinal energy $E_{\text{x}} = \mu_{\text{v}} = -eV_{\text{app}}$. The area S_1 decreases with the compensation voltage because the gain of carriers with longitudinal energy below $\mu_{\text{v}} + \dfrac{\mu_{\text{s}}}{2}$ dominates the negative impact of the barrier deformation. Therefore, as shown in Fig. 6.3(c), a variation of the compensation voltage ultimately translates into an offset for S_1 relatively to S_2. In the voltage range where S_1 is rapidly varying with V_{app}, an increase of V_{comp} will decrease S_1 with respect to S_2, combined with a slight increase of the bias voltage for which the intersection $S_1 = S_2$ occurs. On the other hand, for larger bias, a change in V_{comp} will produce a strong increase of the bias at the intersection $S_1 = S_2$, due to the fact that S_1 and S_2 have nearly the same exponential decay. If we refer to Eqs. (A.4) and (A.6), a similar slope in logarithmic scale would be possible only if the transmission function $T(E, V)$ is large enough to dominate the integral in the definition of S_1. Such is the case if the upper integration limit is large enough. Considering the previous explanation, the large increase of spin detection efficiency under a low applied voltage, and the slow decrease at higher bias, are related to the deviation of S_1 from S_2, (i. e., deviation from the exponential nature of $T(E, V)$). The foregoing argumentation allows us to explain the physical origin of the existence of an optimal value V_{max} for the spin detection efficiency, as indicated in Fig. 6.1(b). On the one hand, the range of electrons energy which participate to the current increases with the bias (from 0 to μ_{v}, if we assimilate the Fermi-Dirac distribution to a step-like function, as is the case

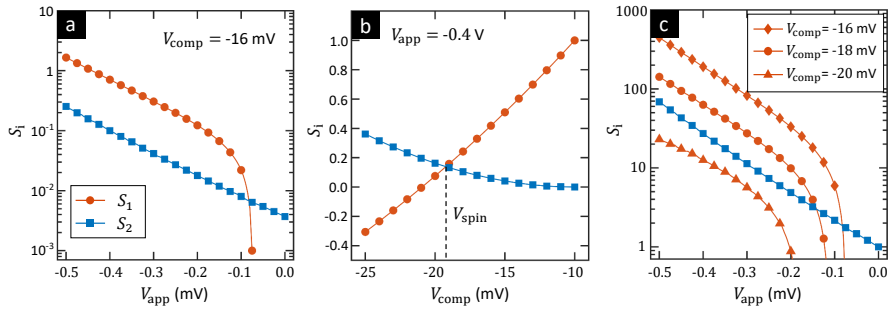

Figure 6.3: *Competition between gain and loss of tunnel current in a spin detection experiment bearing non-linear transport. Evolution of integration areas S_i (index i refers to* 1 *or* 2*) with (a) the applied bias (semi-logarithmic scale) and (b) the compensation voltage (linear scale). (c) Relative shift of S_2 (blue) in comparison to S_1 (orange) for different spin voltages (semi-logarithmic scale).*

for sufficiently low temperatures). The current gain caused by an increase of the spin voltage is then due to electrons of the higher energy levels. On the other hand, the reduction of barrier permeability impacts the transmission probability of all energy levels. When the range of concerned energy levels is narrow enough (V_{app} weak), the transmission function varies slowly with the energy and, subsequently, the participation of low energy electrons is not negligible. Therefore, a higher spin voltage is needed to compensate for the current loss due to the reduction of the tunneling capacity of the electrons for all energy levels. However, as the transmission through the barrier evolves exponentially with the energy, the current due to electrons with energies lower than the NM quasi Fermi level (μ_v in Fig. 6.2(a)) becomes less significant. In addition, this reduction of transmission is progressively compensated by the increase of carriers with high longitudinal energy. For a certain negative bias, the current gain resulting from the spin voltage compensation overcomes the loss due to the barrier deformation, leading to a decrease of P_{det}. The competition between both effects leads to a maximum spin detection efficiency at a bias V_{max}. This result is in agreement with recent experimental observations [176], suggesting that the present description may shed light on how to optimize the spin detection efficiency by tuning the barrier parameters.

Indeed, the energy dependence of the transmission function as well as the way it varies under bias are essential ingredients needed to understand and master the spin detection efficiency. As explained previously, P_{det} is sensitive to the barrier properties (width and height) as well as spin polarity.

Fig. 6.4 summarizes the dependence of P_{det} on the barrier dimensions.

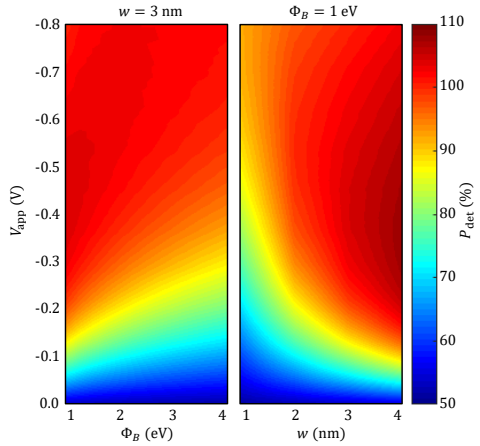

Figure 6.4: *Effect of the variation of a rectangular barrier dimensions on the spin detection efficiency. Results are obtained for* $P_G = 50\%$ *and* $\mu_s = 10$ *meV.*

It can be observed that the variation of the width w and of the height ϕ_B impact oppositely P_{det}. For weak negative biases, the variation of P_{det} with V_{app} is larger for lower and thicker barriers, i. e. for sharper transmission function $T(E)$ slope. It is worth noting that the maximum spin detection efficiency $P_{det}(V_{max})$ also increases for thinner and taller barriers, although the corresponding variations are less significant. This increase is related to a stronger barrier deformation as df/dV increases with w and decreases with ϕ_B (see appendix A.1). On the order hand, as the exponential growth of transmission probability is higher, the voltage at which the high energy electrons dominate the spin detection efficiency is reached at a lower voltage $|V_{max}|$.

6.2.4 Effect of the degeneracy level

Experimental observations in Ref. [176] demonstrated that the spin detection efficiency in a rectangular barrier may overcome the theoretical limit of $2P_G$ to reach spin detection 2.3 times the value predicted by the linear model, and even more when taking into account the drastic reduction of P_G with bias. As the barrier used in that experimental work was rectangular (2 nm-thick MgO [145]), the increase of the spin detection efficiency can not be solely explained by the barrier deformation with the applied bias. Indeed, based on our calculations the spin detection efficiency is expected to be lower than 2 times the barrier spin polarization P_G. However, as shown in the following discussion, the observed excess spin detection can be justified by including

the effect of the band gap in the model. This mechanism is presented here below for a FM/B/SC structure, where SC is a non-magnetic degenerate semiconductor. In order to describe the semiconductor with its band gap, we introduce the parameter ϵ that reflects the degree of degeneracy of the semiconductor. Thus, ϵ represents the difference between the electrochemical potential μ_v and the edge of the conduction band. This effect is included in our calculation by introducing an energy-dependent DOS $N(E)$ in the NM layer given by

$$N(E) = \frac{8\pi\sqrt{2}}{h^3} m^{3/2} \sqrt{E - (\mu_v - \epsilon)}. \tag{6.6}$$

The DOS is therefore null for energies in the band gap, i.e. for $E < \mu_v - \epsilon$. At low temperatures, μ_v corresponds to the maximal occupied energy level in this band. Therefore, the parameter ϵ is linked to the carrier concentration in the conduction band by the Fermi-Dirac distribution. Figure 6.5(a) sketches

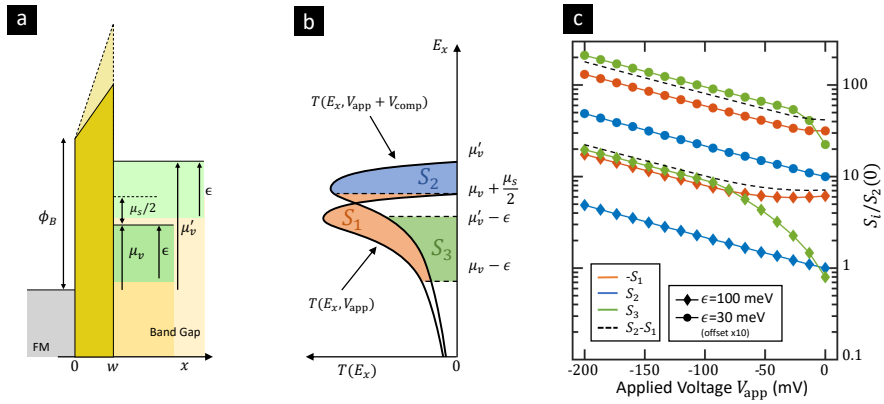

Figure 6.5: *Effect of the SC band gap on the spin detection efficiency. (a) Schematic representation of a FM/B/SC structure for a degenerated SC. The Fermi level is located at an energy value of ϵ above the bottom of the conduction band E_c. The barrier and the E_c edge change as the bias is set to μ_v' (without spin accumulation $\mu_s = 0$ - dark color) instead of μ_v (with spin accumulation - light color). (b) Qualitative sketch of the corresponding transmission function. The S_3 integral is associated to the current loss due to the energy shift of the band gap. (c) Quantitative analysis of the variation of the areas S_1, S_2 and S_3 with the applied junction voltage for $V_{comp} = -20$ mV, $\mu_s = 10$ meV and for two different values of ϵ. Areas (for each value of ϵ) are normalized by $S_1(0)$ and offsetted.*

the basic case of a sandwich structure FM/B/SC, including the band gap. The consequence of the band gap on the transport of electrons through the barrier is visible when the applied electrochemical potential μ_v overcomes the degeneracy level ϵ. In this case, electrons that tunnel from the SC into the

FM have energies limited by the bottom of the conduction band and not by the occupancy in the FM. As a consequence, when a compensation voltage is applied after removing the spin accumulation, the increase of potential from μ_v to μ'_v is accompanied by an increase of the energy level of the bottom of the conduction band. In term of current integration area, it corresponds to a third area S_3 corresponding to a loss of current due to the shift of E_c induced by a change of applied voltage (see Fig. 6.5(b)). It is approximated as

$$S_3 \approx \mu_{comp} \left(\frac{\mu_{comp}}{2} + \epsilon \right) T(\mu_v, V_{app}) \tag{6.7}$$

As demonstrated in appendix A.1, in addition to the area S_3, the insertion of the band gap will modify the definition of S_1

$$\begin{aligned} S_1 &\simeq \left(\frac{\mu_s}{2} + \epsilon \right) \left(\alpha + \beta \frac{df}{dV} + \gamma \frac{df}{dE} \right) T(\mu_v, V_{app}) \\ \alpha &= \left(\frac{\mu_s}{2} - \mu_{comp} \right) \\ \beta &= -V_{comp} \left(\mu_{comp} - \frac{\mu_s}{4} + \frac{\epsilon}{2} \right) \\ \gamma &= \alpha \left(\frac{\mu_s}{2} - \epsilon \right) \end{aligned} \tag{6.8}$$

As μ_{comp} is positive and larger than $\mu_s/2$ (for negative bias at the detector), α is strictly negative. This reflects the gain of tunnel current due to the increase of charge carriers. The second term, $\beta > 0$, is linked to the reduction of the transmission through the barrier and increases with ϵ. The last term, γ, is also positive because $\mu_s/2 < \epsilon$ as the density of spins is limited to the density of carriers. Both S_1 and S_3 contribute to the reduction of the tunnel current and their respective contribution is dependent on the level of degeneracy. As ϵ decreases, S_1 will decrease and S_3 will increase. For weak values of ϵ, $|\alpha| \gg |\beta \frac{df}{dV} + \gamma \frac{df}{dE}|$ and S_1 becomes negative,

$$S_1 \simeq \left(\frac{\mu_s}{2} + \epsilon \right) \left(\frac{\mu_s}{2} - \mu_{comp} \right) T(\mu_v, V_{app}). \tag{6.9}$$

As represented in Fig. 6.5(c), at high applied voltages, all areas follow a similar exponential decay determined by $T(\mu_v, V_{app})$. For lower biases ($\mu_v < \epsilon$), the effect of the band gap shift is limited by the absence of empty states in the FM under the Fermi level, therefore the impact of S_3 on the spin detection efficiency is reduced for highly doped SC (ϵ large). In contrast to that, for a SC with a weaker level of degeneracy, the shift of the band gap will reduce the tunnel current proportionally to the compensation voltage.

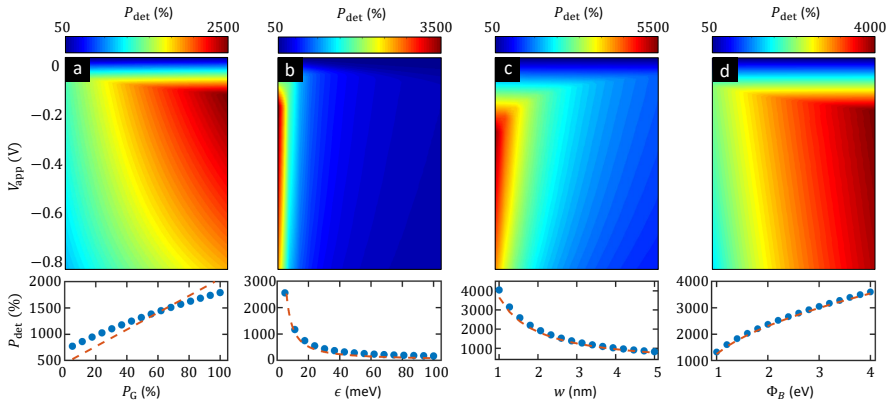

Figure 6.6: *Effect of the variation of a rectangular barrier parameters ((a) P_G, (b) ϵ, (c) w and (d) ϕ_B) on the spin detection efficiency when the band gap affects the tunnel transport. Fixed parameters are $P_G = 50\%$, $\epsilon = 10$ meV, $w = 3$ nm, $\phi_B = 1$ eV. Bottom panels compare results of simulations with the analytical solution from Eq. (6.10) for $V_{app} = -0.8$ V.*

As a consequence, a spin detection efficiency higher than 2 times the barrier polarity is possible. Under the approximation $\mu_v \gg \epsilon > \mu_s/2$, we propose an analytical model to predict the non-linearity of the spin detection efficiency at low temperature. In this case, as demonstrated in the appendix A.1,

$$P_{det} \approx \frac{\frac{\mu_s}{2}\left(1+\frac{\epsilon}{2}\frac{df}{dE}\right)+P_G\left[2\epsilon+\frac{1}{2}\left(\left(\frac{\mu_s}{2}\right)^2-\epsilon^2\right)\right)\frac{df}{dE}\Bigg]}{\epsilon^2\left(\frac{df}{dE}-\frac{1}{e}\frac{df}{dV}\right)} \tag{6.10}$$

where the derivatives of $f(E,V)$ are evaluated for $E=\mu_v$ and $V=V_{app}$. The dependence with respect to the barrier shape and deformation is determined by the partial derivatives of the function $f(E,V)$. As predicted in our simulations, $P_{det} \sim \epsilon^{-1}$. As an indication, in the case of a n-type silicon substrate, a doping level between 5×10^{18} and 1×10^{20} cm^{-3} corresponds to a value of ϵ between 0.01 to 0.1 eV. In Fig. 6.6, the effect of a variation of the barrier height and width is analysed. The presence of the band gap severely modifies the spin detection response due to the barrier deformation under bias (see Fig. 6.4) since now P_{det} decreases with an increase of width and a decrease of the barrier height. We conclude that the impact of S_3 is less important for barriers with a steeper transmission energy dependence. Indeed, for a barrier with a sharp transmission probability, the current due to electrons with a weak energy (range of energy for S_3) is negligible in comparison to those of higher energy (range of S_2). Therefore a reduction of the energy dependence

of the transmission probability acts as an increase of the degeneracy level. Results from Fig. 6.6 show that P_{det} reaches huge values of several thousands of percent while P_G is only 50%. Such a large non-linearity factor may explain the reported deviation of several orders of magnitude between the (linear) theory and the Hanle experiments achieved in 3T devices [130]. While we have focused here exclusively on degenerate semiconductors, we note that the presence of a depletion region at the interface B/SC can influence the detected spin signal due to an additional Schottky barrier with a depletion width depending on the degeneracy level ϵ. For highly doped SC, this barrier is rather thin and therefore, carriers can tunnel through both tunnel barriers [183], resulting in one larger barrier with a non-rectangular shape. Calculations predict that the intensity of spin injection may be enhanced if a two-step tunelling via interfacial states occurs. However this effect is important only for a highly resistive depletion region (which is not the case in our model) [168]. Concerning the spin detection efficiency, a more critical point is to define how the effective barrier height of the depletion layer is changing with the potential (i.e., this change corresponds to the voltage drop at the oxide barrier, which is different from the applied voltage) [184]. Our calculations show that only the latter can impact strongly the spin detection efficiency while P_{det} is only weakly affected by the change of depletion width with doping level. A more in-depth discussion of this point is tackled in appendix B whereas in the next section we focus on the effect of the barrier shape. It is important to stress that our analysis is only dedicated to degenerate SC. For devices with non-degenerate SC where thermionic emission dominates the transport in the depletion region, it was shown that the depletion layer affects drastically the detected spin voltage even if spin signals much higher than the one predicted by the linear model were calculated [185]. To complete the analysis, the intermediary case of moderatly-doped SC should be investigated as unexpected huge spin voltage values were experimentally probed in device where thermally-assisted tunneling occurs [156].

6.2.5 Effect of barrier shape

In a tunnel barrier designed for electrical spin detection, if a negative bias is applied, both the deformation of the barrier transmission and the change of energy range for carriers that participate to the transport are responsible for the observation of a colossal non-linear spin detection efficiency. For rectangular barriers, the second phenomenon seems to dominate, except for highly degenerate SC. The numerical simulations as well as the analytical approach indicate that the non-linearity of the spin detection is sensitive to

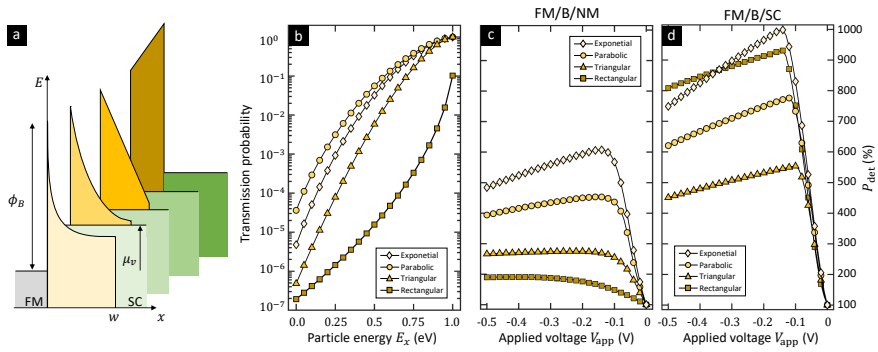

Figure 6.7: *(a) Schematic representation of the different shapes of the interface barrier, from the background to the front: rectangular, triangular, parabolic and exponential evolution of the barrier height with the distance from the SC. (b) Energy dependence of the transmission probability through the barrier. (c,d) Non-linearity of the spin detection efficiency with the applied voltage for tunnel barrier with various shapes. Results depicted on panel (c) show the effect of the barrier shape for a FM/B/NM configuration while those shown on panel (d) focus on the FM/B/SC case. Calculations were performed using $w = 3$ nm (excepted for the rectangular barrier where $w = 2$ nm); $\phi_B = 1$ eV; $P_G = 100\%$; $T = 1$ K; $\epsilon = 50$ meV.*

the steepness of the energy dependence of the transmission function. Steeper transmission may be obtained if a non-rectangular tunnel barrier is used.

At low bias, the behaviour of S_1 is directly dependent on the barrier shape (see appendix A.1). In this section, we quantify the degree of sensitivity of S_1 to that critical feature of the interface. The comparison is made for four different shapes, respectively a rectangular, triangular, parabolic and exponential spatial dependence (see Fig. 6.7(a)). Each barrier is determined by a maximal height ϕ_B, a width w and a level of degeneracy ϵ. The way those parameters influence the shape of the barrier is detailed in the SI. The width associated to each barrier (respectively 2, 3, 3 and 3 nm) has been arbitrarily chosen in order to have transmission probability in the same range of values. The maximal barrier height at zero current is set to $\phi_B = 1$ eV.

The transmission function of each barrier (at $V_{app} = 0$) is plotted in Fig. 6.7(b). As expected, the steepness of the transmission function for electrons with an energy close to the quasi-Fermi level increases from the rectangular barrier to the exponential one.

Spin detection efficiencies under different biases were computed for a constant spin accumulation of $\mu_s = 10$ meV (Fig. 6.7(c,d)). Results are presented for the FM/B/NM and FM/B/SC structures. It allowed us to separate the effect of the barrier shape modification from the effect of the band gap. Indeed, except for the case of the rectangular barrier, a change of ϵ

does lead to a reshaping of the barrier. For the model that does not include the band gap, P_{det} tends to the value of $2P_G$ for a rectangular tunnel barrier, while the maximal spin detection efficiency skyrockets when the barrier height depends on the distance from the FM/B interface. This huge variation of the detected spin signal is explained by two major factors. Firstly, because of their energy-dependent width, non-rectangular barriers have a higher change of transmission probability induced by the voltage compensation. Secondly, as the transmission increases more abruptly with the particle energy, the reduction of available carriers with high longitudinal energy has less impact on the total current (i.e. the negative part of area S_1 is reduced in Fig. 6.2). The higher variation of the transmission probability with the energy is also responsible for the detection efficiency decrease with applied bias, at higher negative voltage. Additional electrons due to the compensation voltage have a higher tunnel probability and therefore compensate more easily the spin accumulation.

For the case of a barrier sandwiched between a FM metal and a degenerate SC, the maximal spin detection efficiency is improved irrespective of the barrier shape. However the rectangular barrier is more sensitive to a change of ϵ since it is correlated with the steepness of the transmission function as explained in section 6.2.4. It is worth noting that a change of ϵ does modify the spin transport through two different mechanisms. First, it reduces the range of energy of carriers involved in the tunnel transport. Secondly, it changes the shape of the barrier, as it could be expected for a Schottky junction. We conclude that the huge spin detection efficiency improvement due to the non-linearity of the tunnel junction arises in every type of barrier, as previously suggested by Jansen *et al*. [176]. However, in contrast to the latter study, we demonstrate that the dominant mechanism varies between an oxide based tunnel junction and a FM/SC contact Schottky junction, which is a nuance that we deem important for understanding the whole picture.

6.3 Influence on electrical spin detection experiments

In this section, we investigate the consequences of the enhancement of the spin detection efficiency on the results obtained using standard experimental methods for spin signal extraction. Firstly, we show that ignoring the dependence of P_{det} with the detector bias may result in a wrong determination of the spin lifetime τ_{sf}. Secondly, we highlight the effect of the local spin signal, i.e. generated by the biased detector junction itself, showing that even a spin-valves experiment does not completely cancel the impact of the local

spin accumulation. Finally, we demonstrate that the spin detection efficiency is less impacting in room temperature experiments.

6.3.1 Dependence on μ_s and spin lifetime

In addition to the correction of the amplitude of the predicted spin accumulation that is formed in the SC, calculations performed in our study suggest that the predicted spin lifetime in Hanle precession experiments needs to be adjusted. Such a correction arises from the fact that, the applied voltage affects the spin detection efficiency, and therefore the spin accumulation μ_s will also induce a deviation of P_{det} from P_G. In the non-linear theory, a higher spin voltage is linked to a higher barrier deformation which, in turn, triggers an increase of the spin voltage. Therefore, the spin voltage is expected to deviate from a linear dependence with the spin accumulation. As shown in Fig. 6.8(a), our results highlight this observation and it is shown that P_{det} is proportional to μ_s [3]. This result obviously impacts the spin diffusion length deduced in Hanle precession measurements. The theory underlying such processes implies that the spin accumulation is destroyed when applying a magnetic field perpendicular to the spin preferential orientation of magnetization (see section 5.3.2). Under a magnetic field B, the spin accumulation $\mu_s(B)$ follows a Lorentzian shape with a maximum value $\mu_s(0)$. From the full width at half maximum (FWHM) of the Lorentzian function, one can deduce the spin lifetime of carriers injected into the NM layer, namely $\tau_{sf} = 2/(\text{FWHM})$. However, this kind of experiment is performed on the spin voltage instead of the spin accumulation.

Therefore, in the non-linear transport regime, a modified Lorentzian distribution is needed. Supposing $P_{det} = \alpha\mu_s + \beta$ for an applied voltage V_{app}, the variation of V_{spin} with the magnetic field becomes

$$V_{spin}(\omega_L) = \frac{\mu_s(0)}{2\,(1+(\omega_L\tau_{sf})^2)}\left[\frac{\alpha\mu_s(0)}{1+(\omega_L\tau_{sf})^2}+\beta\right], \tag{6.11}$$

where ω_L is the Landau frequency, linearly dependent on the magnetic field B. Consequently, we suggest a correction for the equation that allows one to

[3] The deviation of $P_{det}(\mu_s)$ from the linear fit for μ_s close to 0 is due to the definition of P_{det} as the ratio between the spin voltage and half of the spin accumulation, leading to numerical uncertainty. However, our analytical solution shows that the linear approximation for $P_{det}(\mu_s)$ is improved if μ_s and ϵ are small. Moreover, it is worth noting that P_{det} has no physical meaning for the case of zero spin accumulation.

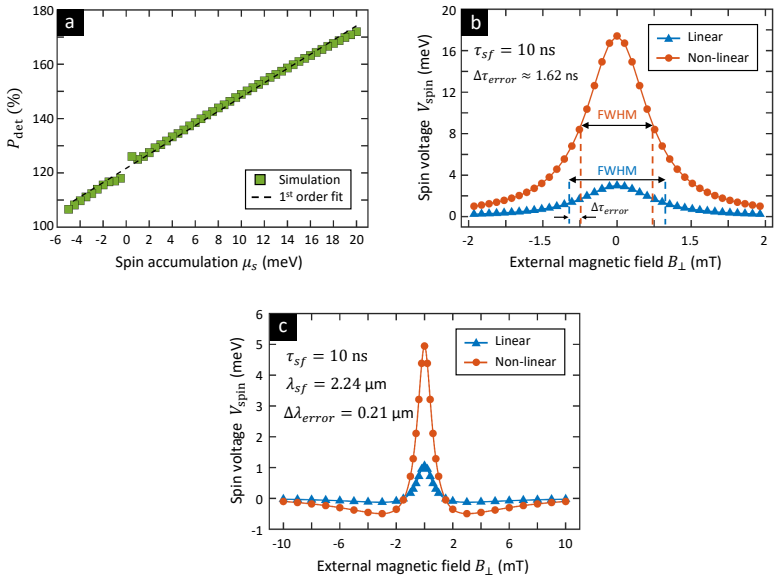

Figure 6.8: *Consequences of the variation of the spin detection efficiency with the spin accumulation. (a) Computed value of P_{det} for different spin accumulations at the vicinity of a tunnel rectangular barrier ($w = 3$ nm; $\phi_B = 1$ eV; $P_G = 30\%$; $V_{app} = -800$ mV; $\epsilon = 50$ meV). (b-c) Numerical simulation of a 3T spin precession experiment (b) and 4T spin diffusion experiment (c). The spin voltage is plotted (based on the linear model and considering the non-linear effect) with the corresponding spin lifetime assuming that both curves are Lorentzian distributions in (b). In (c) the spin diffusion length is extracted by fitting with the analytical solution of the 1D spin diffusion model.*

extract the spin lifetime from Hanle precession measurements,

$$\tau_{sf} = \frac{2}{FWHM}\sqrt{\frac{\sqrt{\beta^2 + 2\alpha\mu_s(0)(\alpha\mu_s(0)+\beta)} - \alpha\mu_s(0)}{\alpha\mu_s(0)+\beta}}. \tag{6.12}$$

According to Eq. (6.10), the ratio between α and β can be simplified to give the following approximation

$$\frac{\alpha\mu_s(0)}{\beta} = \frac{\mu_s}{4P_G\epsilon}. \tag{6.13}$$

As a consequence, the error on the spin lifetime is expected to be negligible for a device with a highly degenerate semiconductor. However for spin accumulation in the range of the degeneracy level, the correction factor may reach a dozen of percent as shown in Fig. 6.8(b). This figure shows the

bell-shape variation of the spin voltage with the perpendicular magnetic field intensity. The spin accumulation is assumed to be 20 meV at zero magnetic field, leading to a detected spin voltage of 3 mV (with $P_G = 30\%$) according to the linear model. The result is compared to the curve obtained for similar $\mu_s(B)$ but including the features of a non-linear transport. While both curves can be accurately fitted using a Lorentzian curve, the extracted value of the spin accumulation and the spin lifetime are not correct due to the non-linearity. An error of 10% for τ_{sf} is probed and the value of μ_s is overestimated by a factor 5 if effects of the non-linearity are neglected.

While having a non-zero voltage is inevitable in the 3T design, the detector is typically free from bias in the non-local spin device. However, as applying a bias to the detector could be used to improve the signal-to-noise ratio in spin precession measurement, it is relevant to evaluate the error for the extraction of the diffusion length. In Fig. 6.8(c), we compare the probed spin signalin the linear condition (no bias voltage to the detector) with the non-linear case. Calculations are achieved by solving the 1D Bloch equation with an added diffusion term that describes spin-diffusion in presence of the spin-orbit coupling and external magnetic field [144]. The spin diffusion coefficient and spin lifetime are materials properties fixed to $D_s = 5$ cm^2/s and $\tau_{sf} = 10$ ns, respectively. The spin diffusion length is extracted by fitting the spin signal with Eq. (5.31). For identical reasons as those presented for the 3T design, the comparison leads to an error close to 10%, which is corrected if the fitting equation is adapted to include the linear dependence between P_{det} and μ_s. It is worth noting that the error due to the non-linearity is directly related to the intensity of the spin accumulation. Indeed, the higher the ratio $\alpha\mu_s/\beta$, the higher the error if a linear model is used.

As these errors are strongly sensitive to the spin tunnel barrier properties as well as to the intensity of the spin accumulation, further calculations have been carried on for different barriers (rectangular and Schottky-like) to evaluate the impact on the determination of the spin lifetime τ_{sf}. In Fig. 6.9(a), the variation of the spin detection efficiency with the spin accumulation for different barrier spin polarization is plotted. As suggested in Eq. (6.10), P_G increases P_{det} with a very small impact on the slope of $P_{det}(\mu_s)$. Therefore, the higher P_G, the smaller the impact of the change of P_{det} with the spin accumulation. This effect is clearly visible in Fig. 6.9(b) and (c) where the relative error on the spin lifetime (for 3T devices) and spin diffusion length (for 4T device) is shown as a function of the barrier spin polarization P_G. Results are

displayed for three kinds of barriers. Typically, for a degeneracy level of 10

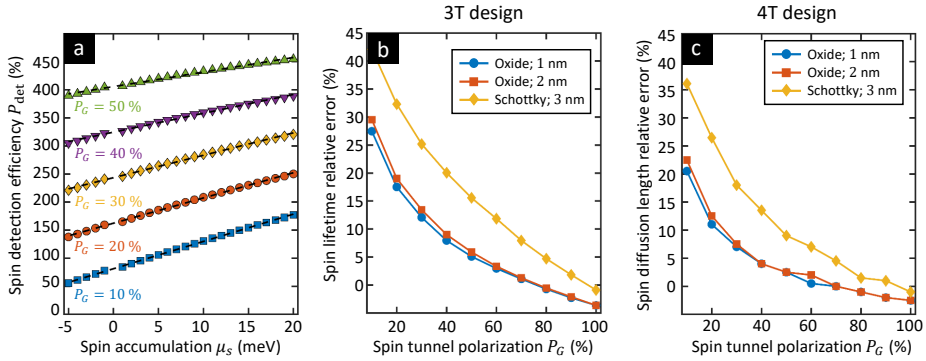

Figure 6.9: *(a) Variation of the spin detection efficiency with the spin accumulation at the detector for different value of P_G. (b-c) Variation of the relative error (%) on (b) the spin lifetime and (c) spin diffusion length when extracted using (b) a typical Lorentzian fit and (c) solution of the 1D bloch function. Calculations have been achieved for $\mu_s(0)$ of 20 meV at the injector, $\epsilon = 50$ meV and $\Phi_B = 1.5$ eV for oxide barrier and 0.6 eV for the Schottky barrier. The detector bias was -0.8 V and -0.5 V, respectively for oxide and Schottky tunnel barrier.*

meV and a spin accumulation of 4 meV, one obtains an error between 0 and 60% depending on the value of P_G. While this effect may appear significant, it depends greatly on the ratio between the spin accumulation at zero magnetic field and the level of degeneracy. The estimation of errors on the spin lifetime based on results currently reported in the literature are minor as the ratio between the detected spin accumulation and the level of degeneracy is low. Indeed, in 3T devices, the detected spin voltage is generally between tenths to hundreds of μV while degeneracy levels are of the order of 10 meV and thus errors are systematically lower than 5% for devices based on oxide tunnel barriers [162, 176, 186, 187]. However, recent advances in fabrication processes progressively lead to an increase of the detected signal by decreasing parasitic effects such as interface roughness [151]. For instance, Spiesser *et al.* achieved a spin detection (without bias detector enhancement) of dozens of mV [145]. In addition, it is worth noting that the error is expected to grow rapidly with the applied current as $\mu_s(0)$ increases while P_G decreases and ϵ remains fixed.

6.3.2 Influence of the local spin accumulation

So far, for the sake of simplicity, we have imposed that the detected spin accumulation only results from a non-local generation. If we now consider the

spin accumulation induced by the charge current flowing through the detector, μ_s^{det}, the change of spin signal with the voltage applied to the detector will be the contribution of both a varying detection efficiency and an increase of the total spin accumulation. In a 3T device, there are only a single FM electrode and the spin accumulation is proportional to the charge current J (assuming a P_J independent of the applied voltage). The spin voltage measured by Hanle precession experiment is expected to increase exponentially with the applied voltage as shown in blue in Fig. 6.10(a), masking the increase of spin detection efficiency. Moreover, as P_{det} is proportional to μ_s, the increase of the spin accumulation with J will lead to a slight increase of the P_{det} which is large enough to compensate the loss of efficiency due to the barrier shape deformation. More importantly, it was postulated in previous work that a

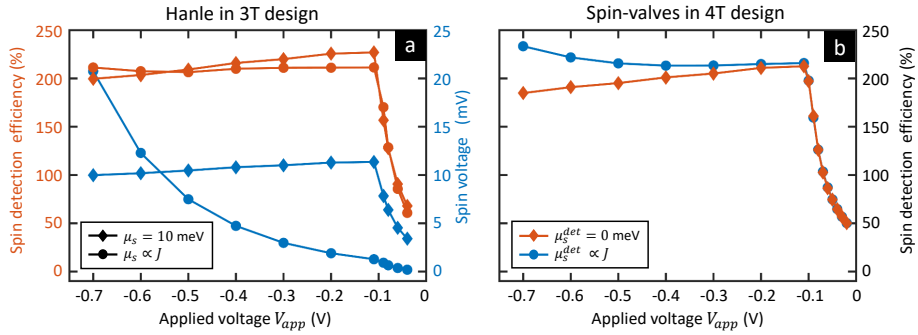

Figure 6.10: *(a) Comparison of the spin detection efficiency and spin voltage as a function of the detector voltage bias in a 3T Hanle device with and without local spin accumulation. (b) Impact of the spin accumulation induced by the detector on a spin-valves (injector magnetization direction is switched).*

spin-valve experiment allows the separation of the signal induced by μ_s^{inj} from the one induced by μ_s^{det} [176]. In Fig. 6.10(b), we show that the spin detection efficiency obtained when a local spin accumulation is taken into account differs from the ideal case. The reasons is attributed to the change of P_{det} with the spin accumulation. In absence of local spin accumulation μ_s^{det} and considering $P_{det} = \alpha\mu_s^{tot} + \beta$, the spin-valves experiment switches the total spin accumulation from μ_s^{inj} to $-\mu_s^{inj}$, leading to a non-local spin voltage

$$V_{spin}^{\uparrow\uparrow} - V_{spin}^{\uparrow\downarrow} = \left(P_{det}^{\uparrow\uparrow} + P_{det}^{\uparrow\downarrow}\right)\frac{\mu_s^{inj}}{2} = \beta\mu_s - _{inj}. \tag{6.14}$$

If $\mu_s^{det} \neq 0$, the spin accumulation varies from $\mu_s^{det} + \mu_s^{inj}$ to $\mu_s^{det} - \mu_s^{inj}$ and the probed signal is

$$V_{spin}^{\uparrow\uparrow} - V_{spin}^{\uparrow\downarrow} = \frac{(\mu_s^{det} + \mu_s^{inj})}{2} P_{det}^{\uparrow\uparrow} - \frac{(\mu_s^{det} - \mu_s^{inj})}{2} P_{det}^{\uparrow\downarrow} = \mu_s^{inj} \left[\beta + 2\mu_s^{det}\right]. \quad (6.15)$$

In Fig. 6.10(b), we simulate the spin-valves experiment for spin injection into a higly degenerated semiconductor layer through a rectangular barrier. Result shows that the presence of a local spin accumulation leads to a higher spin detection efficiency which increases with the bias voltage applied to the detector.

6.3.3 Effect of the temperature

In order to complete our analysis of the non-linearity of the spin detection efficiency under bias, we performed simulations for different temperatures. In Fig. 6.11(a), $P_{det}(V_{app})$ is plotted for a range of temperatures from 1 K to 300 K, and shows that the spin detection is less efficient at high temperatures. This behaviour has been systematically observed in 3T devices in which the reduction of the spin voltage with temperature was attributed to an increase of the thermal noise, an increase of the thermionic emission transport and a simultaneous reduction of the spin polarity of the barrier P_G [145]. As

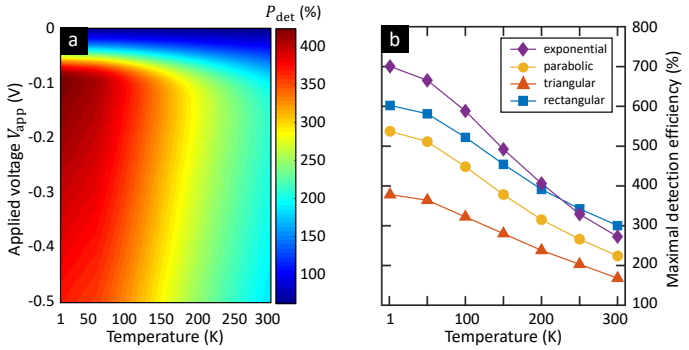

Figure 6.11: *Effect of temperature on the spin detection efficiency. (a) Variation of P_{det} with the temperature and the junction bias. (b) Comparison of temperature effect on different barrier shapes. Calculations were performed using barrier properties as presented in Fig. 6.7. (a) $\epsilon = 50$ meV, $P_G = 50\%$, $\phi_B = 1$ eV and $w = 3$nm; (b) idem except for the rectangular: $w = 2$ nm.*

those effects are not included in the present calculations, the decrease of the detected spin signal with temperature should be ascribed to another phenomenon. More precisely, the temperature dependence of the detection

efficiency can be simply linked to the flattening of the Fermi-Dirac function. As the temperature increases, the Fermi-Dirac distribution deviates from the heaviside step-like function. As a result, carriers with energies slightly higher than the quasi-Fermi level will participate to the charge transport through the tunnel barrier. Consequently, carriers with a higher transmission probability will be involved. Therefore, the gain of current due to the increase of the applied voltage V_{comp} will be increased. This effect may be seen as an increase of the carrier concentration in the conduction band (i.e., an increase of ϵ), which results in a reduction of the spin detection efficiency. The results depicted in Fig. 6.11(b) show the effect of temperature for the different barrier shapes that have been studied in this work. It is noted that the maximal spin detection efficiency decreases for all barrier shapes. At low temperature, the effect is more pronounced for the non-rectangular barrier, suggesting that its origin is related to the steepness of the energy dependence of the transmission function. This outcome tends to confirm the justification that higher temperatures allow to activate carriers with higher energies (associated to higher barrier transmission) and, therefore, that the current is compensated more easily by the increase of the compensation voltage. For barriers with sharp transmission functions, the gain of current due to high energy carriers will obviously be higher.

6.4 Conclusion

In summary, we demonstrate that the non-linearity of the spin detection efficiency under bias results from two different mechanisms: the tunnel barrier deformation and the conduction band shift, leading to spin detection efficiency higher than 10 times the one predicted by the linear model. As a consequence, we emphasize the necessity to take into account the effect of the energy dependence of the tunnelling transmission probability as well as the band gap (even for highly degenerate SC) in the model used to analyse results from local (2T and 3T) spin devices. Effects of the doping level, the barrier shape and the temperature on the magnitude of the probed spin voltage and spin relaxation time have been studied, leading to a better interpretation of spin detection experiments. We believe that our results clarify the complex mechanisms that govern spin injection, transport and detection experiments and help to explain numerous puzzling results reported in the literature.

7

A roadmap for the design of all ferromagnetic four-terminal spin valves and the extraction of spin diffusion length

This chapter is based on the following publication:

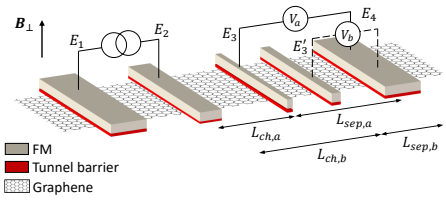

"*Roadmap for the Design of All Ferromagnetic Four-Terminal Spin Valves and the Extraction of Spin Diffusion Length*", E. Fourneau, A. V. Silhanek and N. D. Nguyen,
Phys. Rev. Appl., **15**, 034058 (2021)

7.1 Introduction

The emergence of 2D materials offers new paths for the development of spintronic devices due to their high carrier mobility and low spin-orbit coupling [146, 188]. In graphene, coherent spin transport of tens of micrometers has been reported [189–192]. Currently, efforts are still ongoing to improve the material quality and understand the underlying mechanisms responsible for the spin relaxation phenomenon. Such efforts aim at closing the gap between experimental observations and the theoretical expectation of a 100 μm spin diffusion length [146, 193–195].

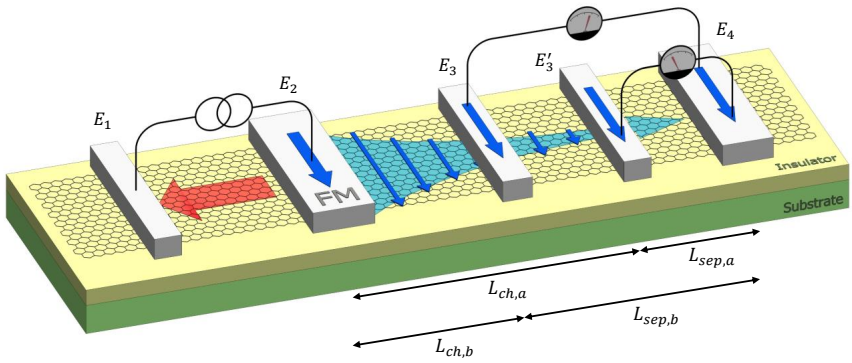

Figure 7.1: *Schematic representation of a typical spin valve with FM contacts, suitable for spin precession experiments, with different channel lengths (e.g. using electrode E_3' instead of E_3) in the same graphene sheet. Two measurement configurations are proposed, with different distances between the detector and the outer electrode.*

Hanle spin precession experiments performed in a four-terminals (4T) non-local spin valves (NLSV) geometry (see Fig. 7.1) provide an elegant method to evaluate the spin transport properties of a material. In such a device, a current is applied between a ferromagnetic (FM) injector (electrode E_2) and the reference electrode (E_1). Consequently, a spin current is generated under those electrodes which also diffuses towards the detection electrode (E_3 or E_3'). Therefore, an electric voltage proportional to the spin accumulation (μ_s) under the detection electrode is probed with respect to the reference electrode (E_4). This electrical potential difference $V_a = V(E_3) - V(E_4)$ is called the spin voltage. In Hanle experiments, the change of spin voltage as function of the intensity of a perpendicular magnetic field ($B_\perp$), which induces precession of spin carriers, is measured. Routinely, experimental results are fitted with the solution of the modified Bloch equations describing

diffusive transport in presence of spin precession, naturally leading to two figures of merit (FoMs) of the spin transport: the spin lifetime τ_{sf} and the spin diffusion coefficient D_s [144, 196]. However, this approach is limited by the following hypotheses:

1. No spin absorption (contact-induced spin relaxation) at any of the contact electrodes,
2. A 1D infinite diffusive medium,
3. An infinite distance between inner (E_2, E_3) and outer (E_1, E_4) electrodes,
4. Zero-width electrodes,
5. Non-magnetic (NM) outer electrodes.

The contact-induced spin relaxation has been widely investigated [197–202] and various models that include the presence of a low resistance injector/detector contacts, as well as the presence of a bias applied to the detector, have been developed [153, 182, 203, 204]. However, limited theoretical efforts have been devoted so far to understand the effect of geometry despite the large variety of designs and layouts implemented in experimental investigations. With a finite diffusive medium, specular reflection is expected at transport material edges, leading to an increase of the spin signal [205] whereas a short separation between FM inner electrodes and NM outer electrodes induces premature relaxation of spin, leading to a decrease of the global spin lifetime when outer electrodes are transparent [206, 207]. In addition, the electrode width can be an important feature when its dimension exceeds several hundreds of nm. Spiesser *et al.* [145] showed that a more accurate theoretical prediction can be obtained by integrating over the injector width[1]. The non-fulfilment of the fifth hypothesis is often observed in spin-valves experiments. In this case, it was shown that the spin signal intensity depends on the magnetic orientation of both inner and outer electrodes [160, 208–212]. However, quite surprinsingly, there is no general study of its impact on the extracted spin transport FoMs in Hanle precession experiments. Only the case of graphene nano-islands smaller than 1 μm was analysed [213].

[1] In their paper, Spiesser *et al.* experimentally tested the correction factor in 4T devices with a highly doped silicon channel. It is acceptable under the hypothesis of a homogeneous current density distribution along the contact width. In 2D materials, a substantial current crowding effect at the injector implies highly inhomogeneous current distributions unless the tunnel barrier is resistive enough, which is indeed the case for the majority of 2D material spin-valves devices reported in the literature.

Moreover, no practical solution (neither for experimental nor modeling purpose) has been suggested to correctly account for the modification introduced by the presence of outer FM electrodes. Addressing the third hypothesis, one can observe that as long as the spin diffusion length ($\lambda_{sf} = \sqrt{\tau_{sf} D_s}$) is short compared to the distance between the contacts ($L_{sep,b}$ in Fig. 7.1), the assumption of infinite distances is acceptable since the injected spin signal vanishes before reaching the outer reference electrodes. For higher values of λ_{sf}, a conflict emerges between the simplification/optimization of fabrication processes and the accuracy on the calculated spin FoMs. Indeed, the most popular method reported in the literature consists in a single lithography step to define multiple contacts followed by the deposition of two successive layers, a tunnel barrier (oxide, h-BN, etc.) and a FM metal. As a consequence, all electrodes can act as a spin injector or detector, with the major benefit of having different channel lengths in a single device depending on the chosen connections. As shown in Fig. 7.1, there are two options for the device configuration: a configuration 'a' with electrode E_3 and a channel length $L_{ch,a}$ and a configuration 'b' using the electrode E_3' and with a larger channel length $L_{ch,b}$. However, the distance between inner and outer electrodes varies as well with the selected set of electrodes ($L_{sep,a}$ and $L_{sep,b}$ respectively), leading to different extracted FoMs as discussed in this chatper.

In light of the results reported previously in the literature, it appears that a great effort has been directed to obtain high quality tunnel barriers, free of pinholes. Fig. 7.2(a) summarizes a selected set of graphene-based spin valves experiments for several barrier materials and sorted in chronological oreder. Whatever material is used as tunnel barrier, a general trend is that the most recent the publication, the higher the reported R parameter, the ratio between contact resistance and channel spin resistance proposed by Popinciuc *et al.* [215] to evaluate the impact of contact-induced spin relaxation. Based on this trend and on the large number of reports addressing the contact spin absorption issue, it is expected that the vast majority of papers to be published will report devices with R parameters respecting the lower bound of 10 suggested by Stecklein *et al.* [201]. On the other hand, all devices reported in Fig. 7.2 make use of FM outer electrodes, except for those with an asterisk [194, 201, 220, 222]. This feature is important because, as shown in panel (b), nearly all devices present a spin diffusion length of the order of the distance between the inner and the outer electrodes, making the comparison between FoMs reported in different papers inaccurate. Experimentally, the position of the outer electrodes is also critical because a short separation distance L_{sep} greatly improves the Hanle measurement quality as it reduces

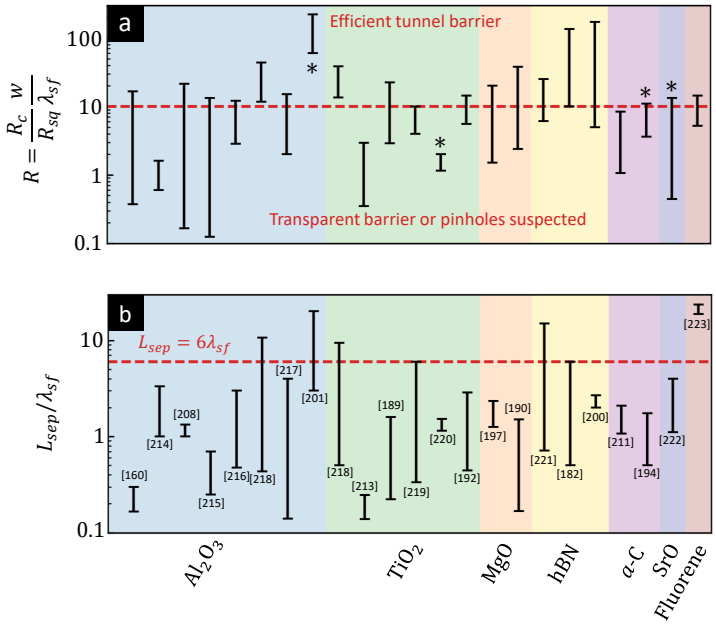

Figure 7.2: *Summary of a representative set of graphene-based NLSV experiments reported in the literature (each bar corresponds to a single scientific publication), for which sufficiently accurate information relative to the contact resistance, dimension and position is provided. The data range is defined by the highest and lowest values reported in the corresponding paper. For each barrier material, results are chronologically sorted. Al_2O_3 [160, 201, 208, 214–218]; TiO_2 [189, 192, 213, 218–220]; MgO [190, 197]; hBN [182, 200, 221]; a-C [194, 211]; SrO [222]; Fluorene [223]. (a) Evaluated $R = R_c W/(R_{sq}\lambda_{sf})$ parameter for different tunnel barrier materials. The red dashed line corresponds to the lower limit for high quality contact suggested in [201]. (b) Ratio of the measured spin diffusion length versus the distance between the inner and the outer detection electrodes. The red dashed line shows the limit of $L_{sep} = 6\lambda_{sf}$ above which negligible effect of outer electrodes is expected.*

drastically the experimental noise. The question naturally arises as how to optimally combine competing requirements from theory and experiment.

In this chapter, the impact of the position and material of the outer electrodes is clarified via spin transport simulations in graphene. More importantly, we deduce a series of criteria that must be fulfilled by nominal spin valve devices. Moreover, an updated version of the solution of the modified classical fit function derived from the solution of the 1D Bloch equations, is proposed in order to include the effect of the distance between electrodes. Even though this work focuses exclusively on graphene as diffusive medium, our findings are applicable to any kind of pseudo-substrate with sufficiently

high quality spin transport properties.

Box 7.1: **Computational details**

Simulations have been performed using the finite element method (FEM) commercial software COMSOL with a geometry based on the cross section of the device presented in Fig. 7.1. The charge current distribution has been calculated via the electrical current (ec) module while spin drift-diffusion equations have been manually included for the three spin directions, as defined by Eq. (5.25). Zero-flux boundary condition has been used at the edge of the graphene ribbon. The charge current is fixed at electrode E_2 while the electrode E_1 is grounded and E_2 and E_3 are floating. Simulations have been performed using the following parameters: the charge current at the injector $I = 5\ \mu$A, the tunnel contact resistivity $\rho_c = 10^{-8}$ Ωm^2 (no spin absorption is expected), the carrier density $n = 3.6 \times 10^{12}$ cm^{-2}, the carrier mobility $\mu_n = eD_s/(k_B T)$, the spin polarization $P = 10\%$, the graphene ribbon width $w = 5\ \mu$m and length $L = 200\ \mu$m (impact of spin carriers reflection at the ribbon edges is negligible), and assuming that the charge and spin diffusion coefficients are equal. Spin figures of merit τ_{sf} and D_s are evaluated based on experimental results reported in [192].

7.2 Spin drift-diffusion and Hanle calculations

To demonstrate the importance of the relative magnetic orientation of the outer contact electrodes, calculations are performed following the method detailed in box 7.1. Solving the spin drift-diffusion equations allows one to obtain the spin accumulation profile along the device, as shown in Fig 7.3(a) for two relative magnetic orientations of the injector (orange and blue curves). We consider first the case where no $B_\perp$ field is applied (solid line). It is worth noting that the model reproduces the diffusive behaviour of the spin injection theory, with an exponential decay depending on the channel properties, leading to no signal far on the right side of the injector (E_2) [123]. On the other hand, the signal never reaches zero on the left side as a specular reflection of the spin is assumed on the graphene edges. Since the reference electrode closest to the injector is also FM, it acts as a second spin source ($\downarrow\uparrow$ configuration - orange line) or a spin well ($\uparrow\uparrow$ configuration - blue line). Indeed, as the charge current direction is opposed for both injection contacts, the anti-parallel configuration leads to an amplified signal. Regarding the detection, as the tunnel contacts are resistive enough to avoid spin absorption, the spin accumulation μ_s is independent of the magnetic orientations and the positions of electrodes E_3 and E_4.

However, the spin-to-charge conversion factor will be positive if the detecting electrode E_3 is parallel to the injecting one and negative if anti-parallel.

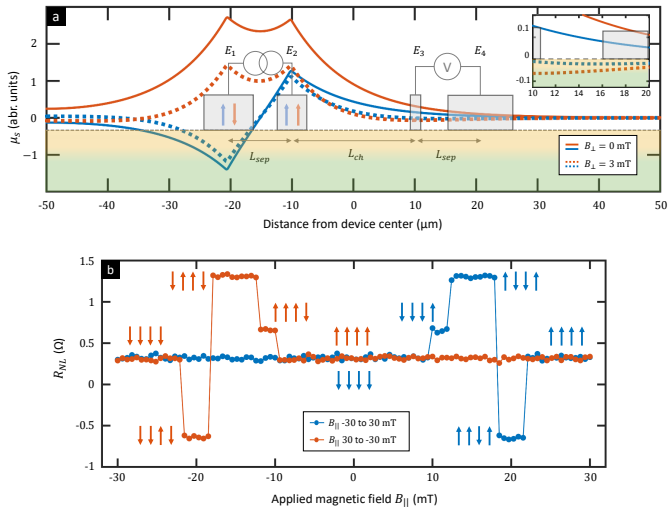

Figure 7.3: *Effect of the magnetic orientation and position of the outer electrodes on the spin FoMs obtained in Hanle precession experiments. (a) Schematic plot of the spin accumulation μ_s with the position in the device for two opposite directions of the injector magnetization (blue and orange curves) and two external $B_\perp$ values (solid and dashed lines). $\uparrow$ and $\downarrow$ refer to in-plane orientation. The inset shows a zoom of the region between E_3 and E_4. (b) Non-local resistance as a function of the in-plane magnetic field in a range covering all possible magnetic moment configurations.*

This is apparent in Fig. 7.3(b), which shows the result of a NLSV measurement as a function of the in-plane magnetic field. A sweeping of the in-plane magnetic field $B_{||}$ is applied in order to change the relative orientation of the electrodes as their coercive field decreases with increasing the contact width. The non-local resistance R_{NL} can assume four different values depending of the relative orientation of the magnetic moments of the electrodes. Fundamentally, the experimental observation of more than 2 values for R_{NL} is a sufficient proof that external electrodes are perturbing the system whereas some uncertainty remains with the observation of only two values of R_{NL}[2].

Practically, a SV signal capturing four different values of resistance offers the possibility to crosscheck the transparency of tunnel contact. This is clearly visible in the work of Kamalakar *et al.* where more than two values of resistance are observed only for highest values of contact resistance [221].

[2]The absence of more than two values for R_{NL} in spin-valves measurements implies that external electrodes have no impact only if one can prove that all configurations have been probed. For example, only two values for R_{NL} will be observed if the external electrodes are narrow enough to sustain large in-plane magnetic field or if each outer electrode has a coercive field similar to the closest inner electrode ($B_c(E_1) \simeq B_c(E_2)$ and $B_c(E_3) \simeq B_c(E_4)$).

Assuming that the spin diffusion length is known (from Hanle experiment), the change of R_{NL} in the detector should scale with the exponential decrease and any deviation can be attributed to unwanted spin absorption by the electrode.

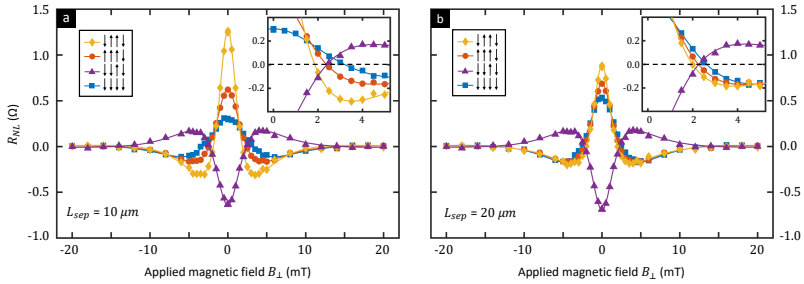

Figure 7.4: *Hanle spin precession simulations for a separation distance L_{sep} of (a) 10 µm and (b) 20 µm. Solid lines are fitting curves while symbols are simulated data. Insets are zooms on the $B_\perp$ range for which the spin signal crosses the zero value.*

7.2.1 Effect of L_{sep} variation

We focus now on the effect of a spin Hanle experiment ($B_\perp \neq 0$). The FoMs cannot be extracted by fitting Hanle spin precession data with the solution of the modified Bloch equation. Indeed, as shown in Fig. 7.4(a), the shape of the Hanle curve depends on the magnetization orientation. In particular, the spin signal vanishes at different values of $B_\perp$ depending on the magnetic configuration of the electrodes. This effect is less pronounced if the distance between inner and outer electrodes increases as shown in panel (b). To understand the origin of the change in the spin Hanle curve, the calculated the spin accumulation profile in presence of a perpendicular magnetic field $B_\perp = 3$ mT (for which the Hanle signal is close to zero in the configuration ↑↑↑↑) is displayed in Fig. 7.3(a) (dashed lines). Under a perpendicular magnetic field, spins diffusing from the injector have a shorter coherence length as $B_\perp$ forces the precession of spins. It results notably in a zero-accumulation point at a specific distance from the injector (see inset for a zoom of the region between the detector and the reference electrode). This position is fully determined by the spin transport properties of the channel and the external magnetic field, and should lead to a root in the Hanle function when the specific position equals the channel length. However, as shown in Fig. 7.4(a), this root varies from one configuration of FM electrodes to the other, as the zero-accumulation situation is obtained

when $\mu_s(E_3) \pm \mu_s(E_4) = 0$, with $'\pm'$ standing for parallel or anti-parallel configurations between E_3 and E_4, respectively. Such a deviation of the experimental data results in an inaccuracy for the estimation of τ_{sf} and D_s when the classical Hanle model is used as fit function. It is worth noting that extracted data look well fitted by the Hanle function in Fig. 7.4(a-b). However, as shown in tab. 7.1, measured spin FoMs from panels (a)

	Theory	↓↓↓↓	↓↓↑↓	↓↑↑↓	↑↑↑↓
τ_{sf} (ns)	3	(a) 1.45	2.5	3.55	2.5
		(b) 2.02	2.95	4.03	2.9
D_s (cm^2/s)	300	280	280	240	280
		250	290	300	280
λ_{sf} (μm)	9.5	6.37	8.37	9.23	8.37
		7.1	9.25	11	9.01
R_{NL} (Ω)	1	0.3	-0.64	1.3	0.64
		0.55	-0.72	0.92	0.71

Table 7.1: *Extracted FoMs from the Hanle curves in Figure 7.4(a) and (b). Depending on the magnetic configuration of the four FM electrodes, the spin diffusion length can vary from 6 to 11 μm.*

and (b) of Fig. 7.4 depart from the theoretical values used as input for calculations. The diffusion length is underestimated whatever the magnetic configuration, except for the (↓↑↑↓) configuration with $L_{sep} = 20$ μm. In this particular magnetic configuration of electrodes, the probed spin signal is maximum and the spin lifetime is overestimated for both values of L_{sep}. In contrast, the detected signal is strongly reduced (less than a third of the theoretical value) when the most common configuration (↓↓↓↓) is used, as both spin sources act oppositely and because the detected voltage is the electrical potential difference between E_3 and E_4 in the parallel configuration. Regarding the diffusion coefficient, the value is also underestimated but, as shown in Fig. 7.5 (see discussion here below), all these results depend strongly and non-monotonically on the separation distance. It is also shown that configurations (↓↑↑↑) and (↑↑↑↓) lead to equivalent spin FoMs even though the spin accumulation profile is different (the small difference is due to artificial measurement noise added to the curve). Indeed, as the key

parameters are the four distances between injection and detection electrodes (E_1-E_3, E_1-E_4, E_2-E_3, E_2-E_4), those two specific configurations probe the same signal as long as the separation distance is the same for the injection and the detection part of the device (i.e. E_1-E_3 is identical to E_2-E_4). The above observations highlight the importance to include the effect of the outer electrodes when the fifth hypothesis is not fulfilled and therefore when the distance E_2-E_3 is no longer the only relevant quantity. In Fig. 7.5, the

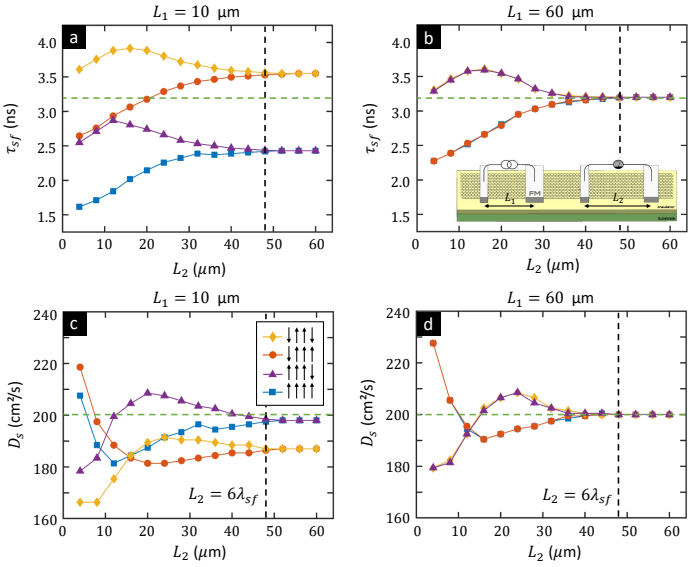

Figure 7.5: *Effect of the separation distance L_2 between the detector and the closest outer electrode for four different relative magnetizations of the electrodes. Panels (a) and (b) show the extracted spin lifetime τ_{sf} as a function of L_2 for $L_1 = 10$ μm and $L_1 = 60$ μm, respectively. Panels (c) and (d) are dedicated to the variation of the spin diffusion coefficient D_s under similar conditions. The horizontal green dashed line refers to the theoretical value of D_s and τ_{sf}. The vertical black dashed lines serve as markers for $L_2 = 6\lambda_{sf}$.*

influence of the separation distance at the detector (L_2) is studied for a fixed separation distance at the injector L_1 (in Fig. 7.4, $L_1 = L_2 = L_{sep}$). The channel length is set to 20 μm. For symmetry reasons, a variation of L_1 with fixed L_2 leads to the same conclusion. Calculations have been performed assuming a spin lifetime of 3.2 ns and a spin diffusion coefficient of 200 cm^2/s which are typical reported values for graphene-based spin experiments [192]. The horizontal dashed lines represent the theoretical values. Results displayed in panels (a) and (c) are obtained using $L_1 = 10$ μm while in (b) and (d) $L_1 = 60$ μm. The careful inspection of Fig. 7.5 leads us to several observations. Firstly,

both the spin lifetime τ_{sf} and the spin diffusion coefficient D_s are incorrectly evaluated, and the variation of the inaccuracy with the separation distance is not monotonic for each configuration. Secondly, the magnitude of the associated error depends strongly on the polarization of the FM electrodes, which confirms the observation made above that the most widely used configuration ($\uparrow\uparrow\uparrow\uparrow$) leads to the largest error for the spin diffusion length. Thirdly, FoMs values do converge towards a common reference when the separation distance is larger than nearly $6\lambda_{sf}$, which is therefore considered as the minimal separation distance to ensure a correct fit. As shown in Fig. 7.2(b), this criterion is rarely met in the literature. It is worth noting that there are two asymptotic values for data in panels (a) and (c), one for each relative polarization of FM electrode with a separation distance fixed to 10 μm. When both separation distances are large enough, τ_{sf} and D_s are correctly extracted using the basic form of the fit function.

7.2.2 Impact of error variation on data interpretation

The two main candidates to explain spin-relaxation in graphene are the Elliot-Yafet (EY) mechanism and the D'yakonov-Perel' (DP) mechanism [146] (see Box 5.3). Theoretically, the first one is characterized by a linear relation between the spin and the quasi-momentum relaxation times $\tau_p \propto \tau_{sf}$, while the second one follows the inverse relation $\tau_p \propto \tau_{sf}^{-1}$. Currently the determination of the dominant spin-relaxation mechanisms remains puzzling. Using NLSV, a common method to distinguish the main relaxation source consists in the evaluation of the reciprocal change in spin lifetime and diffusion coefficient with an external parameter such as the temperature or the charge carrier concentration (via a gate voltage) [216, 224]. However, in presence of four magnetic electrodes with limited L_{sep}, the relation between D_s and τ_{sf} will deviate from its intrinsic behavior due to a change in the FoMs extraction error. To illustrate this effect, simulations have been carried out to map the error when the spin FoMs vary. Values for the ($\uparrow\uparrow\uparrow\uparrow$) configuration with electrodes separated by 10 μm from each other are shown in Fig. 7.6. Panels (a) and (b) show the relative error $(K_{probed} - K_{theo})/K_{theo}$, respectively for $K = D_s$ and $K = \tau_{sf}$. While the error evolves similarly in both panels (negative with τ_{sf} or D_s increase), it is significantly more pronounced for the spin lifetime.

These observations have two consequences on experimental reports as presented in panels (c) and (d). First, there may be a clear misleading dependence of the spin FoMs on the external parameters. For example, the spin diffusion coefficient is theoretically expected to evolve as $D_s \sim \sqrt{n}$ and

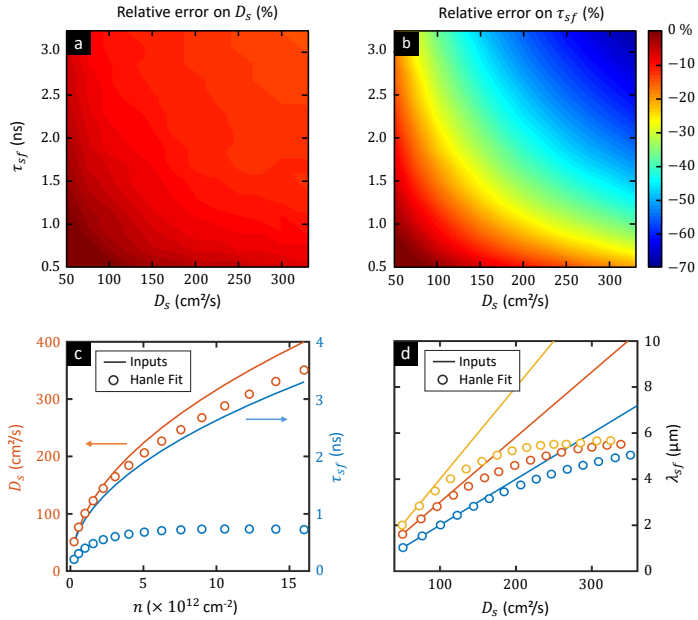

Figure 7.6: *Evolution of the relative error (a) on the spin diffusion constant and (b) on the spin lifetime when using classical Hanle fit curve as a function of τ_{sf} and D_s. (c) Example of deviation of extracted FoMs in carrier density variation experiment. (d) Correlation between λ_{sf} and D_s at different carrier densities. Solid lines are theoretical (exact) values and circles are extracted values using Hanle fit function. Different colors represent different experimental set-ups (different temperatures or substrates for example).*

the same trend is generally observed for τ_{sf} [190, 192, 194]. Therefore, for a device with a short distance between outer and inner electrodes, the extraction error increases when the carrier concentration is experimentally increased to study the change of D_s and τ_{sf}. As a result, experiments will conclude on a different variation of spin FoMs than expected theoretically, such as a spin lifetime independent of or decreasing with, the carrier concentration [192].

As an example, we simulate the deviation from a theoretical $\sqrt{n}$ variation. Results are presented in Fig. 7.6(c). Obviously, similar effects are expected when a temperature variation is considered since it will influence the quasi-momentum scattering time and therefore spin lifetime [188, 219]. Moreover, as the relative error is more pronounced for the spin lifetime, outer electrodes may also lead to incorrect conclusions on the spin relaxation mechanism. As observed in Fig. 7.6(d), a departure from the linear relationship between λ_{sf} and D_s might be attributed to a change of relaxation mechanism while in fact it is due to the proximity of the outer electrodes. Since the question of the

dominant spin relaxation mechanism is still open, it is important to avoid any source of confusion, including the often overlooked impact of the outer electrodes, which could lead to misinterpretation of results. In the following section, we provide clear guidelines for the design of four-terminal NLSV capable of yielding flawless estimations of the spin lifetime and the spin diffusion coefficient without increasing the fabrication process complexity.

7.3 Method for accurate extraction of spin Figures of Merit

In order to correctly extract the spin diffusion length, we propose three methods, each of them with pros and cons. A first way is purely based on the fabrication process. The spin-valves device is designed in such a way that the outer electrodes do not influence the Hanle curve. It can be achieved by ensuring that the distance between the inner and outer FM electrodes is large enough ($L_{sep} > 6\lambda_{sf}$ leads to less than 1% inaccuracy) or by using non-magnetic tunnel outer electrodes. The obvious downside of this approach is the requirement of larger devices for the former or more involved nanofabrication processing for the latter (such as a shadow evaporation process [194] or a double lithography process [201]). An alternative method consists in performing the Hanle experiment in all four different configurations (↑↑↑↑, ↓↑↑↑,↓↑↑↓, ↑↑↑↓) and apply the classical fit method on the mean of those measurements [3]. However, this approach needs specific widths or shapes to obtain a different coercive fields for each FM electrodes. It is worth noting that this method is somehow limited by the fact that it is challenging to ensure an optimal spin injection/detection at each electrode when they are not magnetized at saturation.

The third method consists in magnetizing all electrodes at saturation along the same direction and fit the data with a modified version of equation (24) in [144]. The new fit function sums the contributions of the four injector-detector

[3]Using the four following variations (↑↑↑↑, ↓↑↑↑, ↓↑↑↓ and ↑↑↑↓), we maintain the orientation of the inner electrodes (E_2 and E_3) and take the four different configuration for the outer electrodes (E_1 and E_4). As a result, in half of the configurations E_1 injects spin (↓↑↑↑ and ↓↑↑↓), while it extracts for the two other configurations, leading to spin signal generated with an opposite sign. The same reasoning is used for the sign of the spin voltage detected in E_4. Therefore, only the spin signal generated at E_2 and detected at E_3 remains after calculating the mean of the four signals.

couples in a full FM spin-valve:

$$R_{\mathrm{NL}} = \frac{\pi\hbar^2 v_0^2}{g_s g_v \tilde{\mu}} \frac{P_{\mathrm{G}}^2}{e^2 W} \sqrt{\frac{\tau_{\mathrm{sf}}}{D_{\mathrm{s}}}} \times \left[F\left(L_{\mathrm{ch}}, B\right) - F\left(L_1 + L_{\mathrm{ch}}, B\right) - F\left(L_2 + L_{\mathrm{ch}}, B\right) + F\left(L_1 + L_2 + L_{\mathrm{ch}}, B\right)\right], \tag{7.1}$$

with e the electron charge, $\tilde{\mu}$ the mean electrochemical potential (Appendix C) and W the channel width. The function $F(L, B)$ is given by Eq. (5.27) in section 5.3.2. The major advantage of this approach is that there is no fabrication constraint on the device and therefore, more than four electrodes can be fabricated on one graphene ribbon/flake (for multiple NLSV with varying channel length as shown in Fig. 7.1). It also allows one to work with short separation distances and therefore to drastically reduce the thermal noise. However, as shown in the Tab. 7.1, the non-local resistance is weaker when the configuration $\uparrow\uparrow\uparrow\uparrow$ is used. It is worth noting that in case of NM tunnel contacts for the outer electrodes (see [194]), Eq. (7.1) can be considerably simplified since only $F\left(L_{\mathrm{ch}}, B_{\perp}\right)$ is non zero. Additionally, a solution dealing with NM metallic outer electrodes and FM tunnel inner electrodes does exist [207] and has to be used for devices such as those proposed in references mentioned with an asterisk in Fig 7.2(a). In their work, Vila *et al.* assumed that no spin-sink effect occurs at both injector and detector due to the presence of a pinhole-free tunnel barrier. This hypothesis also holds for Eq. (7.1) as it is claimed by authors of recent experimental publications [192, 194, 225, 226]. Moreover, the application of our method does not require to have electrodes with different widths. Therefore, using only very narrow electrodes, this approach respects or bypasses all hypotheses of Hanle precession equations presented in the introduction, excepted for the condition related to an infinite diffusive medium.

In order to illustrate why it is important to account for the outer electrodes, we apply our observation on data reported in [192] for which geometrical details and magnetic orientation of the four electrodes are given. We compare the classical fit with the one using Eq. (7.1). For the spin lifetime, the value changes from 3 ns using the classical fit to 3.9 ns (increase of 30%). For the spin diffusion coefficient, the value changes from 0.030 to 0.031 m^2/s. It is worth noting that the difference between both fit curves is not visible to the naked eye while the change of values for the spin FoMs is not negligible.

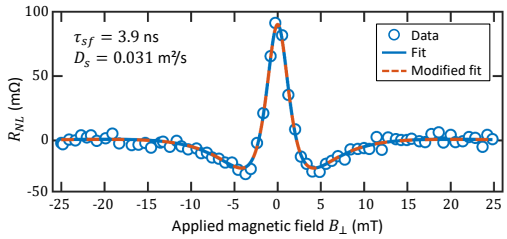

Figure 7.7: *Correction of the spin FoMs extraction using Eq. (7.1) as fit function. Data are from [192].*

7.4 Conclusion

In summary, we demonstrate that the distance between inner and outer electrodes of a spin valve device strongly influences the value of extracted spin FoMs when using a Hanle precession method. Our calculations reveal that a separation distance $L_{\text{sep}} > 6\lambda_{\text{sf}}$ is mandatory to avoid the influence of outer electrodes. As this criterion has been hardly met in previous experimental reports, we anticipate that some conclusions in the literature works concerning the benefits of particular fabrication processes or material choices might need to be revisited in the light of this work. Finally, we demonstrate that working with spin-valves devices with four identical thin ferromagnetic tunnel contacts and a short distance between inner and outer electrodes will simplify the fabrication processes and reduce the experimental noise, while still providing accurate FoMs if a modified version of the Hanle fit equation (Eq. (7.1)) is used.

8

Conclusion and perspectives

Down to the nanoscale, magnetic materials exhibit size-specific properties useful for numerous applications. A host of technologies involving patterned thin ferromagnetic films can be found nowadays and occupy a special place in research and development just as well for industrial purpose as well as for fundamental physics.

In this thesis, we presented the research works on a selection of four micromagnetic devices using both experimental and theoretical approaches. The investigations performed on each magnetic device give rise to conclusive results either by unveiling unexplained physical mechanisms, by pointing out possible weaknesses and suggesting solutions to get around them, or by exploring the perspective of miniaturization towards future on-chip integration.

The first device presented in the dissertation consists in a microscale planar version of a magnetic flux concentrator with a radial permeability largely superior to its angular permeability. Being the first experimental demonstration of an on-chip metasurface for isotropic concentration of magnetic flux, this study contributes to the conception of a future generation of performing concentrator, useful for the detection of weak magnetic fields regardless of the applied direction and to virtually reduce the coercive field of any device placed inside. Our results show that the limits inherent to the thin film aspect ratio of the concentrator can be partially compensated by carefully selecting the geometry (including an optimal thickness), without losing the isotropic response of the metamaterial. This work also demonstrates that calculations assuming a simple linear magnetic response can predict the gain (i.e. the

concentration power) experimentally-observed in the linear regime with fair accuracy. In that way, we provide one step further from the prediction of Prat *et al.* [22, 23, 88] regarding the potential of magnetic metamaterials for low-frequency magnetic applications.

Based on the promising results obtained with pure ferromagnetic flower-shaped concentrator, we foresee multiple tasks for future developments. Firstly, few micrometer-wide devices could be experimentally investigated using anisotropic magnetoresistance sensors in order to confirm the hypothesis of an enhancement of the linear region. Secondly, the fabrication of devices with a drastically reduced angular permeability could by obtained by interleaving superconducting petals coupled with low-temperature experiments. Finally, a study of the high-frequency response of magnetic flux concentrators could open a whole new world of potential technological applications.

In the following chapter, we investigated the unexpected anisotropic magnetoresistance response of conventional permalloy stripes under the influence of an out-of-plane (OOP) magnetic field. Experimental measurements showed an in-plane magnetization reversal process activated even in the absence of any in-plane component of the applied field. Relying on micromagnetic simulations, we demonstrated that a resistance change can be induced by a pefectly OOP field if an important substrate-induced uniaxial anisotropy with a main direction tilted of few degrees from the OOP orientation is present.

Through our experiment, we proved that the switching field (i.e. the magnetic field necessary to trigger a sudden change of resistance) can be controlled by tuning the aspect ratio of the stripe as well as by varying the substrate. So far, the presence of a substrate-induced anisotropy is the only hypothesis suitable to account for the experimental observations. This finding is supported by the fact that the AMR signal is strongly improved when the stripe's thickness is reduced and substantially weakens when flat epitaxial Si substrate is used compared to corrugated LAO substrate.

Our results may eventually be confirmed by future investigations, notably in order to evaluate the intensity of the anisotropy constant of a permalloy thin film deposited on LAO and to explore alternative substrates. This could be done by showing that the critical thickness (for the formation of stripes magnetic domains) of Py is inferior with LAO substrate than with Si. Moreover, by performing oblique material depositions at various incidence angles, one can tune the grain growth direction and therefore the orientation of the substrate-induced anistropy. These results are promising for the design of magnetic sensors and other advanced magnetoresistive devices working with perpendicular magnetic fields by using simple structures. Notably, one

could explore the potential uses to accurately align an out-of-plane external magnetic field, which can not be achieved neither with classical Hall probes, nor with in-plane AMR sensors.

In the second part of this thesis, we presented two works tackling some ambiguous aspects concerning the data interpretation of non-local spin-valves. In the first work, we discussed the importance of the non-linear transport in tunnel contacts on the detected spin signal [153]. On the basis of the recent work of Jansen *et al.* [176], we highlight the origin of the large enhancement of spin detection efficiency (i.e. the probed spin voltage divided by the spin accumulation) observed in spin-valves with a biased tunnel junction at the detector and theoretically investigated the consequences of non-linear transport in different strucutres. Considering the fact that relevant spintronics devices are two-terminal devices, such a spin detection efficiency can not be avoided and therefore, this work provides essential clues to understand the role of the interface on the spin-dependent transport in FM/NM/FM devices. In order to go more deeply in the concept of spin detection efficiency, the study could be extended to alternative transport mechanisms such as thermally-assisted tunneling (more relevant at room temperature) and two-step tunneling. Moreover, the insulator band structure could be taken into account and, since 2D materials are promising candidate for spintronics, exploring the impact of the Dirac cone band structure can eventually lead to unexpected response regarding the spin detection efficiency.

Subsequently, we focused on the discrepancy existing among the experimental measurements of graphene transport properties [227]. More generally, the spin diffusion length probed in 2D materials overcomes largely the state-of-the-art of semiconductor-based devices. In that context, we demonstrated that the outer electrodes, mostly not considered in the literature, play an important role on the intensity of the spin signal but also on the determination of the spin diffusion length. Instead of minimizing the impact of the outer electrodes, we suggest an alternative approach to include their effect by adapting the fit equation and the NLSV design. We believe that our proposition could considerably simplify the experiment as our model does not require non-magnetic materials for outer electrodes (a single lithography process is required), allows shorter distances between the inner and the outer electrodes (reduction of the thermal noise), gives a clear indication of the intensity of contact induced spin-relaxation (through the spin-valves measurement) and finally, it allows the comparison between multiple spin-valves patterned on the same channel.

While the conclusion obtained here can be applied retroactively on results reported in many experimental papers, it is straightforward that a dedicated experimental proof will be required. Finally, it has to be noted that the phenomena investigated in this second part are expected to be more important with the improvement of fabrication processes which will lead to less transparent and more homogeneous tunnel junctions as well as higher spin accumulation and larger diffusion length.

A

Detailed analytical calculations for the spin detection efficiency

A.1 Analytical approach of integration areas S_1, S_2 and S_3

In this section, analytical expressions describing the variation of current through the tunnel barrier are developed. Both cases FM/B/NM and FM/B/SC are addressed by a first order approximation within the non-linear model. The integration area S_1 corresponds to the loss of current through the junction due to the deformation of the tunnel barrier as shown in Fig. A.1(a). This area is given by

$$S_1 = \int_{-\infty}^{\mu_v+\mu_s/2} [(\mu_v + \mu_s/2 - E)\, T(E, V_{app}) - (\mu_v + \mu_{comp} - E)\, T(E, V_{app} + V_{comp})] dE. \tag{A.1}$$

where E is the longitudinal component of the energy of the carrier (in the direction perpendicular to the barrier), μ_s is the spin accumulation and $\mu_v = -eV_{app}$ is the electrochemical potential change due to an applied voltage $-V_{app}$.

In electrical spin detection experiments, the spin voltage (compensation voltage) is of the order of 0.1 to 10 mV, far below the applied voltage V_{app} . If we assume that $|V_{comp}| \ll |V_{app}|$, the transmission function $T(E, V_{app} + V_{comp})$ may be expressed as

$$T(E, V_{app} + V_{comp}) \simeq T(E, V_{app}) + V_{comp} \frac{dT(E, V_{app})}{dV}. \tag{A.2}$$

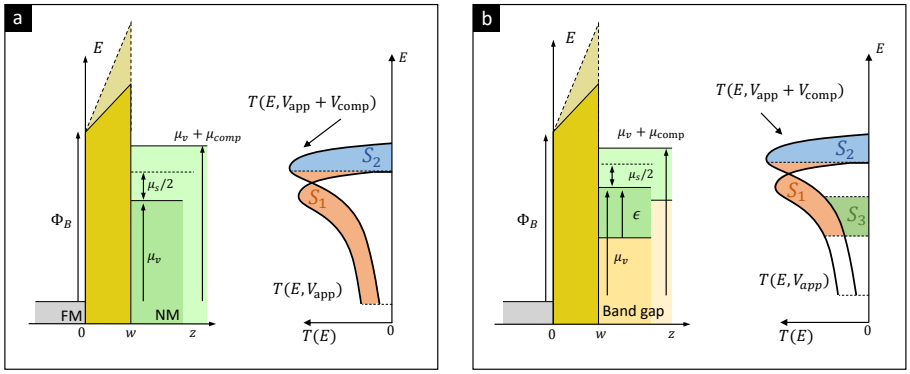

Figure A.1: *(a) Schematic representation of the barrier deformation in a FM/B/NM sandwich for two different values of the applied voltage associated to $\mu_v = -eV_{app}$ (light color) and $\mu_v + \mu_{comp} = -eV_{app} - eV_{comp}$ (dark color). Sketches of the corresponding transmission function under these conditions: the hatched areas correspond to the contributions to current variation due to the bias change. (b) The same schematic representation but in the case of a FM/B/SC sandwich, where the effect of the band gap shift is taken into account.*

Based on the WKB model, the transmission function may be expressed as $T(E,V) = \exp[f(E,V)]$ and the derivative with respect to V is $T(E,V)\frac{df(E,V)}{dV}$. We named $f(E,V)$ the *shape function* as it contains all the information relative to the shape of the barrier and is given by

$$f(E,V) = \int -\frac{2\sqrt{2m}}{\hbar}\sqrt{\Phi(x,V) - E}dx, \tag{A.3}$$

where $\Phi(x,V)$ is the barrier shape, m is the effective mass of the electron and $\hbar$ is the quantum of action. In the case of a rectangular barrier, $\Phi(x,V) = \Phi_B - eV\frac{x}{w}$. As the applied bias V decreases, the barrier height increases and thus $f(E,V)$ decreases, meaning that the derivative of $f(E,V)$ with respect of the variable V is positive, whatever the barrier shape. Finally, the integration area S_1 becomes

$$\begin{aligned} S_1 \simeq & \int_{-\infty}^{0}\left[(\mu_s/2 - \mu_{comp}) - (\mu_v + \mu_{comp})\, V_{comp}\frac{df(E,V_{app})}{dV}\right] T(E,V_{app})dE \\ & + \int_{0}^{\mu_v+\mu_s/2}\left[(\mu_s/2 - \mu_{comp}) - (\mu_v + \mu_{comp} - E)\, V_{comp}\frac{df(E,V_{app})}{dV}\right] T(E,V_{app})dE \end{aligned} \tag{A.4}$$

The first integral deals with the contribution of electrons with lower longitudinal component of their energy whereas the second integral concerns those

electrons with a dominant longitudinal component. For each integral, there are two contributions for the change in the spin current. The term multiplied by the derivative of the f function corresponds to the barrier deformation. The term $(\mu_s/2 - \mu_{comp})$ is directly linked to the change of maximal energy for electrons reflecting the increase of carriers that may participate to the transport. Indeed, this can be visualized as a change of the radius for the Fermi sphere, leading to a spherical shell of constant thickness $(\mu_s/2 - \mu_{comp})$ that is integrated all over the longitudinal component of the energy. S_1 may be simplified furthermore if we include the effect of the band gap (Fig. A.1(b)), assuming that the level of degeneracy is weak (i.e., $\epsilon \ll \mu_v$). Integration limits are $\mu_v - \epsilon$ and $\mu_v + \mu_s/2$. Therefore, only the second integral in Eq. (A.4) is relevant. As the spin accumulation and the degeneracy level are supposed to be weak in comparison to the applied voltage, it is relevant to use the approximation $\lim_{a\to b} \int_a^b f(x)dx = (b-a)f\left((b+a)/2\right)$ in the definition of S_1:

$$\begin{aligned} S_1 &\simeq \left(\frac{\mu_s}{2}+\epsilon\right)\left(\frac{\mu_s}{4}+\frac{\epsilon}{2}\right) T\left(\mu_v+\frac{\mu_s}{4}-\frac{\epsilon}{2}, V_{app}\right) \\ &\quad - \left(\frac{\mu_s}{2}+\epsilon\right)\left(\mu_{comp}-\frac{\mu_s}{4}+\frac{\epsilon}{2}\right) T\left(\mu_v+\frac{\mu_s}{4}-\frac{\epsilon}{2}, V_{app}+V_{comp}\right) \\ &\simeq \left[\frac{\mu_s}{2}-\mu_{comp}-\left(\mu_{comp}-\frac{\mu_s}{4}+\frac{\epsilon}{2}\right) V_{comp}\frac{df}{dV}\right]\left(\frac{\mu_s}{2}+\epsilon\right) T \\ &\quad + \left[\frac{1}{2}\left(\frac{\mu_s}{2}-\epsilon\right)\left(\frac{\mu_s}{2}-\mu_{comp}\right)\frac{df}{dE}\right]\left(\frac{\mu_s}{2}+\epsilon\right) T \end{aligned} \tag{A.5}$$

For practical and aesthetical reasons, $T(\mu_v, V_{app})$, $\frac{df(\mu_v,V_{app})}{dV}$ and $\frac{df(\mu_v,V_{app})}{dE}$ are simply written T, $\frac{df}{dV}$ and $\frac{df}{dE}$.

In this equation, $\frac{df}{dV}$ and $\frac{df}{dE}$ are positive convex growing functions of V_{app} which vary from 3.8 to 4.2 (V^{-1}) and 18.5 to 22 (eV^{-1}) respectively, for a rectangular barrier of height 1 eV and width 2 nm as shown in Fig. A.2. As the shape function varies smoothly with the applied voltage, the slope of S_1 will tend to the slope of the transmission function as long as the condition $\mu_v \gg \mu_{comp}$ is respected.

The second integration area, S_2, corresponds to the gain of current resulting from the non-linearity (Fig. A.1) and is given by the area under the curve $T(E, V_{app} + V_{comp})$ from $\mu_v + \frac{\mu_s}{2}$ to $\mu_v + \mu_{comp}$. The assumption $|V_{comp}| \ll |V_{app}|$

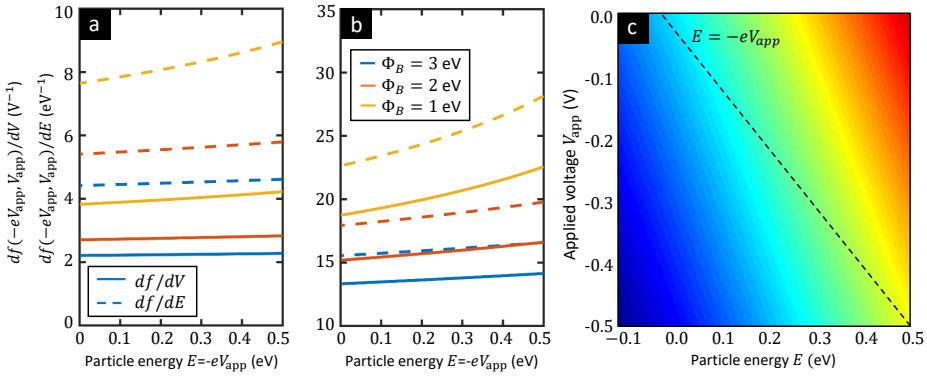

Figure A.2: *Variation of* $\frac{df(E,V)}{dV}$ *and* $\frac{df(E,V)}{dE}$ *with* V_{app} *evaluated in* $E = -eV$*, in case of (a) a rectangular oxide barrier and (b) a Schottky barrier. (c) Calculation of the shape function* $f(E,V)$ *in the case of a rectangular barrier with a width* $w = 2$ *nm and a height* $\Phi_B = 1$ *eV.*

allows us to simplify the integration area S_2.

$$\begin{aligned} S_2 &= \int_{\mu_v+\mu_s/2}^{\mu_v+\mu_{comp}} (\mu_v + \mu_{comp} - E)\, T(E, V_{app} + V_{comp}) dE \\ &\simeq \frac{1}{2}\left(\mu_{comp} - \frac{\mu_s}{2}\right)^2 \left[1 + V_{comp}\frac{df}{dV} + \frac{1}{2}\left(\mu_{comp} + \frac{\mu_s}{2}\right)\frac{df}{dE}\right] T \end{aligned} \tag{A.6}$$

As $V_{comp}\frac{df}{dV} \ll 1$ and $\left(\frac{\mu_s}{4} + \frac{\mu_{comp}}{2}\right)\frac{df}{dE} \ll 1$, S_2 may be expressed as

$$S_2 \simeq \frac{1}{2}\left(\mu_{comp} - \frac{\mu_s}{2}\right)^2 T \tag{A.7}$$

As $S_2(V_{app})$ is proportional to the transmission function, the difference of slope between S_1 and S_2 is due to the derivative of the shape function. This observation explain why the resulting spin detection efficiency P_{det} decreases slightly after reaching its maximal value, but also why it decreases faster for Schottky-like barrier.

The third integration area, S_3, corresponds to a loss of tunnel current due to the reduction of energy range for carriers that participates to the transport (Fig. A.1). It is defined as

$$\begin{aligned} S_3 &= \int_{\mu_v-\epsilon}^{\mu_v+\mu_{comp}-\epsilon} (\mu_v + \mu_{comp} - E)\, T(E, V_{app} + V_{comp}) dE \\ &\simeq \mu_{comp}\left(\frac{\mu_{comp}}{2} + \epsilon\right) T\left(\mu_v - \epsilon + \frac{\mu_{comp}}{2}, V_{app} + V_{comp}\right) \\ &\simeq \mu_{comp}\left(\frac{\mu_{comp}}{2} + \epsilon\right)\left(1 + \left(\frac{\mu_{comp}}{2} - \epsilon\right)\frac{df}{dE} + V_{comp}\frac{df}{dV}\right) T \end{aligned} \tag{A.8}$$

This result may be simplified to yield $S_3 \simeq \mu_{comp}\left(\frac{\mu_{comp}}{2}+\epsilon\right)T$ for weak values of ϵ. Under this assumption, S_3 is larger than S_2. Therefore, a very large V_{comp} is expected (much larger than $\mu_s/2$) and the hypothesis of a low compensation voltage is not fulfilled anymore. Keeping the final form of Eqs. (A.6) and (A.8) allows us to derive an analytic solution for P_{det}.

A.2 Determination of P_{det}

According to our area integration method, the spin voltage is the compensation voltage when $S_1 + S_3 = S_2$. After simplifications, it leads to

$$\frac{1}{2}\left(\frac{\mu_s}{2}+\epsilon\right)^2\left[1+\left(\frac{\mu_s}{2}-\epsilon\right)\frac{df}{dE}\right] = \frac{\epsilon^2}{2}\left[1+\left(\mu_{comp}-\frac{\epsilon}{2}\right)\frac{df}{dE}+V_{comp}\frac{df}{dV}\right] \tag{A.9}$$

$$P_{det} = \frac{\mu_{comp}}{\mu_s/2} \simeq \frac{2\epsilon+\frac{\mu_s}{2}+\frac{1}{2}\left[\frac{\mu_s}{2}\left(\frac{\mu_s}{2}+\epsilon\right)-\epsilon^2\right]\frac{df}{dE}}{\epsilon^2\left(\frac{df}{dE}-\frac{1}{e}\frac{df}{dV}\right)} \tag{A.10}$$

If we consider a barrier with a spin dependent polarization $P_G < 1$, S_1 and S_2 have to be adapted to take into account the transfer of both spin orientations. We have

$$S_i(P_G,\mu_s) = \frac{1+P_G}{2}S_i(1,+\mu_s)+\frac{1-P_G}{2}S_i(1,-\mu_s), \tag{A.11}$$

with $S_i(P_G=1,\mu_s)$ the areas as defined above. It leads to

$$P_{det} = \frac{\mu_{comp}}{\mu_s/2} \simeq \frac{\frac{\mu_s}{2}\left(1+\frac{\epsilon}{2}\frac{df}{dE}\right)+P_G\left[2\epsilon+\frac{1}{2}\left(\left(\frac{\mu_s}{2}\right)^2-\epsilon^2\right)\frac{df}{dE}\right]}{\epsilon^2\left(\frac{df}{dE}-\frac{1}{e}\frac{df}{dV}\right)} \tag{A.12}$$

From this final expression, we observe that P_{det} depends on the barrier shape and deformation but also on the spin accumulation, the barrier spin filtering parameter and the level of degeneracy of the semiconductor. It predicts a linear increase of the spin detection efficiency with the spin accumulation as well as a huge increase for weakly degenerate semiconductor. Effects of the barrier deformation are contained in the derivatives of $f(E,V)$. In the case of a rectangular barrier, those derivatives have analytical solutions

$$\frac{df}{d(E/e)} = \frac{Aw}{-V_{app}}\left(\sqrt{\Phi_B}-\sqrt{\Phi_B+eV_{app}}\right) > 0, \tag{A.13}$$

$$\frac{df}{dV} = \frac{Aw\Phi_B^{3/2}}{3eV_{\text{app}}^2}\left[2\left(\frac{eV_{\text{app}}+\Phi_B}{\Phi_B}\right)^{3/2} - \frac{3eV_{\text{app}}}{\Phi_B} - 2\right] > 0. \tag{A.14}$$

A.3 Barrier shape definition

In this section, the equation used to describe each type of barrier is detailed. For each barrier, the maximal height is Φ_B.

Triangular barrier:

$$\phi(x) = \Phi_B + \frac{x}{w}(\mu_v - \epsilon - \Phi_B) \tag{A.15}$$

Parabolic barrier: Based on the full depletion approximation for a Schottky barrier, the width of the barrier w is defined as the depletion region and $\phi(w) = \phi'(w) = 0$.

$$\phi(x) = (\mu_v - \epsilon - \Phi_B)\left(\frac{x^2}{2w^2} - 2\frac{x}{w}\right) + \Phi_B \tag{A.16}$$

Exponential barrier: The barrier is defined such as the barrier height equals the quasi-Fermi level $\mu_v - \epsilon$ when $x = w$ and $\mu_v - 4\epsilon$ when the barrier width is $2w$

$$\phi(x) = A\exp(\lambda x) + B \tag{A.17}$$

with

$$B = \frac{(\epsilon-\mu_v)^2 + \Phi_B(4\epsilon-\mu_v)}{\mu_v - 2\epsilon - \Phi_B},$$
$$A = \Phi_B - B,$$
$$\lambda = \frac{1}{w}\log\left(\frac{\mu_v - 4\epsilon - B}{\mu_v - 2\epsilon - B}\right).$$

B

Additional results and comments on the spin detection efficiency

B.1 Effect of the energy dependence of P_G

In our work, we have intentionally neglected the variation of P_G with the energy in order to reveal an additional change of spin detection efficiency due to the barrier deformation. In order to complete our analysis, calculations including an energy-dependent P_G have been realized. As the behaviour of the spin conductance polarity is strongly dependent on the FM material used as electrode, we compare the energy-independent case with 2 different models. The first one is evaluated by supposing a square root dependence of the density of states (DOS) with the energy, DOS$\sim \sqrt{E - E_0}$, with a different E_0 for spin up and for spin down [138]. In the second model, $P_G(E) = P_G(0) \exp\left(\frac{-|E-E_F|}{0.55}\right)$, with E_F the Fermi level of FM [185]. Both models are displayed in Fig.B.1(a). Calculations of the spin detection efficiency have been realized using a 2 nm-thick tunnel barrier with a height of 1 eV. Both FM/B/NM and FM/B/SC (ϵ =50 meV) have been evaluated. They are respectively displayed in Fig. B.1(b) and (c). As the spin polarization of high energy electrons is lower than that of low energy electrons, the spin detection efficiency is reduced at higher voltage with a tendency similar to $P_G(-eV_{app})$. As a result, it is a good approximation to express the effect of $P_G(E)$ by multiplying $P_{det}(V_{app})$ evaluated at constant P_G by the ratio $P_G(-eV_{app})/P_G(0)$. This approximation leads to the dashed curves in Fig.B.1(b) and (c). When the NM layer is a degenerate semiconductor, the range of total energy for electrons that participate to the tunnel transport is determined by ϵ. Therefore, the variation of P_G is reduced and the approximation accuracy increases.

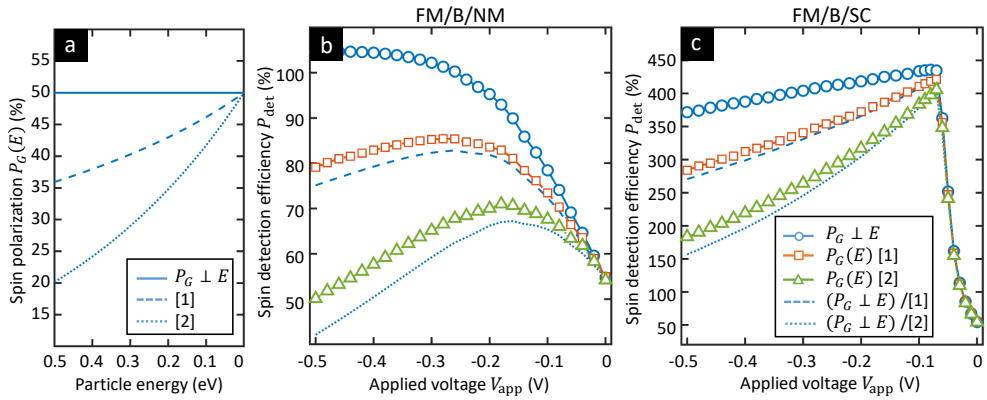

Figure B.1: *(a) Variation of the barrier conductance $P_G(E)$ with the carrier energy based on models proposed by Valenzuela et al. [138] and Jansen et al. [185]. Comparison of the spin detection efficiency for different voltage bias values in a (b) FM/B/NM structure and a (c) FM/B/SC ($\epsilon = 50$ meV), using the three models of $P_G(E)$ displayed in panel (a). In panels (b) and (c), dashed and dotted lines represent the solution with a constant P_G divided by $P_G(-eV_{app})/P_G(0)$ of each model.*

When the effect of the band gap does not impact the spin detection efficiency, this approximation remains acceptable. At low voltage, the range of energy is limited to μ_v and the previous reasoning remains valid. At higher voltage, the range of energy is large and the difference of spin polarization between carriers with high and low energy becomes important. However, this effect is attenuated by the exponential behaviour of the transmission function which limits the impact of carriers with a spin polarization too different from $P_G(\mu_v)$.

B.2 Effect of the thin depletion layer

The depletion region formed at the interface between the semiconductor and the oxide barrier is very thin when the doping concentration is high. Therefore, in contrast to devices with non-degenerate or moderately doped SC, a pure tunnel transport is expected [183]. If we suppose that a direct tunnelling transport is preferred to a two-step tunnelling, the presence of the depletion layer gives a tunnel barrier with a special shape, formed by the combination of an oxide barrier and a Schottky barrier. Indeed, while the barrier width is constant for energies between the maximal barrier height Φ_B and the top of the Schottky barrier Φ_{sc}, it increases rapidly for carriers of lower energy. As we demonstrated in section III.D of the main text, the spin detection is sensitive to the barrier shape and therefore a similar behaviour

is expected in presence of a depletion region. A critical point is to define how the effective barrier height of the depletion layer will change with the applied voltage (i.e., this change corresponds to the voltage drop at the oxide barrier, which is different from the applied voltage). Indeed, the total voltage bias applied to the barrier will be split between the oxide barrier, the depletion region and the SC resistance. Assuming that the bulk resistance is weak compared to the tunnel barrier, the voltage ratio between the depletion and the oxide barrier will be determined by the density of interface states and the resistance of each barrier [184]. To evaluate the impact of the thin depletion region on the spin detection efficiency, calculations have been achieved for different depletion widths (deduced from the doping level ϵ) and a depletion voltage drop ratio from 0 ($V_{\text{dep}} = 0$) to 100% ($V_{\text{dep}} = V_{\text{app}}$). Results are displayed in Fig. B.2(a) for an oxide thickness of 2 nm, $\Phi_B = 1.5$ eV and $\Phi_{sc} = 0.3$ eV. It can be observed that the spin detection efficiency is higher for small value of ϵ (for the same reasons as explained in section III.C), and when the junction resistance is dominated by the oxide barrier. It is worth noting that the voltage drop ratio has been arbitrarily fixed, even if it is influenced by the doping level. In Fig. B.2(b) and (c), we compare the

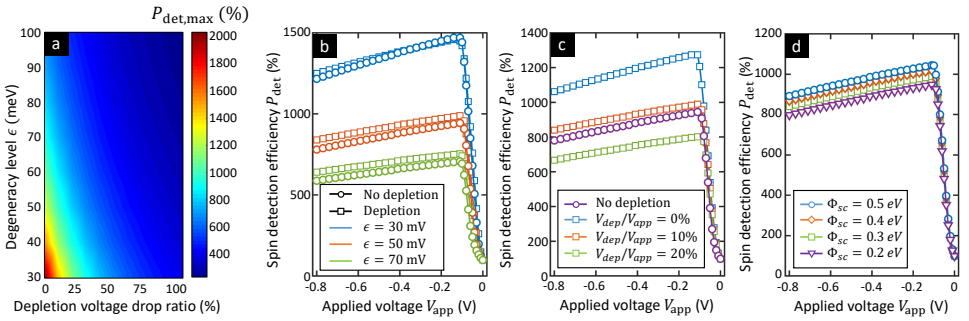

Figure B.2: *Effect of a thin depletion region on the spin detection efficiency. (a) Variation of the maximal spin detection efficiency with the level of degeneracy and the relative contribution of the depletion region to the total voltage drop. (b-d) Effect of a thin depletion region on $P_{det}(V)$ for different (a) doping levels, (b) drop of voltage at the depletion region and (c) depletion barrier height values.*

spin detection efficiency with the applied voltage in presence of a depletion region with the case of a pure oxide barrier. In Fig B.2(b), the comparison is achieved for a depletion voltage drop ratio of 10% (for highly doped SC, the resistance of the tunnel barrier dominates the total junction resistance) and for three different doping levels. We observe that the increase of the spin detection efficiency due to the band gap shift effect is present irrespective

to the presence of the depletion layer. On the other hand, P_{det} is strongly impacted by the voltage drop ratio. Indeed, as shown in Fig. B.2(c), the higher the depletion voltage drop, the lower the spin detection efficiency. When the bias is almost entirely applied to the oxide tunnel barrier, the Schottky barrier is shifted upwards with the applied voltage and its deformation is negligible. Therefore, the depletion layer simply makes the transmission function more peaked, leading to a higher spin detection efficiency (see Fig. 6 of the main text). However, if the voltage drop at the depletion layer is not negligible, the spin detection efficiency is affected by the deformation of the depletion region due to the voltage compensation, leading to a global increase of the tunnel transmission probability which results in a decrease of the detection efficiency. Finally, we investigated the effect of the Schottky barrier height Φ_{sc}. As shown in figure B.2(d), the detected spin signal is slightly influenced by the Φ_{sc}. It supports the conclusion that the shape of the depletion region does not affect strongly the spin detection efficiency.

C

Deriving the spin voltage from spin carrier density in graphene

The spin voltage $V_{spin} = \frac{P_G}{2e}\mu_s$ is deduced from the spin-dependent carrier concentration in the graphene sheet by integrating of the product of the density of states (DOS) by the Fermi-Dirac distribution $f(E-\mu_\pm)$, where $\mu_\pm$ is the spin dependent electrochemical potential. Assuming n-type conductivity in graphene and integrating from 0 to ∞, the following solution can be found with a second-order logarithm integral [228]:

$$\begin{aligned} n_\pm =& \frac{1}{2}\int_0^\infty N(E) f(E-\mu_\pm) dE \\ =& -\frac{1}{\pi}\left(\frac{k_B T}{\hbar v_0}\right)^2 Li_2\left(-e^{\frac{\mu_\pm}{k_B T}}\right). \end{aligned} \tag{C.1}$$

Assuming that $\mu_s = \mu_+ - \mu_- \ll \tilde{\mu} = \mu_+ + \mu_-$ and with Taylor second order approximation, we obtain the linear relation between the spin concentration n_s and the spin accumulation μ_s:

$$n_s = n_+ - n_- \simeq \frac{g_s g_v}{4\pi\hbar^2 v_0^2}\left[\ln(2) k_B T + \frac{\tilde{\mu}}{2}\right]\mu_s \tag{C.2}$$

in case of moderate carrier concentration ($\mu_\pm < 5 k_B T$), whereas for high carrier concentration ($\mu \gg k_B T$),

$$n_s = n_+ - n_- \simeq g_s g_v \frac{\tilde{\mu}}{4\pi\hbar^2 v_0^2}\mu_s. \tag{C.3}$$

It is worth noting that the density of state at the Fermi level at low temperature ($E_F \simeq \tilde{\mu}$), is given by

$$N(E_F) = g_s g_v \frac{\tilde{\mu}}{2\pi\hbar^2 v_0^2}, \tag{C.4}$$

and by combining Eq. (C.3) and (C.4), it leads to

$$V_{\text{spin}} = P_{\text{G}} \frac{\mu_{\text{s}}}{2e} = P_{\text{G}} n_{\text{s}} \frac{1}{eN(E_{\text{F}})}, \tag{C.5}$$

which is equivalent to Eq. (5.31).

Finally, using the same reasoning but calculating the $n_+ + n_-$, we approximate the mean ECP $\tilde{\mu}$ in terms of the temperature and the total carrier concentration (experimentally measurable values):

$$\tilde{\mu} = k_{\text{B}} T \sqrt{\frac{2\pi}{g_{\text{s}} g_{\text{v}}} \left(\frac{\hbar v_0}{k_{\text{B}} T} \right)^2 n - \frac{\pi}{12}}. \tag{C.6}$$

Bibliography

[1] J. M. Coey, "A brief history of magnetism", in *Magnetism and magnetic materials* (Cambridge university press, 2010) Chap. 1.

[2] D. Sander, S. O. Valenzuela, D. Makarov, C. Marrows, E. Fullerton, P. Fischer, J. McCord, P. Vavassori, S. Mangin, P. Pirro, et al., "The 2017 magnetism roadmap", J. Phys. D **50**, 363001 (2017).

[3] E. Y. Vedmedenko, R. K. Kawakami, D. D. Sheka, P. Gambardella, A. Kirilyuk, A. Hirohata, C. Binek, O. Chubykalo-Fesenko, S. Sanvito, B. J. Kirby, et al., "The 2020 magnetism roadmap", J. Phys. D **53**, 453001 (2020).

[4] L. D. Landau and E. Lifshitz, "On the theory of the dispersion of magnetic permeability in ferromagnetic bodies", Phys. Zeitsch. der Sow. **8**, 153 (1935).

[5] P. Weiss, "L'hypothèse du champ moléculaire et la propriété ferromagnétique", J. Phys. Theor. Appl. **6**, 661 (1907).

[6] F. Bitter, "On inhomogeneities in the magnetization of ferromagnetic materials", Phys. Rev. **38**, 1903 (1931).

[7] L. Tonks and K. J. Sixtus, "Propagation of large barkhausen discontinuities IV.[1] regions of reversed magnetization", Phys. Rev. **43**, 931 (1933).

[8] W. Brown, *Micromagnetics, by w.f. brown* (Interscience, 1963).

[9] J. Leliaert, M. Dvornik, J. Mulkers, J. De Clercq, M. Milošević, and B. Van Waeyenberge, "Fast micromagnetic simulations on gpu—recent advances made with", J. Phys. D **51**, 123002 (2018).

[10] A. Vansteenkiste, J. Leliaert, M. Dvornik, M. Helsen, F. Garcia-Sanchez, and B. Van Waeyenberge, "The design and verification of mumax3", AIP Adv. **4**, 107133 (2014).

[11] M. Donahue, *Oommf user's guide, version 1.0*, en, 1999-09-01 1999.

[12] M. E. Schabes, "Micromagnetic simulations for terabit/in2 head/media systems", J. Magn. Magn. Mater. **320**, 2880 (2008).

[13] M. Iwayama, T. Kai, M. Nakayama, H. Aikawa, Y. Asao, T. Kajiyama, S. Ikegawa, H. Yoda, and A. Nitayama, "Reduction of switching current distribution in spin transfer magnetic random access memories", J. Appl. Phys. **103**, 07A720 (2008).

[14] S. S. Parkin, M. Hayashi, and L. Thomas, "Magnetic domain-wall racetrack memory", Science **320**, 190 (2008).

[15] F. Maspero, S. Cuccurullo, D. Mungpara, A. Schwarz, and R. Bertacco, "Impact of magnetic domains on magnetic flux concentrators", J. Magn. Magn. Mater. **535**, 168072 (2021).

[16] Y. Huang, W. Kang, X. Zhang, Y. Zhou, and W. Zhao, "Magnetic skyrmion-based synaptic devices", Nanotechnology **28**, 08LT02 (2017).

[17] C. Back, V. Cros, H. Ebert, K. Everschor-Sitte, A. Fert, M. Garst, T. Ma, S. Mankovsky, T. Monchesky, M. Mostovoy, et al., "The 2020 skyrmionics roadmap", J. Phys. D **53**, 363001 (2020).

[18] M. Dvornik, Y. Au, and V. Kruglyak, "Micromagnetic simulations in magnonics", in *Magnonics* (Springer, 2013), pp. 101–115.

[19] A. Barman, G. Gubbiotti, S. Ladak, A. O. Adeyeye, M. Krawczyk, J. Gräfe, C. Adelmann, S. Cotofana, A. Naeemi, V. I. Vasyuchka, et al., "The 2021 magnonics roadmap", J. Phys. Condens. Matter. **33**, 413001 (2021).

[20] N. I. Zheludev and Y. S. Kivshar, "From metamaterials to metadevices", Nat. Mater. **11**, 917 (2012).

[21] C. Navau, J. Prat-Camps, and A. Sanchez, "Magnetic energy harvesting and concentration at a distance by transformation optics", Phys. Rev. Lett. **109**, 263903 (2012).

[22] J. Prat-Camps, A. Sanchez, and C. Navau, "Superconductor–ferromagnetic metamaterials for magnetic cloaking and concentration", Supercond Sci. Technol. **26**, 074001 (2013).

[23] J. Prat-Camps, C. Navau, and A. Sanchez, "Quasistatic metamaterials: magnetic coupling enhancement by effective space cancellation", Adv. Mater. **28**, 4898 (2016).

[24] R. Mach-Batlle, A. Parra, S. Laut, N. Del-Valle, C. Navau, and A. Sanchez, "Magnetic illusion: transforming a magnetic object into another object by negative permeability", Phys. Rev. Appl. **9**, 034007 (2018).

[25] S. Bader and S. Parkin, "Spintronics", Annu. Rev. Condens. Matter Phys. **1**, 71 (2010).

[26] D. D. Awschalom and M. E. Flatté, "Challenges for semiconductor spintronics", Nat. Phys. **3**, 153 (2007).

[27] N. F. Mott, "The electrical conductivity of transition metals", Proc. R. Soc. A: Math. Phys. Eng. Sci. **153**, 699 (1936).

[28] M. N. Baibich, J. M. Broto, A. Fert, F. N. Van Dau, F. Petroff, P. Etienne, G. Creuzet, A. Friederich, and J. Chazelas, "Giant magnetoresistance of (001) fe/(001) cr magnetic superlattices", Phys. Rev. Lett. **61**, 2472 (1988).

[29] G. Binasch, P. Grünberg, F. Saurenbach, and W. Zinn, "Enhanced magnetoresistance in layered magnetic structures with antiferromagnetic interlayer exchange", Phys. Rev. B **39**, 4828 (1989).

[30] S. Datta and B. Das, "Electronic analog of the electro-optic modulator", Appl. Phys. Lett. **56**, 665 (1990).

[31] C. Chappert, A. Fert, and F. N. Van Dau, "The emergence of spin electronics in data storage", Nat. Mater. **6**, 813 (2007).

[32] S. Maekawa, S. O. Valenzuela, E. Saitoh, and T. Kimura, "Spin current", in *Spin current (2nd ed.) - part i*, Vol. 22 (Oxford University Press, 2017).

[33] I. Žutić and H. Dery, "Taming spin currents", Nat. Mater. **10**, 647 (2011).

[34] A. Slachter, F. L. Bakker, J.-P. Adam, and B. J. van Wees, "Thermally driven spin injection from a ferromagnet into a non-magnetic metal", **6**, 879 (2010).

[35] E. C. Ahn, "2d materials for spintronic devices", NPJ 2D Mater. Appl. **4**, 1 (2020).

[36] J. Panda, M. Ramu, O. Karis, T. Sarkar, and M. V. Kamalakar, "Ultimate spin currents in commercial chemical vapor deposited graphene", ACS nano **14**, 12771 (2020).

[37] J. M. Coey, "Magnetism of electrons", in *Magnetism and magnetic materials* (Cambridge university press, 2010) Chap. 3.

[38] J. M. Coey, "Magnetism of localized electrons on the atom", in *Magnetism and magnetic materials* (Cambridge university press, 2010) Chap. 4.

[39] C. Kittel and P. McEuen, "Ferromagnetism and antiferromagnetism", in *Introduction to solid state physics* (John Wiley & Sons, 2005).

[40] M. E. McHenry and D. E. Laughlin, "Magnetic properties of metals and alloys", in *Physical metallurgy* (Elsevier, 2014), pp. 1881–2008.

[41] S. Blundell, "Interactions", in *Magnetism in condensed matter* (American Association of Physics Teachers, 2003) Chap. 4.

[42] S. Blundell, "Quantum and atomic physics", in *Magnetism in condensed matter* (American Association of Physics Teachers, 2003) Chap. C.

[43] F. Fiorillo, C. Appino, and M. Pasquale, "Hysteresis in magnetic materials", in *Science of hysteresis*, edited by G. Bertotti and I. Mayergoyz (Elsevier, London, 2005) Chap. 3, pp. 1–190.

[44] A. Hubert and R. Schäfer, *Magnetic domains: the analysis of magnetic microstructures* (Springer Science & Business Media, 2008).

[45] S. Blundell, "Domains", in *Magnetism in condensed matter* (American Association of Physics Teachers, 2003) Chap. 6.

[46] L. Landau and E. Lifshitz, "On the theory of the dispersion of magnetic permeability in ferromagnetic bodies", in *Perspectives in theoretical physics* (Elsevier, 1992), pp. 51–65.

[47] J. M. Coey, "Magnetostatics", in *Magnetism and magnetic materials* (Cambridge university press, 2010) Chap. 2.

[48] S. Middelhoek, "Domain walls in thin ni–fe films", J. Appl. Phys. **34**, 1054 (1963).

[49] J. Osborn, "Demagnetizing factors of the general ellipsoid", Phys. Rev **67**, 351 (1945).

[50] E. Huber Jr, D. Smith, and J. Goodenough, "Domain-wall structure in permalloy films", J. Appl. Phys. **29**, 294 (1958).

[51] R. Skomski, P. Manchanda, and A. Kashyap, "Anisotropy and crystal field", in *Handbook of magnetism and magnetic materials*, edited by J. M. D. Coey and S. S. Parkin (Springer International Publishing, 2021), pp. 103–185.

[52] R. Victora and J. MacLaren, "Theory of magnetic interface anisotropy", Phys. Rev. B **47**, 11583 (1993).

[53] M. Johnson, P. Bloemen, F. Den Broeder, and J. De Vries, "Magnetic anisotropy in metallic multilayers", Rep. Prog. Phys. **59**, 1409 (1996).

[54] D. Sander, "The magnetic anisotropy and spin reorientation of nanostructures and nanoscale films", J. Phys. Condens. Matter. **16**, R603 (2004).

[55] A. Aharoni, "Incoherent magnetization reversals in elongated particles", J. Magn. Magn. Mater. **196**, 786 (1999).

[56] T. Schrefl, J. Fidler, J. Chapman, and K. Kirk, "Micromagnetic simulation of domain structures in patterned magnetic tunnel junctions", J. Appl. Phys. **89**, 7000 (2001).

[57] J. M. Coey, "Micromagnetism, domains and hysteresis", in *Magnetism and magnetic materials* (Cambridge university press, 2010) Chap. 7.

[58] W. F. Brown Jr, "Virtues and weaknesses of the domain concept", Rev. Mod. Phys. **17**, 15 (1945).

[59] S. Yang and J. Erskine, "Domain wall dynamics and barkhausen jumps in thin-film permalloy microstructures", Phys. Rev. B **72**, 064433 (2005).

[60] G. Binnig, C. F. Quate, and C. Gerber, "Atomic force microscope", Phys. Rev. Lett. **56**, 930 (1986).

[61] F. J. Giessibl, "Advances in atomic force microscopy", Rev. Mod. Phys. **75**, 949 (2003).

[62] D. Rugar and P. Hansma, "Atomic force microscopy", Physics today **43**, 23 (1990).

[63] D. Rugar, H. Mamin, P. Guethner, S. Lambert, J. Stern, I. McFadyen, and T. Yogi, "Magnetic force microscopy: general principles and application to longitudinal recording media", J. Appl. Phys. **68**, 1169 (1990).

[64] A. Wadas and P. Grütter, "Theoretical approach to magnetic force microscopy", Phys. Rev. B **39**, 12013 (1989).

[65] J. M. Coey, "Experimental methods", in *Magnetism and magnetic materials* (Cambridge university press, 2010) Chap. 10.

[66] M. Koblischka, U. Hartmann, and T. Sulzbach, "Improving the lateral resolution of the mfm technique to the 10nm range", J. Magn. Magn. Mater. **272**, 2138 (2004).

[67] J. Garcıa, A. Thiaville, J. Miltat, K. Kirk, J. Chapman, and F. Alouges, "Quantitative interpretation of magnetic force microscopy images from soft patterned elements", Appl. Phys. Lett. **79**, 656 (2001).

[68] T. Häberle, F. Haering, H. Pfeifer, L. Han, B. Kuerbanjiang, U. Wiedwald, U. Herr, and B. Koslowski, "Towards quantitative magnetic force microscopy: theory and experiment", New Journal of Physics **14**, 043044 (2012).

[69] O. Kazakova, R. Puttock, C. Barton, H. Corte-León, M. Jaafar, V. Neu, and A. Asenjo, "Frontiers of magnetic force microscopy", J. Appl. Phys. **125**, 060901 (2019).

[70] Z. Qiu and S. D. Bader, "Surface magneto-optic kerr effect", Rev. Sci. Instrum. **71**, 1243 (2000).

[71] R. Schäfer, "Investigation of domains and dynamics of domain walls by the magneto-optical kerr-effect", in *Handbook of magnetism and advanced magnetic materials* (Wiley Online Library, 2007).

[72] I. Soldatov and R. Schäfer, "Selective sensitivity in kerr microscopy", Rev. Sci. Instrum. **88**, 073701 (2017).

[73] J. M. Coey, "Ferromagnetism and exchange", in *Magnetism and magnetic materials* (Cambridge university press, 2010) Chap. 5.

[74] H. Ebert, A. Vernes, and J. Banhart, "Magnetoresistance, Anisotropic", in *Encyclopedia of Materials: Science and Technology*, edited by K. H. J. Buschow, R. W. Cahn, M. C. Flemings, B. Ilschner, E. J. Kramer, S. Mahajan, and P. Veyssière (Elsevier, Oxford, 2001), pp. 5079–5083.

[75] T. McGuire and R. Potter, "Anisotropic magnetoresistance in ferromagnetic 3d alloys", IEEE Trans. Magn. **11**, 1018 (1975).

[76] C. Wang, W. Su, Z. Hu, J. Pu, M. Guan, B. Peng, L. Li, W. Ren, Z. Zhou, Z. Jiang, et al., "Highly sensitive magnetic sensor based on anisotropic magnetoresistance effect", IEEE Trans. Magn. **54**, 1 (2018).

[77] W. Gil, D. Görlitz, M. Horisberger, and J. Kötzler, "Magnetoresistance anisotropy of polycrystalline cobalt films: Geometrical-size and domain effects", Phys. Rev. B **72**, 134401 (2005).

[78] S. Tumanski, *Handbook of magnetic measurements* (CRC Press, Series in Sensors, Ed. B. Jones, H. Huang, 2011).

[79] C. Zheng, K. Zhu, S. C. De Freitas, J.-Y. Chang, J. E. Davies, P. Eames, P. P. Freitas, O. Kazakova, C. Kim, C.-W. Leung, et al., "Magnetoresistive sensor development roadmap (non-recording applications)", IEEE Trans. Magn. **55**, 1 (2019).

[80] P. M. Drljača, F. Vincent, P.-A. Besse, and R. S. Popović, "Design of planar magnetic concentrators for high sensitivity hall devices", Sens. Actuator A Phys. **97**, 10 (2002).

[81] P. Leroy, C. Coillot, A. F. Roux, and G. M. Chanteur, "High magnetic field amplification for improving the sensitivity of hall sensors", IEEE Sens. J. **6**, 707 (2006).

[82] A. Edelstein, G. Fischer, M. Pedersen, E. Nowak, S. F. Cheng, and C. Nordman, "Progress toward a thousandfold reduction in 1/ f noise in magnetic sensors using an ac microelectromechanical system flux concentrator", J. Appl. Phys. **99**, 08B317 (2006).

[83] Z. Marinho, S. Cardoso, R. Chaves, R. Ferreira, L. Melo, and P. Freitas, "Three dimensional magnetic flux concentrators with improved efficiency for magnetoresistive sensors", J. Appl. Phys. **109**, 07E521 (2011).

[84] X. Sun, L. Jiang, and P. W. Pong, "Magnetic flux concentration at micrometer scale", Microelectron. Eng. **111**, 77 (2013).

[85] Y. Bi, X. M. Zhang, and W. J. Wang, "Design study of trapezoid-shaped magnetic flux concentrator for axial amplification characteristics", in Applied mechanics and materials, Vol. 875 (Trans Tech Publ, 2018), pp. 77–83.

[86] V. Annapureddy, H. Palneedi, G.-T. Hwang, M. Peddigari, D.-Y. Jeong, W.-H. Yoon, K.-H. Kim, and J. Ryu, "Magnetic energy harvesting with magnetoelectrics: an emerging technology for self-powered autonomous systems", Sustain. Energy Fuels **1**, 2039 (2017).

[87] H. Song, D. R. Patil, W.-H. Yoon, K.-H. Kim, C. Choi, J.-H. Kim, G.-T. Hwang, D.-Y. Jeong, and J. Ryu, "Significant power enhancement of magneto-mechano-electric generators by magnetic flux concentration", Energy Environ. Sci. **13**, 4238 (2020).

[88] J. Prat-Camps, C. Navau, and A. Sanchez, "Experimental realization of magnetic energy concentration and transmission at a distance by metamaterials", Appl. Phys. Lett. **105**, 234101 (2014).

[89] C. Navau, R. Mach-Batlle, A. Parra, J. Prat-Camps, S. Laut, N. Del-Valle, and A. Sanchez, "Enhancing the sensitivity of magnetic sensors by 3d metamaterial shells", Sci. Rep. **7**, 1 (2017).

[90] X. Zhang, Y. Bi, G. Chen, J. Liu, J. Li, K. Feng, C. Lv, and W. Wang, "Influence of size parameters and magnetic field intensity upon the amplification characteristics of magnetic flux concentrators", AIP Adv. **8**, 125222 (2018).

[91] K. Y. Guslienko, V. Novosad, Y. Otani, H. Shima, and K. Fukamichi, "Field evolution of magnetic vortex state in ferromagnetic disks", Appl. Phys. Lett. **78**, 3848 (2001).

[92] H. T. Huang, T. R. Ger, Y. H. Lin, and Z. H. Wei, "Single cell detection using a magnetic zigzag nanowire biosensor", Lab Chip **13**, 3098 (2013).

[93] D. Su, K. Wu, and J. P. Wang, "Large-area GMR bio-sensors based on reverse nucleation switching mechanism", J. Magn. Magn. Mater. **473**, 484 (2019).

[94] T. Wren and O. Kazakova, "Anisotropic magnetoresistance effect in sub-micron nickel disks", J. Appl. Phys. **117**, 17E134 (2015) (2015).

[95] P. Perna, D. Maccariello, F. Ajejas, R. Guerrero, L. Méchin, S. Flament, J. Santamaria, R. Miranda, and J. Camarero, "Engineering Large Anisotropic Magnetoresistance in $La_{0.7}Sr_{0.3}MnO_3$ Films at Room Temperature", Adv. Funct. Mater. **27**, 1 (2017).

[96] P. Vavassori, V. Metlushko, B. Ilic, M. Gobbi, M. Donolato, M. Cantoni, and R. Bertacco, "Domain wall displacement in Py square ring for single nanometric magnetic bead detection", Appl. Phys. Lett. **93**, 10 (2008).

[97] M. Hayashi, L. Thomas, C. Rettner, R. Moriya, X. Jiang, and S. S. P. Parkin, "Dependence of current and field driven depinning of domain walls on their structure and chirality in permalloy nanowires", Phys. Rev. Lett. **97**, 1 (2006).

[98] G. Lin, D. Makarov, G. Lin, and O. G. Schmidt, "Magnetic sensing platform technologies for biomedical applications", Lab Chip **17**, 1884 (2017).

[99] T. Y. Chung and S. Y. Hsu, "Magnetization reversal in single domain Permalloy wires probed by magnetotransport", J. Appl. Phys. **103**, 18 (2008).

[100] V. D. Nguyen, L. Vila, P. Laczkowski, A. Marty, T. Faivre, and J. P. Attané, "Detection of domain-wall position and magnetization reversal in nanostructures using the magnon contribution to the resistivity", Phys. Rev. Lett. **107**, 1 (2011).

[101] J. S. Lee, J. Yoon, M. B. Kang, and C. Y. You, "Low coercivity giant magnetoresistance with perpendicular magnetic anisotropy", J. Magn. Magn. Mater. **358-359**, 159 (2014).

[102] "Thickness-dependent magnetic excitations in Permalloy films with nonuniform magnetization", Phys. Rev. B **69**, 1 (2004).

[103] M. Viret, D. Vignoles, D. Cole, J. M. D. Coey, W. Allen, D. S. Daniel, and J. F. Gregg, "Spin scattering in ferromagnetic thin films", Phys. Rev. B **53**, 8464 (1996).

[104] S. N. Kozlov, O. V. Skryabina, S. V. Egorov, I. A. Golovchanskiy, A. A. Klimenko, K. S. Napolskii, and V. S. Stolyarov, "Magnetoresistance of a single polycrystalline nickel nanowire", J. Appl. Phys. **125**, 0 (2019).

[105] A. Aharoni, "Angular dependence of nucleation by curling in a prolate spheroid", J. Appl. Phys. **82**, 1281 (1997).

[106] L. Sun, Y. Hao, C. L. Chien, P. C. Searson, and P. C. Searson, "Tuning the properties of magnetic nanowires", IBM J. Res. Dev. **49**, 79 (2005).

[107] L. Van Thiem, L. T. Tu, and M. H. Phan, "Magnetization reversal and magnetic anisotropy in ordered CoNiP nanowire arrays: Effects of wire diameter", Sensors **15**, 5687 (2015).

[108] J. Zhang, S. Zhu, H. Li, L. Zhu, Y. Hu, W. Xia, X. Zhang, Y. Peng, and J. Fu, "Direct observation of dynamical magnetization reversal process governed by shape anisotropy in single NiFe2O4 nanowire", Nanoscale **10**, 10123 (2018).

[109] M. S. Sultan, "Angular dependence of switching behaviour in template released isolated NiFe nanowires", Phys. lett. A, **381**, 3896 (2017).

[110] H. Sato, R. Hanada, H. Sugawara, Y. Aoki, T. Ono, H. Miyajima, and T. Shinjo, "Local magnetization rotation in NiFe wire monitored by multiple transverse probes", Phys. Rev. B **61**, 3227 (2000).

[111] S. Singh, H. Gao, and U. Hartmann, "Nucleation of stripe domains in thin ferromagnetic films", Phys. Rev. B **98**, 10.1103/PhysRevB.98.060414 (2018).

[112] J. McCord, B. Erkartal, T. von Hofe, L. Kienle, E. Quandt, O. Roshchupkina, and J. Grenzer, "Revisiting magnetic stripe domains—anisotropy gradient and stripe asymmetry", J. Appl. Phys. **113**, 073903 (2013).

[113] N. Eden, G. Kopnov, S. Fraenkel, M. Goldstein, and A. Gerber, "Longitudinal and transverse magnetoresistance in films with tilted out-of-plane magnetic anisotropy", Phys. Rev. B **99**, 064432 (2019).

[114] Z. Ali, D. Basaula, K. Eid, and M. Khan, "Anisotropic properties of oblique angle deposited permalloy thin films", Thin Solid Films **735**, 138899 (2021).

[115] B. Belyaev, A. Izotov, and P. Solovev, "Competing magnetic anisotropies in obliquely deposited thin permalloy film", Physica B Condens. **481**, 86 (2016).

[116] G. Wang, C. Dong, W. Wang, Z. Wang, G. Chai, C. Jiang, and D. Xue, "Observation of rotatable stripe domain in permalloy films with oblique sputtering", J. Appl. Phys. **112**, 093907 (2012).

[117] Z. Ali, D. Basaula, W. Zhou, J. Brock, M. Khan, and K. Eid, "Controlling the charge transport mode in permalloy films using oblique angle deposition", J. Magn. Magn. Mater. **484**, 430 (2019).

[118] M. Prutton, "Stress and magnetic anisotropy in thin permalloy films", Nature **193**, 565 (1962).

[119] J. O. Rantschler, P. Chen, A. S. Arrott, R. D. McMichael, W. F. Egelhoff Jr, and B. B. Maranville, "Surface anisotropy of permalloy in NM/NiFe/NM multilayers", J. Appl. Phys. **97**, 10J113 (2005).

[120] "Dynamic magnetic properties of amorphous $Fe_{80}B_{20}$ thin films and their relation to interfaces", AIP Adv. **10**, 1 (2020).

[121] T. Valet and A. Fert, "Theory of the perpendicular magnetoresistance in magnetic multilayers", Phys. Rev. B **48**, 7099 (1993).

[122] S. O. Valenzuela, "Nonlocal electronic spin detection, spin accumulation and the spin hall effect", International Journal of Modern Physics B **23**, 2413 (2009).

[123] I. Žutić, J. Fabian, and S. D. Sarma, "Spintronics: fundamentals and applications", Rev. Mod. Phys. **76**, 323 (2004).

[124] F. Jedema, "Electrical spin injection in metallic mesoscopic spin valves", Relation: http://www.rug.nl/, date submitted:2003, Rights: University of Groningen, PhD thesis (2002).

[125] J. Fabian, A. Abiague, C. Ertler, P. Stano, and I. Zutic, "Semiconductor spintronics", Acta Phys. Slovaca **57**, 565 (2007).

[126] M. I. Dyakonov, "Spin injection", in *Spin physics in semiconductors (2nd ed.)* Vol. 157 (Springer, 2017) Chap. 10.

[127] A. Fert and I. Campbell, "Two-current conduction in nickel", Phys. Rev. Lett. **21**, 1190 (1968).

[128] S. Blundell, "Magnetism in metals", in *Magnetism in condensed matter* (American Association of Physics Teachers, 2003) Chap. 7.

[129] M. Johnson and R. Silsbee, "Thermodynamic analysis of interfacial transport and of the thermomagnetoelectric system", Phys. Rev. B **35**, 4959 (1987).

[130] R. Jansen, S. P. Dash, S. Sharma, and B. C. Min, "Silicon spintronics with ferromagnetic tunnel devices", Semicond. Sci. Technol. **27**, 083001 (2012).

[131] G. Schmidt, D. Ferrand, L. Molenkamp, A. Filip, and B. Van Wees, "Fundamental obstacle for electrical spin injection from a ferromagnetic metal into a diffusive semiconductor", Phys. Rev. B **62**, R4790 (2000).

[132] E. Rashba, "Theory of electrical spin injection: tunnel contacts as a solution of the conductivity mismatch problem", Phys. Rev. B **62**, R16267 (2000).

[133] E. L. Wolf, *Principles of electron tunneling spectroscopy* (Oxford University Press, New-York, 1989).

[134] J. C. Slonczewski, "Conductance and exchange coupling of two ferromagnets separated by a tunneling barrier", Phys. Rev. B **39**, 6995 (1989).

[135] G.-X. Miao, M. Münzenberg, and J. S. Moodera, "Tunneling path toward spintronics", Rep. Prog. Phys. **74**, 036501 (2011).

[136] J. S. Moodera, T. S. Santos, and T. Nagahama, "The phenomena of spin-filter tunnelling", J. Phys. Condens. Matter. **19**, 165202 (2007).

[137] J. H. Davies, *The physics of low-dimensional semiconductors: an introduction* (Cambridge university press, 1998).

[138] S. O. Valenzuela, D. J. Monsma, C. M. Marcus, V. Narayanamurti, and M. Tinkham, "Spin Polarized Tunneling at Finite Bias", Phys. Rev. Lett. **94**, 196601 (2005).

[139] A. Fert and H. Jaffrès, "Conditions for efficient spin injection from a ferromagnetic metal into a semiconductor", Phys. Rev. B **64**, 184420 (2001).

[140] S. Parkin, "Origin of enhanced magnetoresistance of magnetic multilayers: spin-dependent scattering from magnetic interface states", Phys. Rev. Lett. **71**, 1641 (1993).

[141] F. J. Jedema, A. Filip, and B. Van Wees, "Electrical spin injection and accumulation at room temperature in an all-metal mesoscopic spin valve", Nature **410**, 345 (2001).

[142] H. Jaffres and A. Fert, "Spin injection from a ferromagnetic metal into a semiconductor", J. Appl. Phys. **91**, 8111 (2002).

[143] O. Van't Erve, A. Hanbicki, M. Holub, C. Li, C. Awo-Affouda, P. Thompson, and B. Jonker, "Electrical injection and detection of spin-polarized carriers in silicon in a lateral transport geometry", Appl. Phys. Lett. **91**, 212109 (2007).

[144] M. Johnson and R. Silsbee, "Coupling of electronic charge and spin at a ferromagnetic-paramagnetic metal interface", Phys. Rev. B **37**, 5312 (1988).

[145] A. Spiesser, H. Saito, Y. Fujita, S. Yamada, K. Hamaya, S. Yuasa, and R. Jansen, "Giant spin accumulation in silicon nonlocal spin-transport devices", Phys. Rev. Appl. **8**, 064023 (2017).

[146] W. Han, R. K. Kawakami, M. Gmitra, and J. Fabian, "Graphene spintronics", Nature Nanotechnology **9**, 794 (2014).

[147] R.
bibinitperiod J. Elliott, "Theory of the effect of spin-orbit coupling on magnetic resonance in some semiconductors", Phys. Rev **96**, 266 (1954).

[148] M. Dyakonov and V. Perel, "Spin relaxation of conduction electrons in noncentrosymmetric semiconductors", Solid State Phys. **13**, 3023 (1972).

[149] G. Dresselhaus, "Spin-orbit coupling effects in zinc blende structures", Phys. Rev. **100**, 580 (1955).

[150] S. P. Dash, S. Sharma, R. S. Patel, M. P. de Jong, and R. Jansen, "Electrical creation of spin polarization in silicon at room temperature.", Nature **462**, 491 (2009).

[151] S. P. Dash, S. Sharma, J. C. Le Breton, J. Peiro, H. Jaffrès, J. M. George, A. Lemaître, and R. Jansen, "Spin precession and inverted Hanle effect in a semiconductor near a finite-roughness ferromagnetic interface", Phys. Rev. B **84**, 1 (2011).

[152] M. Tran, H. Jaffrès, C. Deranlot, J. George, A. Fert, A. Miard, and A. Lemaı, "Enhancement of the Spin Accumulation at the Interface between a Spin-Polarized Tunnel Junction and a Semiconductor", Phys.l Rev. Lett. **102**, 036601 (2009).

[153] E. Fourneau, A. V. Silhanek, and N. D. Nguyen, "Origin of the Giant Spin-Detection Efficiency in Tunnel-Barrier-Based Electrical", Phys. Rev. Appl. **14**, 024020 (2020).

[154] T. Suzuki, T. Sasaki, T. Oikawa, M. Shiraishi, Y. Suzuki, and K. Noguchi, "Room-Temperature Electron Spin Transport in a Highly Doped Si Channel", Appl. Phys. Express **4**, 023003 (2011).

[155] M. Ishikawa, T. Oka, Y. Fujita, H. Sugiyama, Y. Saito, and K. Hamaya, "Spin relaxation through lateral spin transport in heavily doped n -type silicon", Phys. Rev. B **95**, 115302 (2017).

[156] A. Spiesser, H. Saito, R. Jansen, S. Yuasa, and K. Ando, "Large spin accumulation voltages in epitaxial Mn_5Ge_3 contacts on ge without an oxide tunnel barrier", Phys. Rev. B **90**, 205213 (2014).

[157] M. Yamada, M. Tsukahara, Y. Fujita, T. Naito, S. Yamada, K. Sawano, and K. Hamaya, "Room-temperature spin transport in n-Ge probed by four-terminal nonlocal measurements", Appl. Phys. Express **10**, 093001 (2017).

[158] Y. Fujita, M. Yamada, M. Tsukahara, T. Oka, S. Yamada, T. Kanashima, K. Sawano, and K. Hamaya, "Spin Transport and Relaxation up to 250 K in Heavily Doped n -Type Ge Detected Using Co_2 $FeAl_{0.5}Si_{0.5}$ Electrodes", Phys. Rev. Appl. **8**, 014007 (2017).

[159] M. Ohishi, M. Shiraishi, R. Nouchi, T. Nozaki, T. Shinjo, and Y. Suzuki, "Spin injection into a graphene thin film at room temperature", Japan. J. Appl. Phys. **46**, L605 (2007).

[160] N. Tombros, C. Jozsa, M. Popinciuc, H. T. Jonkman, and B. J. Van Wees, "Electronic spin transport and spin precession in single graphene layers at room temperature", nature **448**, 571 (2007).

[161] X. Lou, C. Adelmann, M. Furis, S. A. Crooker, C. J. Palmstrøm, and P. A. Crowell, "Electrical detection of spin accumulation at a ferromagnet-semiconductor interface", Phys. Rev. Lett. **96**, 176603 (2006).

[162] M. Ishikawa, H. Sugiyama, T. Inokuchi, K. Hamaya, and Y. Saito, "Effect of the interface resistance of CoFe / MgO contacts on spin accumulation in silicon", Appl. Phys. Lett. **100**, 252404 (2012).

[163] T. Sasaki, T. Suzuki, Y. Ando, H. Koike, T. Oikawa, Y. Suzuki, and M. Shiraishi, "Local magnetoresistance in Fe / MgO / Si lateral spin valve at room temperature", Appl. Phys. Lett. **104**, 052404 (2014).

[164] S. Datta, "How we proposed the spin transistor", Nat. Electron. **1**, 604 (2018).

[165] Y. Fujita, M. Yamada, M. Tsukahara, T. Naito, S. Yamada, K. Sawano, and K. Hamaya, "Nonmonotonic bias dependence of local spin accumulation signals in ferromagnet/semiconductor lateral spin-valve devices", Phys. Rev. B **100**, 024431 (2019).

[166] A. Spiesser, Y. Fujita, H. Saito, S. Yamada, K. Hamaya, S. Yuasa, and R. Jansen, "Hanle spin precession in a two-terminal lateral spin valve Hanle spin precession in a two-terminal lateral spin valve", Appl. Phys. Lett. **14**, 242401 (2019).

[167] T. Naito, M. Yamada, S. Yamada, and T. Kanashima, "Inverse local magnetoresistance effect up to room temperature in ferromagnet-semiconductor lateral spin-valve devices", Mat. Sci. in Semicon. Proc. **113**, 105046 (2020).

[168] R. Jansen, A. M. Deac, H. Saito, and S. Yuasa, "Injection and detection of spin in a semiconductor by tunneling via interface states", Phys. Rev. B **134420**, 134420 (2012).

[169] R. Jansen, A. Spiesser, H. Saito, and S. Yuasa, "Nonlinear spin transport in a rectifying ferromagnet/semiconductor Schottky contact", Phys. Rev. B **92**, 075304 (2015).

[170] M. Kameno, Y. Ando, E. Shikoh, T. Shinjo, T. Sasaki, T. Oikawa, T. Suzuki, Y. Suzuki, and M. Shiraishi, "Effect of spin drift on spin accumulation voltages in highly doped silicon", Appl. Phys. Lett. **101**, 122413 (2012).

[171] M. Ishikawa, H. Sugiyama, T. Inokuchi, K. Hamaya, and Y. Saito, "Spin transport and accumulation in n^+-Si using Heusler compound Co_2FeSi/MgO tunnel contacts", Appl. Phys. Lett. **107**, 092402 (2016).

[172] T. A. Peterson, S. J. Patel, C. C. Geppert, K. D. Christie, A. Rath, D. Pennachio, and M. E. Flatt, "Spin injection and detection up to room temperature in Heusler alloy / n -GaAs spin valves", Phys. Rev. B **93**, 235309 (2016).

[173] T. Tahara, Y. Ando, M. Kameno, H. Koike, K. Tanaka, S. Miwa, Y. Suzuki, T. Sasaki, T. Oikawa, and M. Shiraishi, "Observation of large spin accumulation voltages in nondegenerate Si spin devices due to spin drift effect : Experiments and theory", Phys. Rev. B **93**, 214406 (2016).

[174] M. Oltscher, F. Eberle, T. Kuczmik, A. Bayer, D. Schuh, D. Bougeard, M. Ciorga, and D. Weiss, "Gate-tunable large magnetoresistance in an all-semiconductor spin-transistor-like device", Nat. Commun. **8**, 1807 (2017).

[175] S. Sato, R. Nakane, T. Hada, and M. Tanaka, "Spin injection into silicon in three-terminal vertical and four-terminal lateral devices with Fe/Mg/MgO/Si tunnel junctions having an ultrathin Mg insertion layer", Phys. Rev. B **96**, 235204 (2017).

[176] R. Jansen, A. Spiesser, H. Saito, Y. Fujita, S. Yamada, K. Hamaya, and S. Yuasa, "Nonlinear electrical spin conversion in a biased ferromagnetic tunnel contact", Phys. Rev. Appl. **10**, 064050 (2018).

[177] M. Razeghi, *Fundamentals of solid state engineering*, 3rd (Springer Publishing Company, Incorporated, 2009) Chap. 4.

[178] J. H. Davies, *The physics of low-dimensional semiconductors: an introduction* (Cambridge University Press, 1997).

[179] K. Gundlach and J. Simmons, "Range of validity of the wkb tunnel probability, and comparison of experimental data and theory", Thin Solid Films **4**, 61 (1969).

[180] R. A. Vega, "Comparison study of tunneling models for schottky field effect transistors and the effect of schottky barrier lowering", IEEE transactions on electron devices **53**, 1593 (2006).

[181] S. Kale and P. N. Kondekar, "Design and investigation of dielectric engineered dopant segregated schottky barrier mosfet with nisi source/drain", IEEE Transactions on Electron Devices **64**, 4400 (2017).

[182] M. Gurram, S. Omar, and B. J. V. Wees, "Bias induced up to 100% spin-injection and detection polarizations in ferromagnet/bilayer-hBN/graphene/hBN heterostructures", Nat. Commun. **8**, 1 (2017).

[183] R. Jansen, B. Min, S. Dash, S. Sharma, G. Kioseoglou, A. Hanbicki, O. van 't Erve, P. Thompson, and B. Jonker, "Electrical spin injection into moderately doped silicon enabled by tailored interfaces", Phys. Rev. B **82**, 241305(R) (2010).

[184] A. Türüt, B. Bati, A. Kökce, M. Saglam, and N. Yalcin, "The bias-dependence change of barrier height of Schottky diodes under forward bias by including the series resistance effect", Phys. Scr. **53**, 118 (1996).

[185] R. Jansen and B. C. Min, "Detection of a Spin Accumulation in Nondegenerate Semiconductors", Phys. Rev. Lett. **99**, 246604 (2007).

[186] M. Kameno, Y. Ando, E. Shikoh, T. Shinjo, T. Sasaki, T. Oikawa, Y. Suzuki, T. Suzuki, and M. Shiraishi, "Effect of spin drift on spin accumulation voltages in highly doped silicon", Appl. Phys. Lett. **104**, 092409 (2014).

[187] A. T. Hanbicki, S. Cheng, R. Goswami, O. M. J. V. Erve, and B. T. Jonker, "Electrical injection and detection of spin accumulation in Ge at room temperature", Solid State Commun. **152**, 244 (2012).

[188] A. Avsar, H. Ochoa, F. Guinea, B. Özyilmaz, B. J. van Wees, and I. J. Vera-Marun, "Colloquium : Spintronics in graphene and other two-dimensional materials", Rev. Mod. Phys. **92**, 21003 (2020).

[189] M. H. D. Guimarães, P. J. Zomer, J. C. Brant, N. Tombros, and B. J. V. Wees, "Controlling Spin Relaxation in Hexagonal BN-Encapsulated Graphene with a Transverse Electric Field", Phys. Rev. Lett. **113**, 086602 (2014).

[190] M. Drögeler, C. Franzen, F. Volmer, T. Pohlmann, L. Banszerus, M. Wolter, K. Watanabe, T. Taniguchi, C. Stampfer, and B. Beschoten, "Spin Lifetimes Exceeding 12 ns in Graphene Nonlocal Spin Valve Devices", Nano lett. **16**, 3533 (2016).

[191] J. Ingla-Aynés, R. J. Meijerink, and B. J. V. Wees, "Eighty-Eight Percent Directional Guiding of Spin Currents with 90 μm Relaxation Length in Bilayer Graphene Using Carrier Drift", Nano lett. **16**, 4825 (2016).

[192] Z. M. Gebeyehu, S. Parui, J. F. Sierra, M. Timmermans, M. J. Esplandiu, S. Brems, C. Huyghebaert, K. Garello, M. V. Costache, and S. O. Valenzuela, "Spin communication over 30 μm long channels of chemical vapor deposited graphene on SiO_2", 2D Mater. **6**, 034003 (2019).

[193] D. Huertas-Hernando, F. Guinea, and A. Brataas, "Spin-Orbit-Mediated Spin Relaxation in Graphene", Phys. Rev. Lett. **103**, 146801 (2009).

[194] B. Raes, J. E. Scheerder, M. V. Costache, F. Bonell, J. F. Sierra, J. Cuppens, J. Van De Vondel, and S. O. Valenzuela, "Determination of the spin-lifetime anisotropy in graphene using oblique spin precession", Nat. Commun. **7**, 1 (2016).

[195] B. Raes, A. W. Cummings, F. Bonell, M. V. Costache, J. F. Sierra, S. Roche, and S. O. Valenzuela, "Spin precession in anisotropic media", Phys. Rev. B **95**, 085403 (2017).

[196] X. Lou, C. Adelmann, S. A. Crooker, E. S. Garlid, J. Zhang, K. S. M. Reddy, S. D. Flexner, C. J. Palmstrøm, and P. A. Crowell, "Electrical detection of spin transport in lateral ferromagnet–semiconductor devices", Nat. Phys. **3**, 197 (2007).

[197] F. Volmer, M. Drögeler, E. Maynicke, N. von den Driesch, M. L. Boschen, G. Güntherodt, and B. Beschoten, "Role of MgO barriers for spin and charge transport in Co/MgO/graphene nonlocal spin-valve devices", Phys. Rev. B **88**, 161405 (2013).

[198] E. Sosenko, H. Wei, and V. Aji, "Effect of contacts on spin lifetime measurements in graphene", Phys. Rev. B **89**, 245436 (2014).

[199] F. Volmer, M. Drögeler, T. Pohlmann, G. Güntherodt, and C. Stampfer, "Contact-induced charge contributions to non-local spin transport measurements in Co/MgO/graphene devices", 2D Mater. **2**, 024001 (2015).

[200] M. V. Kamalakar, A. Dankert, P. J. Kelly, and S. P. Dash, "Inversion of Spin Signal and Spin Filtering in Ferromagnet | Hexagonal Boron Nitride-Graphene van der Waals Heterostructures", Sci. Rep., 21168 (2016).

[201] G. Stecklein, P. A. Crowell, J. Li, Y. Anugrah, Q. Su, and S. J. Koester, "Contact-Induced Spin Relaxation in Graphene Nonlocal Spin Valves", Phys. Rev. Appl. **6**, 054015 (2016).

[202] W. Amamou, Z. Lin, J. V. Baren, S. Turkyilmaz, J. Shi, and R. K. Kawakami, "Contact induced spin relaxation in graphene spin valves with Al_2O_3 and MgO tunnel barriers", APL Mater. **4**, 032503 (2016).

[203] T. Maassen, I. J. Vera-Marun, M. H. D. Guimar, and B. J. van Wees, "Contact-induced spin relaxation in Hanle spin precession measurements", Phys. Rev. B **86**, 235408 (2012).

[204] H. Idzuchi, A. Fert, and Y. Otani, "Revisiting the measurement of the spin relaxation time in graphene-based devices", Phys. Rev. B **91**, 241407 (2015).

[205] M. Wojtaszek, I. J. Vera-Marun, and B. J. van Wees, "Transition between one-dimensional and zero-dimensional spin transport studied by Hanle precession", Phys. Rev. B **89**, 245427 (2014).

[206] M. Drögeler, F. Volmer, C. Stampfer, and B. Beschoten, "Simulations on the Influence of Spatially Varying Spin Transport Parameters on the Measured Spin Lifetime in Graphene Non-Local Spin Valves", Phys. Status Solidi B, 1700293 (2017).

[207] M. Vila, J. H. Garcia, A. W. Cummings, S. R. Power, C. W. Groth, X. Waintal, and S. Roche, "Nonlocal Spin Dynamics in the Crossover from Diffusive to Ballistic Transport", Phys. Rev. Lett. **124**, 196602 (2020).

[208] C. Jozsa, M. Popinciuc, N. Tombros, H. T. Jonkman, B. J. V. Wees, and C. Jo, "Electronic Spin Drift in Graphene Field-Effect Transistors", Phys. Rev. Lett. **100**, 236603 (2008).

[209] W. Han, K. Pi, K. M. Mccreary, Y. Li, J. J. I. Wong, A. G. Swartz, and R. K. Kawakami, "Tunneling Spin Injection into Single Layer Graphene", Phys. Rev. Lett. **105**, 167202 (2010).

[210] W. Han, K. M. Mccreary, K. Pi, W. H. Wang, Y. Li, H. Wen, J. R. Chen, and R. K. Kawakami, "Spin transport and relaxation in graphene", J. Magn. Magn. Mater. **324**, 369 (2012).

[211] I. Neumann, M. V. Costache, G. Bridoux, J. F. Sierra, and S. O. Valenzuela, "Enhanced spin accumulation at room temperature in graphene spin valves with amorphous carbon interfacial layers", Appl. Phys. Lett. **112401**, 112401 (2013).

[212] A. J. Berger, M. R. Page, H. Wen, K. M. Mccreary, V. P. Bhallamudi, K. Roland, and P. C. Hammel, "Correlating spin transport and electrode magnetization in a graphene spin valve : Simultaneous magnetic microscopy and non-local measurements", Appl. Phys. Lett. **107**, 142406 (2015).

[213] M. H. D. Guimarães, J. J. van den Berg, I. J. Vera-Marun, P. J. Zomer, and B. J. van Wees, "Spin transport in graphene nanostructures", Phys. Rev. B **90**, 235428 (2014).

[214] N. Tombros, S. Tanabe, A. Veligura, C. Jozsa, M. Popinciuc, H. T. Jonkman, and B. J. V. Wees, "Anisotropic Spin Relaxation in Graphene", Phys. Rev. Lett. **101**, 046601 (2008).

[215] M. Popinciuc, C. Józsa, P. J. Zomer, N. Tombros, A. Veligura, H. T. Jonkman, and B. J. V. Wees, "Electronic spin transport in graphene field-effect transistors", Phys. Rev. B **80**, 214427 (2009).

[216] C. Józsa, M. Popinciuc, N. Tombros, H. T. Jonkman, and B. J. V. Wees, "Controlling the efficiency of spin injection into graphene by carrier drift", Phys. Rev. B **79**, 081402(R) (2009).

[217] M. H. D. Guimarães, A. Veligura, P. J. Zomer, T. Maassen, N. Tombros, and B. J. V. Wees, "Spin Transport in High-Quality Suspended Graphene Devices", Nano lett. **12**, 3512 (2012).

[218] P. J. Zomer, M. H. D. Guimarães, N. Tombros, and B. J. van Wees, "Long-distance spin transport in high-mobility graphene on hexagonal boron nitride", Phys. Rev. B. **86**, 161416(R) (2012).

[219] M. V. Kamalakar, C. Groenveld, A. Dankert, and S. P. Dash, "Long distance spin communication in chemical vapour deposited graphene", Nat. Commun. **6**, 1 (2015).

[220] W. S. Torres, J. F. Sierra, L. A. Benítez, F. Bonell, M. V. Costache, and S. O. Valenzuela, "Spin precession and spin Hall effect in monolayer graphene/Pt nanostructures", 2D Mater. **4**, 041008 (2017).

[221] M. V. Kamalakar, J. Bergsten, T. Ive, and S. P. Dash, "Enhanced Tunnel Spin Injection into Graphene using Chemical Vapor Deposited Hexagonal Boron Nitride", Sci. Rep. **4**, 6146 (2014).

[222] S. Singh, J. Katoch, T. Zhu, R. J. Wu, A. S. Ahmed, W. Amamou, D. Wang, K. A. Mkhoyan, and R. K. Kawakami, "Strontium Oxide Tunnel Barriers for High Quality Spin Transport and Large Spin Accumulation in Graphene", Nano lett. **17**, 7578 (2017).

[223] A. L. Friedman, C. H. Li, J. T. Robinson, and B. T. Jonker, "Homoepitaxial tunnel barriers with functionalized graphene-on-graphene for charge and spin transport", Nat. Commun. **5**, 3161 (2014).

[224] T. Maassen, F. K. Dejene, M. H. D. Guimarães, C. Jozsa, and B. J. van Wees, "Comparison between charge and spin transport in few-layer graphene", Phys. Rev. B **83**, 115410 (2011).

[225] S. Chen, R. Ruiter, V. Mathkar, B. J. V. Wees, and T. Banerjee, "Temperature and Electric Field Dependence of Spin Relaxation in Graphene on SrTiO 3", Phys. Status Solidi RRL **12**, 1800216 (2018).

[226] J. C. Leutenantsmeyer, J. Ingla-Aynés, M. Gurram, and B. J. van Wees, "Efficient spin injection into graphene through trilayer hBN tunnel barriers", J. Appl. Phys. **124**, 194301 (2018).

[227] E. Fourneau, A. V. Silhanek, and N. D. Nguyen, "Roadmap for the Design of All Ferromagnetic Four-Terminal Spin Valves and the Extraction of Spin Diffusion Length", Phys. Rev. Appl. **15**, 034058 (2021).

[228] G. Zebrev, "Graphene field effect transistors: diffusion-drift theory", in *Physics and applications of graphene - theory*, edited by S. Mikhailov (InTech, Janeza Trdine 9, 51000 Rijeka, Croatia, 2011) Chap. 23, pp. 475–498.

About the author

Personal data

First name	Emile
Last name	Fourneau
Place and	Namur
date of birth	the 27th of October 1992
Nationality	Belgian

Education

2016-2022 Ph.D. Thesis in Science (Physics), University of Liège
Static and dynamic properties of selected micromagnetic devices
Advisors : Prof. Dr. N. D. Nguyen & Prof. Dr. A. V. Silhanek

2013-2015 Master's Degree in material sciences, Civil engineering
Ecole Polytechnique de Louvain
Ab initio study of an superionic conductor, $Li_{10}Ge_2S_{12}$

2010-2013 Bachelor's Degree in Civil engineering
Ecole Polytechnique de Louvain

List of publications

Electromigration-induced resistance switching in indented Al microstrips
J. Lombardo, S. Collienne, A. Petrillo, E. Fourneau, N. D. Nguyen, A. V. Silhanek,
New Journal of Physics, **21**, 113015 (2019).

Origin of the Giant Spin-Detection Efficiency in Tunnel-Barrier-Based Electrical Spin Detectors
E. Fourneau, A. V. Silhanek, N. D. Nguyen,
Physical Review Applied, **14**, 024020 (2020).

Roadmap for the Design of All Ferromagnetic Four-Terminal Spin Valves and the Extraction of Spin Diffusion Length
E. Fourneau, A. V. Silhanek, N. D. Nguyen,
Physical Review Applied, **15**, 034058 (2021).

Mg-doped Cu_2O thin films with enhanced functional properties grown by magnetron sputtering under optimized pressure conditions
N. Sliti, E. Fourneau, T. Ratz, S. Touihri, N. D. Nguyen,
Ceramics International, **48**, 23748–23754 (2022).

Tunable domino effect of thermomagnetic instabilities in superconducting films with multiply-connected topological structures
Lu Jiang, Cun Xue, S. Marinković, E. Fourneau, Xin-Wei Cai, A.V. Silhanek, You-He Zhou,
New Journal of Physics, **24**, 083017 (2022).

From Electric Doping Control to Thermal Defect Nucleation in Perovskites
S. Marinković, A Fernandez-Rodriguez, E. Fourneau, M. Cabero, H. Wang, N. D. Nguyen, J. Gazquez, N. Mestres, A. Palau, A. V. Silhanek,
Advance Materials Interfaces, **Advance online publication**, (2022).